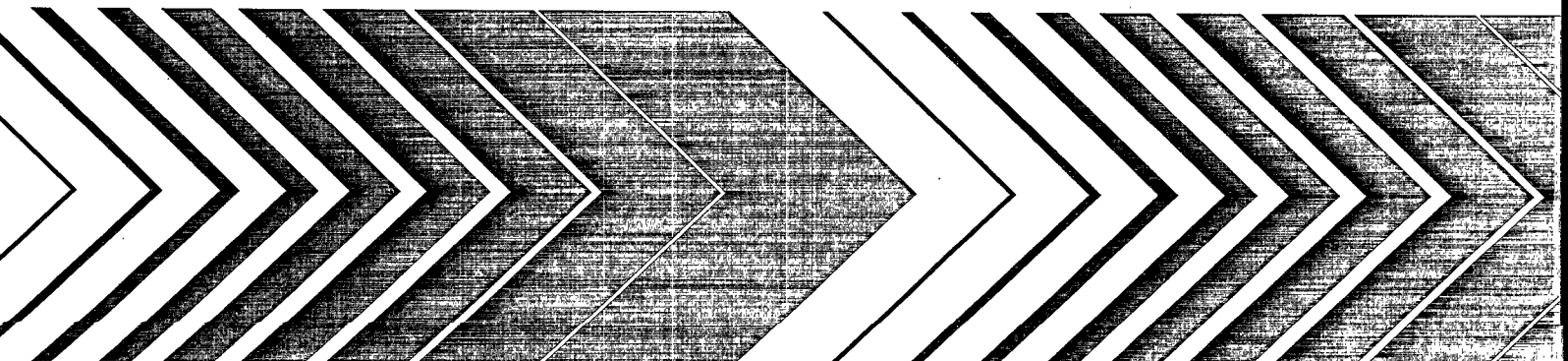
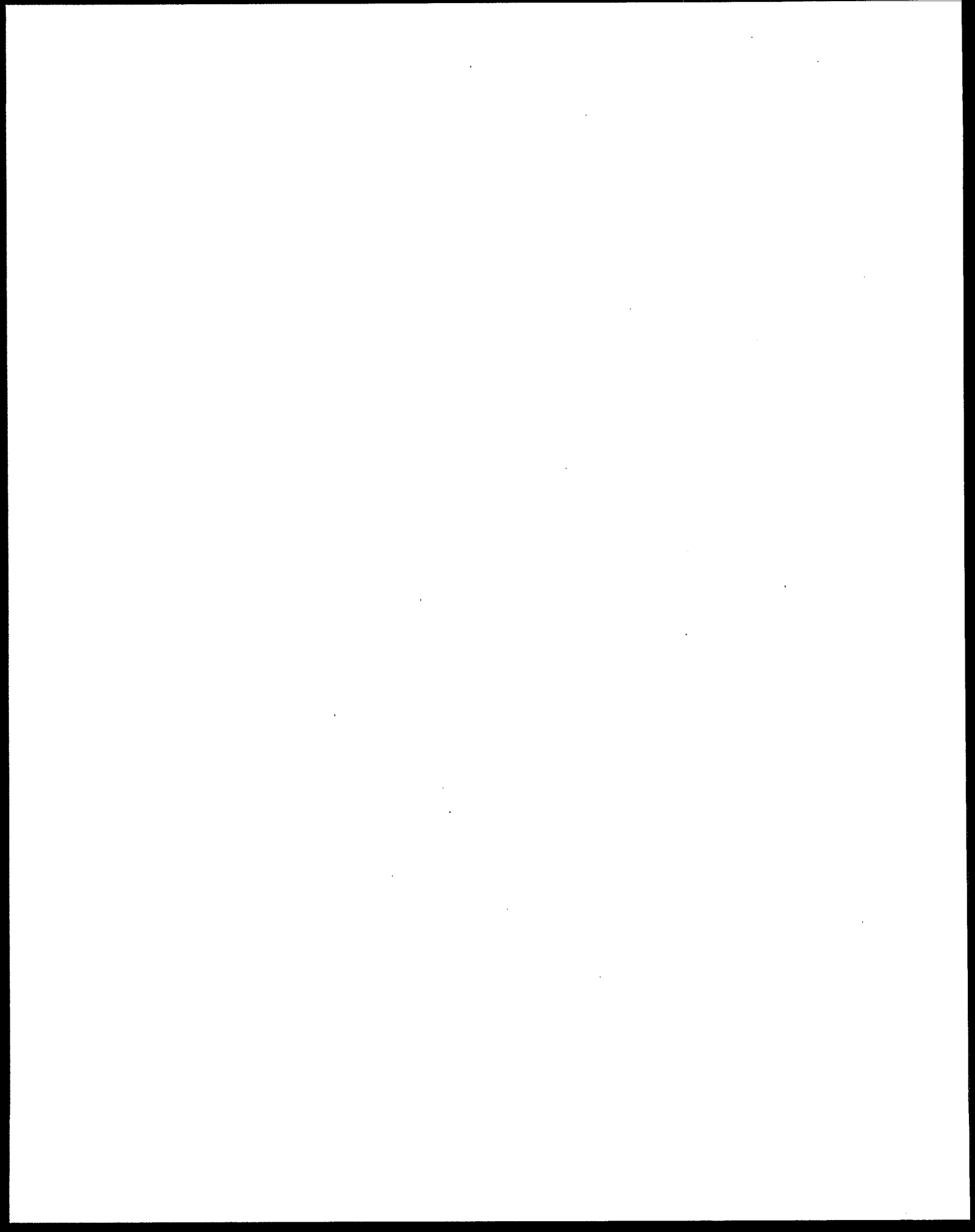




Evaluation and Analysis of Microscale Flow and Transport During Remediation





EVALUATION AND ANALYSIS OF MICROSCALE FLOW AND TRANSPORT DURING REMEDIATION

by

Yanis C. Yortsos
and
Katherine Shing
University of Southern California
Department of Chemical Engineering
Los Angeles, CA 90089-1211

CR-824592

Project Officer

Jong Soo Cho
Subsurface Protection and Remediation Division
National Risk Management Research Laboratory
Ada, Oklahoma 74820

NATIONAL RISK MANAGEMENT RESEARCH LABORATORY
OFFICE OF RESEARCH AND DEVELOPMENT
U.S. ENVIRONMENTAL PROTECTION AGENCY
CINCINNATI, OHIO 45268

NOTICE

The U.S. Environmental Protection Agency through its Office of Research and Development funded and managed the research described here under Cooperative Agreement Number CR-824592 to the University of Southern California, Los Angeles, CA. It has been subjected to the Agency's peer and administrative review, and has been approved for publication as an EPA document. Mention of trade names or commercial products does not constitute endorsement or recommendation for use.

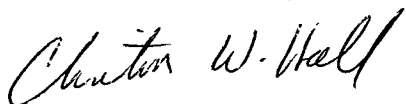
All research projects making conclusions or recommendations based on environmentally related measurements and funded by the Environmental Protection Agency are required to participate in the Agency Quality Assurance Program. This project did not involve environmentally related measurements and did not involve a Quality Assurance Project Plan.

FOREWORD

The U.S. Environmental Protection Agency is charged by Congress with protecting the Nation's land, air, and water resources. Under a mandate of national environmental laws, the Agency strives to formulate and implement actions leading to a compatible balance between human activities and the ability of natural systems to support and nurture life. To meet these mandates, EPA's research program is providing data and technical support for solving environmental problems today and building a science knowledge base necessary to manage our ecological resources wisely, understand how pollutants affect our health, and prevent or reduce environmental risks in the future.

The National Risk Management Research Laboratory is the Agency's center for investigation of technological and management approaches for reducing risks from threats to human health and the environment. The focus of the Laboratory's research program is on methods for the prevention and control of pollution to air, land, water, and subsurface resources; protection of water quality in public water systems; remediation of contaminated sites and ground water; and prevention and control of indoor air pollution. The goal of this research effort is to catalyze development and implementation of innovative, cost-effective environmental technologies; develop scientific and engineering information needed by EPA to support regulatory and policy decisions; and provide technical support and information transfer to ensure effective implementation of environmental regulations and strategies.

The design of in-situ remediation is currently based on a description at the macro-scale. Phenomena at the pore and pore-network scales are typically lumped in terms of averaged quantities, using empirical or *ad hoc* expressions. These models cannot address fundamental remediation issues at the pore and pore network scales, including: The emplacement in-situ of the contaminant *NAPL*, and the displacement patterns; the mass transfer of the contaminant from the *NAPL* to the groundwater or from the groundwater to a sparging fluid, and of the remedial agents to the *NAPL*; and possible microscale flow instabilities during injection of a remedial fluid. The objective of this work is to obtain a fundamental understanding by conducting theoretical, experimental and computational pore-scale studies. Emphasis is placed at the pore network scale. Use of this information can be incorporated in macroscopic simulators to provide fundamentally correct expressions for the various coefficients or parameters, currently treated empirically.



Clinton W. Hall, Director
Subsurface Protection and Remediation Division
National Risk Management Research Laboratory

ABSTRACT

The design of in-situ remediation is currently based on a description at the macroscopic scale. Phenomena at the pore and pore-network scales are typically lumped in terms of averaged quantities, using empirical or *ad hoc* expressions. These models cannot address fundamental remediation issues at the pore and pore network scales, including: The emplacement in-situ of the contaminant *NAPL*, and the displacement patterns; the mass transfer of the contaminant from the *NAPL* to the groundwater or from the groundwater to a sparging fluid, and of the remedial agents to the *NAPL*; and possible microscale flow instabilities during injection of a remedial fluid.

The objective of this work is to obtain a fundamental understanding by conducting theoretical, experimental and computational pore-scale studies. Emphasis is placed at the pore network scale. Use of this information can be incorporated in macroscopic simulators to provide fundamentally correct expressions for the various coefficients or parameters, currently treated empirically. The theoretical findings are compared with findings from experiments in glass micromodels and Hele-Shaw cells.

Specific tasks of the work described include: (1) The determination of immiscible displacement patterns that develop during seepage of *NAPLs* in the groundwater or during air sparging of contaminated groundwater. (2) The pore-scale study of the mass transfer from a trapped *NAPL* to an injected remedial fluid. (3) A sensitivity analysis of the effective mass transfer coefficient on parameters such as the flow rate and the pattern geometry. (4) Studies of pore-scale instabilities developing during miscible displacements in porous media, particularly when non-monotonic viscosity profiles are involved. (5) The up-scaling of the information obtained to the macroscopic scale. (6) Finally, the comparison of theoretical predictions with experimental results obtained in etched-glass micromodels and Hele-Shaw cells in order to validate and improve the theoretical models.

The research described here is expected to improve the fundamental understanding of remediation processes, to help in the more accurate design of remediation projects, to assist in the screening of new or proposed remediation techniques and to help in the design of new ones. More generally, the research will contribute to the advancement of the state of the science in pollution abatement.

This report was submitted in fulfillment of CR-824592 by the University of Southern California under the partial sponsorship of the United States Environmental Protection Agency. This report covers a period from October 1, 1995 to September 30, 1997, and work was completed as of March 30, 1998.

ACKNOWLEDGEMENTS

This research was supported by U.S. EPA Cooperative Agreement No. CR-824592. The encouragement, help, and support of the Project Officer, Dr. Jong Soo Cho, is gratefully acknowledged. We also acknowledge useful interactions with Dr. Carl Enfield, Dr. Candida West, and Dr. Lynn Wood of the EPA's Subsurface Protection and Remediation Division, Ada, Oklahoma.

Parts of this report are in various stages of publication in scientific journals. Certain chapters of this report contain material from the PhD thesis of Chunsan Jia, from current doctoral research by Maryam Shariati and from research to satisfy MS degree requirements by Yuyong Zhang, all in the Chemical Engineering Department at the University of Southern California. The various co-authors of each chapter are identified at the beginning of each chapter. We also note that the research reported in chapters 2 and 6 was also supported by DOE Contract No. DE-FG22-96BC14994/SUB.

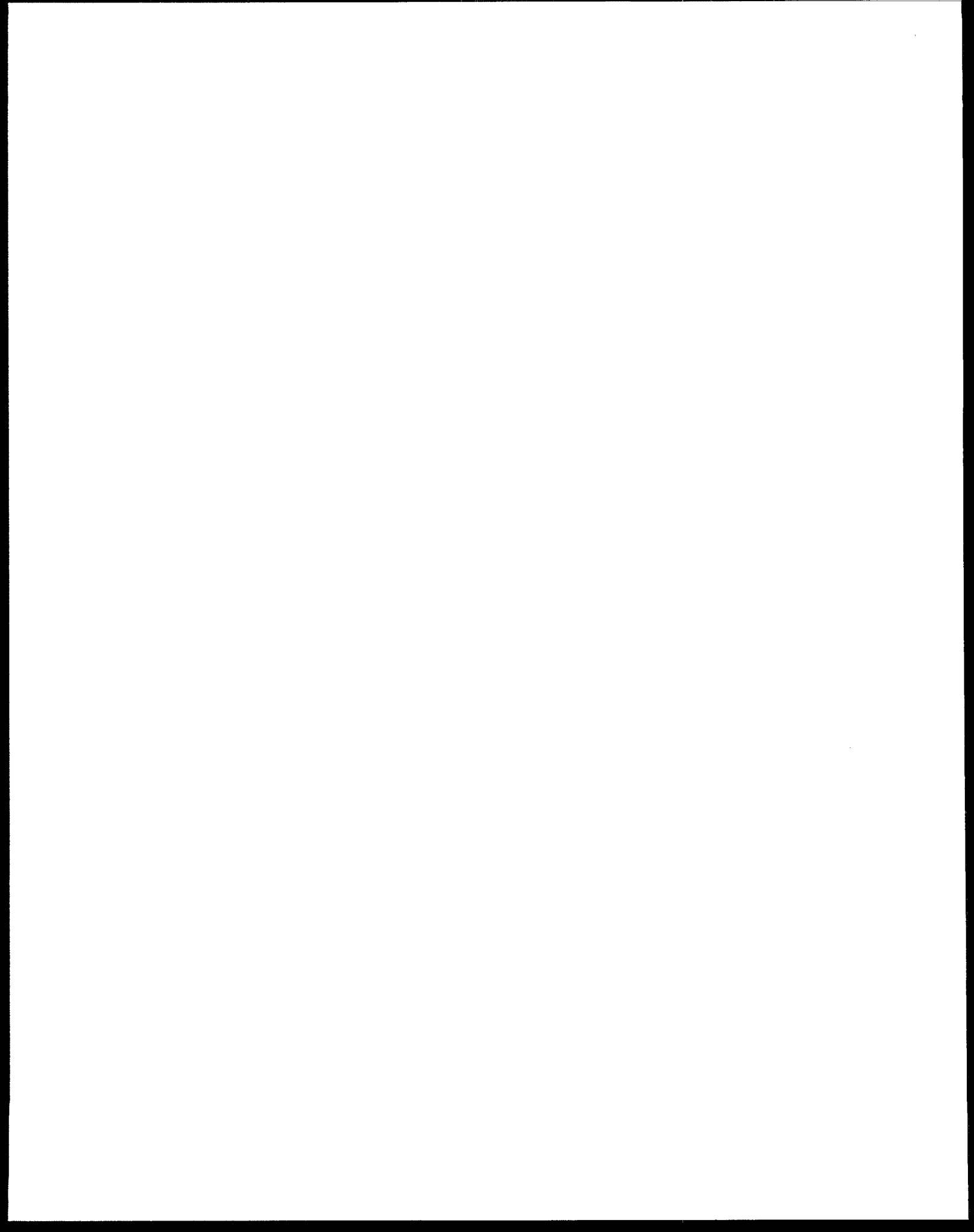


TABLE OF CONTENTS

NOTICE	ii
FOREWORD	iii
ABSTRACT	iv
ACKNOWLEDGEMENTS	v
TABLE OF CONTENTS	vii
LIST OF FIGURES	viii
LIST OF TABLES	xiii
Chapter 1. INTRODUCTION	1
Chapter 2. DISPLACEMENT PATTERNS USING PORE-NETWORK MODELS	8
Chapter 3. VISUALIZATION AND SIMULATION OF NAPL SOLUBILIZATION IN PORE NETWORKS	44
Chapter 4. CONVECTIVE MASS TRANSFER FROM STATIONARY SOURCES IN POROUS MEDIA	75
Chapter 5. PORE-SCALE INSTABILITIES DURING SOLVENT INJECTION	111
Chapter 6. A NOTE ON THE EFFECT OF DISPERSION ON THE STABILITY OF NON-MONOTONIC MOBILITY PROFILES IN POROUS MEDIA	150
Chapter 7. CONCLUSIONS	159

LIST OF FIGURES

2.1	Displacement patterns from numerical simulation of drainage in a 100 x 100 lattice, with $M = 0.1$ and different values of the capillary number: (a) $Ca = 3.2 \times 10^{-8}$ (IP), (b) $Ca = 3.2 \times 10^{-6}$, (c) $Ca = 3.2 \times 10^{-5}$ and (d) $Ca = 3.2 \times 10^{-4}$	23
2.2	Schematic of the front region and the notation used.	24
2.3	Numerical solution of (2.5) vs. the modified capillary number for three different values of M	25
2.4	Percolation probability (dashed line) and saturation (solid line) profiles vs. normalized length, for 3-D VGP: (a) $B = 10^{-4}$ in a lattice of 200 x 200 x 65, (b) $B = 10^{-6}$ in a lattice of 200 x 200 x 500.	26
2.5	Single finger in GP in a destabilizing gradient	27
2.6	Pore network simulations (saturation profile and displacement patterns) for uniform permeability and $Ca = 1.5 \times 10^{-4}$	28
2.7	Pore network simulations (saturation profile and displacement patterns) for permeability increase (1:2) and for $Ca = 1.5 \times 10^{-5}$	29
2.8	Pore network simulations (saturation profile and displacement patterns) for permeability increase (1:2) and for $Ca = 1.5 \times 10^{-4}$	30
2.9	Displacement pattern with parallel gradient in a 2-D 800x 400 lattice: (1) $Bx = -0.1$, (2) $Bx = -0.01$, (3) $Bx = -0.001$, (4) $Bx = -0.0001$	31
2.10	Displacement pattern with parallel gradient in a 3-D 128 x 128 x 128 lattice: (1) $Bx = -0.03$, (2) $Bx = -0.003$, (3) $Bx = -0.001$, (4) $Bx = -0.0003$	32
2.11	The dependence of finger width on the Bond Dumber for (a) 2-D and (b) 3-D lattices	33
2.12	Displacement pattern with transverse gradient in a 2-D 800 x 400 lattice: (1) $By = -0.1$, (2) $By = -0.01$, (3) $By = -0.001$, (4) $By = -0.0001$	34
2.13	Displacement pattern with gradient in a 3-D 128 x 128 x 128 lattice: (1) $By = 0.1$, (2) $By = -0.01$, (3) $By = -0.001$, (4) $By = -0.0005$	35
2.14	The dependence of finger width σ_f on By for (a) 2-D and (b) 3-D lattices	36
2.15	Displacement pattern with both transverse and parallel gradient in a 2-D 800 x 400 lattice: (1) $Bx = 0.01$, $By = -0.001$, (2) $Bx = -0.01$, $By = -0.005$, (3) $Bx = 0.01$, $By = -0.01$, (4) $Bx = 0.005$, $By = -0.01$, (5) $Bx = 0.001$, $By = -0.01$, (6) $Bx = 0.001$, $By = -0.001$	37
2.16	Displacement pattern with both transverse and parallel gradient in a 2-D 400 x 200 lattice: (1) $Bx = 0.1$, $By = -0.01$, (2) $Bx = 0.1$, $By = -0.05$, (3) $Bx = 0.1$, $By = -0.1$, (4) $Bx = 0.05$, $By = -0.1$, (5) $Bx = 0.01$, $By = -0.1$	38
2.17	Displacement pattern with both transverse and parallel gradient in a 2-D 400 x 200 lattice: (1) $Bx = -0.01$, $By = -0.01$, (2) $Bx = -0.001$, $By = -0.01$, (3) $Bx = -0.0005$, $By = -0.01$, (4) $Bx = -0.01$, $By = -0.001$, (5) $Bx = -0.001$, $By = -0.001$, (6) $Bx = -0.0005$, $By = -0.001$	39
2.18	Displacement pattern with both transverse and parallel gradient in a 3-D 128 x 128 x 128 lattice: (1) $Bx = -0.01$, $By = -0.1$, (2) $Bx = -0.01$, $By = -0.005$, (3) $Bx = -0.01$, $By = -0.001$, (4) $Bx = -0.0005$, $By = -0.1$, (5) $Bx = -0.0005$, $By = -0.005$, (6)	

	$B_x = -0.0005, B_y = -0.001$	40
2.19	The dependence of finger width σz on B_x for a 3-D lattice and various values of B_y	41
2.20	The scaling function $f(z)$ from simulations in: (a) 2-D lattice, (b) 3-D lattice	42
2.21	Modified destabilizing <i>IPG</i> patterns to model air sparging for $B = -0.1$ and $P = 0, 1$ and 2, respectively	43
3.1	Schematic of the configuration of trapped NAPL in a porous medium	59
3.2	Typical pattern used for constructing a 2-D pore network	60
3.3	Schematic of the experimental apparatus	61
3.4	Photograph showing the steady-state NAPL distribution in the glass micromodel for typical experimental conditions	62
3.5	A typical effluent curve for the 29×15 micromodel corresponding to the solubilization of benzonitrile by water	63
3.6	Typical NAPL interface configurations in the porespace of the micromodel. Note the cavity-like characteristics	64
3.7	Overall pressure drop vs. injection rate in single-phase flow in the micromodel for two different cases: (a) in the absence of trapped NAPL (top part of the Figure), and (b) in the presence of trapped NAPL (bottom part of the Figure) (for example as shown in Figure 3.4). The solid line is the theoretical prediction and experimental data are bracketed by error bars	65
3.8	Comparison between experimental (top) and numerical (bottom) concentration profiles during miscible displacement of 50% glycerol solution for 0.091 pore volumes injected	66
3.9	Comparison between experimental (top) and numerical (bottom) concentration profiles during miscible displacement of 50% glycerol solution for 0.21 pore volumes injected	67
3.10	Comparison between experiments and simulations for mass transfer from trapped benzonitrile for pattern 1. The concentration at the effluent is normalized with its theoretical solubility value. The solid line is the theoretical prediction, experimental data are bracketed by error bars	68
3.11	Comparison between experiments and simulations for mass transfer from trapped benzonitrile for pattern 2. The concentration at the effluent is normalized with its theoretical solubility value. The solid line is the theoretical prediction and experimental data are bracketed by error bars	69
3.12	Comparison between experiments and simulations for mass transfer from trapped benzonitrile for pattern 1. Only diffusion was used for the simulation of local mass transfer. The concentration at the effluent is normalized with its theoretical solubility value. The solid line is the theoretical prediction, experimental data are bracketed by error bars	70
3.13	Sensitivity analysis of the effect of parameter a in the local mass transfer coefficient equation (3.13) on the effluent concentration curve. The effect of a is minimal as all curves practically coincide (particularly at large values of the Peclet	

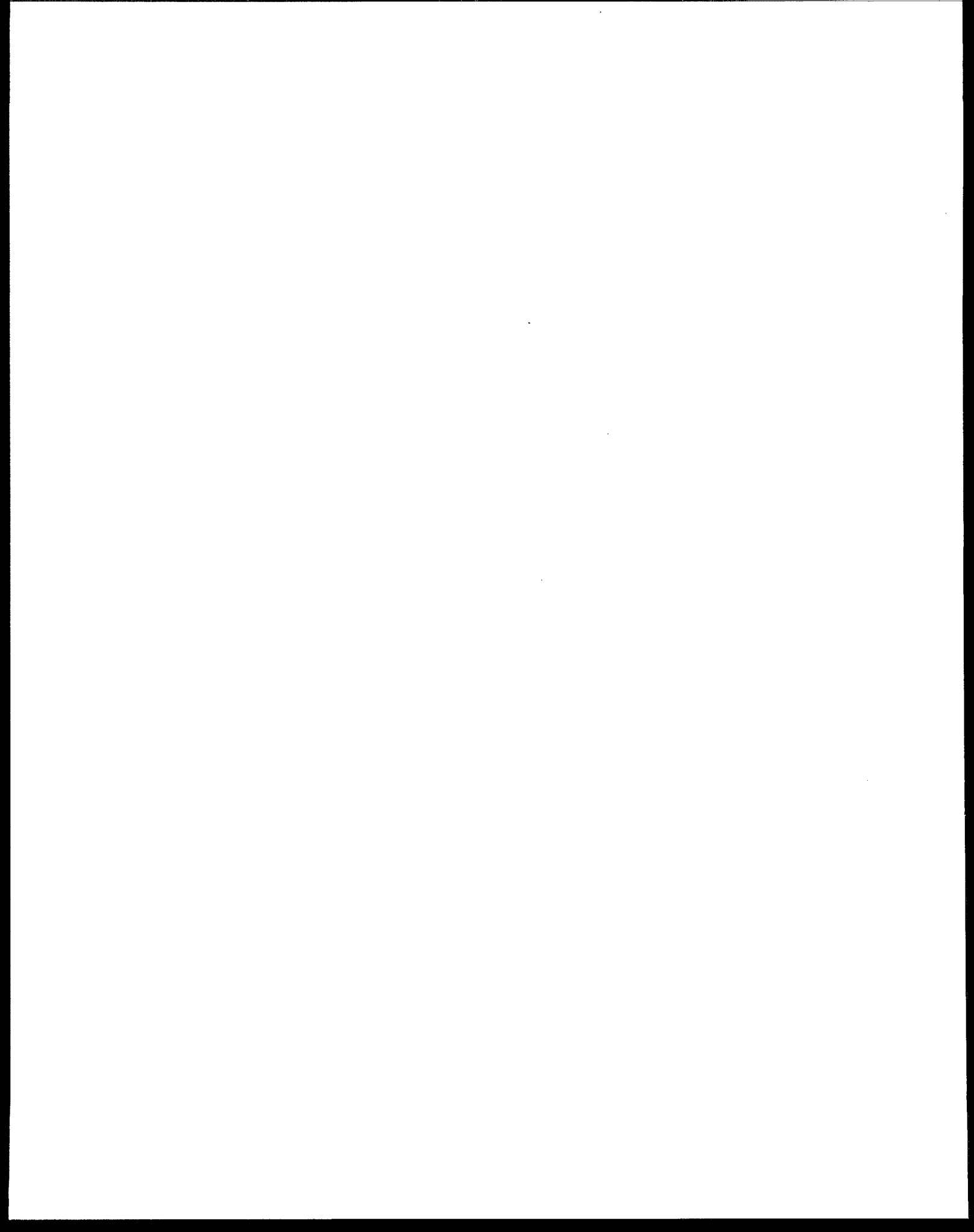
	number)	71
3.14	Sensitivity analysis of the effect of parameter b in the local mass transfer coefficient equation (3.13) on the effluent concentration curve. Four different curves corresponding to $b = 0.2, 0.4, 0.664$ and 1 (from left-to-right) are shown ($a = 1, c = 0.5$). The effect of b is to shift the curve parallel to itself towards the right (essentially rescaling the Peclet number)	72
3.15	Sensitivity analysis of the effect of parameter c in the local mass transfer coefficient equation (3.13) on the effluent concentration curve. Seven different curves corresponding to $c = 0.1, 0.2, 0.3, 0.4, 0.5, 0.6$, and 0.7 (from left-to-right) are shown ($a = 1, b = 0.664$). Note the asymptotic approach to a straight line at large values of the Peclet number	73
3.16	Numerical simulation results for the dependence of the slope s of the effluent concentration curve on the parameter c of equation (3.13). The curve essentially coincides with the theoretical result (3.14)	74
4.1	Photograph showing the steady-state NAPL distribution in the glass micromodel for typical experimental conditions (from Jia et al., 1997)	94
4.2	Schematic of the unit cell used by Quintard and Whitaker (1994)	95
4.3	Typical NAPL interface configurations in the porespace of the micromodel. Note the cavity-like characteristics (from Jia et al., 1997)	96
4.4	The normalized Sherwood number as a function of parameter a	97
4.5	Numerical results of Sh_{avg} vs Pe_L for mass transfer over a flat plate and for three local exponents ($c = 0, c = 1/3$ and $c = 1/2$, from bottom to top, respectively)	98
4.6	Numerical results of Sh_{avg} vs Pe_L for mass transfer over a sphere and for three local exponents ($c = 0, c = 1/3$ and $c = 1/2$, from bottom to top, respectively)	99
4.7	A Koch curve of 3 generations used for the simulation of mass transfer over a self similar surface	100
4.8	Velocity profile for flow over the Koch curve of Figure 4.7	101
4.9	The local mass flux profile over the perimeter of the Koch curve of Figure 4.7 for various values of the Peclet number	102
4.10	The local concentration profile over (a) the streamwise coordinate, (b) the perimeter of the Koch curve of Figure 4.7, for various values of the Peclet number	103
4.11	Numerical results of Sh_{avg} vs Pe_L for mass transfer over the Koch curve of Figure 4.7 for three different generations and for $c = 0$	104
4.12	Numerical results of Sh_{avg} vs Pe_L for mass transfer over the Koch curve of Figure 4.7 for three different generations and for $c = 1/3$	105
4.13	Invasion percolation cluster used for the simulation of flow over a source with percolation characteristics	106
4.14	Numerical results of Sh_{avg} vs Pe_L for mass transfer over the percolation cluster of Figure 4.13 and for three local exponents ($c = 0, c = 1/3$ and $c = 1/2$, from bottom to top, respectively)	107
4.15	Numerical results of Sh_{avg} vs Pe_L for mass transfer over the percolation cluster of Figure 4.13 and for three local exponents ($c = 0, c = 1/3$ and $c = 1/2$, from bottom	

	to top, respectively)	108
4.16	Uniformly-distributed sources to simulate flow over a distributed source	109
4.17	Numerical results of Sh_{avg} vs Pe_L for mass transfer over a uniformly-distributed source and for three local exponents ($c = 0$, $c = 1/3$ and $c = 1/2$, from bottom to top, respectively)	110
5.1	Typical displacement geometries (from Yang and Yortsos, 1997)	124
5.2-a	Concentration profiles for miscible displacement with a monotonic viscosity-concentration profiles between parallel plates at time step = 0.3 and $M = 100$ for various values pf the dipersion coefficient N_{TD} . (from Yang and Yortsos, 1997) ...	125
5.2-b	Concentration profiles for miscible displacement with a monotonic viscosity-concentration profiles between parallel plates at time step = 0.3 and $M = 0.01$ for various values pf the dipersion coefficient N_{TD} . (from Yang and Yortsos, 1997) ...	125
5.3	Monotonic viscosity-unfavorable mobility ratio ($\alpha = 5$, $N_{TD} = 0$, Time = 0.5)	126
5.4	Non-monotonic viscosity- unfavorable mobility ratio ($\alpha = 5$, $\mu_m = 10$, $c_m = 0.5$, $N_{TD} = 0$, Time = 0.5)	127
5.5	Monotonic viscosity. Effect of dispersion ($\alpha = 5$, $N_{TD} = 0.01$, Time = 0.5)	128
5.6	Non-monotonic viscosity. Effect of dispersion ($\alpha = 5$, $\mu_m = 10$, $c_m = 0.5$, $N_{TD} = 0.01$, Time = 0.5)	129
5.7	Monotonic viscosity- favorable mobility ratio ($\alpha = 0.2$, $N_{TD} = 0$, Time = 0.5)	130
5.8	Non-monotonic viscosity- favorable mobility ratio ($\alpha = 0.2$, $\mu_m = 10$, $c_m = 0.5$, $N_{TD} = 0.01$, Time = 0.5)	131
5.9	Monotonic viscosity- favorable mobility ratio. Effect of dispersion ($\alpha = 0.2$, $N_{TD} = 0.01$, Time = 0.5)	132
5.10	Non-monotonic viscosity- favorable mobility ratio. Effect of dispersion ($\alpha = 0.2$, $\mu_m = 10$, $c_m = 0.5$, $N_{TD} = 0.01$, Time = 0.5)	133
5.11	Monotonic viscosity- Poiseuille flow ($\alpha = 1$, $N_{TD} = 0$, Time = 0.4)	134
5.12	Non-monotonic viscosity at Poiseuille flow conditions ($\alpha = 1$, $\mu_m = 10$, $c_m = 0.5$, $N_{TD} = 0$, Time = 0.4)	135
5.13	Effect of t on non-monotonic viscosity for $\alpha = 1$ ($\mu_m = 7$, $c_m = 0.5$, $N_{TD} = 0$)	136
5.14	Monotonic viscosity- Poiseuille flow. Effect of dispersion ($\alpha = 1$, $N_{TD} = 0.01$, Time = 0.4)	137
5.15	Non-monotonic viscosity at Poiseuille flow conditions. Effect of dispersion ($\alpha = 1$, $\mu_m = 10$, $c_m = 0.5$, $N_{TD} = 0.01$, Time = 0.4)	138
5.16	Non-monotonic viscosity- effect of μ_m ($\alpha = 1$, $\mu_m = 8$, $c_m = 0.5$, $N_{TD} = 0$)	139
5.17	Non-monotonic viscosity- effect of μ_m ($\alpha = 1$, $\mu_m = 20$, $c_m = 0.5$, $N_{TD} = 0$)	140
5.18	Non-monotonic viscosity- effect of c_m ($\alpha = 1$, $\mu_m = 10$, $c_m = 0.05$, $N_{TD} = 0$)	141
5.19	Non-monotonic viscosity- effect of c_m ($\alpha = 1$, $\mu_m = 10$, $c_m = 0.9$, $N_{TD} = 0$)	142
5.20	Schematic of the Experimental Apparatus Setup	143
5.21	Viscosity-concentration profile for a 2-propanol/water mixture	144
5.22	Viscosity-concentration profile for a glycerol/water mixture	145
5.23	Typical image of water displacing 1-propanol	146
5.24	Typical image of water displacing glycerol	147

5.25	Close-up of water displacing 2-propanol	148
5.26	Close-up of water displacing glycerol mixture	149
6.1	The dominant eigenvalue $s_{HY}(n)$ for a non-monotonic viscosity profile with $M > 1$ (curve a) and $M < 1$ (curve b)	156
6.2	The dispersion relation $\sigma(k; \epsilon)$ for different values of the dimensionless time $1/4\sigma^2$ as predicted from equation (6.15) for the conditions of case (a) of Figure 6.1	157
6.3	The dispersion relation $\sigma(k; \epsilon)$ for different values of the dimensionless time $1/4\sigma^2$ predicted from equation (6.15) for the conditions of case (b) of Figure 6.1	158

LIST OF TABLES

3.1	A compilation of mass transfer correlations used in NAPL remediation	58
-----	--	----



Chapter 1

INTRODUCTION

A commonly used method for in-situ remediation is *pump-and-treat*, in which the groundwater is pumped out of the site, treated on the surface to remove the contaminant and subsequently reinjected (Mackay and Cherry, 1989). Because of the relatively low solubility of the contaminants, compounded with mass transfer limitations at the pore scale and from low permeability areas (such as clay lenses), the overall process efficiency is much lower than desirable. For its enhancement, various improvements are constantly being developed. The majority involve the injection of *remedial* fluids or chemicals which may enhance the solubility of the contaminant (Pennell et al., 1993, Augustijn et al., 1994) or help to mobilize trapped *NAPL* (Brandes and Farley, 1993). Injection of surfactants (West and Harwell, 1992, Pennell et al., 1993), co-solvents, such as alcohols (Pinal et al., 1990, Wood et al., 1990), and air (sparging) (Ji et al., 1993, Pankow et al., 1993) in the groundwater, or injection of steam in the vadose zone (Itamura and Udell, 1993, Ho et al., 1994), are some of the methods actively under consideration.

A key characteristic of in-situ remediation is the requirement of a high recovery efficiency over relatively small areas (Mercer and Cohen, 1990, Mayer and Miller, 1993). This is qualitatively different from enhanced oil recovery, to which it otherwise has many similarities, where recovery cost is the basic design consideration. Three processes, generic to in-situ groundwater remediation, require increased scrutiny:

- The emplacement in-situ of the contaminant *NAPL*;
- The mass transfer of the contaminant from the *NAPL* to the groundwater or from the groundwater to a sparging fluid, and of the remedial agents to the *NAPL*; and
- The development of miscibility and possible microscale flow instabilities.

As with other processes involving porous media, in-situ remediation must be investigated at the different scales that comprise porous media (Yortsos, 1998). These include

- The pore surface scale (of the order of nm), where adsorption, partitioning between phases, thermodynamic equilibrium, surface chemistry and wettability are important;
- The pore scale (of the order of tens of μm), also called the *microscopic* scale, where pores can be defined, fluid-fluid interfaces are confined and capillary phenomena are important;
- The pore-network scale (of the order of mm), where the collective behavior of a process over an ensemble of pores is investigated;

- The laboratory scale (core scale) (of the order of *cm*), also called the *macroscopic* scale, where laboratory experiments are conducted; and
- The field scale (of the order of *m* and higher), also called the *megascopic* scale, which is of relevance to large-scale spreading.

Phenomena at the different scales have a different manifestation, and input from a lower scale is necessary for their description at the next higher scale.

With the exception of some recent works, the design of in-situ remediation is currently based on a description at the macroscopic (and megascopic) scales using computer simulators. Phenomena at the pore and pore-network scales are typically lumped in terms of averaged quantities, using empirical or *ad hoc* expressions. At best, these are adaptations of macroscopic models developed in enhanced oil recovery (e.g. see Abriola and Pinder, 1985a,b, Brown et al., 1994), and although a significant improvement over earlier empirical models (e.g. Wilson et al., 1992), they cannot address fundamental remediation issues that originate at the pore and pore network scales. The following examples illustrate the inadequacy of the present state of the art.

1. Many aspects of remediation involve immiscible displacements, e.g. the downwards seepage of *NAPL* into the subsurface, or the upwards injection of air in air sparging. Displacement patterns, critically affected by pore-scale heterogeneities, capillary, viscous and gravity forces, dictate the dynamic or equilibrium configurations of the *NAPL*-groundwater interface or the air-groundwater interface (in air sparging), which in turn decisively determine mass transfer. Conventional macroscopic simulation based on averages, is *inherently* unable to provide a detailed description. For mass-transfer purposes, the *NAPL* is typically assumed in the form of isolated spherical globules in an structureless porous medium (Powers et al., 1994b), an assumption that contrasts commonly accepted displacement patterns, which are often disordered or fractal (Feder, 1988, Lenormand, 1990, Sahimi and Yortsos, 1990). In gas sparging, patterns vary from a fluidized-like regime to a disordered, channeled flow, depending on the rate of injection and the disorder of the medium (Ji et al., 1993). Current macroscopic models ignore or lump together these microscale phenomena, with the consequence that capillary or viscous fingering and channeling at the local scale are grossly mis-represented. Recent approaches (Celia et al., 1993, Soll and Celia, 1993, Soll et al., 1993,), paralleling earlier efforts in oil recovery (Heiba et al., 1982, Parlhar and Yortsos, 1988, 1989, Yortsos, 1990), have used Ordinary Percolation theory to relate quantities, such as relative permeabilities and capillary pressures, to the microstructure. These need to be further advanced by considering *dynamic invasion* models that include gravity, viscous forces and correlated heterogeneity.

2. The overall mass transfer coefficient has been estimated by widely different correlations, reflecting the different assumptions made by different investigators. Vigorously debated, but presently inconclusive, are effects of flow velocity, interfacial area and its variation with time (due to dissolution, mobilization, etc.) (Imhoff et al., 1993). Particularly interesting are the reported differences in the exponent relating the mass-transfer Sherwood number to the Reynolds or the Peclet numbers, for which convincing theories have not been provided. This exponent should reflect the relevant flow regime and the interface geometry (Cussler, 1984). In the most advanced model to date, Powers et al. (1994) approximated mass transfer by steady-state diffusion from an *isolated* spherical *NAPL* globule (which is akin to a dilute-limit approximation in a Hele-Shaw cell, Li and Yortsos, 1994). However, such approximations do not adequately represent the true geometrical configurations of *NAPL*-groundwater interfaces in a real system and the concomitant effects on fluid flow and mass transfer. Similarly poor is the estimation of mass transfer rates from the air-groundwater interface in air sparging.

3. The development of miscibility between an injected solvent and in-situ *NAPLs* has also been addressed only by macroscopic models. The most advanced version (Brown et al., 1994) assumes equilibrium phase behavior for the *average* compositions and saturations, similar to analogous models for surfactant flooding (Pope and Nelson, 1978) or CO_2 flooding (Stalkup, 1983) in oil recovery. Implied to such equilibrium and *first-contact miscibility* at the macroscale is the assumption of fast mass transfer (by diffusion and convection) to lead to spatially uniform profiles. This may not be generally true in the presence of multiple fluid-fluid interfaces at the pore scale, however, where mass transfer will be hindered and the interplay of transport, phase equilibrium and flow is much more complex than represented in macroscopic models. Local mixing can be accompanied by changes in fluid viscosity and density, and important viscous or buoyancy-driven instabilities at the pore scale can be induced (Yang and Yortsos, 1997). These are not recognized in macroscopic simulators. In fact, the current models actually employ a formalism of *immiscible* displacements, where miscibility is indirectly accounted for through the dependence of the residual saturation, S_{or} , on the capillary number, Ca (in turn indirectly related to concentration). The $S_{or}(Ca)$ function used corresponds to a sequence of equilibrium states reached in displacements at a constant Ca , which may be questionable when the development of miscibility is dynamic. Finally, the *REV* over which averages are defined (Bear, 1972), becomes ill-defined when there exist gradients in average concentrations or saturations, or when phenomena at the pore-scale are dynamic.

In recent studies, we have addressed some of these issues, although in somewhat different contexts. In a series of papers (Li and Yortsos, 1994, 1995a,b, Satik et al., 1995) we have investigated the pore scale mass transfer towards a growing gas phase from a surrounding liquid in a porous medium, in the context of solution gas-drive. We have shown by experiments in etched-glass micromodels and in Hele-Shaw cells, and by simulation using pore network models that the interface pattern varies from Invasion Percolation (*IP*) to Viscous Fingering (*VF*) (Feder, 1988) and drastically affects the mass transfer, hence the rate of growth (or dissolution) of a phase. The disorder of a real porous medium (even if macroscopically homogeneous) was shown to give rise to qualitatively different phenomena than in effective porous media (such as a Hele-Shaw cell, Li and Yortsos, 1994, 1995a). To our knowledge, these are the first studies, where pore level simulation has been used to understand mass transfer in multiphase flows in porous media. In another recent study (Yang and Yortsos, 1997), we have described the miscible displacement in a single capillary or in the gap of a Hele-Shaw cell using Stokes (rather than Darcy) equations. We have shown that, if the injected fluid is of a lower viscosity, viscous fingers involving a *sharp interface* between injected and initial fluids within a single pore will develop, provided that the transverse Peclet number, which measures convection over diffusion, is sufficiently large. Similar effects are likely to occur in the context of remediation as well.

To better understand and to help design improved remediation methods, we present in this report a pore-scale study of some of the generic aspects of remediation cited above, namely the emplacement in-situ of the *NAPL*, the mass transfer characteristics of remediation processes, and the development of microscale flow instabilities during remedial fluid injection. Experimental, theoretical and computational studies are conducted, with emphasis placed at the pore network scale, although appropriate efforts are also devoted to the single pore scale, whenever appropriate. The information obtained will be incorporated by up-scaling techniques into macroscopic simulators. The specific tasks are organized as follows:

Chapter 2 describes the use of pore-network simulation for the characterization of immiscible displacement patterns expected during *NAPL* emplacement. We briefly present a pore-network approach to study the various immiscible displacement patterns that develop between a percolating *NAPL* and the groundwater, or between an immiscible remedial fluid and the groundwater. The pore network simulation includes capillary, gravity and viscous forces and also accounts for pore

scale heterogeneity.

Chapters 3 and 4 describe our study of mass transfer from or to a trapped, stationary *NAPL*, during a remediation process. Here, the main objective is the determination of the mass transfer coefficient as a function of the flow rate, the interfacial area and other physical and geometrical parameters. Dissolution experiments in etched-glass micromodels are conducted. Then, based on the particular configuration of the trapped *NAPL*, a pore-network simulation is carried out of mass transfer by diffusion and convection in the disordered pore-space occupied by the injected fluid. Mass transfer is computed by a pore network simulator, as described below, with local mass-transfer coefficients determined from single-pore expressions. At sufficiently slow dissolution rates, a quasi-steady state is likely. Then, an overall mass transfer coefficient is computed and its sensitivity to the Peclet number and various other properties of the system is determined. Chapter 3 deals with the etched-glass micromodel experiments, while Chapter 4 presents a general theory of mass transfer from stationary sources in a porous medium.

The third topic to be studied is the various viscous instabilities during miscible displacements. Chapters 5 and 6 describe aspects of instability at the single-pore scale (for example in the gap of a Hele-Shaw cell, which is equivalent to a single capillary) and also at the macroscopic scale for the case of non-monotonic viscosity behavior, respectively. Some experiments in a Hele-Shaw cell are also described in Chapter 5. Because viscosities and densities are composition-dependent, spatial variations in concentration may lead to viscous instabilities or otherwise affect the flow pattern. The studies in a single pore are similar to Yang and Yortsos (1997) for monotonic displacements.

The results to be obtained can be incorporated into a macroscopic description by applying an up-scaling technique (Chapter 4). Included among them are homogenization (Bensoussan et al., 1978), volume-averaging (Quintard and Whitaker, 1994), ensemble averaging (Gelhar and Axness, 1983, Koch and Brady, 1987), and gradient percolation (Gouyet et al., 1988). Depending on whether scales can be separated or not, these approaches either lead to the formulation of a local boundary value problem, the solution of which provides the desired coefficients (case of homogenization and volume averaging), or may lead to an altogether different macroscopic model. When gradients in the average properties are not large, the application proceeds in a standard fashion, as described in Quintard and Whitaker (1994). However, problems will arise at larger rates, where concentration gradients are large, in which case the basic premise of separation of scales breaks down. Asymptotic descriptions and scaling theories for displacement patterns and saturation profiles are described in Chapter 2. Corresponding results for the mass transfer coefficients are provided in Chapter 4.

The simulations on mass transfer are compared against experimental data in etched-glass micromodels. The comparison between theory and experiment will allow a check of the relevance of the pore network description and to seek corrections, particularly at the single-pore level, if there exists a mismatch.

REFERENCES

1. Abriola, L.M. and Pinder, G.F., A multiphase approach to the modeling of porous media contamination by organic compounds: 1. Equation Development, *Water Resour. Res.*, Vol. 21, 11-18 (1985a).
2. Abriola, L.M. and Pinder, G.F., A multiphase approach to the modeling of porous media contamination by organic compounds: 2. Numerical simulation, *Water Resour. Res.*, Vol. 21, 19-26 (1985b).

3. Augustijn, D.C.M., Jessup, R.E., Rao, P.S.C. and Wood, A.L., Remediation of contaminated soils by solvent flushing, *J. Envir. Engin.*, Vol. 120, 42-57 (1994).
4. Bear, J., "Dynamics of fluids in porous media", Elsevier, New York, NY (1972).
5. Bensoussan, A., Lions, J.L. and Papanicolaou, G., "Asymptotic analysis for periodic structures", North-Holland, Amsterdam (1978).
6. Brandes, D. and Farley, K.J., Importance of phase-behavior on the removal of residual *DNAPLs* from porous media by alcohol flooding, *Water Envir. Res.*, Vol. 65, 869-878 (1993).
7. Brown, C.L., Pope, G.A., Abriola, L.M. and Sepehrnoori, K., Simulation of surfactant-enhanced aquifer remediation, *Water Resour. Res.*, Vol. 30, 2959-2977, (1994).
8. Celia, M. A., Rajaram, H. and Ferrand, L.A., A multi-scale computational model for multi-phase flow in porous media, *Advances in Water Resources*, Vol. 16, 81-92 (1993).
9. Cussler, E.L., "Diffusion: Mass transfer in fluid systems", Cambridge University Press (1984).
10. Feder, J., "Fractals", Plenum, New York (1988).
11. Gelhar, L.W. and Axness, C.L., Three-dimensional stochastic analysis of macrodispersion in aquifers, *Water Resour. Res.*, Vol. 19, 161-180 (1983).
12. Gouyet, J.F., Rosso, M. and Sapoval, B., Fractal structure of diffusion and invasion fronts in three-dimensional lattices through the gradient percolation approach, *Phys. Rev. B*, Vol. 37, 1832 (1988).
13. Heiba, A. A., Sahimi, M., Scriven, L.E. and Davis, H.T., Percolation theory of two-phase relative permeabilities, Paper SPE 11015, presented at the 57th SPE Annual Meeting, New Orleans, LA, Sept., 26-29, 1982.
14. Ho, C.K., Liu, S. and Udell, K.S., Propagation of evaporation and condensation fronts during multicomponent soil vapor extraction, *J. Contam. Hydr.*, Vol. 16, 381-401 (1994).
15. Imhoff, P.T., Jaffe, P.R. and Pinder, G.F., An experimental study of complete dissolution of a nonaqueous phase liquid in saturated porous media, *Water Resour. Res.*, Vol. 30, 307-320 (1993).
16. Itamura, M.T. and Udell, K.S., Experimental clean-up of a dense non-aqueous phase liquid in the unsaturated zone of a porous medium using steam injection, Vol. 265, *Multiphase Transport in Porous Media*, ASME, 57-62 (1993).
17. Ji, W., Dahmani, A., Ahlfeld, D.P., Lin, J.D. and Hill III, E., Laboratory study of air sparging: Air flow visualization, *GWMR*, 115-126 (1993).
18. Koch, D.L. and Brady, J.F., A non-local description of advection-diffusion with application to dispersion in porous media, *J. Fluid Mech.* Vol. 180, 387-403 (1987).
19. Lenormand, R., Liquids in porous media, *J. Phys.: Condens. Matter*, Vol. 2, SA79-SA88 (1990).
20. Li, X. and Yortsos, Y.C., Bubble growth and stability in an effective porous medium, *Phys. Fluids A*, Vol. 6, 1663-1676 (1994).

21. Li, X. and Yortsos, Y.C., Visualization and simulation of bubble growth in pore networks, *AIChE J.*, Vol. 41, 214-223 (1995a).
22. Li, X. and Yortsos, Y.C., Bubble growth in porous media, *Chem. Eng. Sci.*, in press (1995b).
23. Mackay, D.M. and Cherry, J.A., Groundwater contamination: Pump-and-treat remediation, *Environ. Sci. Technol.*, Vol. 23, 630-636 (1989).
24. Mayer, A.S. and Miller, C.T., An experimental investigation of pore-scale distributions of nonaqueous phase liquids at residual saturation, *Transport in Porous Media*, Vol. 10, 57-80 (1993).
25. Mercer, J.W. and Cohen, R.M., A review of immiscible fluids in the subsurface: Properties, models, characterization and remediation, *J. Contam. Hydr.*, Vol. 6, 107-163 (1990).
26. Pankow, J.F., Johnson, R.L. and Cherry, J.A., Air sparging in gate wells in cutoff walls and trenches for control of plumes of volatile organic compounds (VOCs), *Ground Water*, Vol. 31, 654-663 (1993).
27. Parlar, M. and Yortsos, Y.C., Percolation theory of vapor adsorption-desorption processes in porous media, *J. Colloid Interface Sci.*, Vol. 124, 162-176 (1988).
28. Parlar, M. and Yortsos, Y.C., Nucleation and pore geometry effects on capillary desorption in porous media, *J. Colloid Interface Sci.*, Vol. 132, 425-443 (1989).
29. Pennell, K.D., Abriola, L.M. and Weber, W.J., Jr., Surfactant-enhanced solubilization of residual dodecane in soil columns. 1. Experimental investigation, *Environ. Sci. Technol.*, Vol. 27, 2332-2340 (1993).
30. Pinal, R., Rao, P.S.C., Lee, L.S., Cline, P.V., and Yalkowski, S.H., Cosolvency of partially miscible organic solvents on the solubility of hydrophobic organic chemicals, *Environ. Sci. Technol.*, Vol. 24, 639-647 (1990).
31. Pope, G.A. and Nelson, R.C., A chemical flooding compositional simulator, *Soc. Pet. Eng. J.*, Vol. 18, 339-354 (1978).
32. Powers, S.E., Abriola, L.M. and Weber, W.J., Jr., An experimental investigation of nonaqueous phase liquid dissolution in saturated subsurface systems: Steady state mass transfer rates, *Water Resour. Res.*, Vol. 28, 2691-2705 (1992).
33. Powers, S.E., Abriola, L.M. and Weber, W.J., Jr., An experimental investigation of nonaqueous phase liquid dissolution in saturated subsurface systems: Transient mass transfer rates, *Water Resour. Res.*, Vol. 30, 321-332, Feb. (1994).
34. Powers, S.E., Abriola, L.M., Dunkin, J.S. and Weber, W.J., Jr., Phenomenological models for transient *NAPL*-water mass-transfer processes, *J. Contam. Hydr.*, Vol. 16, 1-33 (1994).
35. Quintard, M. and Whitaker, S., Convection, dispersion, and interfacial transport of contaminants: Homogeneous porous media, *Advances in Water Resources*, Vol. 17, 221-239 (1994).
36. Sahimi, M. and Yortsos, Y.C., Application of fractal geometry to porous media: A review, paper SPE 20476 presented at the 65th SPE Annual Fall Meeting, Dallas, TX (Oct. 6-9, 1990).

37. Satik, C., Li, X. and Yortsos, Y.C., Scaling of bubble growth in porous media, *Phys. Rev. E*, in press (1995).
38. Soll, W.E., Celia, M.A. and Wilson J.L., Micromodel studies of three-fluid porous media systems: Pore-scale processes relating to capillary pressure-saturation relationships, *Water Resour. Res.*, Vol. 29, 2963-2974 (1993).
39. Soll, W.E. and Celia, M.A., A modified percolation approach to simulating three-fluid capillary pressure-saturation relationships, *Advances in Water Resources*, Vol. 16, 107-126 (1993).
40. Stalkup, F.I., Jr., "Miscible Displacement", SPE Monograph, Vol. 8, SPE, New York (1983).
41. West, C.C. and Harwell, J.H., Surfactants and subsurface remediation, *Environ. Sci. Technol.*, Vol. 26, 2324-2330 (1992).
42. Wilson, D.J., Kayano, S., Mutch, R.D., Jr. and Clarke, A.N., Groundwater cleanup by in-situ sparging 1. Mathematical modeling, *Separation Science and Technology*, Vol. 27, 1023-1041 (1992).
43. Wood, A.L., Bouchard, D.C., Brusseau, M.L. and Rao, P.S.C., Cosolvent effect on sorption and mobility of organic contaminants in soils, *Chemosphere*, Vol. 21, 575-587 (1990).
44. Yang, Z. and Yortsos, Y.C., Asymptotic solutions of miscible displacement in geometries of large aspect ratio, *Phys Fluids*, Vol. 9, 286-298 (1997).
45. Yortsos, Y.C., "Discrete Approach: Percolation Theory, Instabilities: Miscible and Immiscible Flows, Heterogeneity Description Using Fractal Concepts, Reaction and Transport in Porous Media", von Karman Institute Lecture Series on Modeling and Applications of Transport Phenomena in Porous Media, Brussels, Belgium (Feb. 5-Feb. 9, 1990).
46. Yortsos, Y.C., "Fluid Flow and Transport Processes in Porous Media", Springer Verlag (in progress) (1998).

Chapter 2

DISPLACEMENT PATTERNS USING PORE-NETWORK MODELS

Baomin Xu, Yuyong Zhang and Yanis C. Yortsos

INTRODUCTION

The determination of immiscible displacement patterns that develop during seepage of *NAPLs* in the groundwater or during air sparging of contaminated groundwater is important. Displacement patterns are critically affected by pore-scale heterogeneities, and by capillary, viscous and gravity forces, which dictate dynamic or equilibrium configurations of the *NAPL*-groundwater interface or the air-groundwater interface (in air sparging). In turn, interfacial area and geometry are key variables to mass transfer in remediation processes. In this chapter we consider a pore-network study of some generic aspects involved in the emplacement in-situ of the *NAPL* and displacement patterns in air sparging.

To simulate displacement patterns in a pore network, we can use either a generally complex pore network simulator, or a simpler Invasion Percolation in a Gradient (*IPG*) model, to be described below, in which gravity, capillarity and viscous forces dictate the displacement. Although simpler, *IPG* is not less realistic, and rigorously applies to many problems as will be shown. In either case, pore-network simulation or simpler statistical physics models conditions can lead to pore-level configurations for the interface between invading and initial fluid. For example, the spreading of a contaminant phase over a lens of low permeability, etc., can be readily modeled. An interesting configuration is that corresponding to an Invasion Percolation *IP* cluster, where the interface has the fractal structure of the percolation cluster. Such interfaces are highly disordered, they are ubiquitous in displacement processes, even in relatively homogeneous systems, as will be shown below, and cannot be replicated by continuum models. In this chapter we provide a pore-network level study of the particular patterns expected to develop in immiscible displacements under various conditions, and will examine the sensitivity to parameters, such as the capillary and Bond numbers, expressing relative magnitudes of viscous, gravity and capillary forces, and to the disorder of the medium. The interface configuration obtained will be then used as input for solving the associated mass transfer problem in the next tasks.

This chapter is organized as follows: We first present a new approach for understanding drainage (namely the displacement of a wetting by a non-wetting phase in a porous medium) in the presence of viscous forces, based on Invasion Percolation in a Gradient (*IPG*). This method is detailed in Xu et al. (1998) and allows the classification of the various patterns expected. Then, we

describe conventional pore network simulations and provide examples of patterns obtained based on the work of Xu (1995). The effect of gravity on the spreading of *DNAPL* over an impermeable boundary is described in a following section, where the displacement characteristics are analyzed for various parameter values. We close with a description of air sparging patterns obtained with the use of *IPG*. Before we proceed, we note that the application of pore-network models to describe processes in real porous media is a rapidly growing research area. Xu et al. (1997) describe in detail the specific approach they have followed for simulating laboratory experiments in heterogeneous carbonate samples.

DRAINAGE WITH VISCOUS FORCES

The displacement (drainage) of a wetting fluid (subscript w) in a porous medium by the injection of a non-wetting fluid (subscript nw), immiscible to the former, has been analysed in great detail in past studies. In the absence of viscous or gravity forces, slow drainage is controlled solely by the capillary pressure, $P_c = P_{nw} - P_w$ (the difference in pressure between the two fluids), which is spatially uniform. At the pore network level, this problem can be modeled by Invasion Percolation, in which the front separating the two fluids advances by penetrating the pore throat at the front with the largest size (smallest capillary resistance). The properties of *IP* and its close connection to Ordinary Percolation (*OP*) have been extensively studied (Wilkinson and Willemsen, 1983).

In the presence of gravity (Gouyet et al. 1988), or of a gradient in the average pore-size (hence, of a gradient in the permeability) (Chaouche et al., 1994a), and in the absence of viscous forces, slow drainage has been modeled with Invasion Percolation in a Gradient, which is a modified version of Gradient Percolation (*GP*). Here the capillary pressure varies linearly (or almost linearly) in the direction of displacement, x . Because of their direct relationship (see also below), this gradient also results in a gradient in the percolation probability p , usually expressed in terms of the Bond number, B (where $B \sim -dp/dx$). For example, for invasion under a hydrostatic gradient, $B = \frac{\Delta\rho g_x r_m^2}{\gamma}$, where $\Delta\rho$ is the density difference, g_x is the gravity component in the direction of displacement, r_m is a typical throat size and γ is the interfacial tension between the two fluids. For invasion in a permeability gradient, $B = -\frac{dk^{1/2}}{dx}$, where k is the permeability. In *IP* ($B = 0$), the entire displacement pattern is a percolation cluster (see Xu (1995) for further discussion of these patterns). However, in *IPG*, one needs to distinguish between two different cases, depending on whether percolation is in a stabilizing or a destabilizing gradient.

In the first case ($B > 0$), for example in the downwards displacement at capillary control of a heavier fluid by the injection of a lighter fluid, or in drainage in a field of decreasing permeability, the percolation probability decreases in the direction of displacement. The region where the invasion has the characteristics of a percolation cluster is only of a finite extent, σ , which was shown by Gouyet et al. (1988) to scale as

$$\sigma \sim B^{-\frac{\nu}{\nu+1}} \quad (2.1)$$

where ν is the correlation length exponent of percolation (Stauffer and Aharony, 1992). Here σ denotes the width of the front (in 2-D) or of the front-tail (in 3-D), where the displacing pattern has the structure of the percolation cluster and fractal concepts apply. Equivalently, σ measures the maximum extent of the correlation length, which in gradient percolation problems becomes finite due to the applied gradient. Various properties of *GP* and *IPG* have been studied in considerable detail. During invasion in a destabilizing gradient ($B < 0$), the percolation probability increases in the direction of displacement. Then, the displacement proceeds in the form of capillary fingers,

the scaling of the average thickness of which with (the absolute value of) the Bond number also satisfies (2.1) (see Meakin et al., 1992). Typical examples include the downwards displacement at capillary control of a lighter fluid by the injection of a heavier fluid, as in *DNAPL* movement, the upwards displacement of a heavier fluid by the injection of a lighter fluid, as in air sparging, or drainage in a field of increasing permeability,

In the presence of both viscous and capillary forces, the displacement is characterized by three dimensionless numbers: the capillary number, $Ca = q\mu_{nw}/\gamma$, where q is the injection velocity and μ_{nw} the viscosity of the displacing phase; the viscosity ratio, $M = \mu_w/\mu_{nw}$, where μ_w is the viscosity of the displaced phase; and the dimensionless system size L (expressed in units of the average pore length l). As Ca or L increase, the viscous pressure drop in the two fluids becomes comparable to capillarity, and one expects that some form of gradient percolation would also describe this process.

The effect of viscous forces on displacements in porous media is of obvious importance to process scale-up and large-scale simulation. As length scales increase, viscous effects are increasingly dominant over capillarity. An understanding of this competition at the pore-network scale is necessary to provide insight on the validity of the conventional continuum description using relative permeabilities, and to delineate the particular patterns obtained. Here, we consider fully developed drainage in uncorrelated random media in the presence of viscous forces and proceed by postulating an analogy with *IPG*. Depending on the relative magnitude of M , we anticipate the existence of two different regimes, described by *IPG* in a *stabilizing* or a *destabilizing* gradient, respectively. These two regimes dictate the development of the saturation profiles in the respective displacements, as will be shown below.

In the absence of viscous forces, the capillary pressure is spatially uniform and the displacement proceeds by following the usual rules of *IP*, namely by successively invading the perimeter pore with the largest size. In the presence of a viscous pressure drop, a gradient in the capillary pressure (negative or positive) is generally expected to develop. In view of the relations

$$P_c = \frac{2\gamma}{r} \quad (2.2)$$

and

$$p = \int_r^\infty \alpha(r) dr \quad (2.3)$$

(or, more correctly, $p = \int_{r_{min}}^\infty \alpha(r) dr$, where r_{min} is the minimum throat size invaded), this, in turn, implies a gradient in the percolation probability. In the above, $\alpha(r)$ is the probability density function of the pore size distribution. Problems involving a constant gradient in p are amenable to *GP* and *IPG*, thus we expect that a similar description would also be applicable in the present case involving viscous forces. Figure 2.1 shows typical patterns of viscous displacements for $M = 0.1$, obtained from pore network simulation in the absence of trapping (details of the simulation can be found in Xu, 1995, and will also be described below). When Ca is low (Figure 2.1a), viscous forces are negligible and the pattern has the fractal structure of the *IP* cluster. As viscous forces increase at larger Ca (Figures 2.1b-2.1d), however, the front takes the appearance of a rough (self-affine), rather than self-similar, curve and has an extent that decreases with increasing Ca . These trends are consistent with a gradient percolation description.

Following *GP* notions, we will distinguish two different cases, one in which the percolation probability p , (hence P_c) decreases in the direction of displacement, and which has features similar to *GP* in a stabilizing gradient, and another in which p (hence P_c) increases in the direction of displacement, with features similar to *GP* in a destabilizing gradient. Because in our problem, the

capillary pressure P_c is controlled by the viscous pressure drop (rather than gravity), the viscosity ratio M is expected to be an important parameter in delineating these two regimes.

Stabilized Displacement

In the case of a stabilized displacement, we follow Gouyet et al. (1988) and define the location $X_c(t)$, as the place where the transverse average of the percolation probability is equal to the percolation threshold, p_c , namely

$$p(X_c) = p_c \quad (2.4)$$

In 2-D lattices, X_c represents the mean front position. The regions on either side of X_c of an extent σ (namely between $X_c - \sigma$ and $X_c + \sigma$) have the fractal properties of the percolation cluster (Gouyet et al., 1988). In 3-D lattices, however, due to the higher connectivity, X_c does not represent the mean front position (here the front extends far upstream), but rather denotes a mean leading edge. Nonetheless, a percolation pattern is also expected around X_c . We will focus on the front-tail region ($X > X_c$), the extent of which we will also denote by σ . As in the corresponding *IPG* problem, $X_c(t)$ varies linearly with time in either 2-D or 3-D geometries, with a velocity v , to be determined. In both cases, the fractal regions are followed by an upstream region, where both invading and invaded phases are compact and the conventional continuum description is valid. A schematic is shown in Figure 2.2.

After an in-depth analysis, Xu et al. (1998) (see also Yortsos et al., 1997) showed that the frontal region of width σ satisfies the following scaling with the front capillary number Ca_F and the standard deviation of the pore-size distribution Σ ,

$$\sigma \sim \left(\frac{Ca}{2\Sigma} \right)^{-\frac{\nu}{1+\zeta+\nu(D-1)}} \quad (2.5)$$

where exponent ζ is the conductivity exponent of percolation and D denotes the fractal dimension of the percolation cluster. Equation (2.5) expresses the asymptotic scaling of the front (or front-tail) width with Ca_F at small Ca_F for the case of a stabilized displacement.

Using accepted estimates, the exponent in (2.5) is equal to 0.382 or 0.25 in 2-D or 3-D, respectively. The rather small values suggest a weak sensitivity of σ on Ca_F and Σ . A plot of σ as a function of the capillary number and the mobility ratio, M , is shown in Figure 2.3 (see also Xu et al., 1998). It should be kept in mind that the rate dependence in Ca_F has entered through the front velocity, v . This can be of some significance in investigating the effect of M , which also influences v . It is also interesting to note that as the degree of heterogeneity, Σ , increases the front width increases. In fact, Equation (2.5) suggests that for such displacements it is more appropriate to replace, in the definition of the capillary number, γ by the product $\gamma\Sigma$. The scaling (2.5) can be also obtained by using a version of *GP*, termed Viscous Gradient Percolation (*VGP*), to be introduced below for modeling the saturation profile. Although necessary for the saturation profile, *VGP* is not required for the derivation or the validity of the scaling (2.5).

Saturation Profile

Equation (2.5) provides the scaling of the front width with Ca_F . The other important quantity in gradient percolation is the saturation profile. Gouyet et al. (1988) and Hulin et al. (1988) discussed scaling properties of saturation profiles for the classical *GP* and *IPG* problems, where the percolation probability increment across a region scales linearly with its extent. In the case of a constant gradient, the scaling of the profile is given by

$$S_{nw} \sim p B^{\frac{\beta}{1+\nu}} \Pi_f \left(\frac{X_c - X}{\sigma} \right) \quad (2.6)$$

where $\Pi_f(u)$ is a scaling function which approaches the ordinary percolation scaling, $\Pi_f(u) \sim u^\beta$, when $u > 0$, (where β is a percolation exponent) and it is approximately described by the best-fit expression

$$\log \Pi_f(u) = -1.1u^2 + 0.48u + 0.10 \quad (2.7)$$

when $u < 0$. For the case of viscous displacement, we first need to find the variation of Δp across an arbitrary (but suitably constrained) increment, χ , within the fractal region ($\chi < \sigma$). This problem is equivalent to determining the variation of the transversely averaged pressure within a percolation cluster, across which a fixed pressure difference is applied. Xu et al. (1998) showed that this profile is linear, and we have

$$\Delta p \approx \frac{Ca_F C}{2\Sigma} \chi \left(\sigma^{\frac{\zeta+\nu(D-2)}{\nu}} - bM \right) \quad (2.8)$$

The variation of p in (2.8) is linear with respect to χ .

An approximate description of the saturation profile can now be obtained by using a model *GP* in which the percolation probability has the profile suggested by equation (2.8). The resulting composite profile of p is shown in Figure 2.4. The percolation probability gradient at p_c is constant, as we approach X_c from the right, but diverges as we approach it from the left (see Xu et al. 1998). This feature is different from classical *IPG*, where the gradient at p_c is constant. In actuality, the dependence of the profile near p_c is not as extreme as indicated and a more appropriate profile should involve a composite curve which only asymptotically approaches in the far-field the respective limits. The particular profile depicted in Figure 2.4 gives rise to a different *GP* problem, to be termed Viscous Gradient Percolation (*VGP*).

Viscous Gradient Percolation (*VGP*)

We consider a static percolation problem in a lattice with a percolation probability gradient which is constant at the percolation threshold from the right and diverges from the left, namely

$$p - p_c = \begin{cases} -B^a(X - X_c) & \text{for } X > X_c \\ (B(X_c - X))^c & \text{for } X_c \geq X \end{cases} \quad (2.9)$$

Here, $B > 0$ denotes an equivalent Bond number, exponents $a > 0$ and $0 < c < 1$ are arbitrary, and capital letters denote distances in lattice units. In the specific problem under consideration, we have $a = \frac{1+\nu}{1+\zeta+\nu(D-1)}$ and $c = \frac{1}{1+\zeta+\nu(D-2)}$. We conducted numerical simulations for this gradient percolation problem for values of a and c corresponding to 3-D. Figure 2.4 shows probability and saturation (transversely-averaged occupancy) profiles plotted vs. normalized distance for two different values of B . The overall features of the saturation profiles are similar to *GP*: the profile

decreases almost linearly with distance in the region upstream of the front, and the front extent increases as B decreases. (The different lattice sizes used in the normalized plots of these figures should be noted). The scaling of the saturation profile is expected to have the general features of the scaling function (2.6) of the standard GP , with some correction to account for the slightly different VGP profile.

We summarize this section by emphasizing the different description of percolation processes involving viscous forces in the two regions, near and away from the front, at least for relatively low Ca . The different scalings, $Ca_F^{-\frac{\nu}{1+\zeta+\nu(D-1)}}$ and Ca^{-1} (for the continuum case) obtained indicate that near the front, the continuum description for the profile should be replaced with the more appropriate VGP Equation (2.6). Either theory suggests an advancing front. In the VGP model, the profile is a function of $X - X_c$, Ca_F and M , the time-dependence entering through X_c , which varies with time. A travelling state with constant velocity is also contained in the continuum description. However, the latter predicts a *hypodiffusive* behavior, namely a profile with a divergent derivative at the front (a sharp “knee”), in contrast to the tail involved in VGP . Thus, appropriate caution must be exercised in using the continuum approach in this region.

Capillary-Viscous Fingering

When the *nw* fluid has a much smaller viscosity (namely $M \gg 1$), most of the pressure drop occurs within the displaced phase. In such cases p increases in the direction of displacement. IPG problems with spatially increasing percolation probability involve a negative Bond number and describe invasion in a destabilizing gradient (Meakin et al., 1992) (see also below). In particular, capillary invasion in a destabilizing gravity field corresponds to the release of a lighter fluid at the bottom of a porous column filled with a heavier fluid, for example in air sparging. It was found that the displacement occurs in the form of distinct capillary (but not DLA -type, namely only viscous-dominated) fingers. For a sufficiently long column, one single finger emerged. Figure 2.5 reprinted from Chaouche et al. (1994a) shows the structure of such a finger for capillary invasion in a field of increasing permeability. Scaling arguments similar to the self-consistency arguments of GP can be used here to show that the finger consists of a string of beads of average width σ with the following scaling behavior

$$\sigma \sim |B|^{-\frac{\nu}{\nu+1}} \quad (2.10)$$

To apply these findings to the viscous problems of interest here, an expression for B is needed. Xu et al. (1998) have identified a suitable Bond number for this problem, namely

$$B \approx -\frac{CaM}{2\Sigma} \quad (2.11)$$

Using this definition, a direct comparison with (2.10) gives the following result for the finger width

$$\sigma \sim \left(\frac{CaM}{2\Sigma} \right)^{-\frac{\nu}{\nu+1}} \quad (2.12)$$

The power law of (2.12) has the familiar GP exponent, with values 0.571 or 0.469 in the respective geometries (compared to 0.382 or 0.25 of the previous case). Comparison with (2.5) shows that the scaling exponent almost doubles as the mobility ratio increases from the one limiting regime to the other, implying a higher sensitivity on the capillary number. Equation (2.12) also shows that the finger width decreases with an increase in the capillary number Ca and the mobility ratio M , and

that it eventually reduces to a single thin finger of the size of a single pore (and where the above scaling fails and a *DLA* regime emerges). This behavior is as expected.

We also note that equation (2.12) can be approximated rather well (at least in 3-D) with the expression

$$\sigma \sim Ca^{-0.5} \quad (2.13)$$

This scaling is consistent with that of the fastest (most dangerous) growing finger predicted by the linear stability analysis of Chuoke et al. (1959), which suggests an exponent equal to $1/2$. However, the two should not be confused. The present analysis is based on finger widths of the order of the pore-scale, while the linear stability analysis of Chuoke et al. (1959) is based on a continuum, large-scale description.

The analysis of the above sections shows that the displacement behavior is different depending on the relative magnitude of M . This is a direct consequence of the pressure drop in the frontal region in the two cases of low or high M , respectively. In either case, the pressure drop is associated with the higher flow resistance. In the first case, it is due to the invading phase, which near the front occupies a percolation-like cluster. In the second case, it is due to the displaced phase, which near the front occupies a compact region. The different behavior in these two limits is the origin of the difference in the scaling exponents in the two limits. These results are helpful in the understanding of patterns and also in the delineation of conditions where fractal behavior is expected.

In summary, in this section, the effect of viscous forces on drainage displacements in porous media was studied. We recognized that the process, at least near the front, shares common aspects with *IPG*. When M is sufficiently small, the displacement can be modeled by a form of Gradient Percolation in a *stabilizing* gradient. We developed the scaling of the front width and the saturation profile, in terms of the capillary number. These results generalize the theory of Gouyet et al. (1988). As the stabilized regime is described by the Buckley-Leverett equation, the two share the same constraints for their validity. In the opposite case, the displacement is described by Gradient Percolation in a *destabilizing* gradient and leads to fingering. The particular regime involves a competition between capillary and viscous forces and was identified for the first time in the context of viscous displacements. The theory shows that the conventional continuum approach should be used with caution near the front.

PORE NETWORK SIMULATION

To complement the previous section, we describe here the elements of pore network simulation for drainage processes. As pointed out, pore network simulators are used to simulate processes in pore-networks or glass micromodels. A key assumption is the porous medium representation in terms of a collection of pores, connected to each other by pore throats in a network-like fashion. Conventional networks include regular lattices, such as square or cubic, or Voronoi lattices (Blunt and King, 1991). Either lattice can be readily constructed, although regular lattices are computationally more manageable. Pore networks are ideal for replicating experiments in etched-glass micromodels (see Haghighi et al., 1994, and Li and Yortsos, 1995, for a recent application). Whether for miscible or immiscible flow, their basic aspects include the following:

- Pores provide volumetric storage, throats control the conductance to flow, heat and mass. Geometrical characteristics can be statistically distributed.
- Capillary equilibrium at the pore scale is controlled by pore throats during drainage (a non-wetting (nw) fluid displacing a wetting (w) fluid), and by sites during imbibition (which is the

inverse of drainage). The capillary pressure across an interface is given by the Laplace-Young equation, $P_{nw} - P_w = 2\gamma\mathcal{H}$, where γ is the interfacial tension, and at equilibrium the mean interface curvature, \mathcal{H} , is controlled by the pore geometry.

- Pore bodies can be occupied by one or both of the two fluid phases. Pores occupied by one phase can become trapped by the other phase, if topologically possible. When a pore is trapped, liquid phase movement is not allowed, although mass diffusion continues.
- Local pore-scale coefficients are calculated from single-pore studies. Thermodynamic equilibrium applies within any given pore, although adjacent pores can be at non-equilibrium.

In the simulations, the governing equations are discretized over the pores (nodes) of the network. For example, the overall mass balance at node i is $\sum_j \rho_{ij} Q_{ij} = 0$, where ρ_{ij} , Q_{ij} refer to density and volume flow rate between adjacent sites i and j . The sum is over all neighboring sites j , and we may use Poiseuille's law, $Q_{ij} = \frac{G_{ij}}{\mu_{ij}} (\Delta P_{ij} - \rho_{ij} g_{ij})$, where the overall fluid conductance, $G_{ij} = \frac{A_{ij} r_{ij}^2}{8l_{ij}}$, can be a distributed variable. Here, μ is viscosity, A_{ij} denotes the cross-sectional area of the pore throat joining sites i and j , r is the throat radius, l is the bond length and g is the corresponding component of gravity. Subscript ij indicates quantities pertaining to the throat ij . Fluid properties, such as viscosity, density and interfacial tension can be allowed to vary in different pores, due to compositional dependence.

In the past, simulators have been developed to model immiscible displacement (Lenormand, 1990, Blunt and King, 1991, Chaouche et al., 1994b, Haghighi et al., 1994). These simulators provide a pore-by-pore account of the displacement of interfaces during drainage or imbibition, and can be used to study effects of the viscosity ratio, M , the capillary number, $Ca = \frac{q\mu}{\gamma}$, the gravity Bond number, $B_g = \frac{\Delta\rho g k}{\gamma}$, and various heterogeneities (including spatial correlations at the pore scale). Here, q is the flow velocity, k is the medium permeability and $\Delta\rho$ the density difference. As pointed out above, in certain limits, the displacement patterns can be well characterized by simpler statistical physics models: When $Ca \ll 1$, the pattern is given by *IP*, if $B_g \ll 1$, or by Invasion Percolation in a Gradient (*IPG*), if gravity is also important (see Chaouche et al., 1994a). When Ca is not small, it is viscous forces that control the displacement, giving rise to a viscous fingering pattern (characterized by the *DLA* model, Feder, 1988), if $M \gg 1$, or to a compact (piston-like) displacement, if $M \ll 1$. Simulation of the statistical models *IP*, *IPG* and *DLA* is computationally simple and it is often used to represent displacement patterns. This was demonstrated in the previous section using *VGP* and will be shown again in the next section. For more realistic simulations, the full pore network simulator can be used to explore displacement patterns under general conditions.

In the following we will illustrate applications of pore network simulations for the description of displacement patterns in heterogeneous porous media. We present simulation results, using the full pore network simulator of Xu (1995), carried out in 2-D square lattices of size 100×21 and 100×60 , and for various parameter values. Because of the connection between permeability and average pore size, the simulation of permeability heterogeneity can be accomplished by a variation of the pore size. The latter included a sudden increase or decrease in the average pore size in the direction of displacement by a factor of 2 or 4. Pore sizes were randomly and uniformly distributed around their mean value. We shall present results with $M = 1$. More details can be found in Xu (1995).

First, we show results for drainage in a homogeneous medium (Figure 2.6). The displacement has the typical features of a unit mobility ratio displacement. We note that these features are similar to those obtained in the previous section using the simpler *VGP* model. A certain amount of capillary

trapping occurs at this capillary number. It is important to note the significant fluctuations in the saturation profile due to the finite size of the pore network, however. These effects must be kept in mind, when assessing the subsequent simulations in heterogeneous systems. Numerical simulations for a pore size ramp increase of five lattice spaces are shown in Figures 2.7 and 2.8 for two different values of the capillary number. A response similar to the one predicted by the continuum model and also observed in experiments (Chaouche et al., 1994b) is evident, namely the reduction of the non-wetting phase saturation as the region of permeability increase is approached, followed by a sharp increase. The downward kink diminishes as the capillary number increases (Figure 2.8), although not as smoothly as in the experiments, mostly we suspect as a result of finite size effects. Also, because of the overlap with the boundary end effect at the outlet of the lattice, the saturation following the jump does not rise to the high level observed in either experiments or continuum simulations. A better agreement was found in the simulations involving a larger lattice, however. In all cases, the response diminished substantially as the capillary number increased to levels higher than 10^{-3} .

A comparison between experiments and pore network simulations is given in Chaouche et al. (1994b). Both experiments and pore-network models confirmed the validity of the macroscopic predictions, at least as far as the basic features of the saturation response is concerned. An analysis of the results based on percolation arguments provided additional support to the adequacy of continuum models in describing the response of the saturation to the heterogeneity. The sensitivity of the saturation to heterogeneity at low displacement rates suggests the possibility of heterogeneity identification from saturation maps.

PATTERNS OF DNAPL SPREADING UNDER THE INFLUENCE OF GRAVITY

The previous sections illustrated the relevance and utility of pore network models, both full-scale simulation and simpler statistical physics models, in describing immiscible displacement patterns. In this section, we will use a similar approach to examine the spreading of *DNAPLs*.

Spreading of *DNAPLs* in the subsurface, when they encounter a low-permeability region, is subject to capillary, gravity and viscous forces. The previous pore-network approach is equally well applied to describe these displacement patterns. While a full-scale simulation is possible, however, we shall use here the simpler model of *IPG*. As discussed above, in a stabilizing *IPG*, a fractal front with a width satisfying the scaling (2.5) is followed by a compact front. In a destabilizing *IPG*, on the other hand, the invasion process is dominated by the growth of a single finger, assuming sufficiently large gradients. The corresponding scaling of the finger width is also given by the same equation. It was shown in the previous sections, that *IPG* can describe both the effect of gravity and the effect of viscous forces. In the typical application of *IPG*, the gradient is specified in the direction of displacement. For example, this is the case in viscous gradients presented above. In the case of a *DNAPL* spreading at the bottom of an impermeable barrier, however, the gradient due to gravity will be *perpendicular* to the direction of displacement. This gives rise to a new and interesting problem of *IPG*, in which two gradients exist: one in the direction of displacement (for example, due to viscous forces), and another in the direction perpendicular to the displacement (due to gravity). To our knowledge, this problem has not been addressed in the literature, so far. This section explores aspects of the solution of this problem.

Consider *IPG* in the presence of gradients both transverse and parallel to the direction of displacement. Simulations were carried out in 2-D (square) and 3-D (cubic) lattices of sizes 800×400 and $128 \times 128 \times 128$, respectively. The algorithm is an *IP* algorithm, in which the site with the *lowest* threshold among all sites in the advancing front is the next site to be penetrated. Each site is assigned a threshold according to

$$\tau = \text{rand} + B_X \times X + B_Y \times Y \quad (2.14)$$

where rand is a random number in the interval (0,1), and B_X and B_Y are the Bond numbers in the parallel, X , and transverse, Y , directions, respectively. Coordinates X and Y express dimensionless distance in terms of pore lengths and the transverse coordinate Y increases upwards. Stabilizing gradients correspond to a positive Bond number, destabilizing gradients to a negative Bond number. To simulate *DNAPL* spreading at the bottom of the boundary, a destabilizing (negative) Bond number was selected. (The opposite case would correspond to a smaller density fluid, e.g. a gas, penetrating the medium and collecting at the top boundary). Recall that for the case of gravity, the Bond number expresses the ratio of buoyancy to viscous forces, while for the case of viscous forces it is related to the capillary number Ca . In the presence of a gradient in the transverse direction, we considered injection from the entire face (edge injection) $X = 1$, all sites of which are occupied. For the case of only a parallel destabilizing gradient, injection from the middle point of the face $X = 1$ was considered. In the latter case, we also used periodic boundary conditions across the lateral boundaries. A number of different realizations were carried out, most results shown corresponding to averages over 50 runs.

Results

We first present simulations of a destabilizing *IPG*, where $B_Y = 0$. Figures 2.9 and 2.10 correspond to 2-D and 3-D simulations, respectively, for various values of the parallel Bond number, B_X , the physical picture corresponding to spreading due to viscous and capillary (but not gravity) forces. As expected, the single finger dominates the process, the width of which increases, as the Bond number decreases. As before, the relation between the width and the (absolute value of) the Bond number must be the power law of equation (2.10). Results are shown in Figure 2.11. We obtain the exponent values of 0.6303 for 2-D and 0.5335 for 3-D. These should be compared to Meakin et al. (1992), where the values of 0.60 and 0.58, respectively, are found. The corresponding theoretical values from percolation theory are 0.57 and 0.47, respectively. This discrepancy is probably due to the relatively small number of realizations used and the limited length scale of the lattice covered by the simulations, as also explained in Meakin et al. (1992).

Figures 2.12 and 2.13 shows displacements using only a transverse gradient ($B_X = 0$). The physical picture corresponding to this problem is *DNAPL* spreading subject to capillary and gravity (but not viscous) forces. The pattern spreads on the top of the impermeable boundary, as expected physically, and it has the characteristic percolation features. Of interest is the width, σ_Y , of the invaded zone along the vertical direction. A theoretical analysis indicates that the problem belongs to the same class as *IPG*, thus we expect the same power-law scaling as in (2.10), namely

$$\sigma_Y \sim |B_Y|^{-\frac{\nu}{\nu+1}} \quad (2.15)$$

Results plotted in Figure 2.14 confirm the validity of (2.15) in this case, and indicate exponents equal to 0.6339 and 0.5326 for 2-D and 3-D, respectively. These values compare very well with the previous case of destabilizing *IPG*. Thus, it can be concluded that *IPG* with a single *transverse* gradient has the same features as *IPG* in a destabilizing *parallel* gradient. This means that in the absence of viscous forces, the spreading *DNAPL* has percolation characteristics and a thickness which decreases as $B_Y \equiv \frac{\Delta \rho g_Y k}{\gamma}$ increases, namely as the permeability k increases or the interfacial tension decreases.

Consider, next, the case where both gradients are combined. This would be the case of *DNAPL* spreading in the presence of capillary, gravity and viscous forces. A series of simulations were conducted for stabilizing and destabilizing parallel gradients.

The case of a stabilizing gradient corresponds to viscous-stabilized displacement, which was described in a previous section. Here, we expect that B_X would be related to the velocity through a relationship of the type $B_X \sim (\frac{Ca}{\Sigma})^a$, where $a = \frac{\nu+1}{1+\zeta+\nu(D-1)}$ (e.g. compare with equation (2.9), and which takes values equal to 0.66 and 0.53, in the respective geometries. Thus, larger Ca corresponds to larger B_X . Figures 2.15 and 2.16 show 2-D invasion patterns corresponding to a variety of values of B_X and B_Y . The patterns are characterized by a leading front with a fractal structure, which is expected to scale as (2.5), followed by a compact front. A simple analysis suggests that this problem is actually *IPG* in a stabilizing gradient but with a Bond number which is the geometric sum of the two Bond numbers, namely

$$B = \sqrt{B_X^2 + B_Y^2} \quad (2.16)$$

Thus, the size of the front width decreases with an increase in B . For sufficiently large B , the front is quite sharp and it is well described as a straight line of slope B_X/B_Y (note that this slope is negative). Figures 2.15 and 2.16 demonstrate indeed the validity of this result. Similar features were found for invasion in a 3-D lattice. In this case of stabilized displacement, therefore (namely when M or Ca are sufficiently small, see Yortsos et al., 1997), the slope of the front scales as

$$\text{slope} \sim \frac{Ca_F^a}{\Delta\rho|g_Y|k\Sigma^a} \quad (2.17)$$

namely the front is more horizontal (has more of a tongue-like shape) when the velocity is small or buoyancy is strong, as expected. However, note the exponent a in the scaling of the front with the velocity or the heterogeneity, which reflects percolation characteristics. This result should be contrasted to the classical, effective medium result for the slope of a propagating sharp interface in a porous medium, which is

$$\text{slope} \sim \frac{q\mu}{\Delta\rho|g_Y|k} \quad (2.18)$$

corresponding effectively to $a = 1$. We conclude that *IPG* leads to a non-trivial new result on the pattern structure.

The case of a destabilizing parallel gradient corresponds to the problem of unfavorable mobility ratio (sufficiently large M). Now, the Bond number is of the type shown in (2.11), namely $B_X \sim -\frac{CaM}{2\Sigma}$. Patterns obtained from simulations for various values of B_X and B_Y are shown in Figures 2.17 and 2.18. We note that in 3-D the width, σ_Z , along the lateral (Z) direction of the invading cluster depends on the parallel gradient. However, the thickness σ_Y along the transverse direction depends on both gradients. Figure 2.19 shows the dependence of the width along the lateral Z direction for the 3-D case. As before, the width is a power-law, this time of the parallel gradient, B_X , only, with an exponent estimated at 0.59. This value compares reasonably well with the previous value 0.5335, above, and 0.58 of Meakin et al. (1992). This result indicates that the transverse gradient has little influence on σ_Z , which behaves essentially as in the presence of only one destabilizing parallel gradient.

To understand the extent of the invasion zone along the transverse direction Y , we consider a simple analysis based on *IPG* arguments. This suggests the following scaling

$$\sigma_Y = B_X^{-\frac{\nu}{\nu+1}} f(z) \quad (2.19)$$

where we denoted $z = \frac{B_X}{B_Y}$ and the scaling function $f(z)$ is determined with the following reasoning. In the limit of small transverse gradients, the problem should reduce to that portrayed in Figures 2.9-2.11, hence we should expect the result $f(z) \sim 1$ as $z \rightarrow \infty$. On the other hand, in the limit of small parallel gradients, the result pertaining to Figures 2.12-2.14 applies, hence we should expect the different behavior, $f(z) \sim z^{\frac{\nu}{\nu+1}}$ as $z \rightarrow 0$. Combining the two we have

$$f(z) \sim z^{\frac{\nu}{\nu+1}} \text{ as } z \rightarrow 0 \text{ and } f(z) \sim 1 \text{ as } z \rightarrow \infty \quad (2.20)$$

To test the validity of these predictions, we plotted the results according to the scaling function above in Figure 2.20. For the 2-D simulations a total of 220 different combinations is shown (where the range of B_X is $(10^{-5} - 4 \times 10^{-1})$, and the range of B_Y is $(6 \times 10^{-6} - 4 \times 10^{-1})$), while for the 3-D simulations a total of 44 combinations of B_X and B_Y is plotted (where the range of B_X is $(10^{-5} - 10^{-1})$, and the range of B_Y is $(5 \times 10^{-4} - 10^{-1})$). For each combination of parameters, the ensemble average of 50 realizations was obtained. Figure 2.20 shows that the data collapse on a single scaling curve with the scaling properties described in (2.20), thus supporting well the scaling result.

We summarize this section by concluding that the spreading of *DNAPL* on the top of an impermeable medium may well have strong percolation (namely fractal-like) characteristics, when the rate of penetration is slow, so that gravity and capillarity dominate over viscous forces (and also in the case of unfavorable mobility ratio). In such cases, the percolation characteristics must be carefully considered in the design of remediation processes.

USE OF IPG FOR DESCRIBING AIR SPARGING PATTERNS

We close this chapter with a very brief presentation of the use of *IPG* for the description of air sparging patterns. Experiments of Dumore (1970) in oil recovery and of Ji et al. (1993) in air sparging have showed that the upward migration of gas depends on two conditions related to the capillary pressure. At conditions of high capillarity, the air-occupied region is essentially a conical region, while at conditions of low capillarity, only one gas channel develops. These two conditions were termed dispersive and non-dispersive, respectively. As discussed previously, air sparging could possibly be described as a destabilizing *IPG*. However, Figures 2.9 and 2.10 above show that destabilizing *IPG* leads to a single finger, regardless of the value of the Bond number. This contrasts to the experiments for the dispersive case. To model this problem using *IPG*, we proceeded with a modification of the traditional algorithm.

Assume that at a given stage, the invading phase penetrates not only the site with the smallest capillary threshold, but also several sites. The justification is that in reaching "steady-state", pressure fluctuations in both invading and defending phases develop, so that more than one site can be penetrated. One algorithm to implement this idea involves penetrating all neighboring sites, the threshold of which is close to the maximum threshold at the front, at a given stage, namely

$$|\tau - \tau_{max}| < P \quad (2.21)$$

Here the thresholds τ are defined as $\tau = \text{rand} + B_g Y$, where B_g is a gravity Bond number and Y indicates the vertical coordinate, while parameter P measures the extent of the fluctuations and controls the transition from non-dispersive (small P) to dispersive (large P). Using (2.21) we can apply *IPG* except that now multiple sites can be penetrated. The simulations were carried out in a 200×200 lattice. Typical results are shown in Figure 2.21 for a given value of the Bond number and different values of the fluctuation extent, P . We note that as P increases, multiple sites are penetrated resulting in a conical-shape pattern (the artifact at the top of the pattern should be

disregarded), in qualitative agreement with published experiments. Further work is in progress to improve the modeling of such patterns.

ACKNOWLEDGEMENTS

This research was also partly supported by DOE Contract No. DE-FG22-93BC14899.

REFERENCES

1. Blunt, M. and King, P.R, Relative permeabilities from two- and three-dimensional pore-scale network modeling, *Transp. Porous Media*, Vol. 6, 407-433 (1991).
2. Chaouche, M., Rakotomalala, N., Salin, D., Xu, B., and Yortsos, Y.C., Invasion percolation in a hydrostatic or a permeability gradient: Experiments and simulations, *Phys. Rev. E*, Vol. 49, 4133-4139 (1994a).
3. Chaouche, M., Rakotomalala, N., Salin, D., Xu, B., and Yortsos, Y.C., Capillary effects in drainage in heterogeneous media: Continuum modeling, experiments and pore network simulations, *Chem. Eng. Sci.*, Vol. 49, 2447-2466 (1994b).
4. Chuoke, R.L., van Meurs, P., and van der Poel, L.B., The instability of slow, immiscible, viscous liquid-liquid displacements in permeable media, *Trans. AIME*, Vol. 216, 188-194 (1959).
5. Dumore, J.M., Development of gas-saturation during solution-gas drive in an oil layer below a gas cap, *SPEJ*, Vol. 10, 211-218 (1970).
6. Gouyet, J.-F., Sapoval, B. and Rosso, M., Fractal structure of diffusion and invasion fronts in three-dimensional lattices through the gradient percolation, *Phys. Rev. B*, Vol. 37, 1832-1842 (1988).
7. Haghighi, M., Xu, B. and Yortsos, Y.C., Visualization and simulation of immiscible displacement in fractured systems using micromodels: I. Drainage, *J. Coll. Interface Sci.*, Vol. 166, 168-179 (1994).
8. Hulin, J.-P., Clément, E., Baudet, C., Gouyet, J.-F., and Rosso, M., Quantitative analysis of an invading fluid invasion front under gravity, *Phys. Rev. Lett.*, Vol. 61, 333-336 (1988).
9. Ji, W., Dahmani, A., Ahlfeld, D.P., Lin, J.D., and Hill, E., Laboratory study of air sparging: Air flow visualization, *GWMR*, 115-126 (1993).
10. Lenormand, R., Liquids in porous media, *J. Phys.: Condens. Matter*, Vol. 2:SA, 79-88 (1990).
11. Li, X., and Yortsos, Y.C., Visualization and simulation of bubble growth in pore networks, *AICHEJ*, Vol. 41, 214-222 (1995).
12. Meakin, P., Birovljev, A., Frette, V., Feder, J., and Jøssang, T., Gradient stabilized and destabilized invasion percolation, *Phys. Rev. A*, Vol. 46, 227-239 (1992).
13. Stauffer, D., and Aharony, A., "Introduction to Percolation Theory", Francis-Taylor (1992).
14. Wilkinson, D., and Willemsen, J.F., "Invasion percolation: A new form of percolation theory", *J. Phys. A*, Vol. 16, 3365-3376 (1983).
15. Xu, B., Ph.D. dissertation, University of Southern California, (1995).
16. Xu, B., Yortsos, Y.C. and Salin, D., Invasion percolation with viscous forces, *Phys. Rev. E*, Vol. 57, 739-751 (1998).

17. Xu, B., Kamath, J., Yortsos, Y.C. and Lee, S.H., "Use of Pore Network Models to Simulate Laboratory Corefloods in a Heterogeneous Carbonate Sample", paper SPE 38879 presented at the 1997 SPE Annual Conference, San Antonio, TX (Oct. 5-8, 1997).
18. Yortsos, Y.C., Xu, B., and Salin, D., Phase diagram of fully-developed drainage, Phys. Rev. Lett, Vol. 79, 4581-4584 (1997).

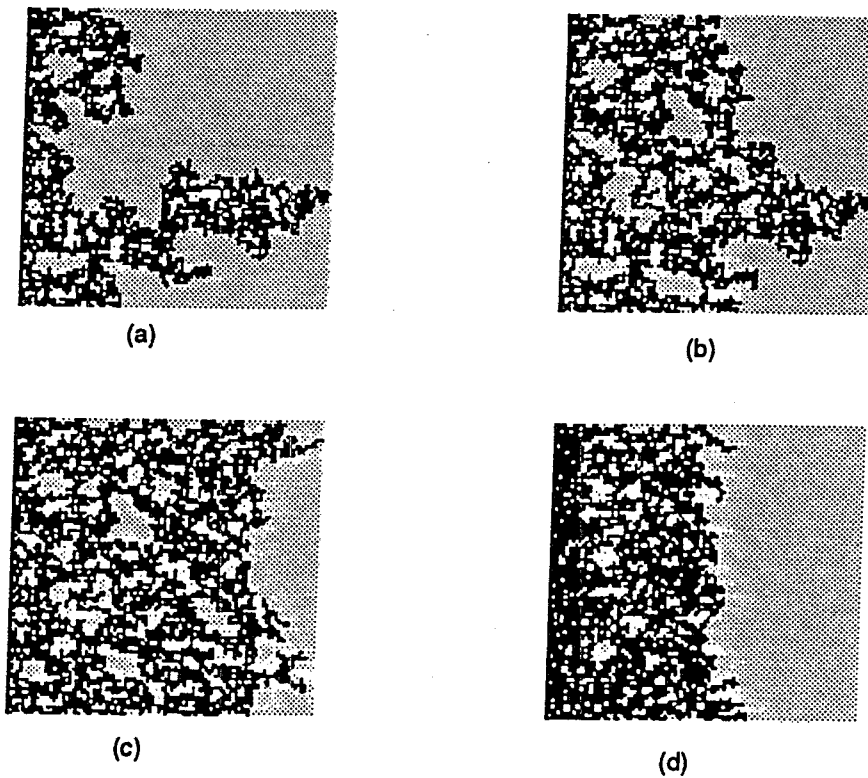


Figure 2.1. Displacement patterns from numerical simulation of drainage in a 100×100 lattice, with $M = 0.1$ and different values of the capillary number: (a) $Ca = 3.2 \times 10^{-8}$ (IP) , (b) $Ca = 3.2 \times 10^{-6}$, (c) $Ca = 3.2 \times 10^{-5}$ and (d) $Ca = 3.2 \times 10^{-4}$.

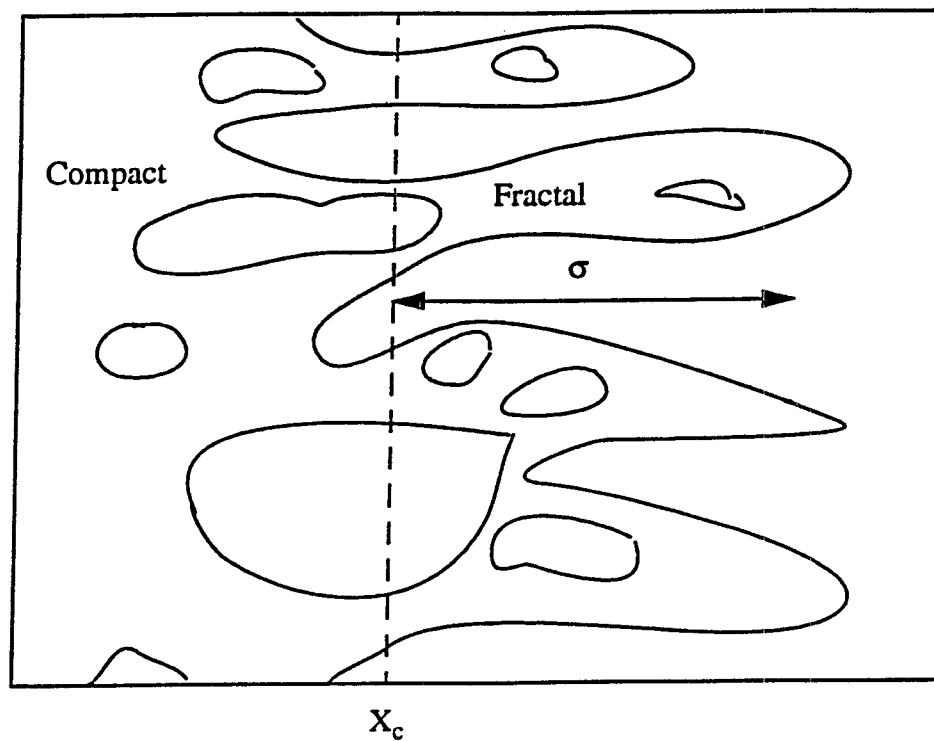


Figure 2.2. Schematic of the front region and the notation used.

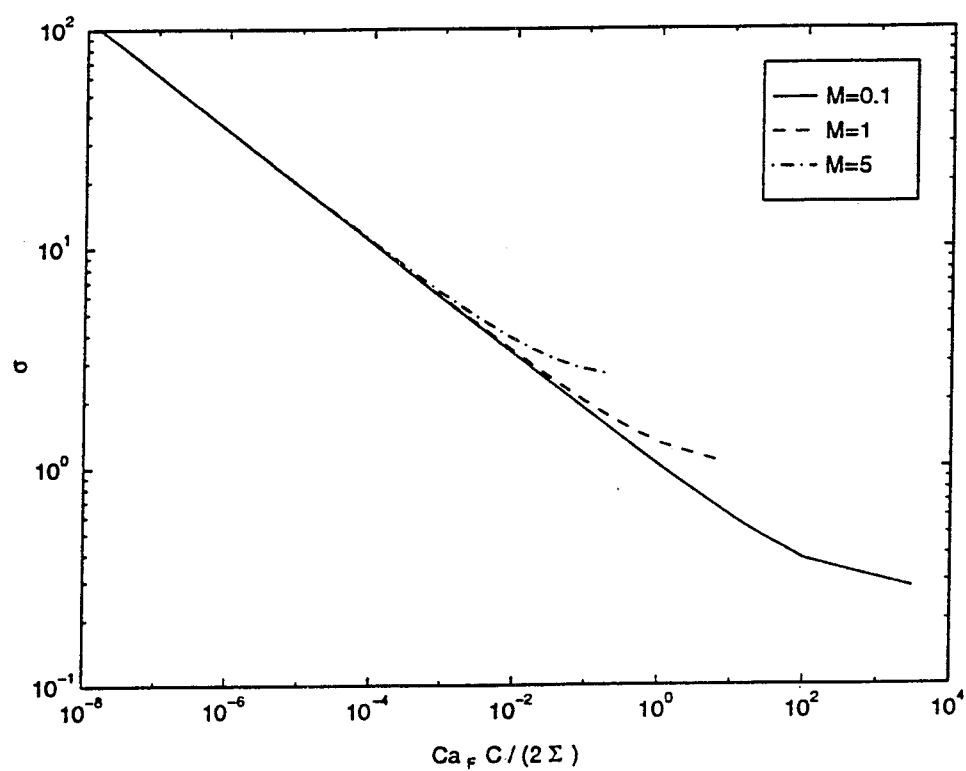
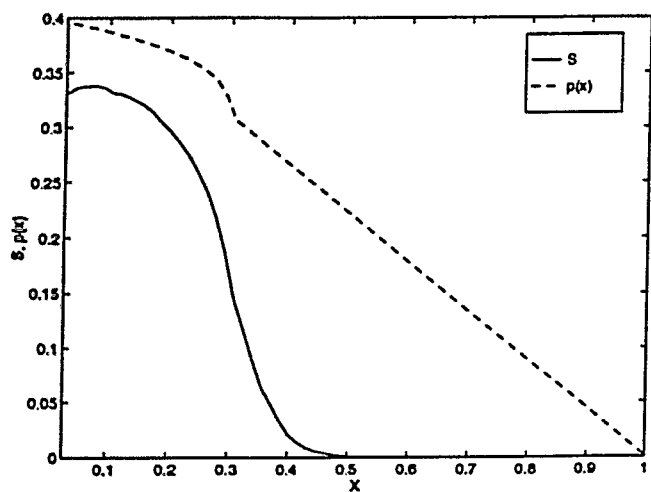
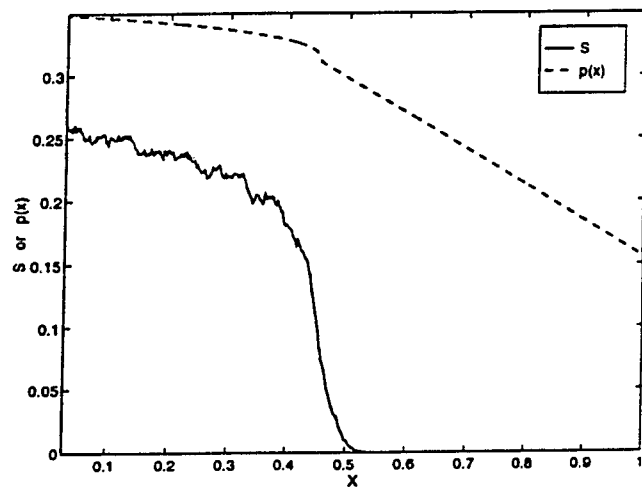


Figure 2.3. Numerical solution of (2.5) vs. the modified capillary number for three different values of M .



(a)



(b)

Figure 2.4. Percolation probability (dashed line) and saturation (solid line) profiles vs. normalized length, for 3-D VGP: (a) $B = 10^{-4}$ in a lattice of $200 \times 200 \times 65$, (b) $B = 10^{-6}$ in a lattice of $200 \times 200 \times 500$.

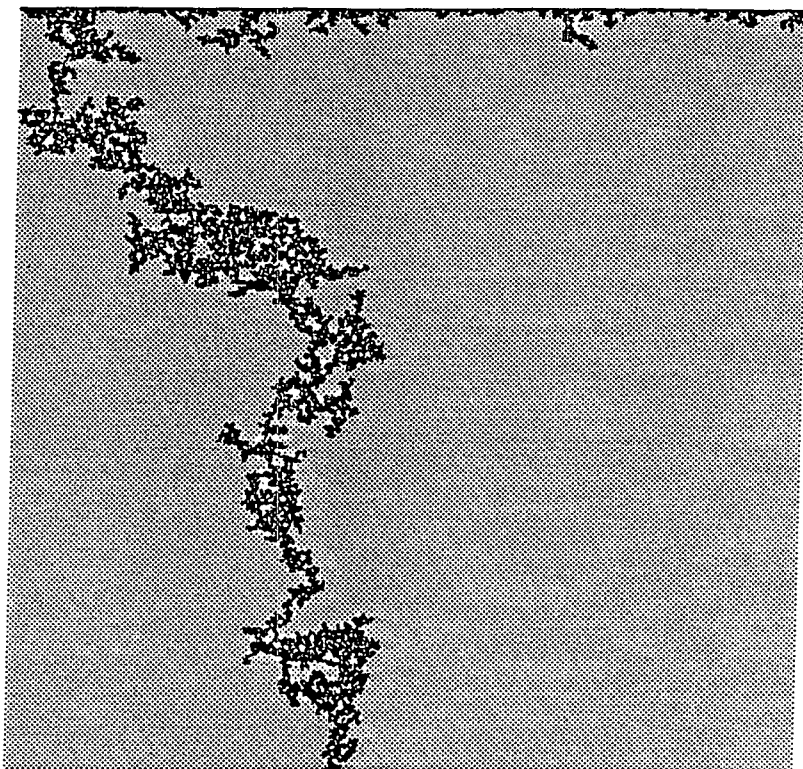


Figure 2.5. Single finger in GP in a destabilizing gradient.

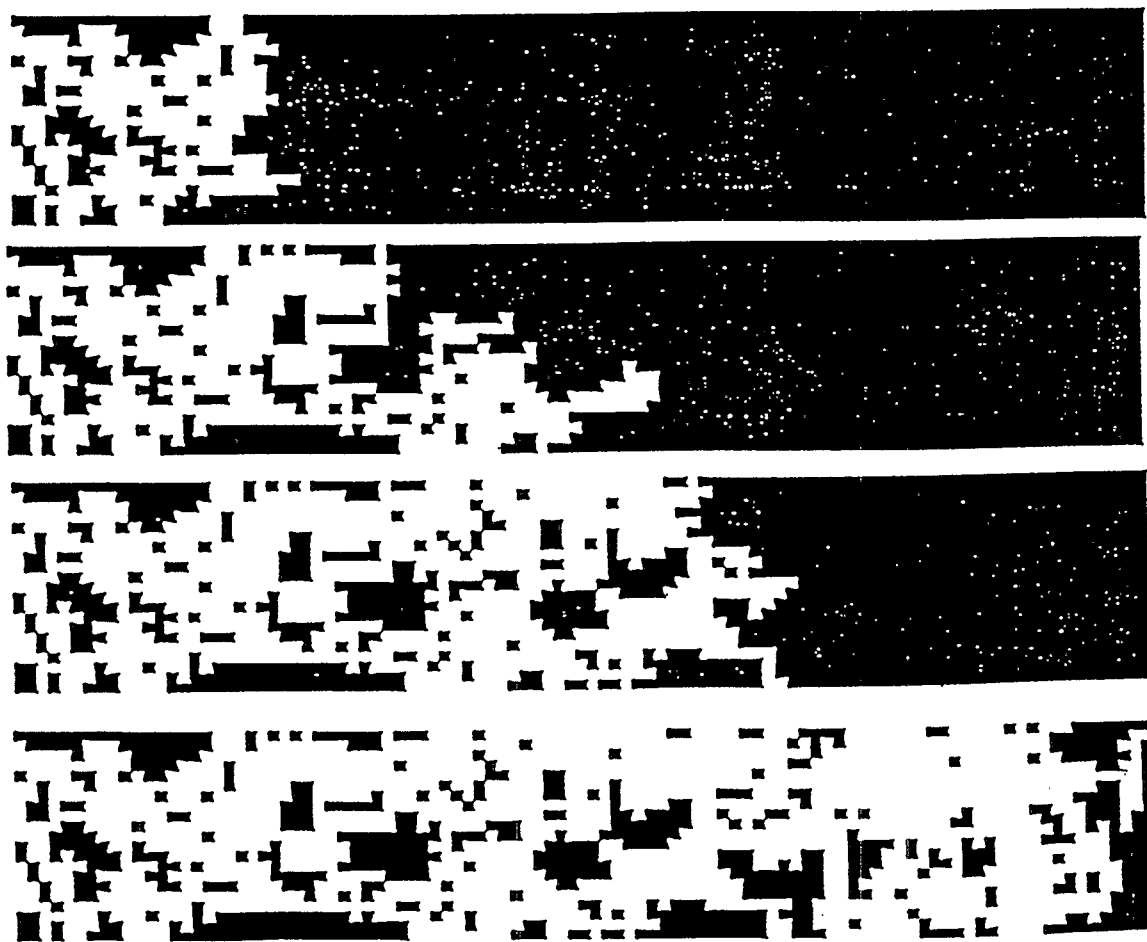
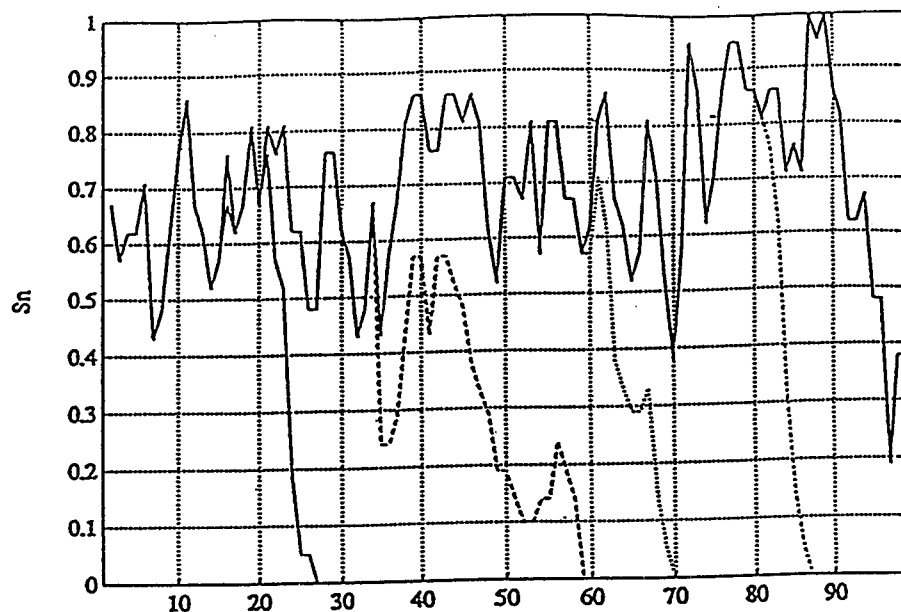


Figure 2.6. Pore network simulations (saturation profile and displacement patterns) for uniform permeability and $Ca = 1.5 \times 10^{-4}$.

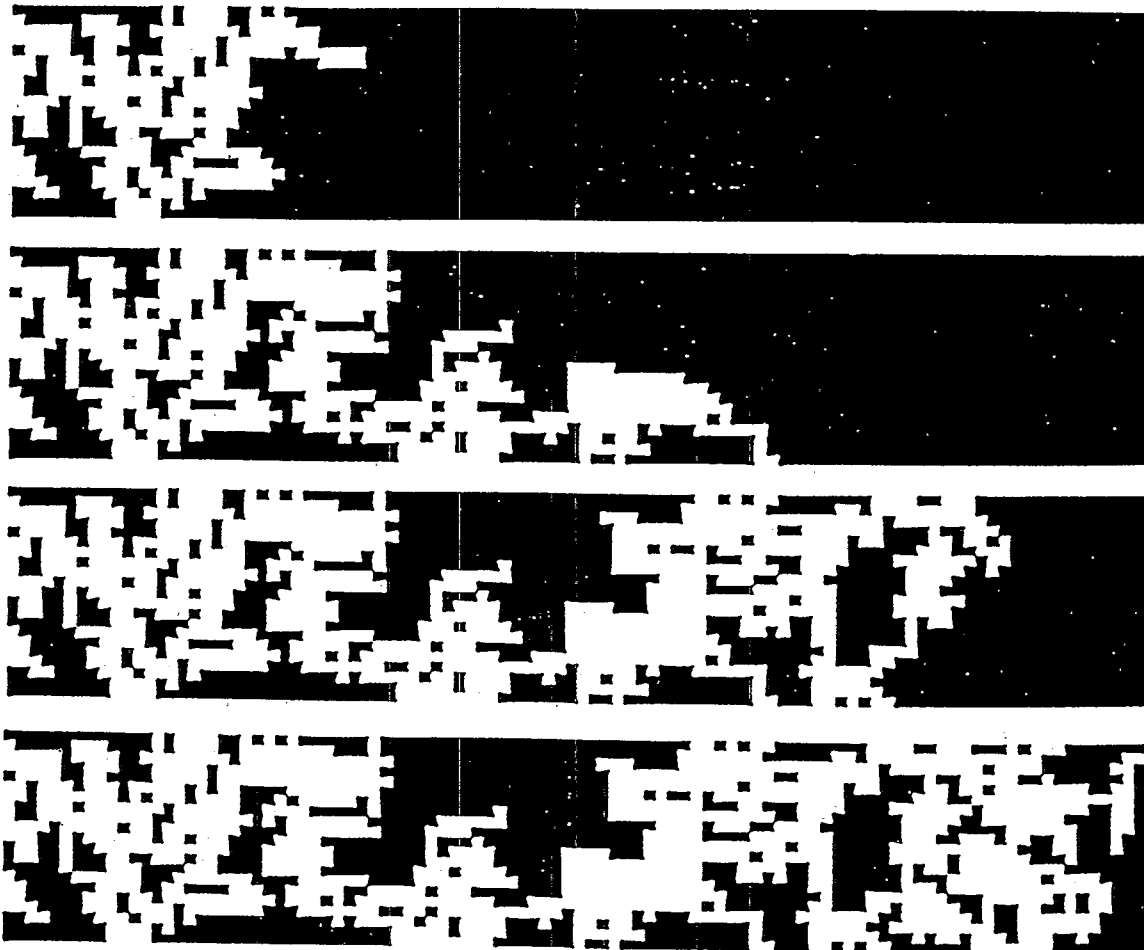
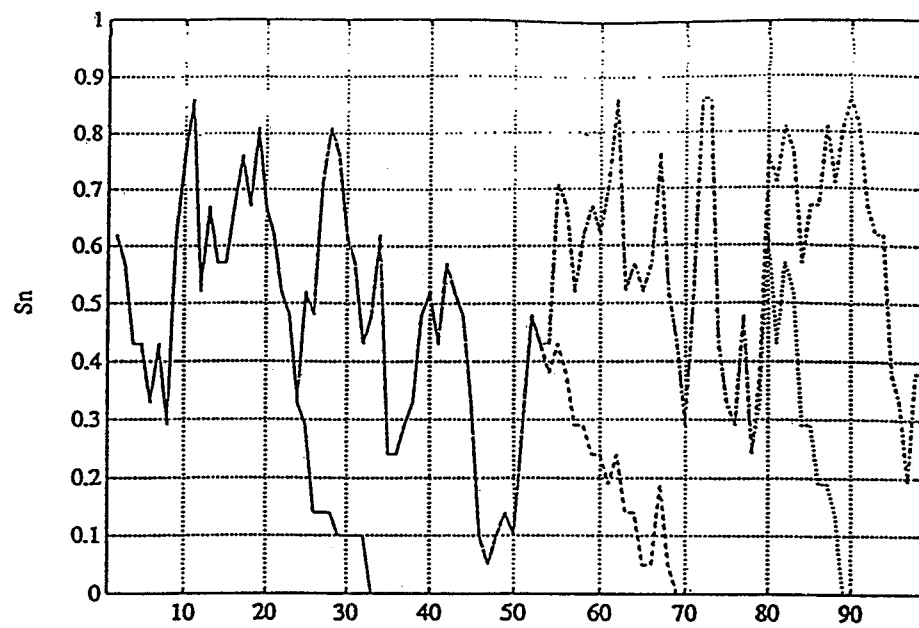


Figure 2.7. Pore network simulations (saturation profile and displacement patterns) for permeability increase (1:2) and for $Ca = 1.5 \times 10^{-5}$.

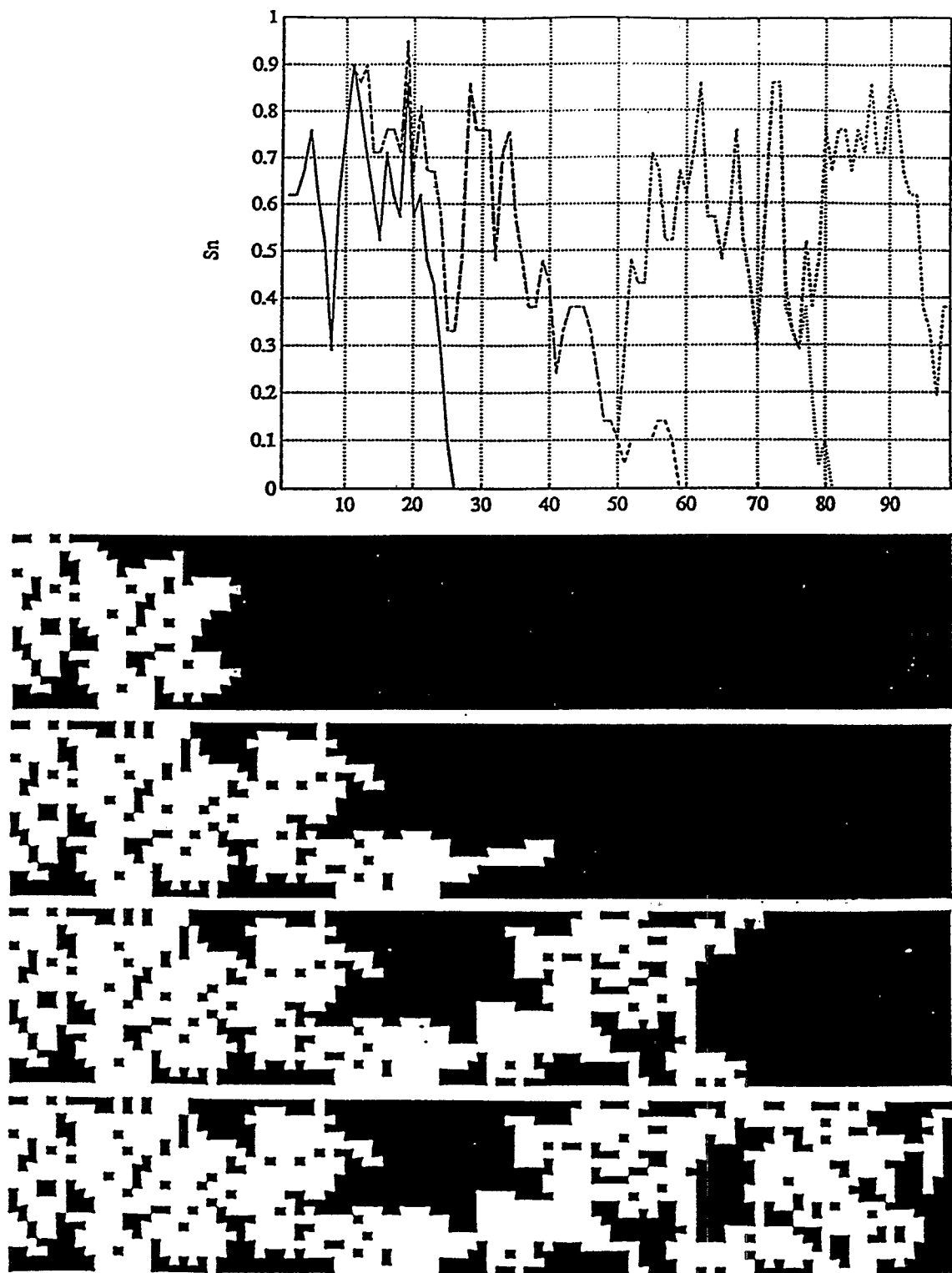
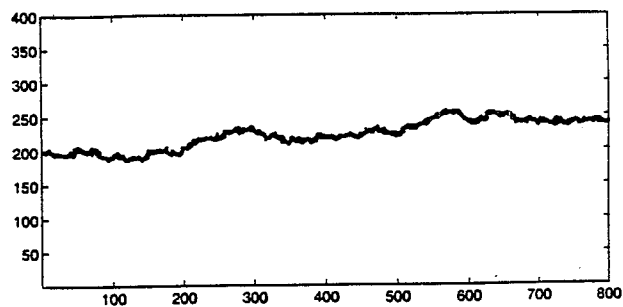
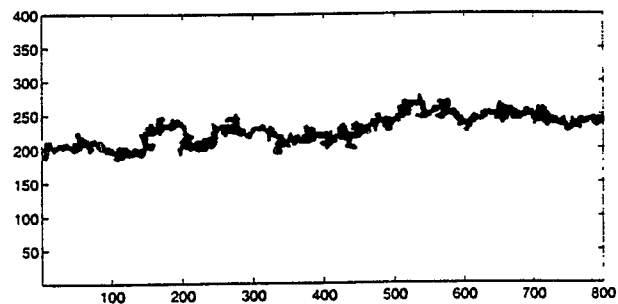


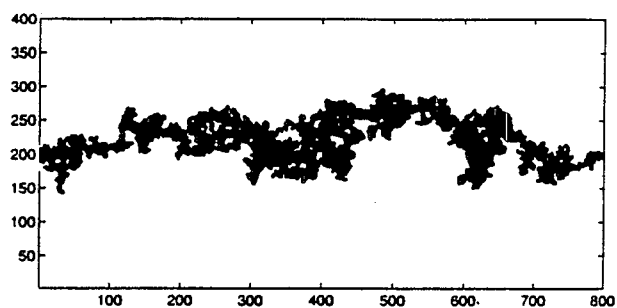
Figure 2.8. Pore network simulations (saturation profile and displacement patterns) for permeability increase (1:2) and for $Ca = 1.5 \times 10^{-4}$.



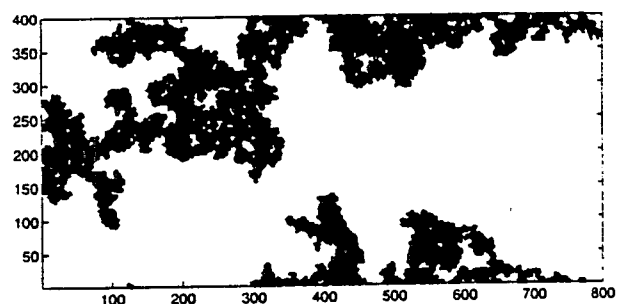
(1)



(2)

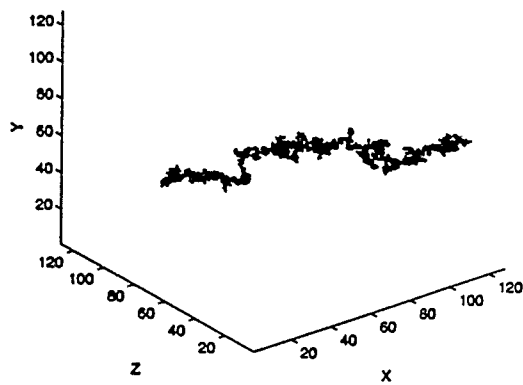


(3)

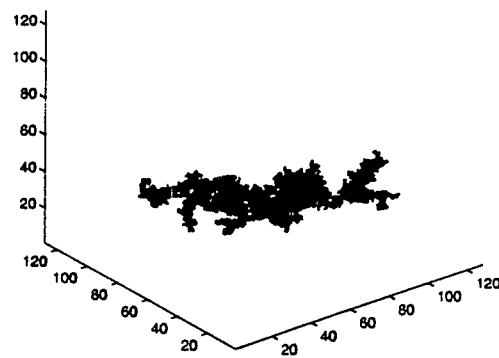


(4)

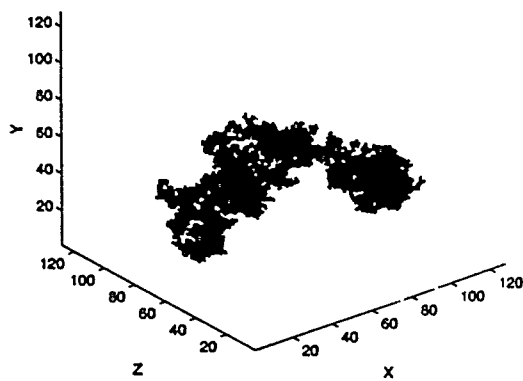
Figure 2.9. Displacement pattern with parallel gradient in a 2-D 800×400 lattice: (1) $B_X = -0.1$, (2) $B_X = -0.01$, (3) $B_X = -0.001$, (4) $B_X = -0.0001$.



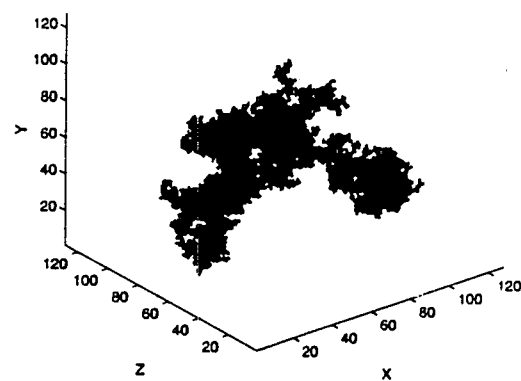
(1)



(2)



(3)



(4)

Figure 2.10. Displacement pattern with parallel gradient in a 3-D $128 \times 128 \times 128$ lattice: (1) $B_X = -0.03$, (2) $B_X = -0.003$, (3) $B_X = -0.001$, (4) $B_X = -0.0003$.

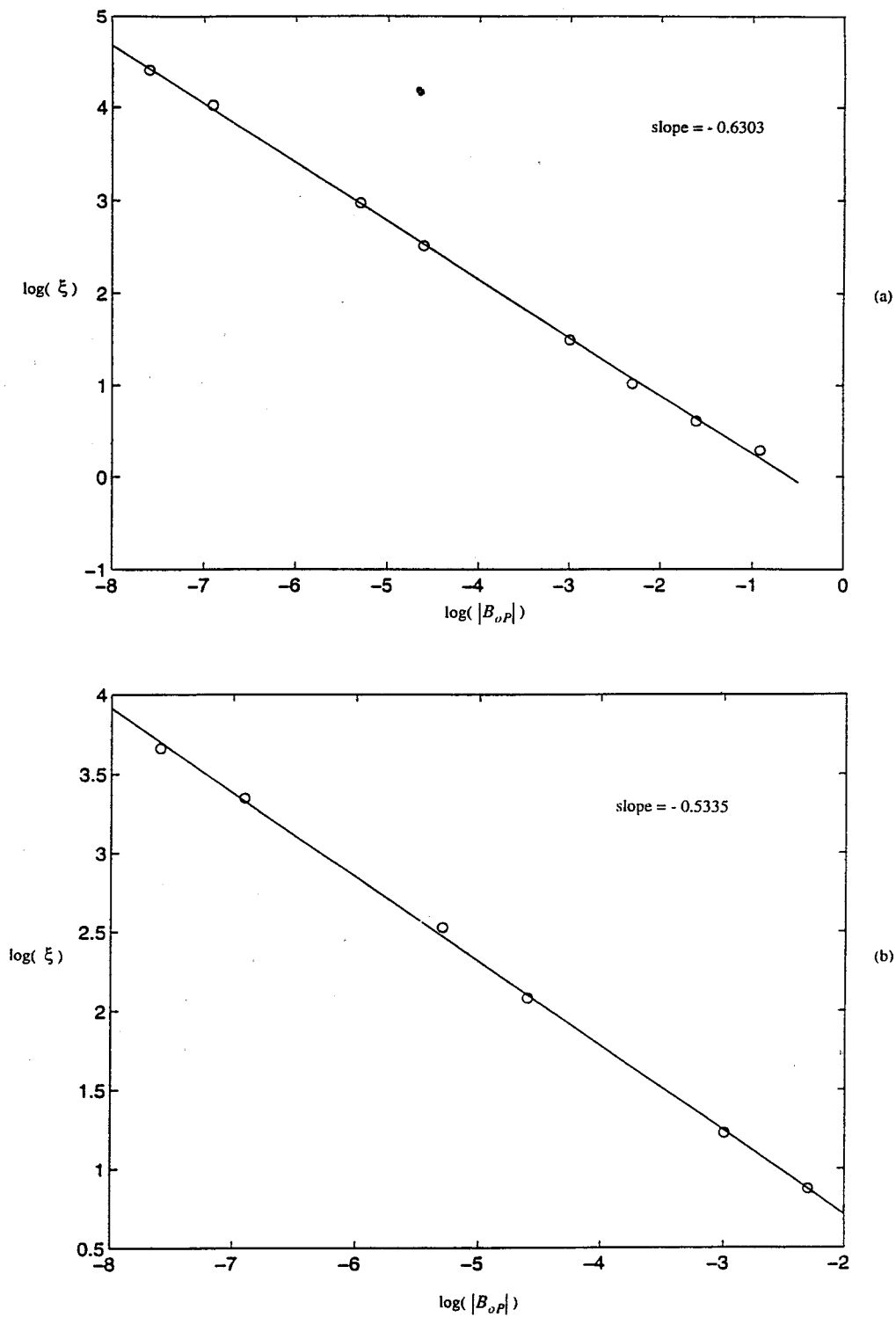
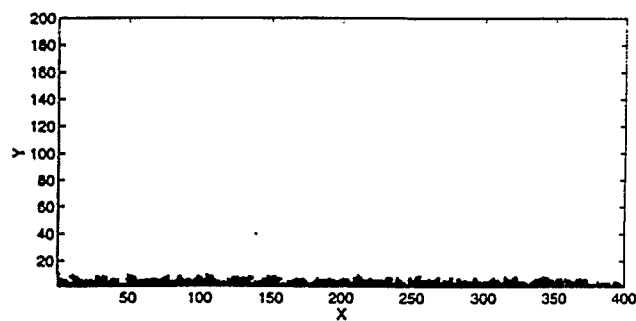
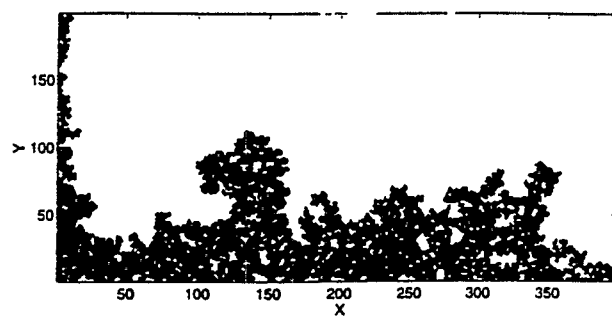


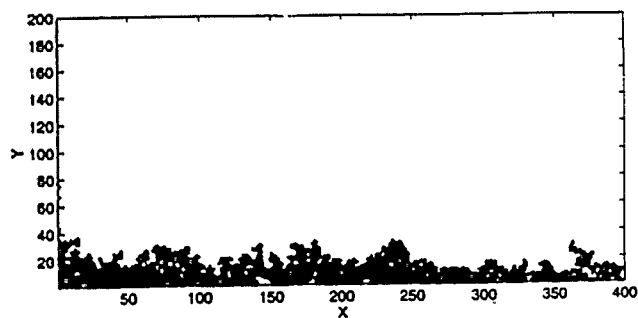
Figure 2.11. The dependence of finger width on the Bond number for (a) 2-D, and (b) 3-D lattices.



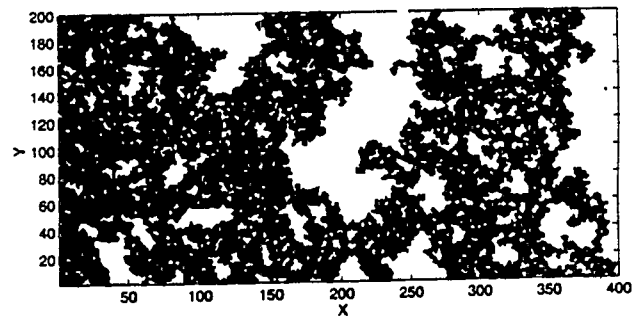
(1)



(3)

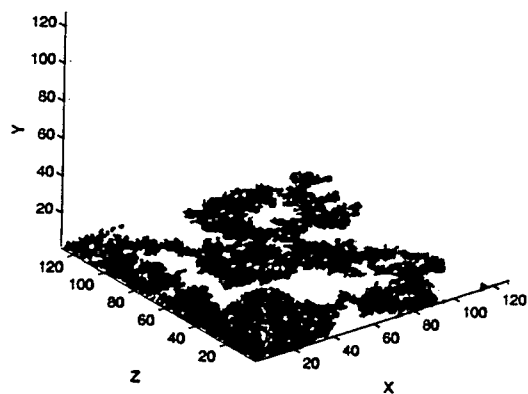


(2)

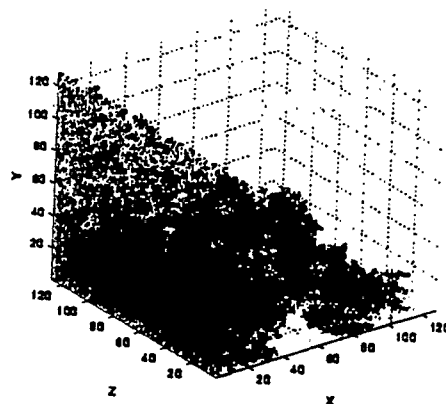


(4)

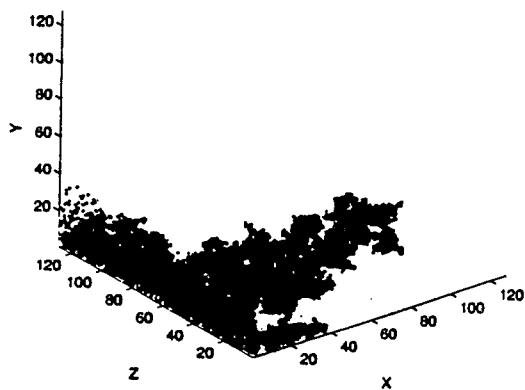
Figure 2.12. Displacement pattern with transverse gradient in a 2-D 800×400 lattice: (1) $B_Y = -0.1$, (2) $B_Y = -0.01$, (3) $B_Y = -0.001$, (4) $B_Y = -0.0001$.



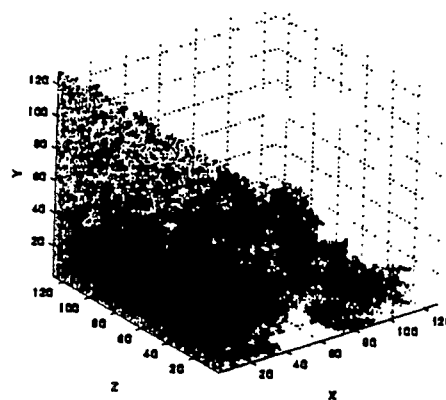
(1)



(2)



(3)



(4)

Figure 2.13. Displacement pattern with gradient in a 3-D $128 \times 128 \times 128$ lattice: (1) $B_Y = -0.1$, (2) $B_Y = -0.01$, (3) $B_Y = -0.001$, (4) $B_X = -0.0005$.

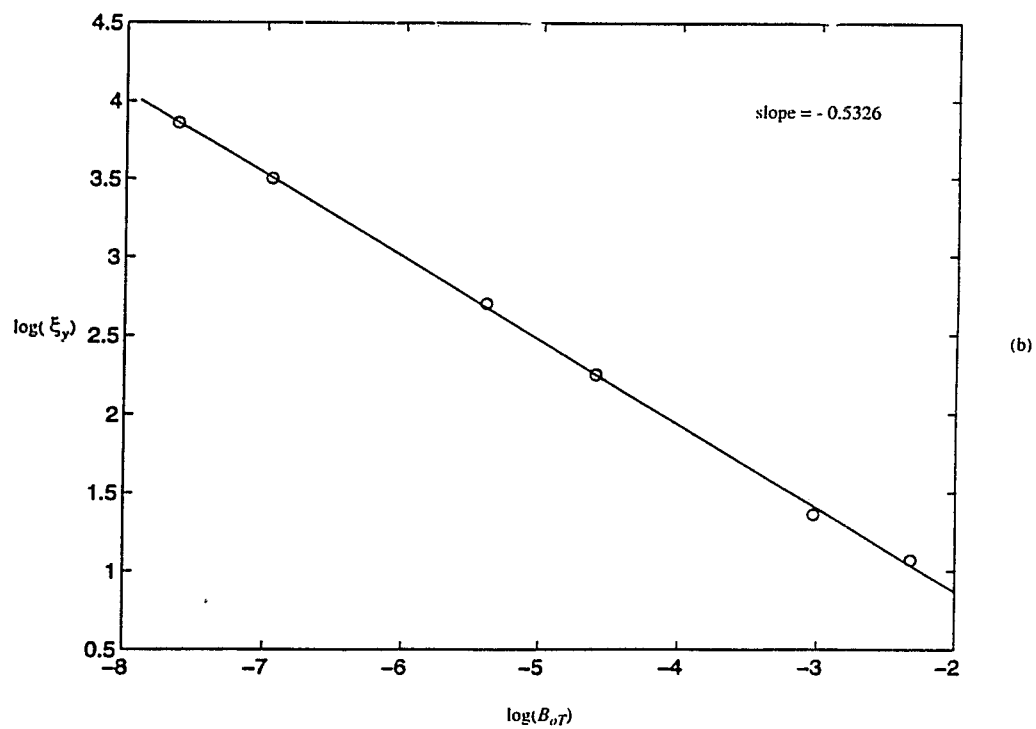
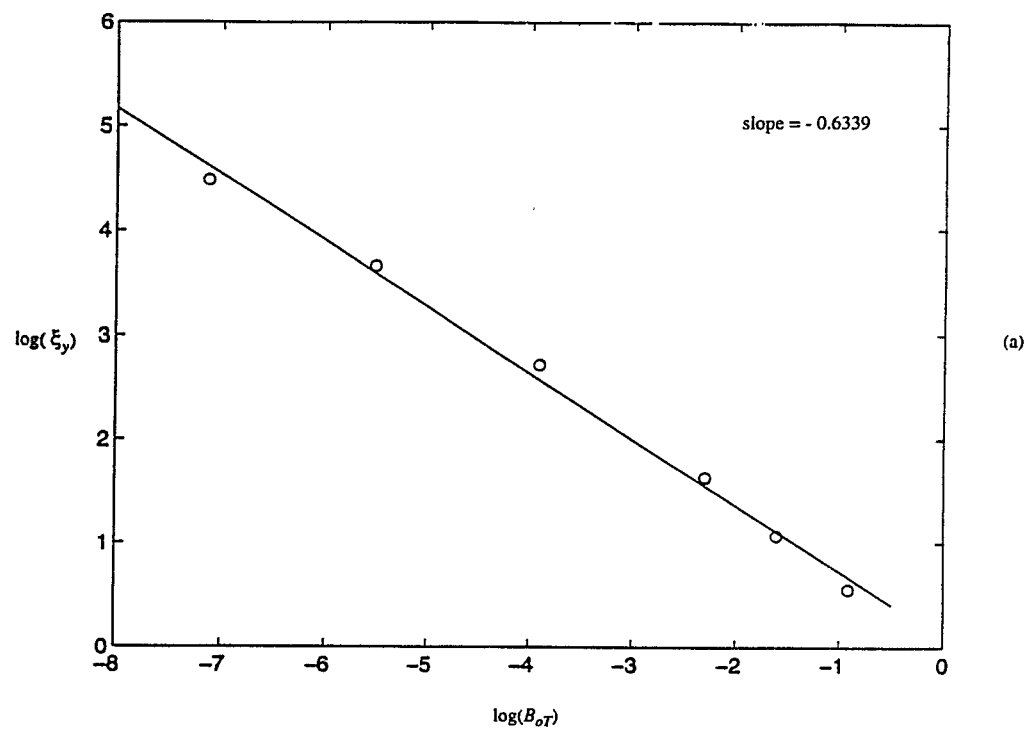
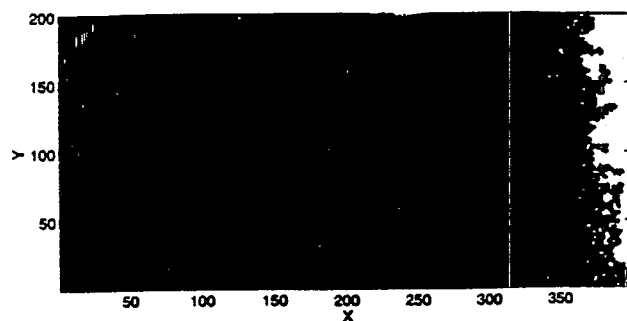
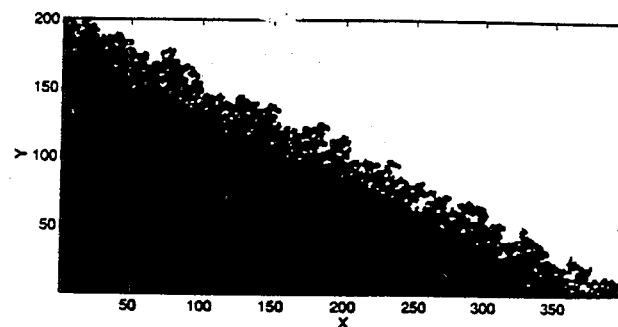


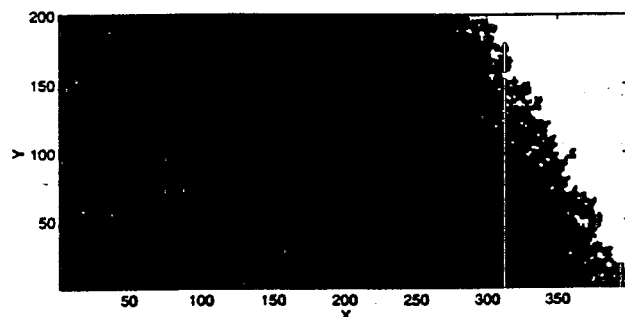
Figure 2.14. The dependence of finger width σ_Y on B_Y for (a) 2-D, and (b) 3-D lattices.



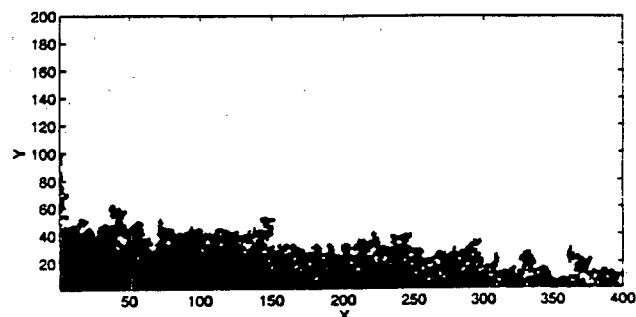
(1)



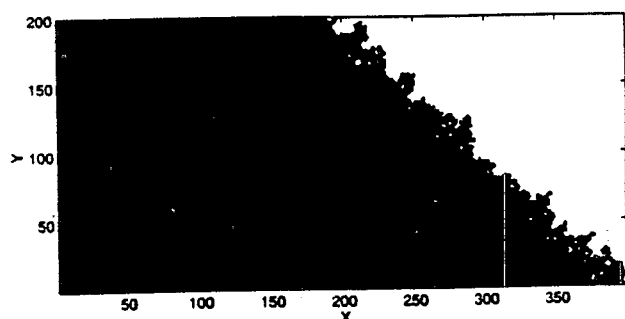
(4)



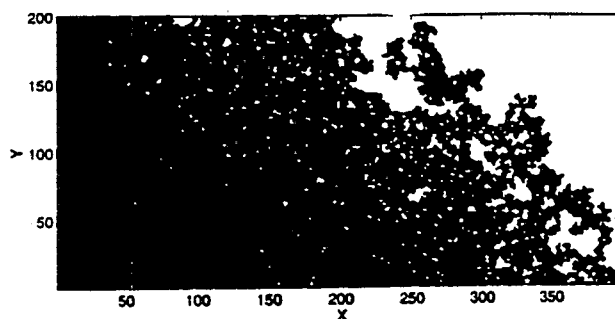
(2)



(5)

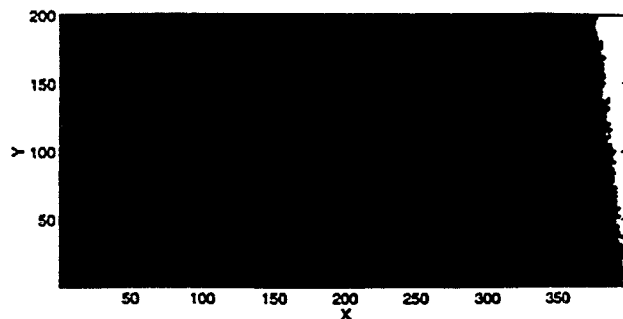


(3)

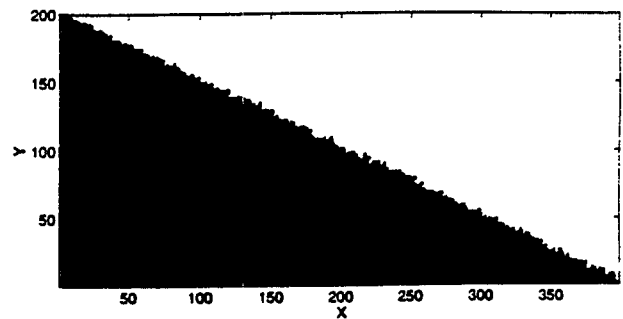


(6)

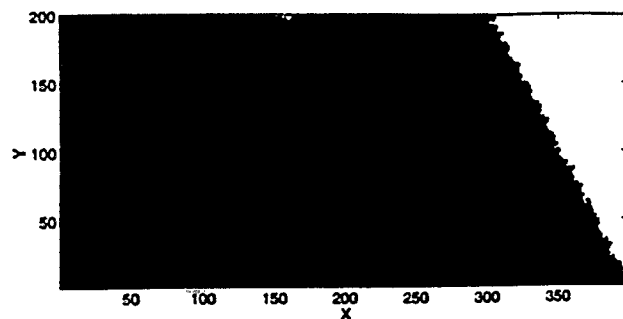
Figure 2.15. Displacement pattern with both transverse and parallel gradient in a 2-D 800×400 lattice: (1) $B_X = 0.01$, $B_Y = -0.001$, (2) $B_X = 0.01$, $B_Y = -0.005$, (3) $B_X = 0.01$, $B_Y = -0.01$, (4) $B_X = 0.005$, $B_Y = -0.01$, (5) $B_X = 0.001$, $B_Y = -0.01$, (6) $B_X = 0.001$, $B_Y = -0.001$.



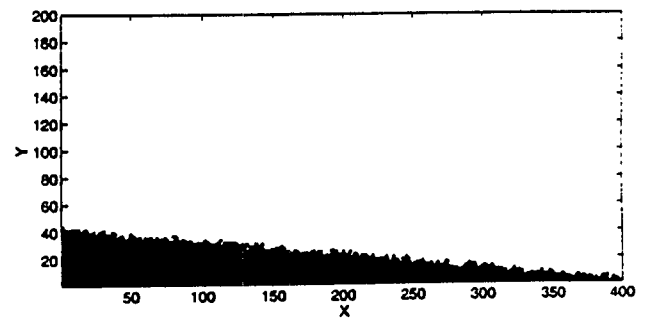
(1)



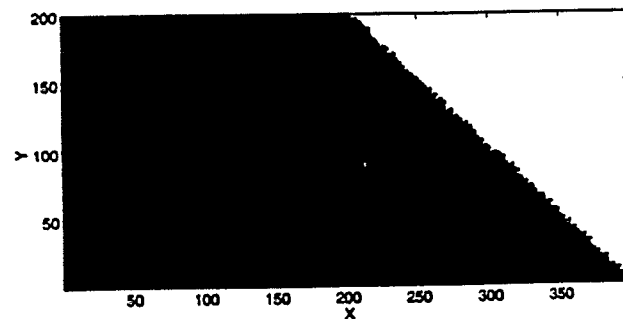
(4)



(2)

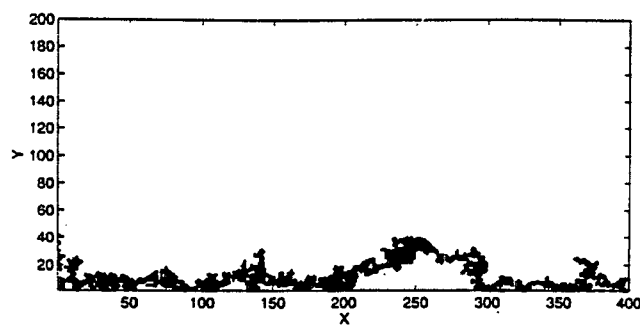


(5)

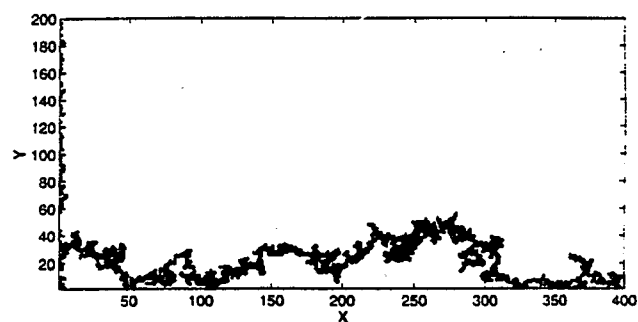


(3)

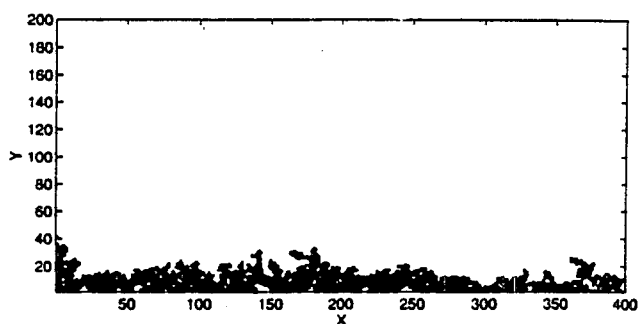
Figure 2.16. Displacement pattern with both transverse and parallel gradient in a 2-D 400×200 lattice: (1) $B_X = 0.1$, $B_Y = -0.01$, (2) $B_X = 0.1$, $B_Y = -0.05$, (3) $B_X = 0.1$, $B_Y = -0.1$, (4) $B_X = 0.05$, $B_Y = -0.1$, (5) $B_X = 0.01$, $B_Y = -0.1$.



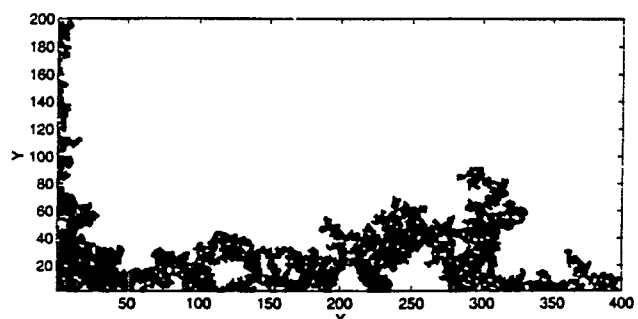
(1)



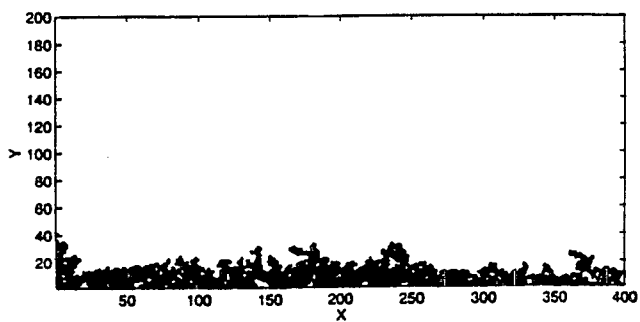
(4)



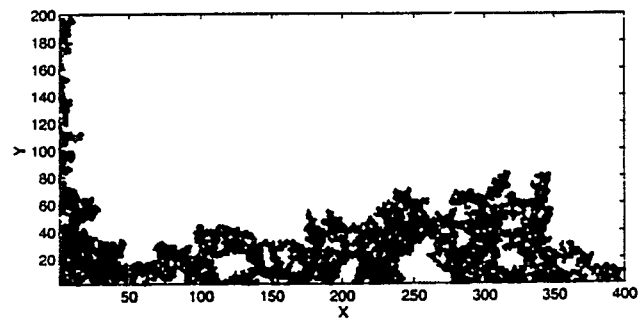
(2)



(5)



(3)



(6)

Figure 2.17. Displacement pattern with both transverse and parallel gradient in a 2-D 400×200 lattice: (1) $B_X = -0.01$, $B_Y = -0.01$, (2) $B_X = -0.001$, $B_Y = -0.01$, (3) $B_X = -0.0005$, $B_Y = -0.01$, (4) $B_X = -0.01$, $B_Y = -0.001$, (5) $B_X = -0.001$, $B_Y = -0.001$, (6) $B_X = -0.0005$, $B_Y = -0.001$.

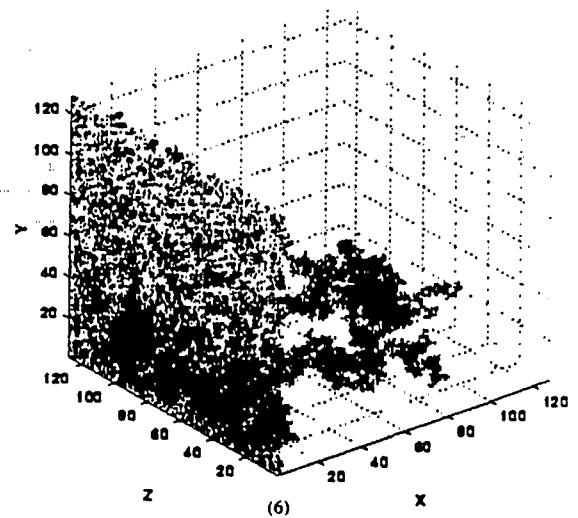
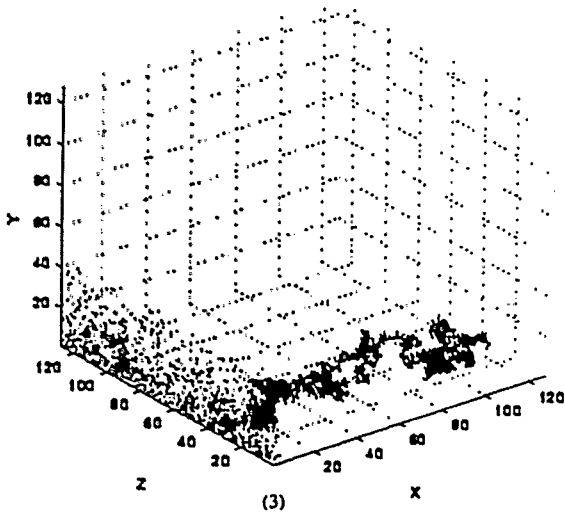
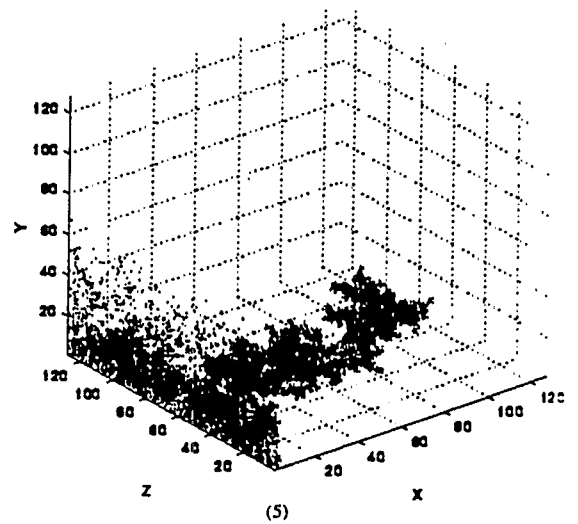
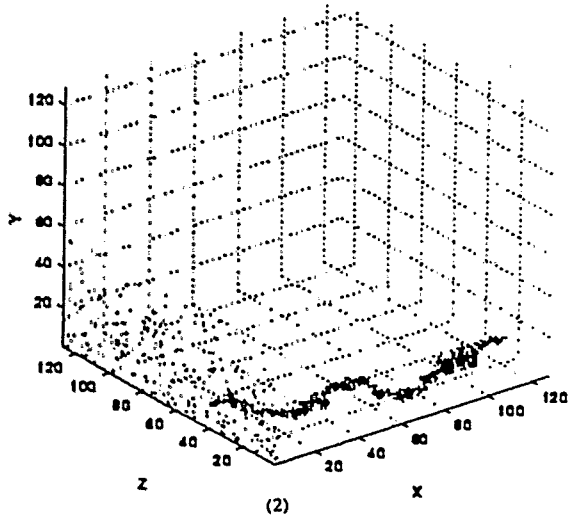
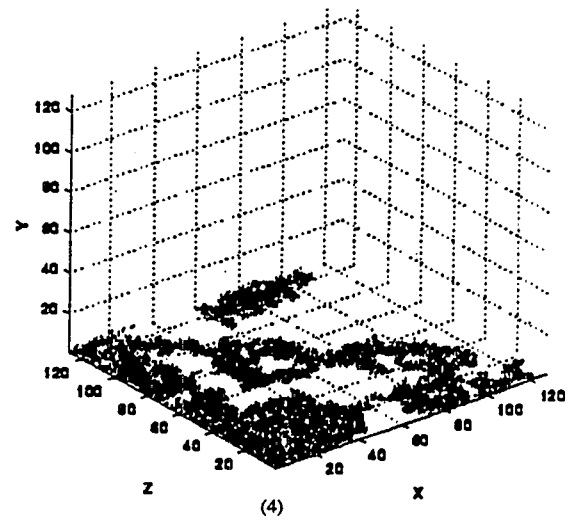
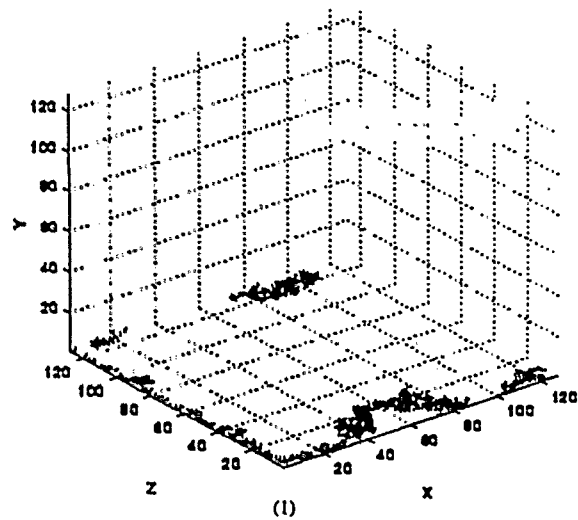


Figure 2.18. Displacement pattern with both transverse and parallel gradient in a 3-D $128 \times 128 \times 128$ lattice: (1) $B_X = -0.01$, $B_Y = -0.1$, (2) $B_X = -0.01$, $B_Y = -0.005$, (3) $B_X = -0.01$, $B_Y = -0.001$, (4) $B_X = -0.0005$, $B_Y = -0.1$, (5) $B_X = -0.0005$, $B_Y = -0.005$, (6) $B_X = -0.0005$, $B_Y = -0.001$.

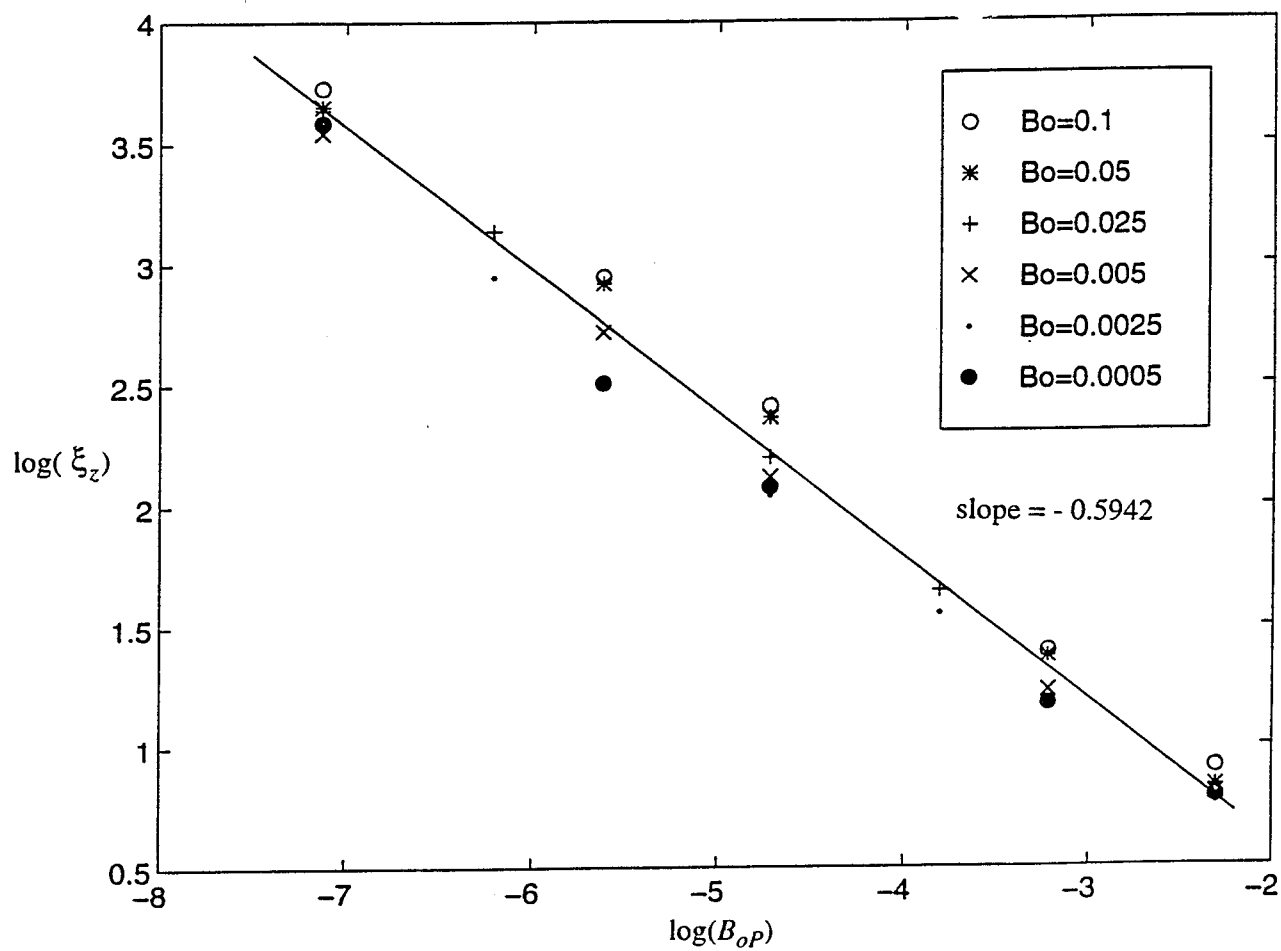


Figure 2.19. The dependence of finger width σ_Z on B_X for a 3-D lattice and various values of B_Y .

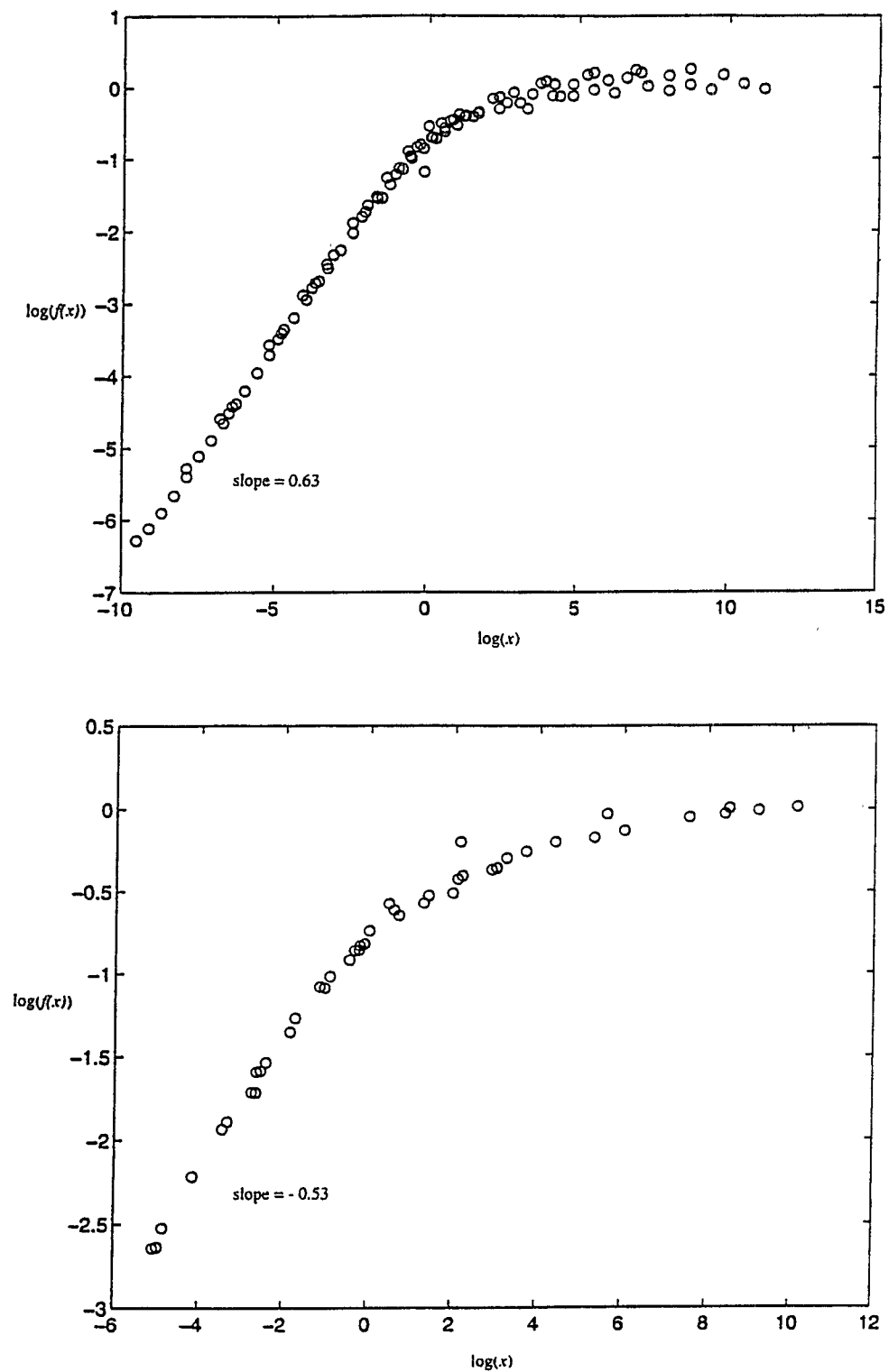


Figure 2.20. The scaling function $f(z)$ from simulations in: (a) 2-D lattice, (b) 3-D lattice.

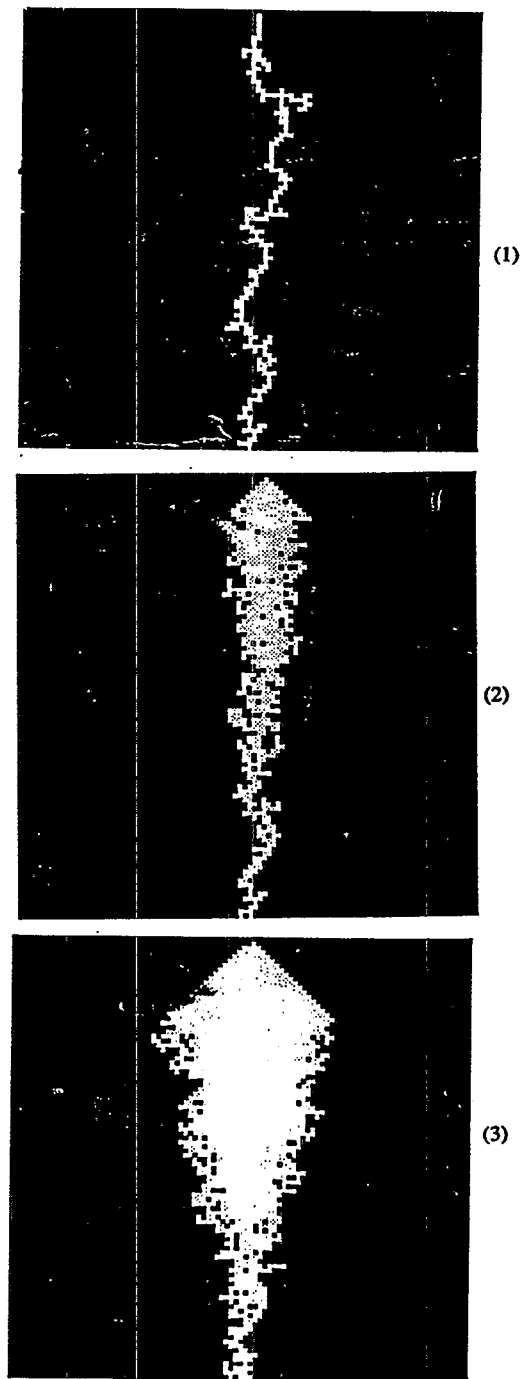


Figure 2.21. Modified destabilizing *IPG* patterns to model air sparging for $B = -0.1$ and $P = 0$, 1 and 2, respectively.

Chapter 3

VISUALIZATION AND SIMULATION OF NAPL SOLUBILIZATION IN PORE NETWORKS

Chunsan Jia, Katherine Shing and Yanis C. Yortsos

INTRODUCTION

A common source of soil and water aquifer contamination is the accidental release or spill of organic liquids, commonly known as Non-Aqueous Phase Liquids (NAPL), which percolate to the subsurface due to gravity. This well-known problem is quite extensive and poses potential health hazards, particularly if the NAPLs reach and contaminate aquifers. A variety of remediation techniques have been developed to mitigate the problem.

As pointed out in the Introduction, the most commonly used method is *pump-and-treat*, in which the groundwater is pumped out of the site, treated on the surface to remove the contaminant and subsequently reinjected (Mackay and Cherry, 1989). In-situ remediation involves the injection of remedial fluids or chemicals which may enhance the solubility of the contaminant (Pennell et al., 1993, Augustin et al., 1994) or help to mobilize trapped NAPL (Brandes and Farley, 1993). Injection of surfactants (West and Harwell, 1992, Pennell et al., 1993), co-solvents, such as alcohols (Pinal et al., 1990, Wood et al., 1990), and air (sparging) (Ji et al., 1993, Pankow et al., 1993) in the groundwater, or injection of steam in the vadose zone (Itamura and Udell, 1993, Ho et al., 1994), are some of the methods actively under consideration.

Of interest to this work is the mass transfer of contaminants from residual NAPLs. As with other processes, this must be investigated at the different scales that comprise porous media. These include the pore scale or microscopic scale (of the order of tens of μm), where capillary phenomena are important, the pore-network scale (of the order of mm), where the collective behavior of a process over an ensemble of pores is investigated, the laboratory (core) scale (of the order of cm), and the field or megascopic scale (of the order of m and higher), of relevance to large-scale spreading. Phenomena at the different scales have a different manifestation, and input from a lower scale is necessary for their description at the next higher scale.

With the exception of some recent works, the design of in-situ remediation is based on a description at the macroscopic (or megascopic) scales. Phenomena at the pore and pore-network scales are typically lumped in terms of averaged quantities, using empirical or *ad hoc* expressions. At best, these are adaptations of macroscopic models developed in enhanced oil recovery (e.g. see Abriola and Pinder, 1985a,b, Brown et al., 1994), and cannot address remediation issues originating at the pore and pore network scales. Recent approaches (Celia et al., 1993, Soll and Celia, 1993, Soll et al., 1993), paralleling earlier efforts in oil recovery (e.g. Heiba et al., 1982) have used percolation theory to relate quantities, such as relative permeabilities and capillary pressures, to the microstructure. However, the problem of mass transfer, which is fundamental to NAPL remediation is currently based on macroscopic simulation.

The overall mass transfer coefficient has been estimated by different correlations (Table 1), reflecting the different assumptions made by different investigators. Thus, inconclusive at present are the effects of flow velocity, interfacial area and its variation with time (due to dissolution, mobilization, etc.) (Imhoff et al., 1993). Particularly interesting are the reported differences in the exponent relating the mass-transfer Sherwood number to the local Reynolds number, for which convincing theories have not been provided. In principle, this exponent should reflect the relevant flow regime and the interface configuration (Cussler, 1984). In the most advanced model to date, Powers et al. (1994) approximated mass transfer by steady-state diffusion from an isolated spherical NAPL globule in a structureless porous medium. However, this approximation does not adequately represent the true geometrical configuration of NAPL-groundwater interfaces in a real system, which are disordered (and possibly fractal) (Feder, 1988, Lenormand, 1990, Sahimi and Yortsos, 1990) and the concomitant effects on fluid flow and mass transfer.

Issues of mass transfer between immiscible phases in disordered porous media at the pore-network scale were addressed in recent studies, although in a somewhat different context. In a series of papers, Li and Yortsos (1994, 1995a,b), Satik et al. (1995) and Satik and Yortsos (1996) used pore-network models to study mass transfer towards a growing gas phase from a surrounding liquid in a porous medium, in the context of solution gas-drive and/or boiling. Experiments in etched-glass micromodels and in Hele-Shaw cells and simulations with pore network models showed that the interface pattern, varying between Invasion Percolation (IP) and Viscous Fingering (VF) (Feder, 1988), drastically affects the mass transfer, hence the rate of growth (or dissolution) of a phase. The disorder of a real porous medium (even if macroscopically homogeneous) was shown to give rise to qualitatively different phenomena than in effective porous media (such as a Hele-Shaw cell, compare for example Li and Yortsos, 1994, 1995a). We expect that similar effects will occur in remediation processes as well.

To better understand and to help design improved remediation methods, we present in this paper a pore scale study of the mass transfer of the remediation of residual phases. From a mass transfer perspective, the problem is interesting from two points of view: That mass transfer occurs in a disordered pore space from a disordered stationary source, and that it involves the interplay between small (pore-size) and large (pore-network size) length scales. The basic problem is described as follows. An immiscible to water NAPL has percolated through the action of gravity or otherwise to the subsurface and displaced part of the water in place. As a result of the subsequent displacement of the NAPL by a displacing fluid, e.g. water, the NAPL phase has been trapped due to capillarity in various pores in the form of trapped and disconnected ganglia (as shown in the schematic of Figure 3.1). To remove this trapped liquid, a solubilizing agent, fully miscible to the original fluid in place, but not to NAPL, to which is partly miscible, is injected. We are interested in evaluating the mass transfer rates from the trapped NAPL to the solubilization agent and its dependence on parameters such as the flow rate, in order to be able to upscale the process and to develop appropriate mass transfer expressions. The particular study in this paper is restricted to mass

transfer from residual NAPLs, the interfaces of which remain stationary during the experiment, thus solubilization by the mobilization of trapped blobs is not considered.

The paper is organized as follows: First, we report on visualization experiments, conducted in etched glass micromodels. The solubilization of various residual NAPL phases, trapped in the micromodel following displacement with a driving fluid, is studied. We monitor the variation of the effluent concentration with time and, after it reaches a steady-state, with the injected flow rate. Subsequently, a pore network simulator is developed to describe mass transfer. The simulator is calibrated by comparison against tracer displacement experiments. Then, the experiments are simulated with the use of the pore network model. It is found that appropriately modified local mass transfer coefficients need to be introduced in the pore-network model in order to match the experimental results. Sensitivity studies are then conducted to analyze the dependence of the response to the microstructure and particularly to the assumed local mass transfer coefficients. Implications on the upscaling of the results are also discussed.

EXPERIMENTS

To obtain insight on mass transfer processes during NAPL remediation, visualization experiments in an etched-glass micromodel were conducted. Such micromodels are prepared by etching a 2-D square network pattern of pores and throats on a glass plate (Figure 3.2), which was subsequently fused to another glass plate to create a 2-D pore network (see Chatzis, 1982, Buckley, 1990, also Li and Yortsos, 1995a). One injection port and one production port at opposite sides of the micromodel were drilled to control the injection and production of fluids. Various patterns, with randomly distributed pore widths were etched, the typical micromodel size being 29×15 pores. The pores have a rectangular cross-section with a channel depth of about 0.0312 cm in the typical case. In all patterns, the lattice coordination number was equal to 4 (square lattices). The pore volume in the various micromodels ranged between 0.5 cm^3 to 2.0 cm^3 (see also below).

The schematic of the experimental setup is shown in Figure 3.3. The experimental procedure was as follows:

- (1) First, the micromodel was saturated with distilled water.
- (2) Subsequently, using a syringe pump (Harvard Apparatus model 850), water was displaced at sufficiently high rates (order of 0.053 ml/min) by a NAPL containing a visualization dye, until all water was completely removed from the micromodel. Often, this required tilting the micromodel for gravity to assist in the displacement process. Various liquids were used to represent NAPL, including TCE, PCE and benzonitrile. However, complete sets of experiments were conducted only for benzonitrile. These are the only reported here.
- (3) The next step involved displacing the NAPL by a solvent, usually water or a water-alcohol mixture, at high rates (of the order of 2.85 ml/min) (see also below). Following a transient stage, of approximately 1 hour, during which much of the NAPL was displaced, the system reached a stage in which the NAPL was trapped in well-defined ganglia. During the time of the subsequent mass transfer experiments in this state, there was a negligible reduction of the NAPL-water interfacial configuration, suggesting a steady-state as far as mass transfer is concerned. All processes and patterns were videotaped. Comparison of the patterns at different times ensured that there was no significant change in the pattern, hence in the flow distribution.

- (4) Samples at the production port were collected and analyzed immediately (less than a minute elapsed) after collection using a Varian 3300 gas chromatograph with a thermal conductivity detector (TCD) for measuring concentrations. The accuracy of the measurements was validated by independent comparison of saturated samples with published solubility data. In this approach, a saturated solution (with solubility obtained from the literature) was analyzed using the GC. The area under the concentration peak was measured and served to scale the subsequently obtained concentrations. After ascertaining that a steady-state was indeed reached, the effluent concentration was recorded. Then, the injection rate was reduced, another steady-state was established and the effluent samples were analyzed. The process was repeated for a range of injection rates covering more than three decades (between 0.0007 ml/min and 2.8 ml/min). The transient times required to reach the steady-state varied between 20 and 30 minutes for the high rates to several hours for the lower rates. All the experiments were carried out at room temperature.

Miscible displacement experiments of a passive tracer, in the absence of a NAPL, were also conducted to test the validity of the pore-network simulator which will be subsequently used to analyse the results. In these experiments, a 50% glycerol solution was displaced by the same mixture containing a coloring dye. During fluid injection, the pressure difference across the two ports was periodically monitored, using water-filled U tubes.

Shown in Figure 3.4 is a typical picture of the configuration of the trapped NAPL at the onset of a mass transfer experiment. Note the disconnected state of the NAPL, the existence of ganglia of various sizes, and the varying local interface configuration of the different ganglia. It should be pointed out that because of the rather high velocity used to isolate and trap the NAPL, the geometric configuration is not that of a percolation cluster, which one would expect at lower trapping velocities, where viscous forces are small. However, this is of no significant consequence for this paper, where the analysis and simulation will be based on the actual, rather than a theoretical, pattern. All mass transfer experiments were carried out in order of decreasing flow rate in order to keep the NAPL interfaces fixed, thus allowing for a meaningful sensitivity analysis of the effect of flow rate on mass transfer. The inverse order, from low to high rates, would have resulted in the mobilization of some trapped ganglia at increasing velocities (compare with Figure 3.1) with a resulting change of the interfacial geometry. Such mobilization was indeed observed at high capillary numbers. This process will be investigated in a separate study.

Some additional remarks are also in order. To keep a relatively fixed interface between NAPL and solvent, which is necessary for the study of the effect of velocity on mass transfer, requires that the interface recedes only very slightly during the experiments. Given that the solubility of most NAPLs in water is generally low, this can be readily accomplished by using water as a solubilizing agent. On the other hand, low solubility presented resolution problems in the GC analysis. In addition, during the collection and analysis of the samples, particularly at low rates, which involve longer transients, the losses of NAPL due to its volatility must be minimal. We sought, therefore, to work with NAPLs whose solubility is low, but not beyond the resolution of our GC, and with small volatility. Benzonitrile with a solubility of 0.2 g/100 cm³, which is comparable to TCE solubility, but with a much higher boiling point (190.7 °F, compared to 86.7 °F for TCE), was one such liquid used. All results shown here pertain to this specific *NAPL*.

A typical effluent curve from the 29 × 15 micromodel is shown in Figure 3.5 corresponding to the solubilization of benzonitrile by water. This curve shows the variation of the effluent concentration, normalized with respect to its solubility at the given temperature, as a function of the injection flow rate. The curve has a characteristic erfc-like shape, approaching asymptotically zero at large rates and 1 at smaller rates, where the actual concentration becomes equal to its solubility. The

approach to the latter solubility value was tested independently by measuring the solubility of the NAPL and also by comparison with published data. The experimental error bars shown in Figure 3.5 are associated with errors in the GC measurement and sample collection, due to the rather low injection rates used. The analysis of the effluent curve is presented in more detail in a following section.

MATHEMATICAL FORMULATION

To simulate the experiments and to provide a working model for the process, we proceeded with a mathematical formulation. The problem considered is mass transfer in the porespace of a porous medium, such as the micromodel of Figure 3.4, containing a trapped liquid phase, which becomes solubilized in the flowing solvent. The lateral boundaries of the micromodel are closed to flow, with the exception of two producing sites at opposites ends. The location of the interfaces was directly inserted in the simulations from observations of the experiments. (An invasion percolation, or other displacement, algorithm could also be used to determine this configuration, although it will not necessarily correspond to the particular experiment, for the reasons described.)

Mass transfer of the solubilized NAPL occurs from the direction of the trapped liquid towards the effluent end, described in the pore-space by the usual convection-diffusion equation

$$\frac{\partial C}{\partial t} + \mathbf{u} \cdot \nabla C = D \nabla^2 C \quad (3.1)$$

where C is concentration, \mathbf{u} is velocity, and D is the molecular diffusivity. At creeping flow conditions and in the absence of gravity, the injected solvent velocity \mathbf{u} obeys in the pore-space Stokes' law

$$\nabla P_l = \mu \nabla^2 \mathbf{u} \quad (3.2)$$

where P_l is liquid pressure and μ is viscosity. The trapped NAPL is taken to be stationary, and so is the interface between NAPL-solvent, for the reasons explained above. A receding interface algorithm could also be used, but the conditions of slow dissolution examined here do not warrant it. At the interface, the local concentration of the NAPL in the solvent is that of thermodynamic equilibrium

$$C = C_s \quad (3.3)$$

These equations are subject to the appropriate flux or concentration conditions at the boundaries, and to the condition that the concentration on the interface of each cluster is spatially constant.

A detailed simulation of the full problem is possible with the use of lattice gas simulation (Rothmann and Zaleski, 1997). Here, we elect to work, instead, with the simpler, although perhaps less accurate, approach of pore network simulation. In the pore network simulations, mass and momentum balances will be discretized, with the latter being approximated using Poiseuille's law. This is a standard approximation in pore-network models.

Pore Network Simulation

Pore network simulators are used to simulate processes in pore-networks or glass micromodels. The key approximation is the porous medium representation in terms of a collection of pores, connected to each other by pore throats in a network-like fashion (Dullien, 1992). Conventional

networks include regular lattices, such as square or cubic, or Voronoi lattices (Blunt and King, 1991). Either lattice can be readily constructed, although regular lattices are computationally more manageable. Pore networks are ideal for replicating experiments in etched-glass micromodels (see Li and Yortsos, 1995a, for a recent application). Whether for miscible or immiscible flow, their basic aspects include the following:

- Pores provide volumetric storage, throats control the conductance to flow, heat and mass. Geometrical characteristics can be statistically distributed.
- Capillary equilibrium at the pore scale is controlled by pore throats during drainage (a non-wetting (nw) fluid displacing a wetting (w) fluid), and by sites during imbibition (which is the inverse of drainage). The capillary pressure across an interface is given by the Laplace-Young equation, $P_{nw} - P_w = 2\gamma\mathcal{H}$, where γ is the interfacial tension, and at equilibrium the mean interface curvature, \mathcal{H} , is controlled by the pore geometry.
- Pore bodies can be occupied by one or both of the two fluid phases. Pores occupied by one phase can become trapped by the other phase, if topologically possible. When a pore is trapped, liquid phase movement is not allowed, although mass diffusion continues.
- Local pore-scale coefficients are calculated from single-pore studies. Thermodynamic equilibrium applies within any given pore, although adjacent pores can be at non-equilibrium.

In the past, pore-network simulators have been developed to model immiscible displacement (e.g. see Lenormand, 1990, Blunt and King, 1991, Haghghi et al., 1994). These simulators provide a pore-by-pore account of the displacement of interfaces during drainage or imbibition. In multicomponent displacements, mass transfer of various species to and from interfaces must also be computed. In recent papers (Li and Yortsos, 1995a,b, Satik et al., 1995, Satik and Yortsos, 1995) we have described how such a simulator must be constructed for a problem involving phase change.

The governing equations are discretized over the pores (nodes) of the network. For an incompressible fluid, the overall mass balance at node i is

$$\sum_j Q_{ij} = 0 \quad (3.4)$$

where Q_{ij} refers to volume flow rate between adjacent sites i and j . The sum is over all neighboring sites j , and we use Poiseuille's law to relate flow rates to pressure drops

$$Q_{ij} = G_{ij}\Delta P_{ij} \quad (3.5)$$

where the overall fluid conductance, G_{ij} , is a distributed variable. For the square cross-section channels of the glass micromodel, we have in particular,

$$G_{ij} = \frac{w_{ij}h^3}{lk_{ij}\mu} \quad (3.6)$$

where w_{ij} is the width of the pore throat joining sites i and j , h is the pore depth (taken to be spatially uniform due to etching), l is the bond length (uniform for this problem), μ the fluid viscosity, and k_{ij} is a geometric correction factor given by the following correlation of data from Purday (1949)

$$k_{ij} = -0.03312r_{ij}^5 + 0.8011r_{ij}^4 - 7.1576r_{ij}^3 + 30.3497r_{ij}^2 - 3.0355r_{ij} + 67.6754 \quad (3.7)$$

where $r = w_{ij}/h$.

The mass balance for solute in site i not neighboring the NAPL-solvent interface reads

$$V_s \frac{\Delta C_i}{\Delta t} = \sum_j \left[D A_{ij} \frac{\Delta C_{ij}}{l} \right] + \sum_j \left[\frac{G_{ij} \Delta P_{ij}}{l} C_{ij} \right] \quad (3.8)$$

where V_s is the site volume, D is diffusivity and $A_{ij} = w_{ij}h$ is the cross-section of the pore throat. Here, concentrations were assigned to sites only, and the mass transfer between adjacent sites was assumed to occur by both diffusion and convection. If a site neighbors a NAPL, however, a modification to account for local mass transfer is necessary, to be described below. Published values were used to estimate fluid properties, such as viscosity and diffusivity. Contaminant diffusivity can be approximated by infinite-dilution coefficients, in the case of low concentrations, using methods such as Tyn and Calus (1975), or by more complex models (Taylor and Krishna, 1993) in the case of concentrated solutions. Solubility parameters for various systems were estimated from currently available data (Mercer et al., 1990, Edwards et al., 1994, Glinski et al., 1994). The set of concentration and pressure equations was simultaneously solved by a numerical method using *SOR*.

Local mass transfer coefficients

As previously noted, the NAPL-water interface could reside in throats or in bodies (sites). Discretization (3.8) for mass transfer applies only to cases in which interfaces are not within the site, or within pore throats adjacent to the site over which the mass balance is written. For sites which are nearest neighbors of the NAPL-solvent interface, however, the mass transfer expression needs to be more carefully examined. Indeed, near a stagnant interface, the local mass transfer cannot be captured simply by diffusion and convection, where the flow field obeys Poiseuille's (or effectively, Darcy's) law, even if a more refined grid was to be used (for example, if we were to also assign concentrations to throats, which has also been considered here). Consider, for example, typical configurations of the NAPL-solvent interface, shown in Figure 3.6, obtained from photographs of the micromodel. To more properly account for the mass transfer rate from the interface under these conditions requires accounting for Stokes flow dynamics, near the interface, which, however, are not inherent to our pore network.

To proceed, we will keep the hydrodynamic field as dictated by Darcy's law (3.4) and (3.5), but modify the terms for mass transfer from the interface to an adjoining site by introducing a local mass transfer coefficient k and expressing the corresponding flux to site i as

$$N_{si} = k A_{si} (C_s - C_i) \quad (3.9)$$

Thus, the local hydrodynamic effect to mass transfer is kept through the local (pore-scale) mass transfer coefficient, while the global effect is to be computed by solving the flow field, subject to Darcy's law in the entire pore network.

Various mass transfer correlations (analytical and numerical) have been developed over simplified geometries, e.g. for flow over a sphere, a flat plate, etc. For example, for flow over a flat plate and typical conditions, we have (Cussler, 1984)

$$Sh = 0.664 Re^{1/2} Sc^{1/3} \quad (3.10)$$

where $Sh = \frac{kL}{D}$ is the Sherwood number, $Re = \frac{qL\rho}{\mu}$ is the Reynolds number and $Sc = \frac{\mu}{\rho D}$ is the Schmidt number. For the more complex geometries of the type shown in Figure 3.6, the literature is

more limited. A close analogue of this geometry is mass transfer over a closed cavity. This problem has been addressed in the context of pit corrosion in electrochemistry (for example, see Alkire and Deligianni, 1988, Alkire et al., 1990). Experimental and numerical work has led to correlations of the mass transfer coefficient of the form

$$Sh = 0.3 \left(\frac{W}{H} \right)^{0.83} Pe^{0.33} \quad (3.11)$$

where we introduced the Peclet number, $Pe = \frac{qW}{D}$, and the cavity aspect ratio W/H . Occhialini and Higdon (1992) proceeded with another calculation of the same quantity using a spectral technique. Their numerical results were fitted using different correlations depending on the cavity aspect ratio. For example, we have found that

$$Sh = 0.1647Pe^{0.33} \quad \text{for} \quad \frac{W}{H} = 1 \quad ; \quad Sh = 0.1778Pe^{0.4} \quad \text{for} \quad \frac{W}{H} = 2 \quad (3.12)$$

We have proceeded with adopting (3.12) to represent the local mass transfer rates to sites adjacent to the interface for various geometries of this type. Wherever appropriate as dictated from a visual observation of the pattern, expression (3.10) is also used. Of course, in real porous media, correlations of similar form have to be developed to account for the more complex local geometries expected.

SIMULATION OF THE EXPERIMENTAL RESULTS

Using the above pore-network simulator, we proceeded to simulate the mass transfer experiments performed at various rates. Because of the 2-D nature of the micromodel, the throats were approximated as equivalent rectangular channels. Even though the etching depth of the glass micromodel is unknown, it can be estimated by measuring the pore volume or by the system permeability (see below). The geometry of the network and the width of the pores in the simulation are the same with the computer pattern used to construct the glass micromodel, although the true sizes of the micromodel pores are likely to be somewhat different due to various defects during the fabrication process. Before attempting to simulate and match the mass transfer experiments, we considered a partial validation of the model using a simple miscible displacement experiment.

(a) Validation

The validity of the pore-network simulator was tested by comparing simulated and measured pressure drops and a simple miscible displacement experiment. First, we matched the measured pressure drop at various rates and at conditions of single-phase flow in the absence of NAPL. This comparison is a test of the ability of the simulator to match the overall hydraulic conductivity. In the simulations, we used as input the measured pore widths and a uniform depth of 0.0312 cm. Measured and predicted results are shown in Figure 3.7a. As expected from Darcy's law, the curves are linear at these flow rates. Agreement between theory and experiment is good, except for low flow rates, where the experimental error is relatively large. A second flow rate experiment was also conducted, in which we compared theoretical and experimental pressure drops for single-phase flow around the trapped NAPL (for example, for the geometry corresponding to Figure 3.4). This is a rather more stringent test, due to the more tortuous pore-space involved. The results, shown in Figure 3.7b, also indicate a good agreement. We conclude from these two independent

mesasurements that the flow conductances are well represented (at least on the average) with the hydraulic expression (3.6) and (3.7).

Next, we compared experimental and theoretical predictions for the evolution of the front in a miscible displacement process at unit mobility ratio, in the absence of NAPL, which is a test of the ability of the pore-network simulator to simulate mass transfer. A 50% glycerol solution was displaced by the same mixture containing a coloring dye. This mixture has a relatively higher viscosity than water and was also used for pressure drop calculations. The following values were assigned to the two physical parameters, $\mu = 1$ cp and $D = 1.0 \times 10^{-5}$ cm²/s. Figures 3.8 and 3.9 show a comparison of the position of the miscible front in the glass micromodel and as predicted by the pore-network simulator, respectively, at two different times corresponding to 0.091 and 0.21 injected pore volumes, respectively. The agreement in the front positions between the two models is good and shows that the simulator represents well the flow dynamics in the micromodel.

(b) Simulation of mass transfer experiments

The simulator was next used to simulate the mass transfer experiments. In each experiment, the actual position of the interface of the trapped NAPL was used as input to the numerical model. Local mass transfer coefficients were used, as appropriate as discussed above. Figure 3.10 shows the comparison between simulated and measured effluent concentration profiles in an experiment with benzonitrile, as a function of the Peclet number, Pe_L . The latter was based on the overall system size and is defined as $Pe_L = \frac{uL}{D}$, where u is the flow velocity at the entrance port ($u = Q/A$, where A is the cross-sectional area of the entrance pore). We must note that in the experiments (and the simulations) we only varied the overall injection rate, which also affects the local mass transfer coefficient through expression (3.11)). No adjustable parameters were used in the simulation. The agreement between experimental and numerical results is quite good for the range of injection rates tried, which spans more than two decades. Figure 3.11 shows another comparison between experiments and simulations using a different pattern. Here, we used the same parameters as in the previous simulation, except that the position of the NAPL-liquid interface is different. The agreement is equally good. Certainly, a more stringent test of the simulator would involve comparison of local concentration profiles. However, such data were not collected. Overall, the agreement in matching the overall behavior is encouraging of the ability of the simulator to match important aspects of the mass transfer process under the conditions of the experiments.

A key finding from the comparison between experiments and simulation was the importance of properly accounting for the local mass transfer rates. This is illustrated with the simulation of Figure 3.12, where the local mass transfer from the interface to the site was taken to be by diffusion only (using film theory with constant film thickness (Cussler, 1984)), namely here we used locally $Sh = 1$. Experiments and simulations are in reasonable agreement in the region of low Peclet numbers, where diffusion is still predominant. However, they fail to match each other at higher flow velocities, where local convection is progressively more important, the deviation increasing with the Peclet number. In fact, this inadequacy motivated the use of the local mass transfer coefficients. Appropriate accounting of the local geometry in the mass transfer coefficients led to the much more satisfactory agreement shown in Figures 3.10 and 3.11.

(c) Sensitivity study

The pore-network simulator was subsequently used to explore two issues: The derivation of effective mass transfer coefficients for use in a macroscopic model, and the effect of the local mass

transfer on the effluent concentration. In this paper we will focus on the second issue for the particular experimental setup described here, the first belonging to the more general problem of scale-up, which will be considered in a subsequent chapter.

To explore the sensitivity of the effluent concentration on the local mass transfer coefficient, we assigned the following expression

$$Sh = a + bPe^c \quad (3.13)$$

uniformly for all pores. Parameters a , b and c were independently varied, while the Peclet number in (3.13) is based on the microscale (which can be one to two orders of magnitude smaller than that based on the macroscale). All simulations were performed for the micromodel and interface geometries of Figure 3.11. The corresponding effects are shown in Figures 3.13-3.15.

Figure 3.13 shows the sensitivity to the parameter a , with values in the range 0.001 to 2. Because the term containing a is independent of Pe , its effect reflects the importance of diffusion. We note that the effect of a is minimal, despite the significant range in its variation (the various curves essentially coincide in the figure). Some effect exists at relatively low velocities, where diffusion predominates, as expected from an asymptotic study of the low rates regime, which will be published elsewhere. At relatively large flow rates, however, the effect is negligible, as convection dominates the local mass transfer expression (3.13) and all curves approach a limiting curve, which in a log-log plot eventually becomes a straight line. Figure 3.14 shows the sensitivity to the parameter b , which is varied in the range 0.0001 to 2. In contrast to the previous, the effect is significant, and results in a parallel shift of the effluent curve to the right, as b increases. This effect essentially reflects the rescaling of the Peclet number by the factor $b^{1/c}$, and corresponds to a shift of the axis in the log Pe coordinate. Finally, Figure 3.15 shows the effect of c , which was varied in the physically realistic range (0,1). We note that in the log-log plot of the Figure, the effluent concentration approaches a straight line asymptote, with a negative slope, $-s$, which decreases as c increases. In fact, the variation of s is almost linear and obeys the relation

$$s = 1 - c \quad (3.14)$$

as shown in Figure 3.16. These results can be analytically explained as follows:

At steady state, the effluent concentration C_e is obtained from a mass balance

$$qC_e = - \int_A D \frac{\partial C}{\partial n} dA \quad (3.15)$$

where the integral is evaluated over the NAPL interface A , n is the outer normal and q is the injection rate. Using the local mass transfer coefficient k , the local mass transfer rate under the integral is given by (3.9). Now, at sufficiently large Peclet numbers, the site concentration is small, namely $C_i \ll C_s$. Equation (3.15), then, reads

$$qC_{D,e} \approx kl^2 A_D \quad (3.16)$$

where the prefactor is a dimensionless expression of the interface area, and we defined $C_{D,e} = C_e/C_s$. At large Peclet numbers, we also have

$$k \sim \frac{DbPe^c}{l} \quad (3.17)$$

which inserted in (3.16) leads to

$$C_{D,e} \sim Pe_L^{c-1} \quad (3.18)$$

as also found numerically.

The asymptotic dependence found can be used to infer an estimate of the value of the effective parameter c in the experiments. By fitting the late part of the effluent concentration vs. Peclet number curve in a log-log plot to a straight line we find the values of 0.45 for the experiments in Figure 3.10 and Figure 3.11. These numbers reflect the distribution of c in the local mass transfer coefficients used in the experiments (where the exponent c in the local coefficient varies between 0 (pure diffusion) and 0.5 (flow over a flat interface)).

CONCLUSIONS

In this chapter, we conducted visualization experiments and numerical simulations in pore networks to understand basic aspects of mass transfer during the solubilization of residual NAPLs. The experiments were carried out in 2-D etched-glass micromodels with randomly distributed pore sizes. We monitored the concentration of the effluent at steady-state as a function of the Peclet number to study the dependence of the overall mass transfer rate on injection velocity. A pore network numerical model, based on the convection-diffusion equation using appropriate modifications for the local mass transfer coefficients, was developed to simulate mass transfer during the solubilization of a residual phase. The pore network simulator was found to match well the experimental results, provided that the local mass transfer was properly accounted for. Expressions for mass transfer over cavities were used to represent the latter. Sensitivity studies were subsequently conducted to investigate the dependence of the overall solubilization rate on parameters, such as the Peclet number. A scaling law was developed for the resulting overall mass transfer rate assuming a uniform local mass transfer coefficient. The results obtained here can be used in a macroscopic model to predict mass transfer rates, as shown in the next chapter. Issues of scale-up and the effect of macroscopic heterogeneities, are further discussed there.

REFERENCES

1. Abriola, L.M. and Pinder, G.F., A multiphase approach to the modeling of porous media contamination by organic compounds: 1. Equation Development, *Water Resour. Res.*, Vol. 21, 11-18 (1985a).
2. Abriola, L.M. and Pinder, G.F., A multiphase approach to the modeling of porous media contamination by organic compounds: 2. Numerical simulation, *Water Resour. Res.*, Vol. 21, 19-26 (1985b).
3. Alkire, R., and Deligianni, H., The role of mass transport in electrochemical pattern etching, *J. Electrochem. Soc.: Electrochemical Science and Technology*, Vol. 135, No. 5, 1093-1100 (1988).
4. Alkire, R., Deligianni, H. and J.-B. Ju, Effect of fluid flow on convective transport in small cavities, *J. Electrochem. Soc.*, vol. 137, No.3, 818-824 (1990).
5. Augustijn, D.C.M., Jessup, R.E., Rao, P.S.C. and Wood, A.L., Remediation of contaminated soils by solvent flushing, *J. Envir. Engin.*, Vol. 120, 42-57 (1994).
6. Blunt, M. and King, P.R., Relative permeabilities from two- and three-dimensional pore-scale network modeling, *Transport in Porous Media*, Vol. 6, 407 (1991).
7. Brandes, D. and Farley, K.J., Importance of phase-behavior on the removal of residual DNAPLs from porous media by alcohol flooding, *Water Envir. Res.*, Vol. 65, 869-878 (1993).

8. Brown, C.L., Pope, G.A., Abriola, L.M. and Sepehrnoori, K., Simulation of surfactant-enhanced aquifer remediation, *Water Resour. Res.*, Vol. 30, 2959-2977, (1994).
9. Buckley, J.S., in "Interface Phenomena in Petroleum Recovery", Morrow, N.R. (ed), Marcel Dekker, Inc., New York (1990).
10. Celia, M. A., Rajaram, H. and Ferrand, L.A., A multi-scale computational model for multi-phase flow in porous media, *Advances in Water Resources*, Vol. 16, 81-92 (1993).
11. Chatzis, I., PRRC Report No. 82-12, New Mexico Petroleum Recovery Research Center, Socorro, NM (1982).
12. Cussler, E.L., "Diffusion: Mass transfer in fluid systems", Cambridge University Press (1984).
13. Dullien, F.A.L., "Fluid transport and pore structure", Academic Press, New York (1992).
14. Edwards, D.A., Liu, Z. and Luthy, R.G., Experimental data and modeling for surfactant micelles, HOCs, and soil, *J. Envir. Engin.*, Vol. 120, 23-41 (1994).
15. Feder, J., "Fractals", Plenum, New York (1988).
16. Friedlander, S.K., "Mass and heat transfer to single sphere and cylinders at low Reynolds numbers, *AIChEJ*, vol. 3, No. 1, 43-48 (1957).
17. Geller, J. T. and Hunt, J.R., Mass transfer from nonaqueous phase organic liquids in water-saturated porous media, *Water Resour. Res.*, Vol. 29, 833-845 (1993).
18. Glinski, J., Chavepeyer, G., Platten, J-K., An empirical relation between mutual solubilities and interface tension for two partially miscible liquids, *Physica B*, Vol. 193, 154-160 (1994).
19. Guarnaccia, J.F., Imhoff, P.T., Missildine, B.C., Oostrom, M., Celia, M.A., Dane, J.G., Jaffe, P.R. and Pinder, G.F., Multiphase chemical transport in porous media, Environmental Protect Agency report, contract EPA/600/5-92/002, Kerr Environ. Res. Lab., Ada, Okla. (1992).
20. Haghighi, M., Xu, B. and Yortsos, Y.C., Visualization and simulation of immiscible displacement in fractured systems using micromodels: I. Drainage, *J. Colloid Interface Sci.*, Vol. 166, 168-179 (1994).
21. Heiba, A. A., Sahimi, M., Scriven, L.E. and Davis, H.T., Percolation theory of two-phase relative permeabilities, Paper SPE 11015, presented at the 57th SPE Annual Meeting, New Orleans, LA, Sept., 26-29 (1982).
22. Ho, C.K., Liu, S. and Udell, K.S., Propagation of evaporation and condensation fronts during multicomponent soil vapor extraction, *J. Contam. Hydr.*, Vol. 16, 381-401 (1994).
23. Imhoff, P.T., Jaffe, P.R. and Pinder, G.F., An experimental study of complete dissolution of a nonaqueous phase liquid in saturated porous media, *Water Resour. Res.*, Vol. 30, 307-320 (1993).
24. Itamura, M.T. and Udell, K.S., Experimental clean-up of a dense non-aqueous phase liquid in the unsaturated zone of a porous medium using steam injection, Vol. 265, *Multiphase Transport in Porous Media*, ASME, 57-62 (1993).

25. Ji, W., Dahmani, A., Ahlfeld, D.P., Lin, J.D. and Hill III, E., Laboratory study of air sparging: Air flow visualization, GWMR, 115-126 (1993).
26. Lenormand, R., Liquids in porous media, J. Phys.: Condens. Matter, Vol. 2, SA79-SA88 (1990).
27. Levich, V.G., Physicochemical Hydrodynamics, Prentice-Hall, Englewood Cliffs, NJ (1962).
28. Li, X. and Yortsos, Y.C., Bubble growth and stability in an effective porous medium, Phys. Fluids A, Vol. 6, 1663-1676 (1994).
29. Li, X. and Yortsos, Y.C., Visualization and simulation of bubble growth in pore networks, AIChE J., Vol. 41, 214-223 (1995a).
30. Li, X. and Yortsos, Y.C., Bubble growth in porous media, Chem. Eng. Sci., Vol. 50, 1247-1271 (1995b).
31. Mackay, D.M. and Cherry, J.A., Groundwater contamination: Pump-and-treat remediation, Environ. Sci. Technol., Vol. 23, 630-636 (1989).
32. Mayer, A.S. and Miller, C.T., An experimental investigation of pore-scale distributions of nonaqueous phase liquids at residual saturation, Transport in Porous Media, Vol. 10, 57-80 (1993).
33. Mercer, J.W. and Cohen, R.M., A review of immiscible fluids in the subsurface: Properties, models, characterization and remediation, J. Contam. Hydr., Vol. 6, 107-163 (1990).
34. Miller, C. T., Poirier-McNeill, M.M. and Mayer, A.S., Dissolution of trapped nonaqueous phase liquids: Mass transfer characteristics, Water Resour. Res., Vol. 26, 2783-2796 (1990).
35. Occhialini, J.M., and Higdon, J.J.L., Convective mass transport from rectangular cavities in viscous flow, J. Electrochem. Soc., vol. 139, No. 10, 2845-2855 (1992).
36. Pankow, J.F., Johnson, R.L. and Cherry, J.A., Air sparging in gate wells in cutoff walls and trenches for control of plumes of volatile organic compounds (VOCs), Ground Water, Vol. 31, 654-663 (1993).
37. Parker, J.C., Katyal, A.K., Kaluarachchi, J.J., Lenhard, R.J., Johnson, T.J., Jayaraman, K., Unlu, K. and Zhu, J.L., Modeling multiphase organic chemical transport in soils and ground water, Rep. EPA/600/2-91/042, U.S. Environ. Protect. Agency, Washington, D. C. (1991).
38. Pennell, K.D., Abriola, L.M. and Weber, W.J., Jr., Surfactant-enhanced solubilization of residual dodecane in soil columns. 1. Experimental investigation, Environ. Sci. Technol., Vol. 27, 2332-2340 (1993).
39. Pfeffer, R., and Happel, J., "An analytical study of mass and heat transfer in multiparticle systems at low Reynolds numbers, AIChEJ, vol. 10, No. 5, 605-611 (1964).
40. Pinal, R., Rao, P.S.C., Lee, L.S., Cline, P.V., and Yalkowski, S.H., Cosolvency of partially miscible organic solvents on the solubility of hydrophobic organic chemicals, Environ. Sci. Technol., Vol. 24, 639-647 (1990).

41. Powers, S.E., Abriola, L.M. and Weber, W.J., Jr., An experimental investigation of nonaqueous phase liquid dissolution in saturated subsurface systems: Transient mass transfer rates, *Water Resour. Res.*, Vol. 30, 321-332, Feb. (1994).
42. Sahimi, M. and Yortsos, Y.C., Application of fractal geometry to porous media: A review, paper SPE 20476 presented at the 65th SPE Annual Fall Meeting, Dallas, TX (Oct. 6-9, 1990).
43. Satik, C. and Yortsos, Y.C., A pore-network study of bubble growth in porous media driven by heat transfer, *J. Heat Transfer*, Vol. 118, 455-462 (1996).
44. Satik, C., Li, X. and Yortsos, Y.C., Scaling of bubble growth in porous media, *Phys. Rev. E*, Vol. 51, No. 4, 3286-3295 (1995).
45. Soll, W.E., Celia, M.A. and Wilson J.L., Micromodel studies of three-fluid porous media systems: Pore-scale processes relating to capillary pressure-saturation relationships, *Water Resour. Res.*, Vol. 29, 2963-2974 (1993).
46. Soll, W.E. and Celia, M.A., A modified percolation approach to simulating three-fluid capillary pressure-saturation relationships, *Advances in Water Resources*, Vol. 16, 107-126 (1993).
47. Stalkup, F.I., Jr., "Miscible Displacement", SPE Monograph, Vol. 8, SPE, New York (1983).
48. Taylor, R. and Krishna, R., "Multicomponent Mass Transfer", John Wiley and Sons (1993).
49. Tyn, M.T. and Calus, W. F., Diffusion Coefficients in dilute binary-liquid systems, *J. Chem. Eng. Data*, Vol. 20, 106-109 (1975).
50. Wakao, N., and Kaguei, S., Heat and mass transfer in packed beds, Gordon and Breach Science, New York (1982).
51. West, C.C. and Harwell, J.H., Surfactants and subsurface remediation, *Environ. Sci. Technol.*, Vol. 26, 2324-2330 (1992).
52. Wood, A.L., Bouchard, D.C., Brusseau, M.L. and Rao, P.S.C., Cosolvent effect on sorption and mobility of organic contaminants in soils, *Chemosphere*, Vol. 21, 575-587 (1990).

Table 1: A compilation of mass transfer correlations used in NAPL remediation.

Reference	Equation .	Valid Conditions
Friedlander, 1957 ^a	$Sh = 0.89Re^{0.33}Sc^{0.33}$	$Pe > 1000$
Levich, 1962 ^a	$Sh = \frac{1}{\sqrt{6\pi}}Re^{0.5}Sc^{0.5}$	$Re < 1$
Pfeffer and Happel, 1964 ^b	$Sh = bRe^{0.33}Sc^{0.33}$ $b=b(n)$	all Pe
Wakao and Kaguei, 1982 ^c	$Sh = 2 + 1.1Re^{0.6}Sc^{0.33}$	$3 < Re < 3000$
Miller et al., 1990 ^d	$Sh = 425Re^{0.75}\theta_n^{0.60}$	$0.016 < \theta_n < 0.07$ $0.0015 < Re < 0.1$
Parker et al., 1991 ^c	$Sh = 1240Re^{0.75}\theta_n^{0.60}$	$0.02 < \theta_n < 0.03$ $0.1 < Re < 0.2$
Powers et al., 1992 ^d	$Sh = 57.7[(\phi - \theta_n)Re]^{0.61}d_{50}^{0.64}U_i^{0.41}$	$\theta_n = \text{constant}$ $0.012 < (\phi - \theta_n)Re < 0.2$ $0 < Re < 0.14$
Guarnaccia et al., 1992 ^d	$Sh' = 107[\frac{Re}{(\epsilon - \theta_n)}]^{0.98}\theta_n^{0.54}$	$0.002 < Re/(\epsilon - \theta_n) < 0.017$ $\theta_n < 0.05$
Imhoff et al., 1993 ^d	$Sh = 340\theta_n^{0.87}Re^{0.71}(\frac{x}{d_p})^{-0.31}$	$0 \leq \theta_n \leq 0.056$
Geller et al., 1993 ^d	$Sh = 70.5Re^{\frac{1}{3}}\theta_n^{\frac{4}{3}}S_{ni}^{\frac{5}{9}}\phi^{-\frac{2}{3}}(\frac{\tilde{d}_p}{d_{ni}})^{\frac{5}{3}}$	$0 < \theta_n < 0.056$
Powers et al., 1994 ^d	$Sh' = \alpha Re'^{\beta_1}\delta^{\beta_2}U_i^{\beta_3}(\frac{\theta_n}{\theta_{no}})^{\beta_4}$ $\alpha = 4.13 \pm 1.01$ $\beta_1 = 0.598 \pm 0.073$ $\beta_2 = 0.673 \pm 0.156$ $\beta_3 = 0.369 \pm 0.119$	$0.039 < \theta_n < 0.060$ $0.013 < Re < 0.058$
	$\beta_4 = 0.667$	sphere
	$\beta_4 = 0.50$	long cylinder with changing dimension of diameter
	$\beta_4 = 0.8 - 1.0$	long cylinder with changing dimension of length
	$\beta_4 = 0.87$	Disk shaped cylinder with changing dimension of diameter

a Boundary layer flow around single spheres.

b Boundary layer flow in packed beds.

c Combination of experimental data.

d Oil dissolution in porous media.

Table 3.1. A compilation of mass transfer correlations used in NAPL remediation.

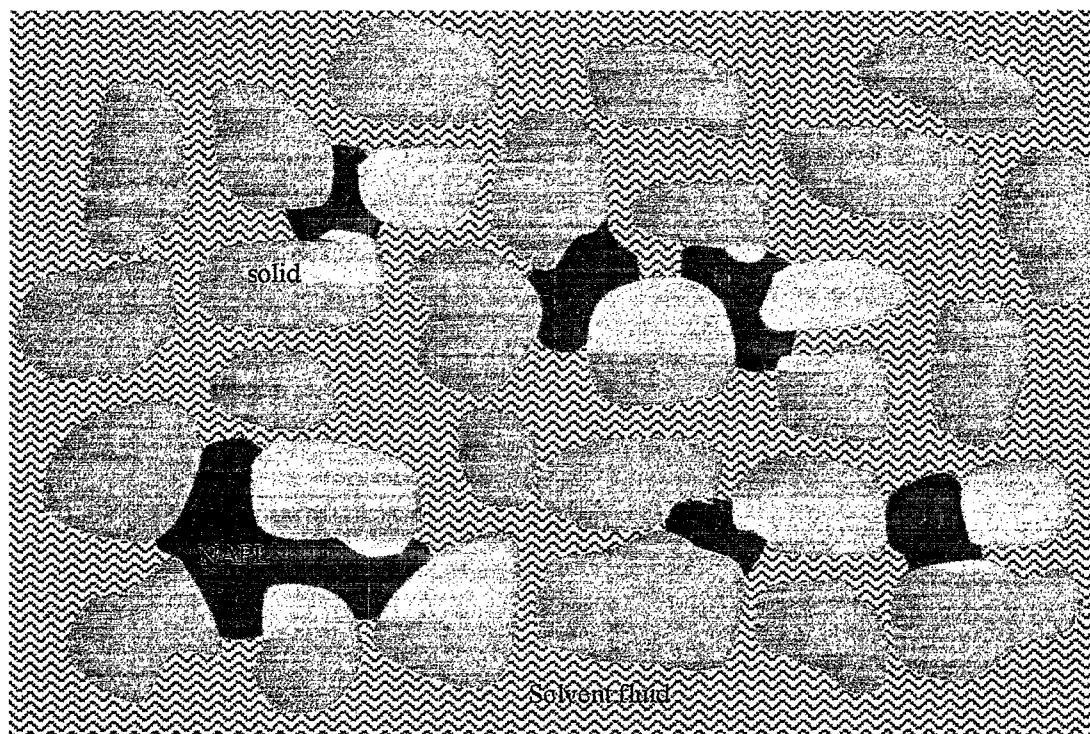


Figure 3.1. Schematic of the configuration of trapped NAPL in a porous medium.

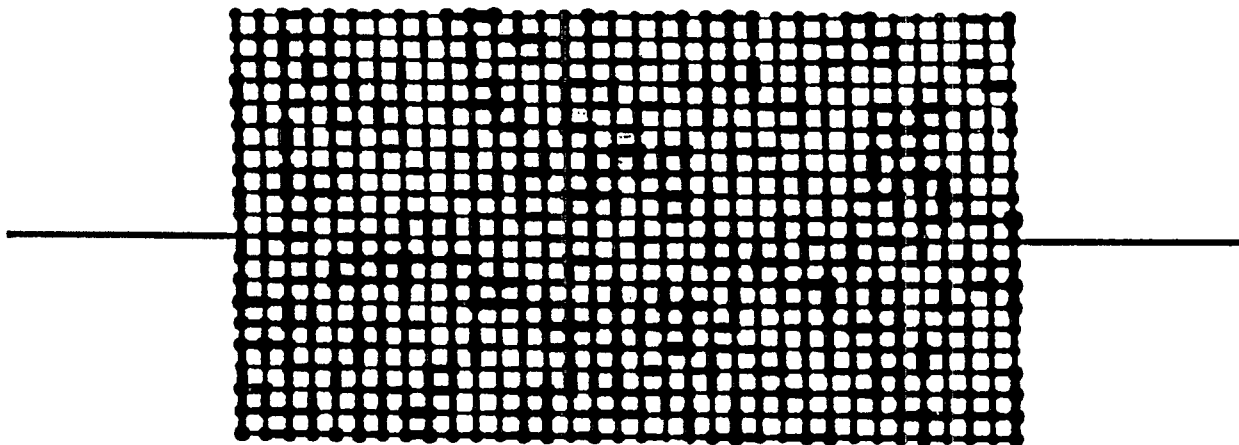


Figure 3.2. Typical pattern used for constructing a 2-D pore network.

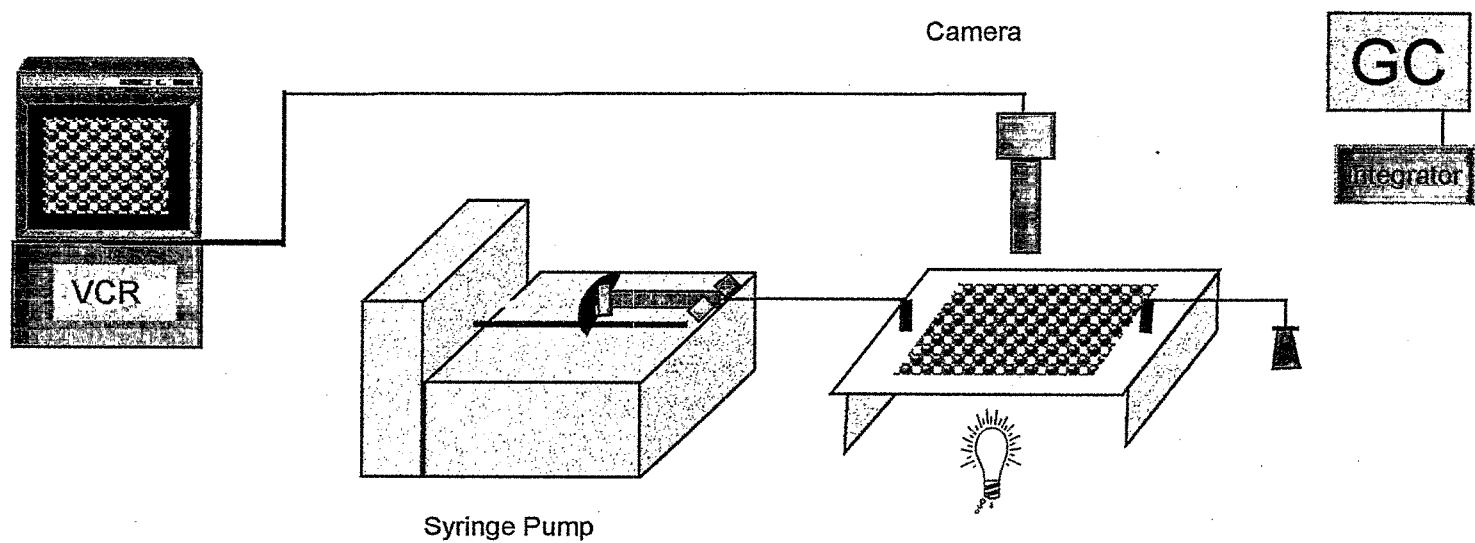


Figure 3.3. Schematic of the experimental apparatus.

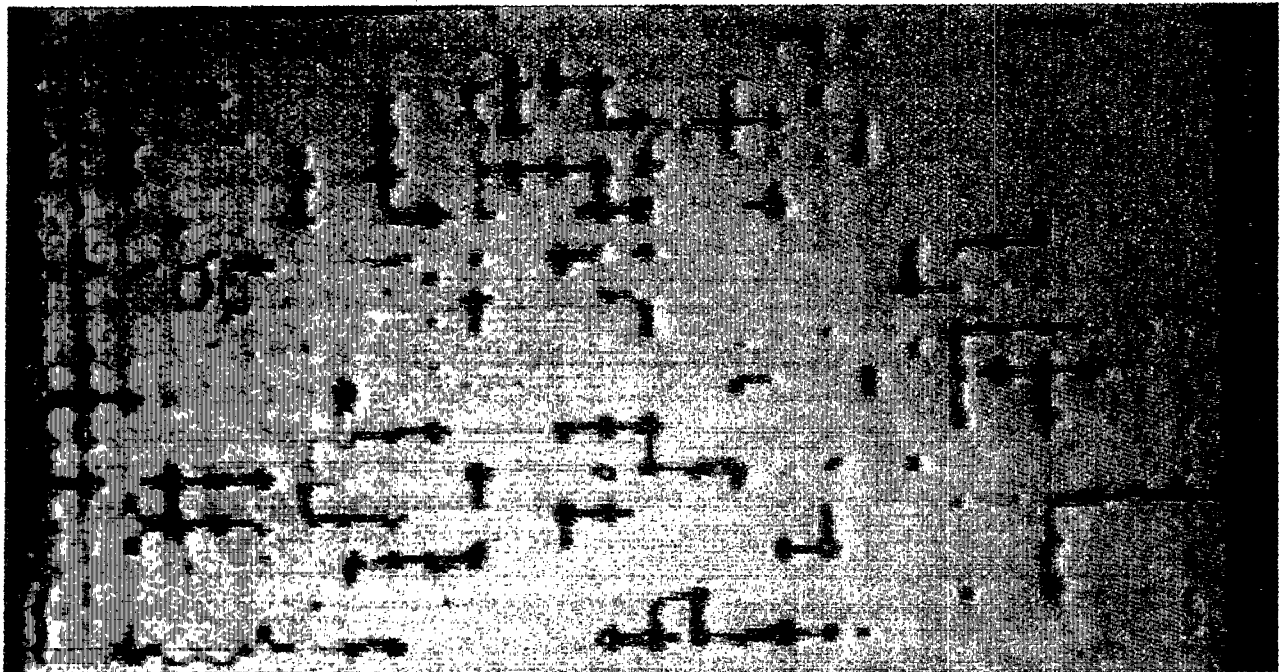


Figure 3.4. Photograph showing the steady-state NAPL distribution in the glass micromodel for typical experimental conditions.

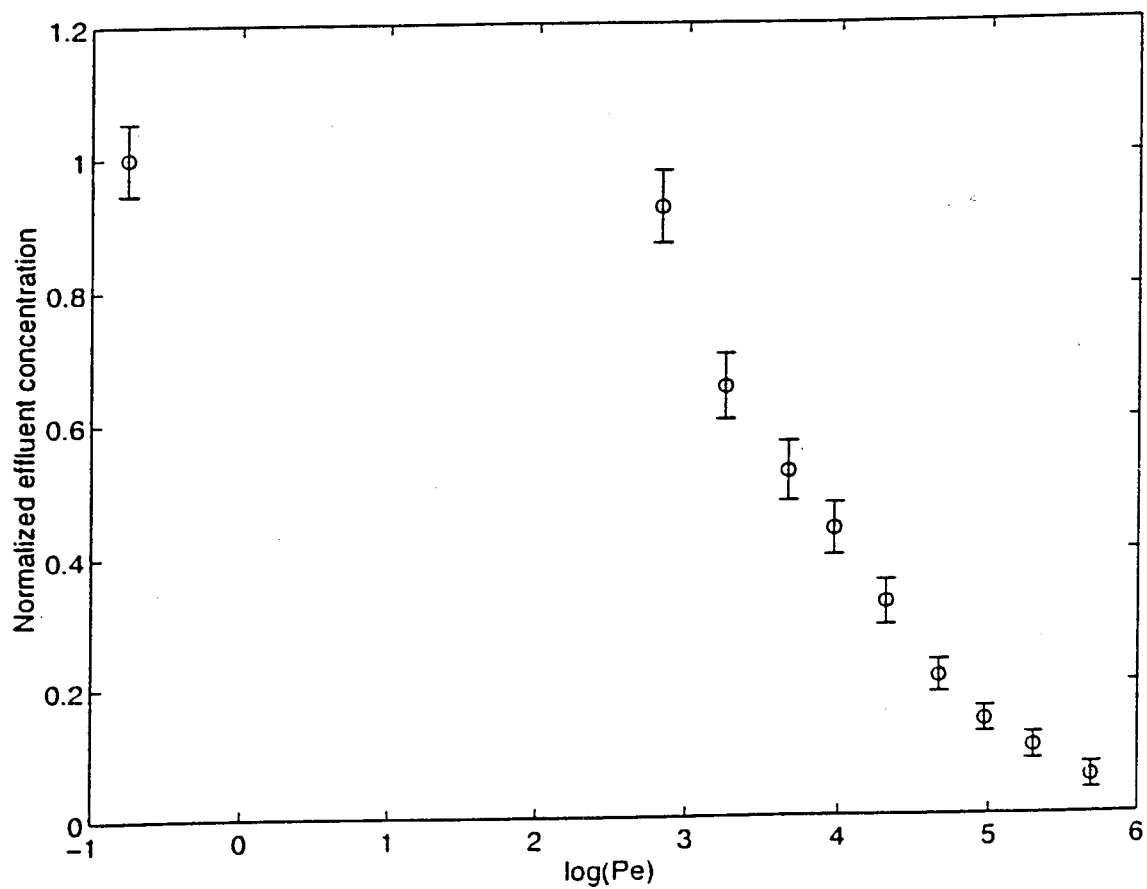


Figure 3.5. A typical effluent curve for the 29×15 micromodel corresponding to the solubilization of benzonitrile by water.

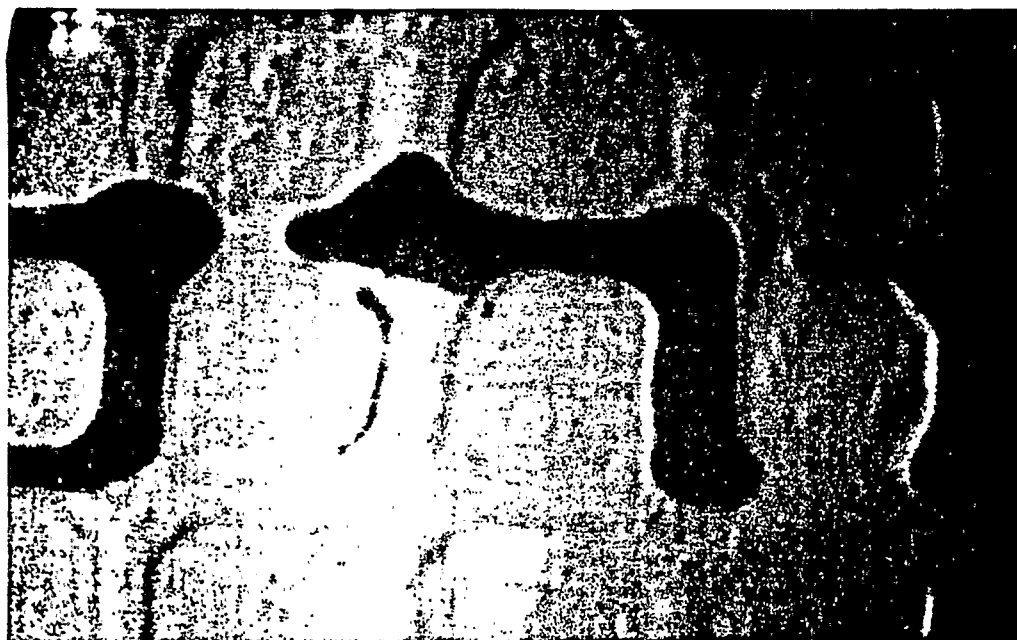


Figure 3.6. Typical NAPL interface configurations in the porespace of the micromodel. Note the cavity-like characteristics.

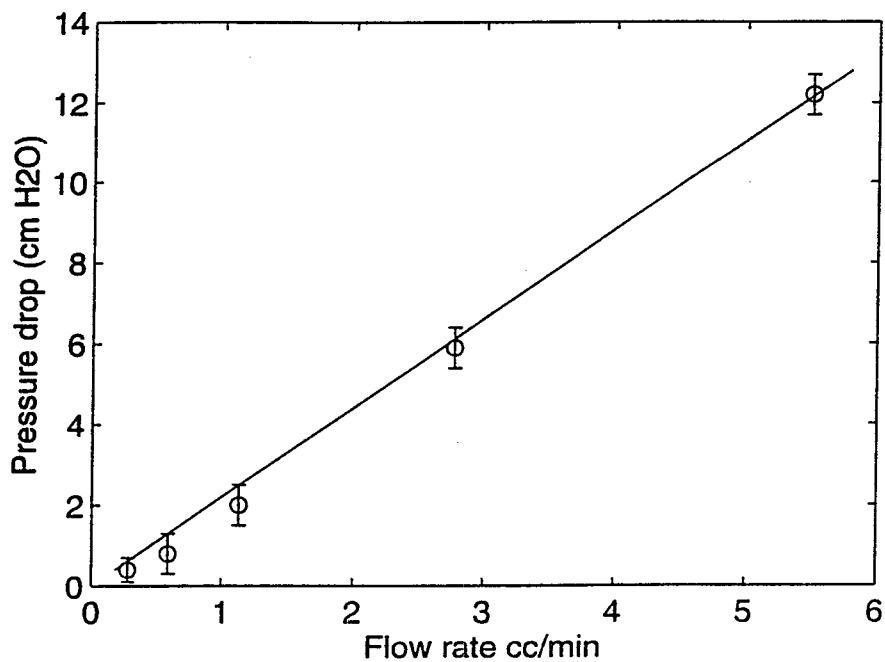
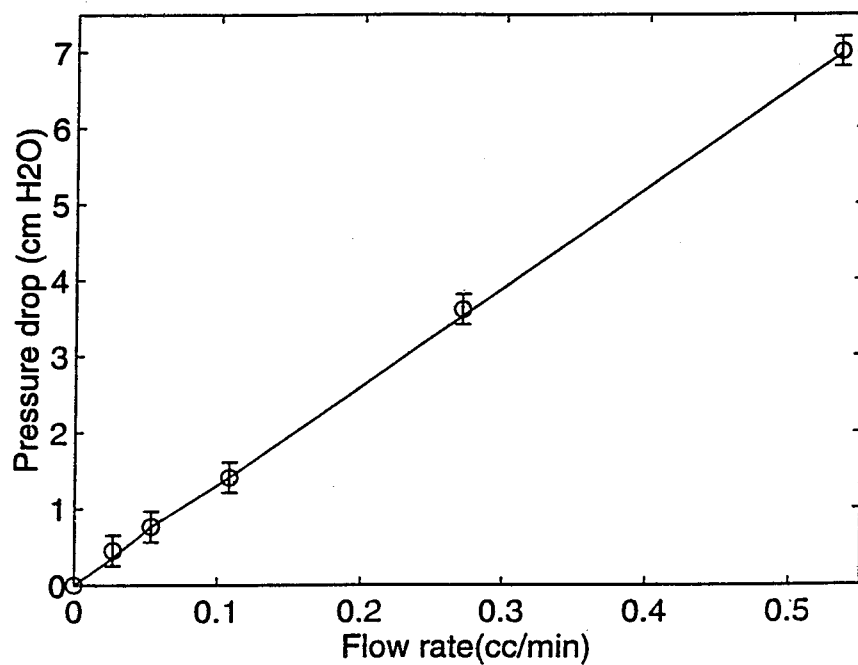


Figure 3.7. Overall pressure drop vs. injection rate in single-phase flow in the micromodel for two different cases: (a) In the absence of trapped NAPL, and (b) in the presence of trapped NAPL (for example as shown in Figure 4). The solid line is the theoretical prediction, experimental data are bracketed by error bars.

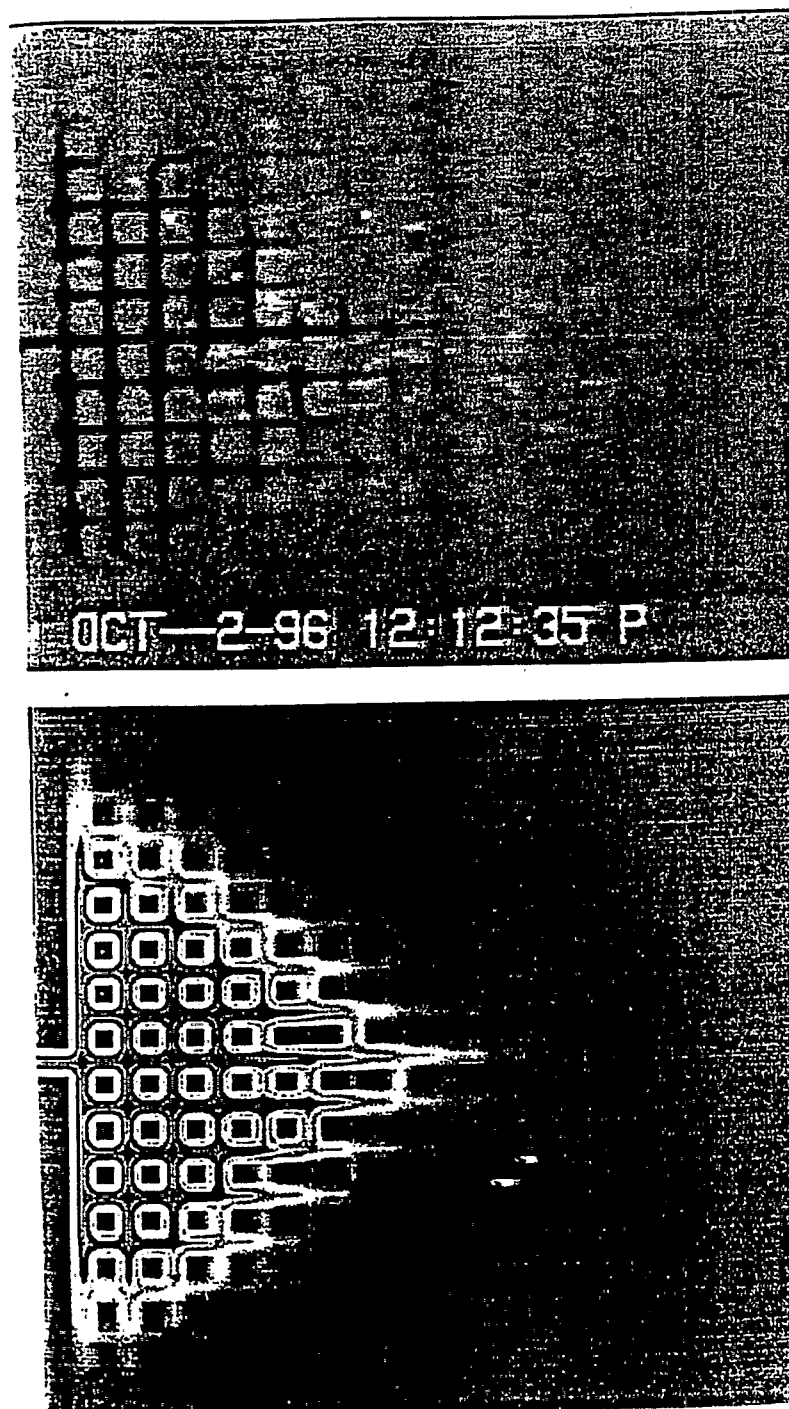


Figure 3.8. Comparison between experimental (top) and numerical (bottom) concentration profiles during miscible displacement of 50% glycerol solution for 0.091 pore volumes injected.

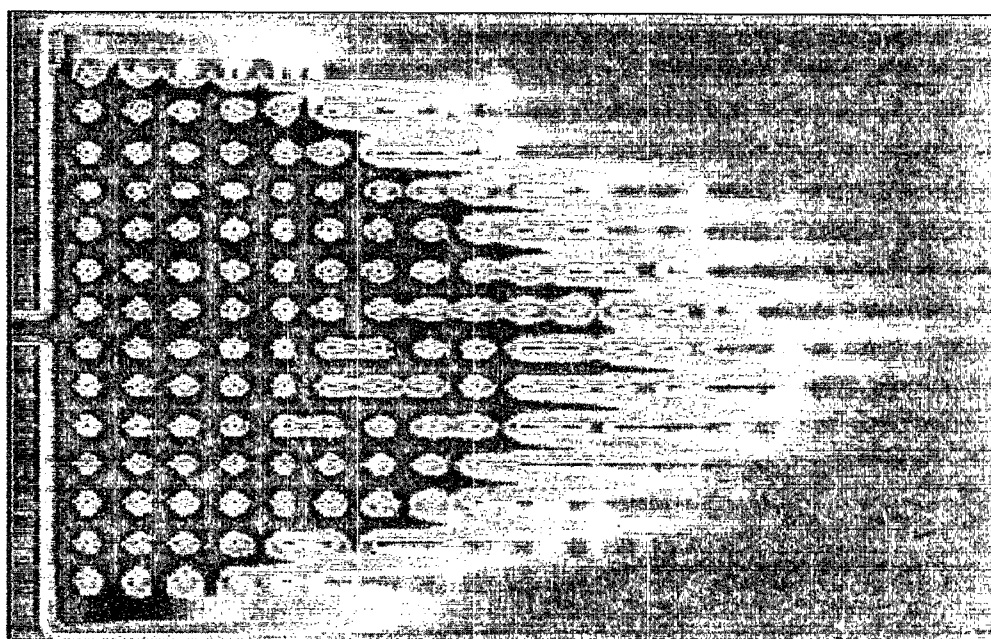
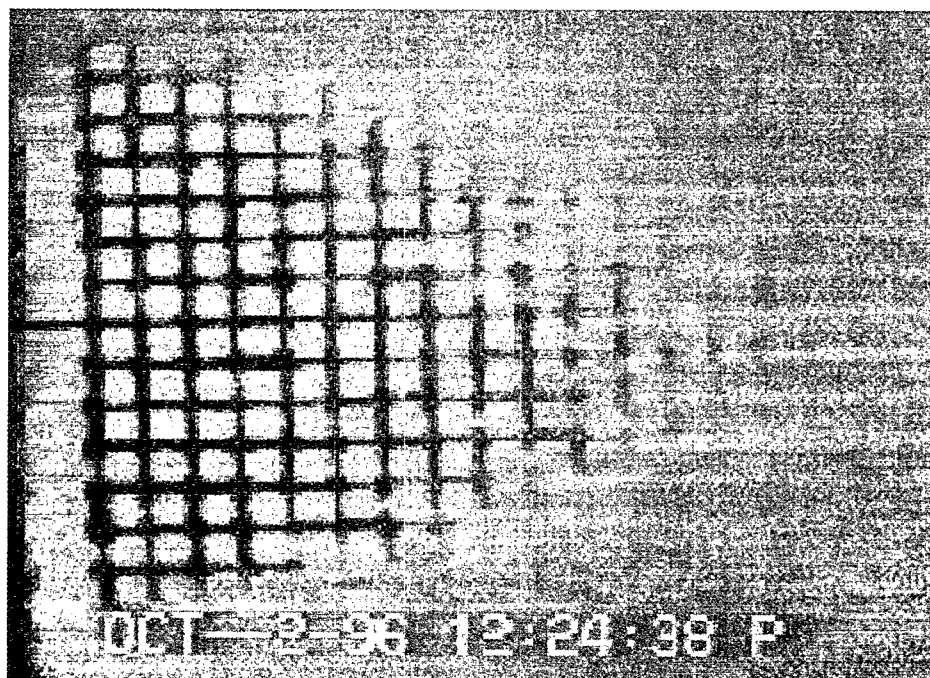


Figure 3.9. Comparison between experimental (top) and numerical (bottom) concentration profiles during miscible displacement of 50% glycerol solution for 0.21 pore volumes injected.

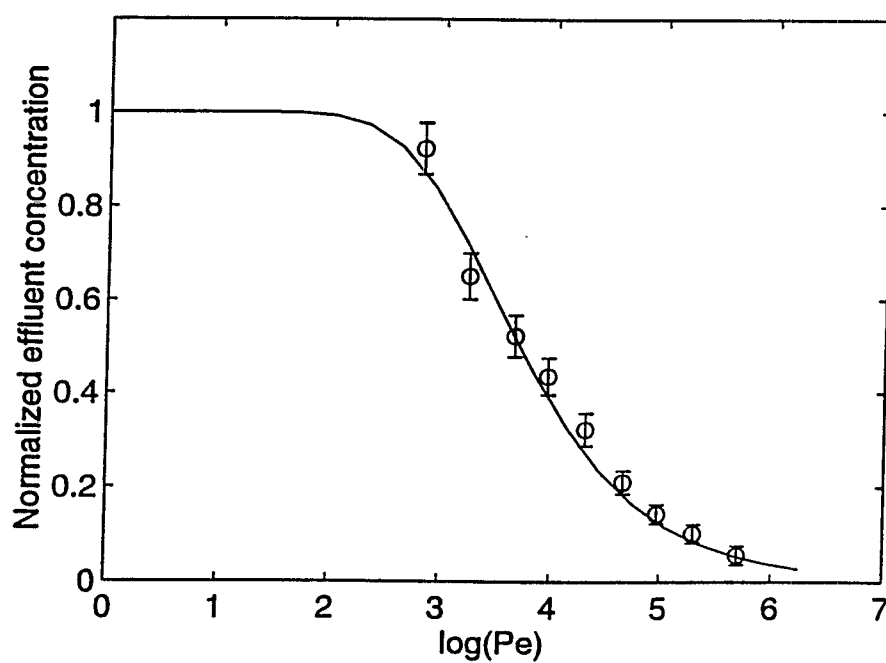


Figure 3.10. Comparison between experiments and simulations for mass transfer from trapped benzonitrile for pattern 1. The concentration at the effluent is normalized with its theoretical solubility value. The solid line is the theoretical prediction, experimental data are bracketed by error bars.

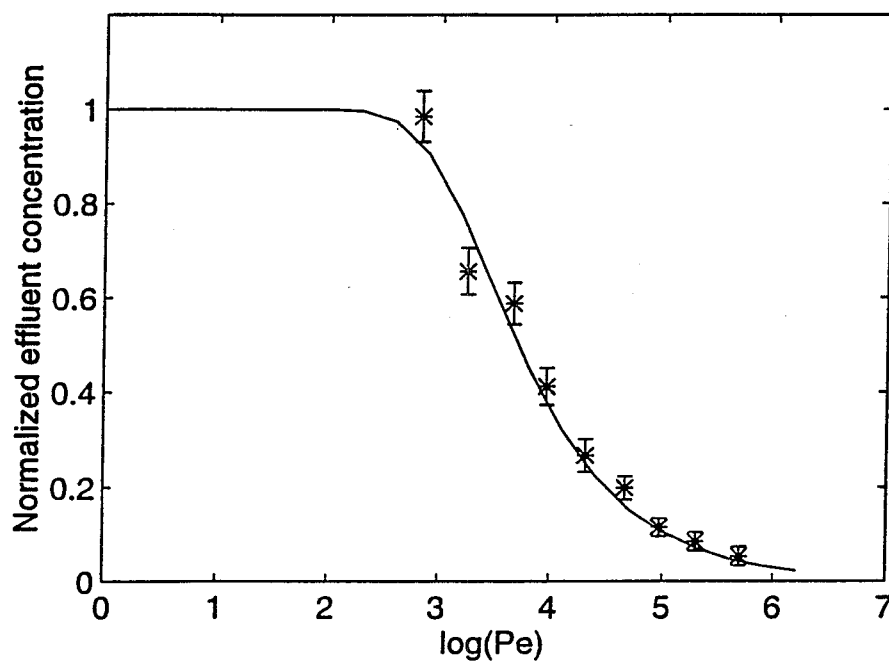


Figure 3.11. Comparison between experiments and simulations for mass transfer from trapped benzonitrile for pattern 2. The concentration at the effluent is normalized with its theoretical solubility value. The solid line is the theoretical prediction, experimental data are bracketed by error bars.

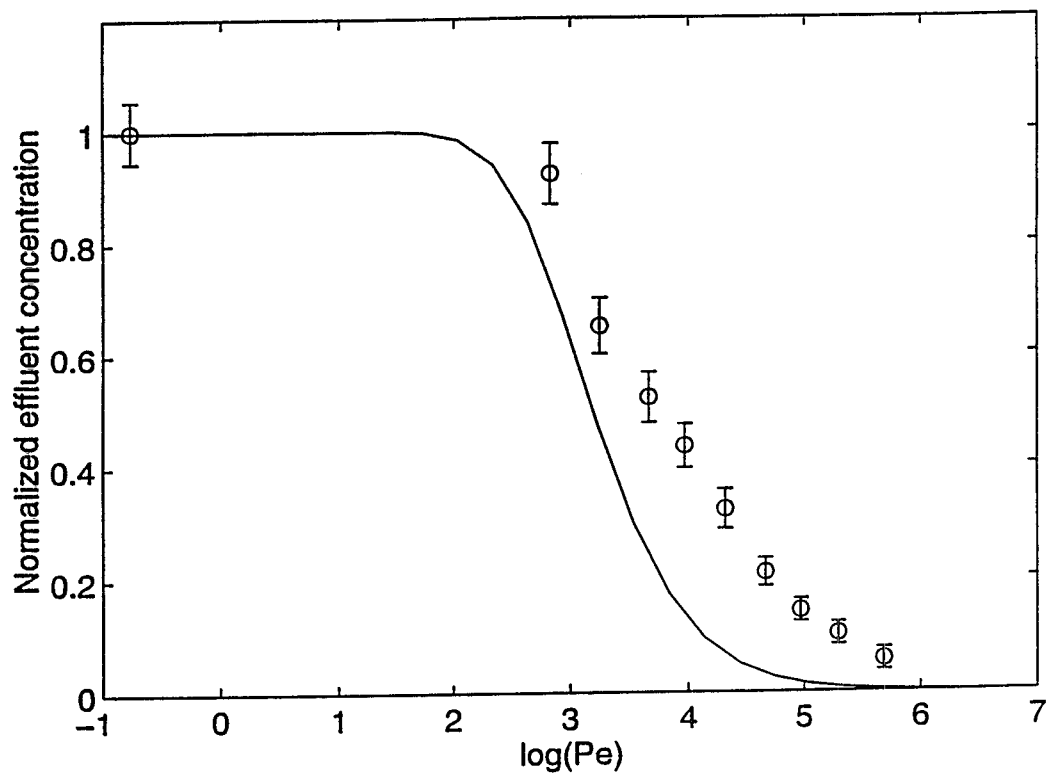


Figure 3.12. Comparison between experiments and simulations for mass transfer from trapped benzonitrile for pattern 1. Only diffusion was used for the simulation of local mass transfer. The concentration at the effluent is normalized with its theoretical solubility value. The solid line is the theoretical prediction, experimental data are bracketed by error bars.

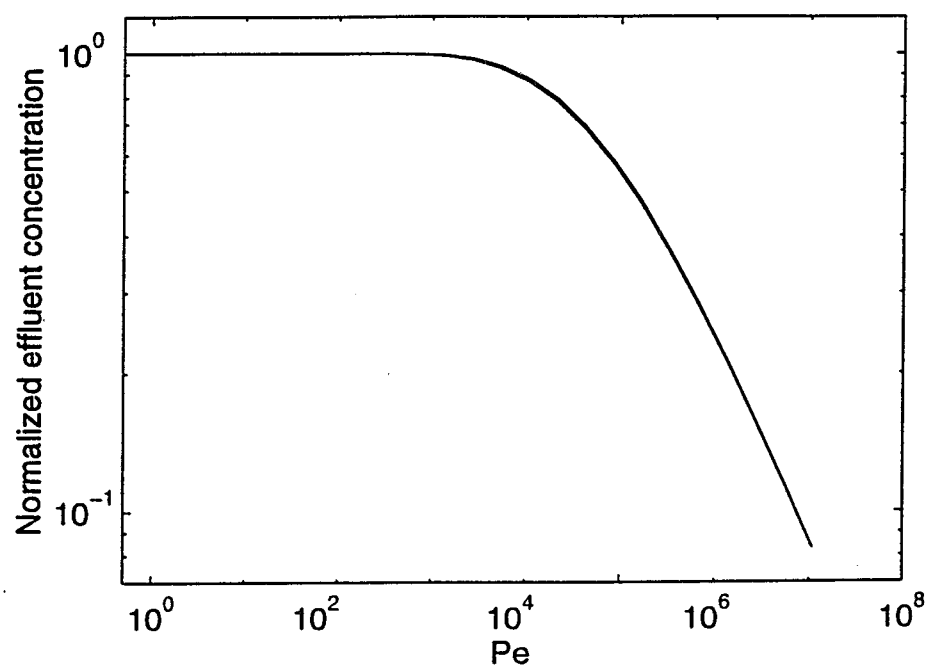


Figure 3.13. Sensitivity analysis of the effect of parameter a in the local mass transfer coefficient equation (3.13) on the effluent concentration curve. The effect of a is minimal at large values of the Peclet number.

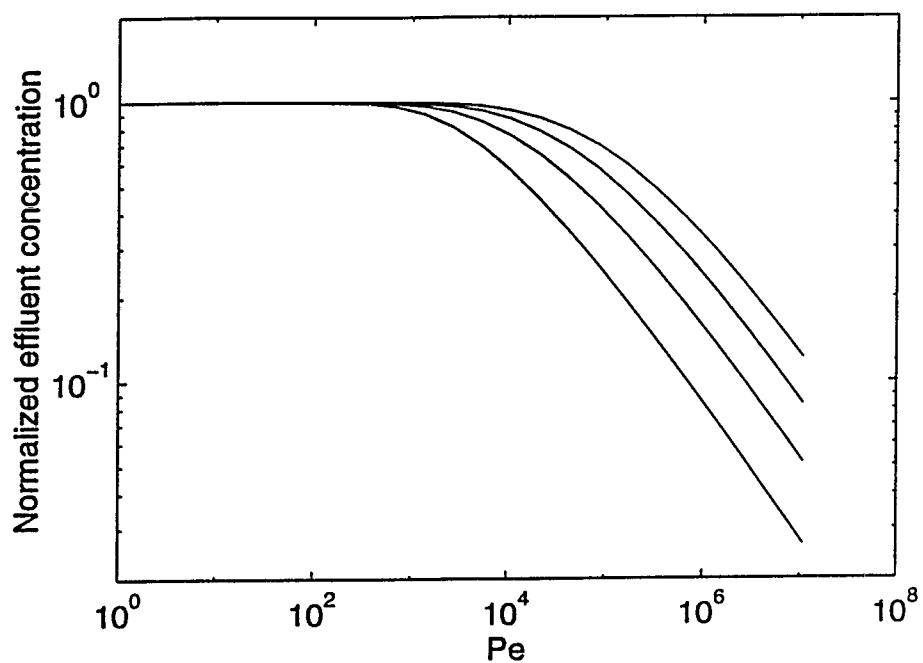


Figure 3.14. Sensitivity analysis of the effect of parameter b in the local mass transfer coefficient equation (3.13) on the effluent concentration curve. The effect of b is to shift the curve parallel to itself towards the right (essentially rescaling the Peclet number).

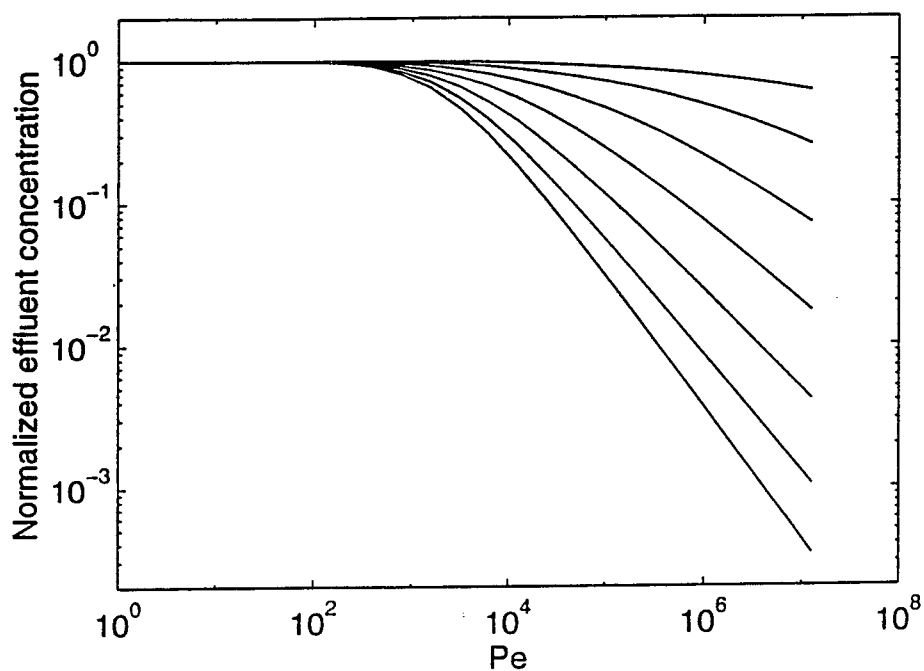


Figure 3.15. Sensitivity analysis of the effect of parameter c in the local mass transfer coefficient equation (3.13) on the effluent concentration curve. Note the asymptotic approach to a straight line at large values of the Peclet number.

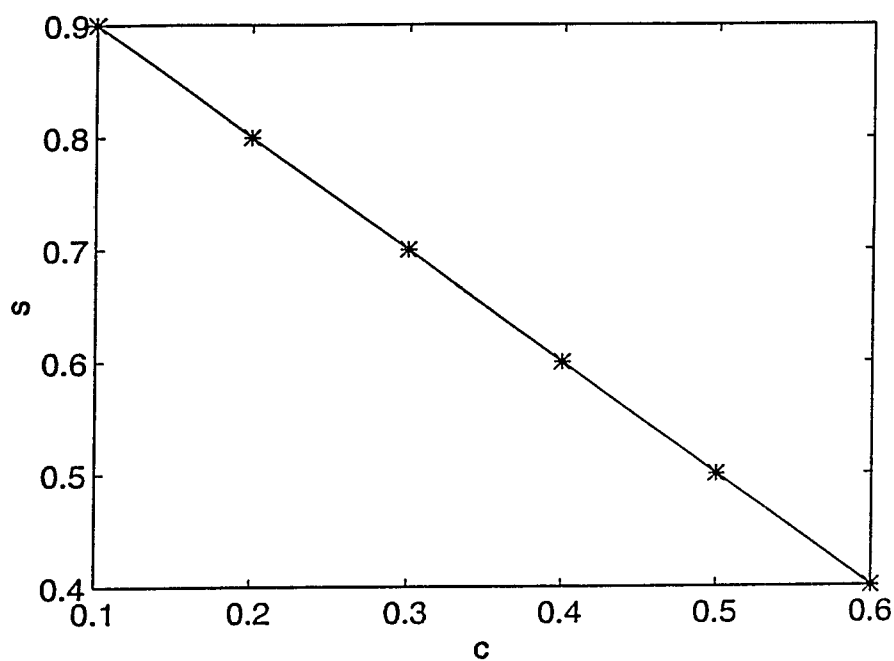


Figure 3.16. Numerical simulation results for the dependence of the slope s of the effluent concentration curve on the parameter c of equation (3.13). The curve essentially coincides with the theoretical result (3.14).

Chapter 4

CONVECTIVE MASS TRANSFER FROM STATIONARY SOURCES IN POROUS MEDIA

C.Jia, K. Shing and Y.C. Yortsos

INTRODUCTION

Many applications involve the mass transfer of a component from a stationary source to a flowing liquid in a porous medium. A particular example of interest to environmental remediation is the dissolution of trapped organic phases, commonly known as NAPLs (Non Aqueous Phase Liquids), by the injection of a solvent. The NAPL may be a single or a distributed source, for example in the form of an organic liquid phase trapped in a low-permeability region or as disconnected ganglia trapped by capillarity. The removal of this residual phase is typically attempted by the injection of another fluid, which solubilizes the NAPL (for example, see Powers et al., 1994, Augustijn et al., 1994). In the case of partial solubility, the mass transfer of the solute from the NAPL is the rate-controlling process and needs to be determined. Then, the basic problem becomes mass transfer by convection and diffusion in a porous medium with distributed sources. Similar problems also arise in oil recovery from subsurface rocks, if the oil phase is trapped and components partition in a liquid or gas phase flowing around it.

The geometric configuration of the trapped ganglia depends on a variety of factors, including the method by which the NAPL first percolated to the subsurface, and the heterogeneity of the soil. Figure 4.1 shows a typical configuration from the experiments reported in Chapter 3 on the dissolution of a trapped NAPL in a glass micromodel. If a percolation process, in which capillary forces solely control the fluid displacement is in effect, the geometry of the NAPL is that of an invasion percolation cluster, which for a random and spatially uncorrelated medium has a fractal structure with well-studied properties (Wilkinson and Willemsen, 1983, Feder, 1988). More generally, the medium heterogeneity affects significantly the configuration of the source. The resulting disorder in the source geometry and transport introduce important elements, which are absent from classical mass transfer problems.

A common engineering approach to modeling mass transfer in this context is by assuming that the source is extensively distributed, so that the rate of transfer from the stationary source to the flowing liquid is similar to a first-order reaction. For unidirectional flow, for example along the

z -direction in a cylindrical core, the following volume-average mass balance of solute in the flowing phase is typically postulated

$$\phi \frac{\partial C}{\partial t} + U \frac{\partial C}{\partial z} = D_{eff} \frac{\partial^2 C}{\partial z^2} + K(c_s - C) \quad (4.1)$$

where ϕ is the porosity of the porous medium, C is a volume-averaged concentration of the solute in the liquid, c_s is the equilibrium NAPL solubility concentration, t is time, U is the Darcy velocity, D_{eff} is an appropriate dispersion coefficient and K is an effective mass transfer kinetic coefficient with dimensions of inverse time. The latter is, in principle, related to the interfacial area between NAPL and solvent per unit total volume and the local mass transfer kinetics. Equation (4.1) is routinely used to estimate mass transfer coefficients from steady-state experiments in laboratory cores. A partial compilation of the various results obtained with this approach is given in Table 3.1. The wide-spread variation in the dependence of the mass transfer coefficient on various transport parameters, and the flow rate in particular, should be noted. Given that the exponent in the flow rate dependence reflects the underlying flow geometry, the variation shown needs to be further explored.

Although widely used, equation (4.1) was not rigorously derived until recently, when Quintard and Whitaker (1994) applied a volume-averaging approach in periodic media to obtain an effective equation of a similar type. In this approach, the effective reaction-rate coefficient is obtained from the solution in a unit cell of a closure problem involving a variant of Stokes' equation for fluid momentum and a convection-diffusion equation for mass transfer. Quintard and Whitaker (1994) computed the variation of this coefficient with the Peclet number for the simplified unit of Figure 4.2. In the same general context are also the studies of Koch and Brady (1987) and Mauri (1991).

In many applications, features of the microstructure at the pore-network level, such as pore-size distribution and connectivity, may dominate the process and need to be accounted for. This is particularly true for sources emplaced by a percolation process, as is often the case in NAPL contamination, where the configuration can be a self-similar fractal spanning many length scales (Feder, 1988). In such cases, a detailed analysis of the effects of the pore microstructure and the source configuration is needed in order to obtain a better understanding of the various empirical mass transfer correlations.

A detailed simulation of the problem in lattices of some degree of complexity is possible, for instance with the use of lattice gas simulation (Rothman and Zaleski, 1997). Here, we will take a simpler, although perhaps less accurate, approach, that of pore network simulation, where mass and momentum balances are discretized across neighboring pores. This discretization allows one to explore large-scale effects, related to the medium or the source disorder, over reasonably large lattices. Pore-network models have been successfully used in the simulation of immiscible displacements in porous media, for example in drainage and wetting (for a recent work see Bakke and Oren, 1997). They have also been successfully applied in porous media processes where diffusive transport of mass or heat is important, for example in the evolution of a gas phase from a supersaturated or a superheated liquid (Li and Yortsos, 1995, Satik and Yortsos, 1996), or in drying (Nowicki et al., 1992, Prat, 1993). In these applications it is diffusion of mass (or heat) that forms the predominant transport mechanism. For the case of mass transfer from a stationary source to a flowing fluid, however, convection by the flowing fluid is controlling and must be also considered.

In Chapter 3 we reported on experimental investigations of convective mass transfer from a trapped NAPL in the geometries shown in Figure 4.1. The effluent concentration was measured as a function of the Peclet number. The process was simulated successfully with a pore-network model. A systematic study of the effect of the various source geometries and of the particular mass transfer characteristics was not attempted, however. In addition to establishing the viability

of pore-network simulation in such problems, an important finding from the study of Chapter 3 was that the accurate matching of the experimental results required the use of appropriate mass transfer coefficients near the source interface. For example, it was found that if the local mass transfer from the trapped ganglia to the adjacent pores was approximated using diffusion only, the overall transport rates were underpredicted as the Peclet number increased. Good agreement was reached, on the other hand, when local mass transfer coefficients appropriate to the local geometries and flow conditions were used. Recognizing that a diffusive boundary condition at the source is associated with an "effective" medium description in the absence of microstructure, its inadequacy to provide a good match of the experiments reflects a breakdown of the corresponding "effective porous medium" description near the source interface (namely in places of porous media "discontinuities").

Consider, for example, flow over a "flat plate" embedded in a porous medium (the flat plate representing in this analogy a "flat" NAPL interface), which is a problem encountered in various applications in porous media (e.g. see Vafai and Thiyagaraja, 1987). Although macroscopically flat, however, the variability of the interface at the pore-scale cannot be neglected. There, both Darcy's law for momentum transport and the conventional effective mass transfer equation lose validity. To resolve the difficulty with the momentum transport, two different approaches have been proposed: (i) Replacing Darcy's law by Brinkman's equation, in which a macroscopic viscous shear is retained throughout the porous medium (done for example by Vafai and Thiyagaraja, 1987); and (ii) Retaining Darcy's law, but introducing an appropriate boundary condition at the discontinuity. The latter is obtained from an analysis of the local problem (e.g. see Tio and Sadhal, 1994, and references therein). The two approaches are similar in that Brinkman's equation essentially reduces to Darcy's law everywhere except within a narrow interface boundary layer, which scales with the square root of permeability (and it is of the order of a typical pore size, Katz and Thompson, 1986).

Analogous problems should exist with the transport of heat or mass near a discontinuity, where the effective equation formalism cannot capture the detailed transport process, particularly at high flow rates. However, the approach typically taken in the literature is to modify only the equation for momentum transport, while retaining an effective equation for the transport of heat (or mass) (e.g. see Vafai and Thiyagaraja, 1987). This approach is commonly used in the study of natural convection in porous media (e.g. see Gouyeau et al., 1996, for a recent application). Given the predominant contribution of the heat conduction in the solid, this approximation may lead to acceptable results in heat transfer problems. However, it is unclear whether it also applies for mass transfer, particularly when convection is dominant. Here, the local mass transfer near the source interface must be properly accounted, particularly at larger values of the Peclet number.

The objective of this chapter is to study mass transfer in porous media from stationary sources of various geometries in which the effects of the porous medium and the source geometry are explored using a pore-network representation, and where to account for the Stokes flow dynamics near the interface, we will use a local modification of the mass transfer coefficient. Our motivation is to improve the understanding of the dependence of overall mass transfer rates on the various parameters shown in Table 3.1, and particularly on the flow rate. We must remark, in advance, that some of these correlations may reflect the combined effects of dissolution and mobilization of residual phases. In this chapter, only dissolution from stationary sources will be considered. Deriving an effective equation similar to (4.1) will not be attempted. However, equation (4.1) will be used to define effective Damkohler and Sherwood numbers for the case of distributed sources, and to investigate their dependence on various parameters.

The chapter is organized as follows: First, we present the mathematical formulation, which includes a modification of the local interface condition. Its effect is explored by analyzing two

different cases: Flow over an isolated source of macroscale size, such as flow over a flat plate, a sphere and over distributed sources. The first geometry allows for an analytical solution, while for the other geometries, asymptotics at small and at large Peclet numbers are derived. Subsequently, we consider the more general problem of mass transfer over distributed sources of microscale size. Asymptotic and numerical solutions are derived. Pore-network simulations are conducted to test the theoretical predictions. The flow over self-similar surfaces is particularly analyzed. Using overall mass balances, the effective Sherwood number corresponding to equation (4.1) is computed for various geometries. The results are then compared to the various experimental correlations.

MATHEMATICAL FORMULATION

Consider mass transfer from a stationary source to a fluid flowing in the pore-space of a porous medium. As pointed out previously, the source geometry may be an effective flat plate, or an effective sphere, a self-similar percolation cluster or a distributed, disconnected interface, such as shown in Figure 4.1. Mass transfer in the pore-space is described by the usual convection-diffusion equation, the steady-state of which reads

$$\mathbf{u} \cdot \nabla c = D_m \nabla^2 c \quad (4.2)$$

where D_m is molecular diffusivity and \mathbf{u} is the local velocity. At the creeping flow conditions assumed, Stokes' equations describe the momentum balance. The solute is assumed at a sufficiently small concentration to not affect properties of the mixture, such as density or viscosity. At the source interface, the solute concentration is equal to its thermodynamic solubility value

$$c = c_s \quad (4.3)$$

These equations are subject to the appropriate flux or concentration conditions at the far-field boundaries. Typically, we assume uniform flow with zero net flux at the inlet, a Dankwerts boundary condition at the outlet and no-flux boundary conditions at the lateral boundaries. For flow over a flat plate, a sphere or a self-similar surface, the medium is assumed infinitely large.

As previously noted, our objective is to study the solution of the above problem using a pore-network analogue or its corresponding effective equation analogue, where appropriate. In general, the first approach must be taken for the case of sources of a size comparable to the microscale l , while an effective medium description is possible for macroscale sources. For the latter, and at conditions of low volumetric content of the source (for example, in the case of flow over a flat plate, etc.) the effective equation corresponding to (4.2) is a volume-averaged mass balance

$$\mathbf{U} \cdot \nabla C = \nabla (\mathbf{D}_{eff} \cdot \nabla C) \quad (4.4)$$

Here \mathbf{D}_{eff} is a velocity-dependent dispersion tensor, and \mathbf{U} is the Darcy velocity satisfying

$$\mathbf{U} = -\frac{k}{\mu} \nabla P \quad (4.5)$$

where k is the permeability of the porous medium and μ represents fluid viscosity. Alternatively, the full problem can be discretized by assuming a pore-network description.

Pore network simulation is a useful tool for processes in pore-networks or in experiments involving glass micromodels. The key approximation is the porous medium representation in terms of pores, connected to each other by pore throats in a network-like fashion (Dullien, 1992). In the network, sites represent pores and provide volumetric storage, while bonds represent throats and

control the conductance to flow, heat and mass. The various geometrical and transport characteristics can be spatially distributed. The governing equations are discretized over the sites of the network. For example, velocity and pressure fields are determined using the overall mass balance

$$\sum_j Q_{ij} = 0 \quad (4.6)$$

where Q_{ij} refers to volume flow rate between adjacent sites i and j , and the sum is over all sites j neighboring site i , and the use of Poiseuille's law

$$Q_{ij} = G_{ij} \Delta P_{ij} \quad (4.7)$$

where the overall conductance, G_{ij} , can be distributed. For mass balance purposes, concentrations are assigned to sites only, and the mass transfer between adjacent sites (except those neighboring the interface, see below) is assumed to occur by conventional modes of diffusion and convection. Then, the mass balance for solute in site i reads

$$V_s \frac{\Delta C_i}{\Delta t} = \sum_j \left[D_m A_{ij} \frac{\Delta C_{ij}}{l} \right] + \sum_j \left[\frac{G_{ij} \Delta P_{ij}}{l} C_{ij} \right] \quad (4.8)$$

where V_s denotes the site volume and A_{ij} is the cross-section of the pore throat. If site i neighbors a source, however, a modification for local mass transfer is necessary, as noted above.

Local mass transfer coefficients

In a boundary layer near the interface (of the order of \sqrt{k}), the above description breaks down and needs to be replaced. Indeed, local mass transfer cannot be described simply by diffusion and convection using Poiseuille's law for fluid flow (or Darcy's law, in the respective effective continuum case), but requires coupling Stokes flow to convection and diffusion. This is not inherent to the pore network approach (or to an effective medium) used here. One alternative is to keep Poiseuille's law (or Darcy's law in the effective problem) for the hydrodynamics outside this boundary layer and modify the mass flux, by using a mass transfer coefficient h_l ,

$$N_{si} = h_l (c_s - C_i) \quad (4.9)$$

where, N_{si} is the mass flux from the interface to an adjoining site i . The corresponding modification of the boundary condition for the effective medium problem is then

$$h_l (c_s - C) = -\mathbf{D}_{eff} \cdot \nabla C \cdot \mathbf{n} \quad (4.10)$$

where \mathbf{n} is the unit normal vector to the interface pointing outwards. We note that in the effective medium problem, equation (4.10) would be evaluated at the edge of the boundary layer, which for all practical purposes we may take to coincide with the source interface itself. (This assumption works well provided that the source volumetric density is not very high).

The coefficient h_l reflects the local mass transfer appropriate to the particular geometry. Examples of various local configurations expected in a NAPL-solvent system are shown in Figure 4.3 reprinted from the experiments of Chapter 3. In general, h_l is related to the local flow velocity at the edge of the boundary layer, given here by the outer (or effective medium) solution, using mass transfer correlations appropriate to the local geometry. For simple interface geometries, various mass transfer expressions (for example, flow over a flat plate, etc.) have been developed (Cussler,

1984). For the more complex geometries of the type shown in Figure 4.3, however, the literature is rather limited. A close analogue to some of these is mass transfer over a cavity, which is a problem in electrochemical pit corrosion studied in some detail by Alkire and Deligianni (1988) and Alkire et al. (1990) (see also Occhialini and Higdon, 1992). These authors developed correlations of the following type

$$\text{Sh}_l = 0.3 \left(\frac{w}{h} \right)^{0.83} \text{Pe}_l^{0.33} \quad (4.11)$$

where $\text{Sh}_l = \frac{h_l l}{D_m}$ denotes the local Sherwood number, $\text{Pe}_l = \frac{w w}{D_m}$ denotes the local Peclet number, and w/h is the cavity aspect ratio. This analogy was successfully used in the pore-network simulations in Chapter 3 to match the etched-glass micromodel experiments. More generally, however, we will take in this chapter the general dependence (see also Browning and Fogler, 1996)

$$\text{Sh}_l = A + b \text{Pe}_l^c \quad (4.12)$$

This relationship contains the expected asymptotic behavior of the local mass transfer rates in the two limits, namely the approach to a constant at small Pe_l and to a power-law at large Pe_l . In (4.12) the dependence of mass transfer on the local flow velocity is through exponent c , parameters A and b being functions of the geometrical and physical properties only. In general, all these parameters can be spatially distributed, reflecting the pore geometry disorder (Figures 4.1 and 4.3), hence Sh_l is in general position-dependent. Using a characteristic macroscale velocity U_o , we can rewrite (4.12) as

$$\text{Sh}_l = A + b \left(\frac{u}{U_o} \right)^c \text{Pe}_{l,o}^c \quad (4.13)$$

where an obvious notation was implied for $\text{Pe}_{l,o}$. The new boundary conditions (4.9) and (4.10), respectively, will be used to simulate the mass transfer problem.

EFFECTIVE POROUS MEDIA: MACROSCALE SOURCES

To obtain an insight on the effect of the new interface condition on the overall problem, we will first analyze the problem in a homogeneous effective medium with sources of a macroscopic size. Pore-network simulations will be described in a later section for mass transfer with distributed sources of a microscale size. Using for characteristic length the macroscale of the source, L , for characteristic velocity the free-stream velocity, U_o , and for characteristic concentration the equilibrium value, c_s , the steady-state mass transfer equation for an effective medium reads in dimensionless notation

$$\mathbf{U}_D \cdot \nabla C_D = \frac{1}{\text{Pe}_L} \nabla (\mathbf{D}_{D,eff} \cdot \nabla C) \quad (4.14)$$

where subscript D denotes dimensionless quantities. The velocity \mathbf{U}_D satisfies potential flow (for the case of a homogeneous medium), $\mathbf{D}_{D,eff}$ is a dimensionless velocity-dependent dispersion tensor and we introduced the macroscale Peclet number $\text{Pe}_L = \frac{U_o L}{D_{eff,o}}$, where $D_{eff,o}$ is a measure of the transverse dispersion coefficient at the velocity U_o . We make the following remarks:

1. For an effective continuum description to be valid, the ratio of length scales, $\frac{L}{l}$, must be sufficiently large.

2. The dependence of $D_{eff,o}$ on the velocity can be approximated for the present purposes by

$$D_{eff,o} = \phi D_m [1 + \lambda Pe_l] \quad (4.15)$$

where λ is an $O(1)$ positive constant. Captured in (4.15) are the two asymptotic limits of molecular diffusion, at low velocities, and of mechanical dispersion, at high velocities. In the latter, we used the well-known result that for an uncorrelated and random porous medium, the dispersivity is proportional to the microscale l (e.g. see Koch and Brady, 1987).

3. As a result of (4.15), the macroscale Peclet number can be expressed as

$$Pe_L = \frac{U_o L}{\phi [D_m + \lambda U_o l]} = \left(\frac{L}{\phi l} \right) \frac{Pe_l}{1 + \lambda Pe_l} \quad (4.16)$$

Thus, for macroscale problems ($L \gg l$), Pe_L is generally large, unless Pe_l is sufficiently small (and of the order of $\frac{1}{L}$).

Finally, in terms of this dimensionless notation, the boundary condition corresponding to (4.10) becomes

$$Sh_L(1 - C_D) = -D_{D,eff} \cdot \nabla C_D \cdot \mathbf{n} \quad (4.17)$$

where we introduced the macroscale Sherwood number,

$$Sh_L \equiv \frac{h_l L}{D_{eff,o}} = \left(\frac{L}{l} \right) \frac{D_m Sh_l}{D_{eff,o}} \quad (4.18)$$

Because of its dependence on the local Peclet number Pe_l , Sh_L is in general spatially variable. This introduces a significant complexity in the analysis of the problem. However, certain source geometries, and specifically a flat plate, allow for an analytical solution. In this section, we will discuss in order flow over a flat plate and flow over a sphere and develop analytical and asymptotic results. In these three geometries, the source is embedded in an infinite medium. An asymptotic analysis of the more general problem, in which the source is distributed throughout the medium, will also be provided subsequently.

Flow over a flat plate

Consider flow over a flat plate embedded in an infinitely large porous medium. Because the velocity profile is uniform ($U_D = 1$) the effective dispersion coefficient and the local Sherwood number are spatially constant. Of interest here is mass transfer at relatively large Pe_L , thus we will keep convection in the streamwise direction, x , and dispersion in the transverse direction, y . According to (4.16), large Pe_L occurs under two conditions: When Pe_l is $O(1)$ or larger, or when $Pe_l \ll 1$ and simultaneously $\frac{1}{L} \ll \frac{U_o}{D_m} \ll \frac{1}{l}$ (and where the effective medium condition $L \gg l$ was tacitly implied). Then, the equation reads

$$\frac{\partial C_D}{\partial x_D} = \frac{1}{Pe_L} \frac{\partial^2 C_D}{\partial y_D^2} \quad (4.19)$$

which is to be solved subject to the interface condition

$$Sh_L(1 - C_D) = -\frac{\partial C_D}{\partial y_D} \quad \text{at } y_D = 0 \quad (4.20)$$

and the boundary conditions

$$C_D = 0 \text{ at } x_D = 0 \text{ and } y_D = \infty \quad (4.21)$$

The solution of this problem is readily obtained using a Laplace transform. We find

$$C_D = -\exp(\text{Sh}_L y_D + a^2 x_D) \text{erfc} \left(a\sqrt{x_D} + 1/2\sqrt{\frac{\text{Pe}_L}{x_D}} y_D \right) + \text{erfc} \left(1/2\sqrt{\frac{\text{Pe}_L}{x_D}} y_D \right) \quad (4.22)$$

where we introduced the parameter $a \equiv \text{Sh}_L \text{Pe}_L^{-1/2}$. From this we can evaluate the effective mass transfer coefficient over a flat plate of length L ,

$$\text{Sh}_{avg} \equiv \frac{h_{avg} L}{D_{eff,o}} \equiv - \int_0^1 \frac{\partial C_D}{\partial y_D} \Big|_{y_D=0} dx_D = \text{Sh}_L \frac{1}{a^2} (\exp a^2 \text{erfc} a - 1 + \frac{2a}{\sqrt{\pi}}) \quad (4.23)$$

Equation (22) shows that the normalized overall mass transfer rate (namely the ratio $\text{Sh}_{avg}/\text{Sh}_L$) is a function of the parameter a only. This function is plotted in Figure 4.4. One distinguishes two limits:

(i) At small a , we have the asymptotic behavior

$$\text{Sh}_{avg} = \text{Sh}_L \left[1 - \frac{4}{3\sqrt{\pi}} \text{Sh}_L \text{Pe}_L^{-1/2} + O(a^2) \right] \quad (4.24)$$

Using (4.16) and (4.18), we find that this is possible under the conditions $\text{Pe}_l \gg 1$ and $\sqrt{\frac{L}{l}} \text{Pe}_l^{c-1} \ll 1$, a necessary constraint for which is $c < 1$. The latter is more difficult to be satisfied as c approaches 1. In this limit, the effective mass transfer coefficient has to leading-order in a the same scaling with the Peclet number as the local mass transfer coefficient, and reflects only *local* geometry effects. The overall mass transfer is dominated by the local mass transfer at the source interface and follows the velocity scaling of the local coefficient, namely $h_{avg} = h_l$ to leading order. Indeed, here, the interface concentration is to leading-order proportional to a , thus it vanishes as $a \rightarrow 0$.

(ii) At large a , on the other hand, we obtain from (4.23)

$$\text{Sh}_{avg} = \frac{2}{\sqrt{\pi}} \text{Pe}_L^{1/2} + O(a^{-1}) \quad (4.25)$$

This result arises when Pe_l is generally finite. Now, mass transfer is dominated by the external problem. Indeed, in this limit, the interface boundary condition reduces to $C_D = 1$, and the problem admits the classical erfc solution. Here, the overall mass transfer is dominated by the macroscale geometry and is insensitive to the local mass transfer.

These two limits correspond to two different mass transfer regimes in the macroscale problem, namely where local or global characteristics dominate, respectively. We note that the local mass transfer characteristics dominate the overall mass transfer rates only in the case of sufficiently large Pe_l . Then, the coefficient h_{avg} has the following scaling

$$h_{avg} \sim U_o^c, \quad \text{Pe}_l \gg 1 \quad (4.26)$$

In all other cases, the global problem masks the mass transfer characteristics at the microscale, and the conventional effective continuum description with boundary condition (4.3) applies. Now, the overall coefficient has the different scaling

$$h_{avg} \sim \sqrt{D_{eff,o} U_o}, \quad \text{Pe}_l \text{ finite} \quad (4.27)$$

which, if approximated by a power-law in U_o would lead to an exponent ranging between 0.5 and 1. These conclusions also reflect the dependence of the dispersion coefficient on velocity. For example, in the absence of the latter ($\lambda = 0$), the first regime would require the more stringent condition $\sqrt{\frac{L}{l}} \text{Pe}_l^{c-1/2} \ll 1$, namely $c < 1/2$.

Numerical results for Sh_{avg} for flow over a flat plate are shown in Figure 4.5 for various dependences of Sh_L on the local Peclet number. It must be pointed out that in this Figure both Sh_{avg} and Pe_L are normalized with D_m instead of $D_{eff,o}$. Essentially, the vertical axis scales with h_{avg} , while the horizontal with U_o , hence we should expect scalings of the form (4.26 and (4.27) to arise. Indeed, it is shown that there exists a segment common to all three curves, with a scaling close to (4.27), while at larger values of Peclet number, equation (4.26) is obeyed, as expected.

Flow over a sphere

Consider, next, flow over a sphere embedded in an effective porous medium. Working in r and θ coordinates, the potential flow solution is (see for example, Lamb, 1932)

$$U_{D,r} = \cos\theta \left[1 - \frac{1}{r_D^3} \right] \quad (4.28)$$

and

$$U_{D,\theta} = -\frac{1}{2} \sin\theta \left[2 + \frac{1}{r_D^3} \right] \quad (4.29)$$

where we have normalized lengths with the sphere radius R . The interface boundary condition ($r_D = 1$) now reads

$$(1 - C_D) \text{Sh}_L(\sin\theta) = -\mathbf{D}_{D,eff} \cdot \nabla C_D \cdot \mathbf{n}_r \quad (4.30)$$

where we have explicitly expressed the dependence of Sh_L on the interface velocity $U_{D,\theta} = -\frac{3}{2} \sin\theta$. An analytical solution to this problem is generally difficult. Instead, we will focus on the asymptotic behavior of the problem in the limits considered above.

At relatively large Pe_L (namely for any non-negligible value of Pe_l), a boundary layer of order $\text{Pe}_L^{1/2}$ develops. Neglecting longitudinal dispersion, as well as the variation of the dispersion coefficient with velocity inside the boundary layer, the mass transfer equation reduces to

$$3\eta Y \frac{\partial C_D}{\partial Y} + \frac{3}{2}(1 - \eta^2) \frac{\partial C_D}{\partial \eta} = \frac{\partial^2 C_D}{\partial Y^2} \quad (4.31)$$

in terms of the streamwise coordinate $\eta \equiv \cos\theta$, $-1 < \eta < 1$, and the boundary layer coordinate $Y = \text{Pe}_L^{1/2}(r - 1)$. In these variables, the interface condition at $Y = 0$ becomes

$$\text{Pe}_L^{-1/2} \text{Sh}_L(\eta)(1 - C_D) = -\frac{\partial C}{\partial Y} \quad (4.32)$$

Even under these conditions, the exact solution of this problem is difficult since parameter $a \equiv \text{Sh}_L \text{Pe}_L^{-1/2}$ is position-dependent. However, the leading-order dependence can be extracted in a relatively straightforward fashion, as follows.

(i) If a is uniformly small, the problem will be dominated by the local mass transfer, as in the case of the flat plate. Then, the leading scaling is expected to be

$$\text{Sh}_{avg} \approx \frac{1}{2} \int_{-1}^1 \text{Sh}_L(\eta) d\eta \quad (4.33)$$

which is the equivalent of the flat plate expression (4.24). Using equation (4.13) for the evaluation of Sh_L , we obtain after some manipulations

$$\text{Sh}_{avg} \approx \frac{D_m L}{D_{eff,o} l} (A + b' \text{Pe}_{lo}^c) \quad (4.34)$$

where $b' = b \left(\frac{3}{2}\right)^c \int_{-1}^1 (\sqrt{1-\eta^2})^c d\eta = 3^c 2b \frac{\Gamma^2(c/2+1)}{\Gamma(c+2)}$ and $\Gamma(z)$ is the Gamma function. We note that the local power-law dependence on the velocity (exponent c) has survived, although now with a modified prefactor. The previous conditions for a flat plate (but now in terms of Pe_{lo}) also hold for the applicability of this result.

(ii) In the opposite case of large a , the overall mass transfer will be dominated by the external problem. Now, the boundary condition becomes $C_D = 1$ and the problem can be solved with classical methods, namely using the similarity variable $\zeta = \frac{Y}{g(\eta)}$, where $g(\eta) = \frac{4\sqrt{1+\frac{3}{2}\eta-\frac{1}{2}\eta^3}}{3(1-\eta^2)}$. We find

$$C_D = \text{erfc}\zeta \quad (4.35)$$

thus, the average mass transfer coefficient is

$$\text{Sh}_{avg} = -\text{Pe}_L^{1/2} \int_{-1}^1 \frac{\partial C_D}{\partial Y} |_{Y=0} d\eta = \frac{4}{\sqrt{2\pi}} \text{Pe}_L^{1/2} + \dots \quad (4.36)$$

This power law has the $1/2$ scaling, which is identical to the equivalent expression (4.25) for the flat plate problem.

Numerical results for Sh_{avg} for flow over a sphere are shown in Figure 4.6 for various dependences of Sh_L on the local Peclet number. As in the simulations of Figure 4.5, both Sh_{avg} and Pe_L are normalized with D_m instead of $D_{eff,o}$. We should expect, therefore, a common segment with a slope of about $1/2$, in the log-log plot, followed by a slope equal to c , at large velocities. These results are well obeyed in the respective limits, as expected.

For completeness, we also present the asymptotic behavior in the other limit of small Peclet numbers, where the problem is diffusion-dominated. Because this geometry (as well as that of the self-similar surface to follow) corresponds to a finite source embedded in an infinite medium, the Sherwood number should approach a constant. Now, the concentration profile becomes simply

$$C_D = \frac{\text{Sh}_{L,0}}{(\text{Sh}_{L,0} + 1)r_D} \quad (4.37)$$

where $\text{Sh}_{L,0} = \lim_{\text{Pe}_l \rightarrow 0} \text{Sh}_L$, and the dimensionless mass transfer coefficient is

$$\text{Sh}_{avg} = \frac{2\text{Sh}_{L,0}}{1 + \text{Sh}_{L,0}} \quad (4.38)$$

This expression reduces to the classical diffusion-only result for a sphere, $\text{Sh}_{avg} = 2$, when we invoke the continuum limit $L \gg l$, in which case $\text{Sh}_{L,0} \gg 1$ (compare with (4.18)).

Asymptotic Behavior With Distributed Sources

In the previous section we discussed flow over a finite source embedded in an infinite medium. In the more general problem, the source is distributed throughout the volume. We should expect a similar behavior at large Pe_L , but a different behavior at small Pe_L . We note, again, that although distributed, the source volume fraction cannot be taken too large if the present method is to be valid. Indeed, the assumption was made in this chapter that we can capture the effect of Stokes dynamics in boundary layers around the source. For this to be valid, layers from adjacent sources should not overlap, which requires a sufficiently small volume fraction. Again, we will examine the mass transfer behavior in the two limits of small and large Peclet numbers, respectively.

Consider, first, the asymptotic solution at small Peclet numbers, where diffusion predominates, and take the expansion

$$C = C_0 + Pe_L^n C_1 + \dots \quad (4.39)$$

where n is a positive exponent to be determined and we have used the extent of the domain L , as the characteristic length scale. Here, and in the following, we will suppress subscript D for simplicity in notation. Note that from physical considerations it follows that $C_1 < 0$. Substitution of the expansion into equation (4.14) gives

$$U \cdot [\nabla C_0 + Pe_L^n \nabla C_1 + \dots] = \frac{1}{Pe_L} [\nabla^2 C_0 + Pe_L^n \nabla^2 C_1 + \dots] \quad (4.40)$$

where, for simplicity, we omitted the dependence of the dispersion coefficient on velocity at this level. At the interface boundary, the condition reads as

$$(Sh_{L,0} + Pe_L Sh_{L,1} + \dots)(1 - C_0 - Pe_L^n C_1 + \dots) = - \frac{\partial(C_0 + Pe_L^n C_1 + \dots)}{\partial n} \quad (4.41)$$

where we expanded Sh_L in powers of Pe_L , while at the upstream boundary $x = 0$, we have

$$C_0 + Pe_L^n C_1 + \dots - \frac{1}{Pe_L} \frac{\partial C_0}{\partial x} - Pe_L^{n-1} \frac{\partial C_1}{\partial x} + \dots = 0 \quad (4.42)$$

where x is the streamwise coordinate. Finally, at the downstream and the lateral boundaries

$$\frac{\partial C_i}{\partial n} = 0 \quad (4.43)$$

The exponent n is determined by applying in (4.40)-(4.43) a dominant balance. It is easily shown that $n = 1$, hence the leading-order term satisfies $C_0 = 1$, everywhere, which is expected at conditions of diffusion control. The next term in the expansion satisfies the steady-state diffusion equation

$$\nabla^2 C_1 = 0 \quad (4.44)$$

with upstream boundary condition $\frac{\partial C_1}{\partial x} = 1$, with interface condition at the source boundary $Sh_{L,0} C_1 = \frac{\partial C_1}{\partial n}$ and with the no-flux boundary conditions $\frac{\partial C_1}{\partial n} = 0$ on all other boundaries. The solution of this problem depends on the source configuration.

Substitution of the above results in the definition for Sh_{avg} leads to the following for the mass transfer coefficient in this limit

$$Sh_{avg} = a_1 Pe_L (1 + Pe_L \frac{1}{A_e} \int_{A_e} U_n C_1 dA + O(Pe_L^2)) \quad (4.45)$$

where $a_1 = \frac{A_e}{A_i}$ is the ratio of the cross-sectional (entrance or exit) area to that of the area of the sources, U_n is the normal component of the velocity at the exit and we made use of the relation

$$-\int_{A_i} \frac{\partial C}{\partial n} dA = \text{Pe}_L \int_{A_e} U_n C_e dA \quad (4.46)$$

We conclude that in the small Pe_L limit, Sh_{avg} is to leading-order proportional to Pe_L , reflecting the finite size of the domain used. This is to be contrasted to the previous problem of transport over a source of finite size, embedded in an infinite medium, where Sh_{avg} approaches a constant. To obtain the next-order term in the expansion requires solving the boundary value problem for C_1 , which must be obtained numerically, in general. Because $C_1 < 0$, however, we can infer a priori that the second-order correction would be negative.

In the other limit of large Pe_L , the concentration field practically vanishes everywhere in the domain, except in narrow boundary layers near the source interfaces, where the local mass transfer dominates. The problem becomes analogous to flow over a finite source in an infinite medium, discussed in the previous sections, hence in accordance with the previous analysis, we should expect the scaling

$$\text{Sh}_{avg} \sim b \frac{L}{\phi l} \text{Pe}_{lo}^{\epsilon-1} \quad (4.47)$$

or

$$h_{avg} \sim b \frac{D_m}{l} \text{Pe}_{lo}^{\epsilon} \quad (4.48)$$

for the average mass transfer coefficient. These predictions will be tested numerically below.

PORE NETWORKS: MICROSCALE SOURCES

The pore-network simulator was subsequently used to evaluate mass transfer coefficients and their dependence on the flow parameters and the geometrical configuration of the source. A description of the simulator was given in Chapter 3. Here, both Sh_{avg} and Pe_L were defined based on a macroscale L (equal to the size of the domain) and on the molecular diffusivity (rather than dispersion), essentially corresponding to $\lambda = 0$ in (4.15), (4.16) and (4.18). Dispersion is inherent in the solution of the problem from the variation of the velocity in the pores of the pore network. We also note that the pore-network approach can also be viewed as a finite-difference analog of the effective equations (although it stands on its own right as a model of real physical system). As a result, some of the asymptotic predictions of the continuum problem may also apply here as well. The following source geometries were investigated: a Koch surface, a percolation cluster and a periodically distributed source.

Flow over a self-similar surface

The study of self-similar objects is important in the context of porous media, since the source geometry may very well have self-similar characteristics as a result of the method of emplacement (for example, if a percolation process has controlled the spatial distribution of the source). Self-similar objects are characterized by a cascade of length scales, ranging from an upper cut-off, L_u , to a lower cut-off, L_l . As a result, length-scale dependent quantities, for example the Peclet number

or the Reynolds number need to be carefully defined. In accordance with the previous, we define the average mass transfer coefficient as

$$\text{Sh}_{avg} = -\frac{1}{A_i} \int_{A_i} \frac{\partial C_D}{\partial n_D} dA \quad (4.49)$$

where A_i refers to the total surface area of the source and lengths have been dimensionalized with the upper cut-off L_u (which here coincides with the linear extent L). In this section, we consider the solution of the mass transfer problem over the geometry of a Koch curve (Figure 4.7) (Mandelbrot, 1983, Feder, 1988). A corresponding problem involving a percolation cluster, which is quite relevant to remediation problems, and where L_l coincides with l , will be discussed later in conjunction with the effective equation (4.1). As in the previous geometries, we will discuss the asymptotic behavior of the problem in the two limits of small and large Pe_L , respectively.

At small Pe_L (namely small Pe_l), diffusion predominates and at all scales the problem is steady-state diffusion from a source of constant concentration, although of a self-similar geometry, into a quiescent medium. The particular problem of diffusion from a self-similar surface was studied by Cates and Witten (1987), who showed that the overall mass transfer rate is equivalent to that for diffusion from an equivalent homogeneous source of size equal to the effective radius of the self-similar source. Their conclusions were confirmed in a related study of mass transfer-driven bubble growth in porous media by Satik et al. (1995). We should expect, therefore, that at small Peclet numbers, the overall mass flow rate from the Koch curve will be equivalent to that from a flat plate, that from a percolation cluster to be equivalent to diffusion from an equivalent sphere, etc. Using definition (4.49), it follows that in this limit we should have the scaling

$$\text{Sh}_{avg} \sim \left(\frac{L}{L_l}\right)^{-D} (1 + O(\text{Pe}_L)) \quad (4.50)$$

if the source is embedded in an unbounded medium, or

$$\text{Sh}_{avg} \sim \text{Pe}_L \left(\frac{L}{L_l}\right)^{-D} (1 + O(\text{Pe}_L)) \quad (4.51)$$

if the bounding medium is finite (for example, compare with (4.45)). Here D is the surface fractal dimension (and E is the Euclidean dimension embedding the object). For the Koch curve of Figure 4.7, we have $E = 2$ and $D = \ln 5 / \ln 3 = 1.4645$, while for a 3-D percolation cluster (Stauffer and Aharony, 1992) $D \approx 2.5$. Note that because the exponent in (4.50) is negative, the so defined Sh_{avg} decreases as the surface roughness (namely L/L_l) increases. Equation (4.50) states that in the limit of small Pe_L , the average Sherwood number is a power law of the ratio of the characteristic length scales. This means that under otherwise identical conditions, Sh_{avg} is size dependent.

As Pe_L increases, the situation is more complex. Figure 4.8 shows a plot of the velocity vectors corresponding to flow over the Koch curve of Figure 4.7. The decrease of the velocity magnitude as cavities of lower accessibility are probed is apparent. The velocity inside the cavities is smaller, as the cavity size decreases, thus even though mass transfer may be controlled by convection at the external surface, it becomes progressively diffusion-controlled inside smaller size cavities. At sufficiently large Pe_L , however, we expect that the system would eventually approach a state in which the local mass transfer coefficient controls the mass transfer rate. This is illustrated in Figure 4.9 which shows a plot of the local mass fluxes along a coordinate tangential to the Koch curve for various values of the Peclet number. For most of the cases shown, the local flux is quite low in the inaccessible areas, but increases rapidly in the part of the surface which is exposed. At sufficiently large Pe_L , however, all fluxes increase and may eventually equalize, reflecting the increased role of

convection inside the surface. The corresponding dimensionless concentration profile is plotted in Figure 4.10: along the streamwise coordinate x on the top of the surface of Figure 4.7, in Figure 4.10a, and along the coordinate tangential to the perimeter in Figure 4.10b. Profiles at different Peclet numbers are shown. The concentration at the top reflects the existence of the various surface cavities, but it is otherwise relatively smooth. On the other hand, the profile along the cavities of the self-similar surface fluctuates significantly, particularly at larger Pe_L . The concentration is smaller near the surface exposed to flow, but increases substantially inside the cavities, reflecting the fact that mass transfer by convection is substantially slower inside inaccessible cavities. However, for a sufficiently large Peclet number, given a fixed ratio of cutoff scales, the interface concentration becomes small almost everywhere, reflecting the fact that mass transfer is convection-controlled even at the small scale. We should note that these simulations correspond to the case $b = 0$, namely the local Sherwood number is independent of the local velocity.

The transition from a diffusion-dominated to a convection-dominated regime occurs when the minimum local Peclet number inside the surface, namely the minimum in $\frac{u_l}{U_o}$, becomes sufficiently large, where u_l denotes the tangential velocity at the surface. For a fractal surface, we expect this minimum to scale as a power of the ratio of the length scales $\frac{L}{L_l}$, and more specifically

$$\min \frac{u_l}{U_o} \sim \left(\frac{L}{L_l} \right)^\alpha \quad (4.52)$$

where α is a negative exponent. Then, the transition between the two regions should be controlled by a scaling function $f(z)$, in terms of the variable $z = U_o \left(\frac{L}{L_l} \right)^\alpha \frac{L}{D_m} \equiv Pe_{lo} \left(\frac{L}{L_l} \right)^\alpha$. The properties of this function are discussed below.

At sufficiently large Pe_L , the local mass transfer dominates, and using equation (4.49) we have

$$Sh_{avg} \sim b \frac{L}{\phi l} Pe_{lo}^\epsilon \frac{1}{A_i} \int_{A_i} \left(\frac{u_l}{U_o} \right)^c dA \quad (4.53)$$

For the same reasons cited above we should expect that the geometric factor above also scales as a power of the ratio of the two scales, namely

$$\frac{1}{A_i} \int_{A_i} \left(\frac{u_l}{U_o} \right)^c dA \sim \left(\frac{L}{L_l} \right)^{\beta(c)} \quad (4.54)$$

where $\beta(c)$ is another exponent that depends on c ($\beta(0) = 0$). Substitution in (4.53) gives the result

$$Sh_{avg} \sim b \frac{L}{\phi l} Pe_{lo}^\epsilon \left(\frac{L}{L_l} \right)^{\beta(c)} \quad (4.55)$$

The transition from diffusion- to convection- control is modulated by the scaling function. For the case of a bounded embedding medium, equation (4.51), small and large Pe_L behaviors may be combined using the following scaling ansatz

$$Sh_{avg} = Pe_L \left(\frac{L}{L_l} \right)^{-D} f_c(z) \quad (4.56)$$

where the scaling function $f_c(z)$ has the behavior

$$f_c(0) \sim \text{const} \quad \text{and} \quad f_c(z) \sim z^{c-1} \quad \text{as} \quad z \rightarrow \infty \quad (4.57)$$

This scaling works if $\alpha = -D$ and $\beta(c) = \alpha c$. Equation (4.57) reflects the fact that given a ratio of upper to lower cutoff scales, a sufficiently large Peclet number exists, such that the problem

becomes convection-controlled. Inversely, for a fixed macroscale Peclet number, self-similar objects of sufficiently many generations eventually become diffusion-controlled. Although it appears to collapse the two behaviors correctly, however, a more robust scaling theory must be developed. This requires further investigation.

Figure 4.11 shows a plot of Sh_{avg} as a function of Pe_L for $b = 0$ and for three different Koch curves corresponding to different generations. The curves have the general behavior expected from the previous analysis. Indeed, the asymptotic behavior shown is consistent with (4.51) and (4.55). The low Pe_L scaling with the scale ratio was tested and found to obey (4.51), as anticipated. Figure 4.12 shows corresponding results for $c = 1/3$, which also support the previous scalings. We are still in the process of investigating the validity of the scaling function, however.

Numerical results for flow around the percolation cluster of Figure 4.13 are shown in Figure 4.14 for three different values of the local exponent c . The results confirm the validity of the previous asymptotic expressions in the two limits of small and large Pe_L . The scaling for mass transfer on the available surface area similar to (4.51) was also verified for the percolation cluster problem.

The numerical results for flow over distributed sources at the microscale, will be analyzed in relation to the effective equation (4.1). For this it is necessary to establish a connection between Sh_{avg} and the corresponding mass transfer coefficients. To proceed we note that Sh_{avg} was calculated as defined in (4.49). The overall mass flow rate, J , is then, $J = \frac{D_{eff} A_i c_s}{L} Sh_{avg}$. We also note that Sh_{avg} is related to the dimensionless effluent concentration $C_{D,e}$ through

$$Sh_{avg} = \frac{A_e}{A_i} C_{D,e} Pe_L \quad (4.58)$$

a result obtained from a mass balance. Note that the ratio $\frac{A_e Pe_L}{A_i}$ is essentially independent of L . Equation (4.58) will be used to evaluate the Damkohler number and the effective mass transfer coefficient corresponding to equation (4.1).

Effective Thiele Modulus and Mass Transfer Coefficient

In dimensionless notation with length scaled with the extent of the domain L and concentration with the solubility value c_s , the steady-state boundary value problem at constant fluid injection rate U_o reads as

$$\frac{dC_D}{dx_D} = \frac{1}{Pe_L} \frac{d^2 C_D}{dx_D^2} + Da(1 - C_D) \quad (4.59)$$

with boundary conditions

$$C_D - \frac{1}{Pe_L} \frac{dC_D}{dx_D} = 0 \quad \text{at} \quad x_D = 0 \quad (4.60)$$

and

$$\frac{dC_D}{dx_D} = 0 \quad \text{at} \quad x_D = 1 \quad (4.61)$$

Here we introduced the macroscopic Peclet number $Pe_L = \frac{U_o L}{D_{eff}}$ and we also defined the Damkohler number $Da = \frac{KL}{U_o}$. Parameter K can also be expressed in terms of an effective mass transfer coefficient, h_{eff} , such that $K = h_{eff} a_{Vi}$, where a_{Vi} is the source surface area per total volume. This leads to an effective Sherwood number, $Sh_{eff} \equiv \frac{h_{eff}}{a_{Vi} D_{eff}}$. Note that here we used the source

size for characteristic length scale. For example, Quintard and Whitaker (1994) have used an analogous definition in their study of mass transfer. This coefficient is *not* equal to the Sherwood number, Sh_{avg} defined previously, although the two can be related as shown below.

We will use the results of the simulation of the full problem, as well as the asymptotic dependence of Sh_{avg} discussed previously, to relate Da and Sh_{eff} to Pe_L and the other parameters of the problem. This step is important for comparison against experimental correlations. To do so we will use equation (4.58), substitute numerical or asymptotic results for Sh_{avg} from the full problem and an expression for the effluent concentration, $C_{D,e} = C_D(x_D = 1)$, by solving (4.59)-(4.61). The solution of this problem can be obtained analytically. The effluent concentration is readily found to be

$$C_{D,e} = 1 - \frac{2m \exp\left(\frac{Pe_L}{2}\right)}{(1 + m^2) \sinh\left(\frac{mPe_L}{2}\right) + 2m \cosh\left(\frac{mPe_L}{2}\right)} \quad (4.62)$$

where $m = \sqrt{1 + \frac{Da}{Pe_L}}$. Thus, by using (4.58) Da can be determined as a function of Pe_L and other parameters (note though that this does *not* necessarily confirm the validity of (4.1), which as was pointed out above is, in general, empirical). Because the asymptotic behavior of Sh_{avg} with Pe_L is known, we can directly assess the behavior of Da in the respective limits.

For example, in the limit $Pe_L \ll 1$, we obtain from (4.62)

$$C_{D,e} = 1 - \frac{Pe_L}{\Phi \sinh(\Phi)} + O(Pe_L^2) \quad (4.63)$$

where $\Phi \equiv \sqrt{DaPe_L}$ is an equivalent Thiele modulus. In view of the scaling (4.45), equation (4.58) leads to the following leading-order result

$$\frac{1}{\Phi \sinh(\Phi)} = -\frac{1}{\mathcal{A}_e} \int_{\mathcal{A}_e} C_1|_e dA \quad (4.64)$$

where C_1 is evaluated at the effluent end. Equation (4.64) shows that Φ depends only on the geometrical configuration through the solution of the problem for C_1 . Recall that C_1 solves a boundary value problem, controlled by the source geometry only. In the same limit, the effective Sherwood number, Sh_{eff} , approaches also a constant obtained by using its relation with Φ , namely

$$Sh_{eff} = \frac{\Phi^2}{a_{V_i}^2 L^2} \quad (4.65)$$

and substituting the solution for Φ from (4.64). Thus, the small Pe_L behavior of Sh_{eff} is also directly related to the microstructure.

On the other hand, in the limit $Pe_L \gg 1$, equation (4.62) shows that

$$C_{D,e} = \frac{\Phi^2}{Pe_L} + O(Pe_L^{-2}) \quad (4.66)$$

where it was assumed that Φ grows at most as Pe_L^σ , where $\sigma < 1$. Then, use of (4.47) in (4.58) leads to the following result

$$\Phi \sim Pe_L^{\frac{\sigma}{2}} \quad \text{for } \sigma < 1 \quad (4.67)$$

With the use of (4.67) and (4.65), it can be readily shown that Sh_{eff} has the same scaling at large Pe_L as Sh_{avg} (equation (4.47)).

Numerical results for the flow around a percolation cluster are shown in Figure 4.15. Plotted is the effective Sherwood number as a function of Pe_L for various dependences of the local exponent c , corresponding to Figure 4.14. The results appear to agree well with the analytical predictions, namely the approach to a constant at low Pe_L and the asymptote to a power law at large Pe_L . Figures 4.16-4.17 show results corresponding to convective mass transfer from uniformly distributed sources in a cubic array. These results are also similar to those for a percolation cluster and they agree well with the theoretical predictions.

CONCLUSIONS

In this chapter, we developed a theoretical analysis and a corresponding numerical simulation of convective mass transfer from stationary distributed sources in a porous medium. The key assumption made in the analysis is the use of a traditional, effective porous medium description in the pore-space outside of the sources, coupled with a flux condition (rather than a constant concentration condition) at the source interface, to reflect the effect of the local microstructure on the mass transfer rate, as well as the fact that the effective description breaks down in such places. We developed theoretical predictions for the dependence of the overall mass transfer coefficient on the flow velocity and the source geometry. In general, we derived the asymptotics of the problem at both small and large Pe_L . We expect that the asymptotics at low Pe_L should be particularly useful to macroscopic simulations. It was shown that the large Pe_L behavior reflects the local mass transfer exponent c , thus offering an interpretation on the various experimental correlations. Particular emphasis was placed on mass transfer from a self-similar surface, such as a Koch curve or a percolation cluster. A scaling theory was proposed for these surfaces but not proved. Additional work is needed in this direction. Finally, we established a connection between the empirical equation (4.1) and the microstructure of the problem, and used pore-network simulation to compute the effective parameters. This methodology should be useful for macroscopic simulation.

REFERENCES

1. Alkire, R. and Deligianni, H., The role of mass transport in electrochemical pattern etching, *J. Electrochem. Soc.: Electrochemical Science and Technology*, Vol. 135, No. 5, 1093-1100 (1988).
2. Alkire, R., Deligianni, H. and Ju, J.-B., Effect of fluid flow on convective transport in small cavities, *J. Electrochem. Soc.*, vol.137, No.3, 818-824 (1990).
3. Augustijn, D.C.M., Jessup, R.E., Rao, P.S.C. and Wood, A.L., Remediation of contaminated soils by solvent flushing, *J. Envir. Engin.*, Vol. 120, 42-57 (1994).
4. Bakke, S. and Oren, P.-E., 3-D pore-scale modeling of sandstones and flow simulations in the pore network, *SPEJ*, Vol. 2, No. 2, 136-149 (1997).
5. Browning, F.H. and Fogler, H.S., Fundamental study of the dissolution of calcium phosphonates from porous media, *AIChEJ*, Vol. 42, No. 10, 2883-2896 (1996).
6. Cates, M.E. and Witten, T.A., *Phys. Rev. A.*, Vol.35, 1809 (1987).
7. Cussler, E.L., "Diffusion: Mass transfer in fluid systems", Cambridge University Press (1984).
8. Dullien, F.A.L., "Fluid transport and pore structure", Academic Press, New York (1992).

9. Feder, J., "Fractals", Plenum, New York (1988).
10. Friedlander, S.K., Mass and heat transfer to single sphere and cylinders at low Reynolds numbers, *AIChEJ*, vol. 3, No. 1, 43-48 (1957).
11. Geller, J. T. and Hunt, J.R., Mass transfer from nonaqueous phase organic liquids in water-saturated porous media, *Water Resour. Res.*, Vol. 29, 833-845 (1993).
12. Gouyeau, B., Songbe, J.-P. and Gobin, D., Numerical study of double-diffusive natural convection in a porous cavity using the Darcy-Brinkman formulation, *Int. J. Heat Mass Transfer*, Vol. 39, No. 7, 1363-1378 (1996).
13. Guarnaccia, J.F., Imhoff, P.T., Missildine, B.C., Oostrom, M., Celia, M.A., Dane, J.G., Jaffe, P.R. and Pinder, G.F., Multiphase chemical transport in porous media, Environmental Protect Agency report, contract EPA/600/5-92/002, Kerr Environ. Res. Lab., Ada, Okla. (1992).
14. Imhoff, P.T., Jaffe, P.R. and Pinder, G.F., An experimental study of complete dissolution of a nonaqueous phase liquid in saturated porous media, *Water Resour. Res.*, Vol. 30, 307-320 (1993).
15. Katz, A.J. and Thompson, A.H., Quantitative prediction of permeability in porous rock, *Phys. Rev. B*, Vol. 34, 8179-8181 (1986).
16. Koch, D.L. and Brady, J.F., A non-local description of advection-diffusion with application to dispersion in porous media, *J. Fluid Mech.* Vol. 180, 387-403 (1987).
17. Lamb, H., "Hydrodynamics", Dover, New York (1945).
18. Levich, V.G., "Physicochemical Hydrodynamics," Prentice-Hall, Englewood Cliffs, NJ (1962).
19. Li, X. and Yortsos, Y.C., Visualization and simulation of bubble growth in pore networks, *AIChE J.*, Vol. 41, 214-223 (1995).
20. Mandelbrot, B., "The fractal geometry of nature", Freeman, San Francisco (1983).
21. Mauri, R., Dispersion, convection and reaction in porous media, *Phys. Fluids A*, Vol. 3, No. 5, 743-756 (1991).
22. Miller, C. T., Poirier-McNeill, M.M. and Mayer, A.S., Dissolution of trapped nonaqueous phase liquids: Mass transfer characteristics, *Water Resour. Res.*, Vol. 26, 2783-2796 (1990).
23. Nowicki, S.C., Davis, H.T. and Scriven, L.E., Microscopic determination of transport parameters in drying porous media, *Drying Technology*, Vol. 10, 925-946 (1992).
24. Occhialini, J.M. and Higdon, J.J.L., Convective mass transport from rectangular cavities in viscous flow, *J. Electrochem. Soc.*, vol. 139, No. 10, 2845-2855 (1992).
25. Parker, J.C., Katyal, A.K., Kaluarachchi, J.J., Lenhard, R.J., Johnson, T.J., Jayaraman, K., Unlu, K. and Zhu, J.L., Modeling multiphase organic chemical transport in soils and ground water, Rep. EPA/600/2-91/042, U.S. Environ. Protect. Agency, Washington, D. C. (1991).
26. Pfeffer, R. and Happel, J., An analytical study of mass and heat transfer in multiparticle systems at low Reynolds numbers, *AIChEJ*, vol. 10, No. 5, 605-611 (1964).

27. Powers, S.E., Abriola, L.M. and Weber, W.J., Jr., An experimental investigation of nonaqueous phase liquid dissolution in saturated subsurface systems: Steady state mass transfer rates, *Water Resour. Res.*, Vol. 28, 2691-2705 (1992).
28. Powers, S.E., Abriola, L.M. and Weber, W.J., Jr., An experimental investigation of nonaqueous phase liquid dissolution in saturated subsurface systems: Transient mass transfer rates, *Water Resour. Res.*, Vol. 30, 321-332, Feb. (1994).
29. Prat, M., Percolation model of drying under isothermal conditions in porous media, *Int. J. Multiphase Flow*, Vol. 19, 691-704 (1993).
30. Quintard, M. and Whitaker, S., Convection, dispersion, and interfacial transport of contaminants: Homogeneous porous media, *Advances in Water Resources*, Vol. 17, 221-239 (1994).
31. Rothman, D. and Zaleski, S., "Lattice gas automata", Cambridge University Press (1997).
32. Satik, C., Li, X. and Yortsos, Y.C., Scaling of single-bubble growth in a porous medium, *Phys. Rev. E*, Vol. 51, 3286-3295 (1995).
33. Satik, C. and Yortsos, Y.C., A pore-network study of bubble growth in porous media driven by heat transfer, *J. Heat Transfer*, Vol. 118, 455-462 (1996).
34. Stauffer, D., and Aharony, A., "Introduction to Percolation Theory", Taylor and Francis, London (1992).
35. Tio, K.K. and Sadhal, S.S., Boundary conditions for Stokes flows near a porous membrane, *Applied Sci. Res.*, Vol. 52, 1 (1994).
36. Vafai, K. and Thiyagaraja, R., Analysis of flow and heat transfer at the interface region of a porous medium, *Int. J. Heat Mass Transfer*, Vol. 30, No. 7, 1391-1405 (1987).
37. Wakao, N. and Kaguei, S., Heat and mass transfer in packed beds, Gordon and Breach Science, New York (1982).
38. Wilkinson, D., and Willemsen, J.F., Invasion percolation: A new form of percolation theory, *J. Phys. A*, Vol. 16, 3365-3376 (1983).

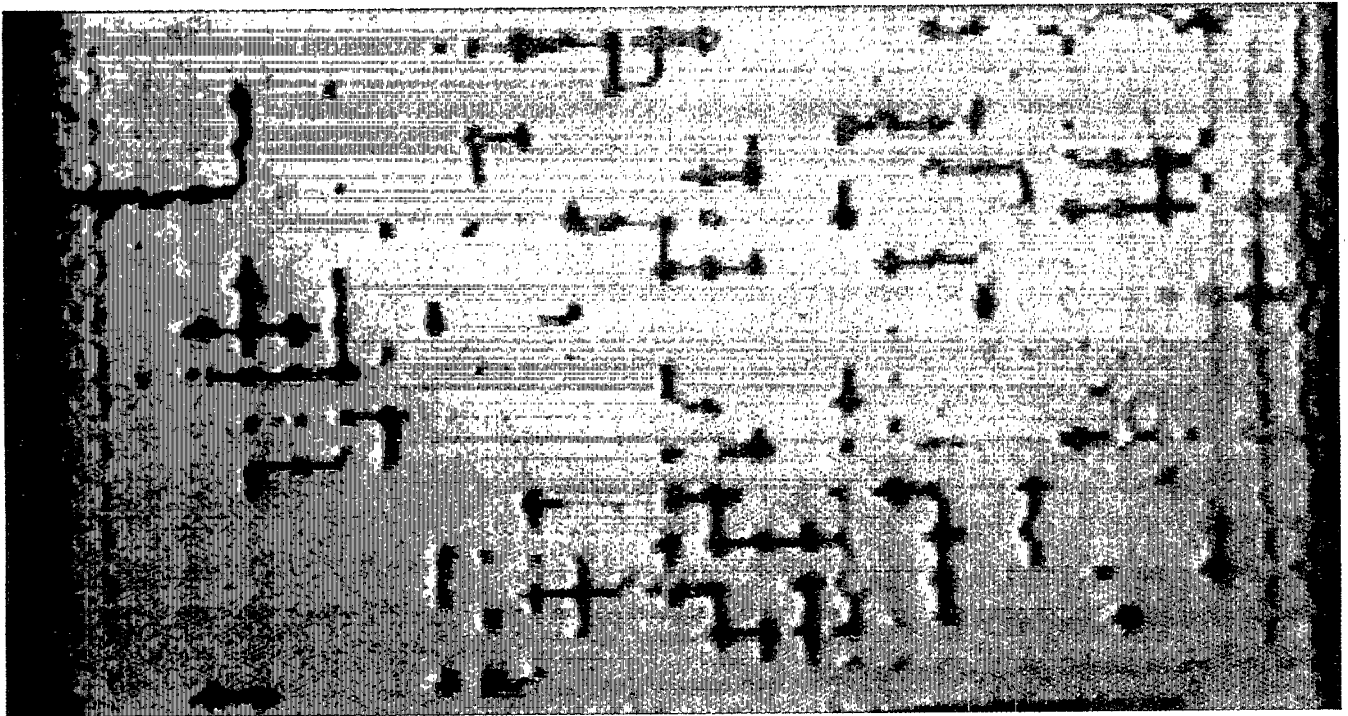


Figure 4.1. Photograph showing the steady-state NAPL distribution in the glass micromodel for typical experimental conditions (from Jia et al., 1997)

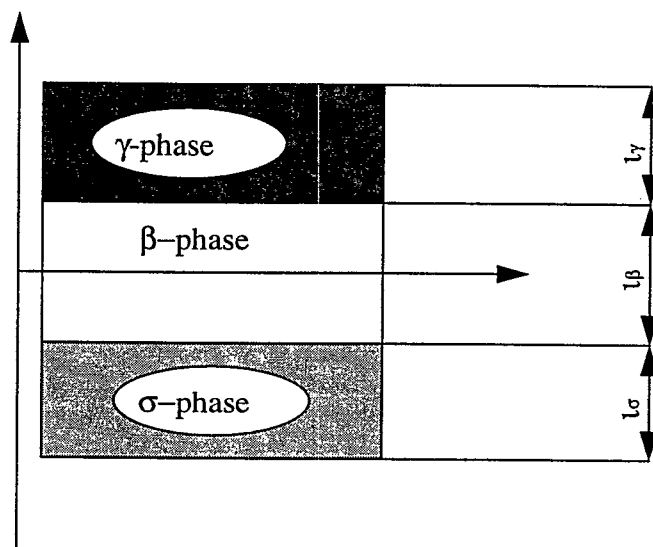


Figure 4.2. Schematic of the unit cell used by Quintard and Whitaker (1994).

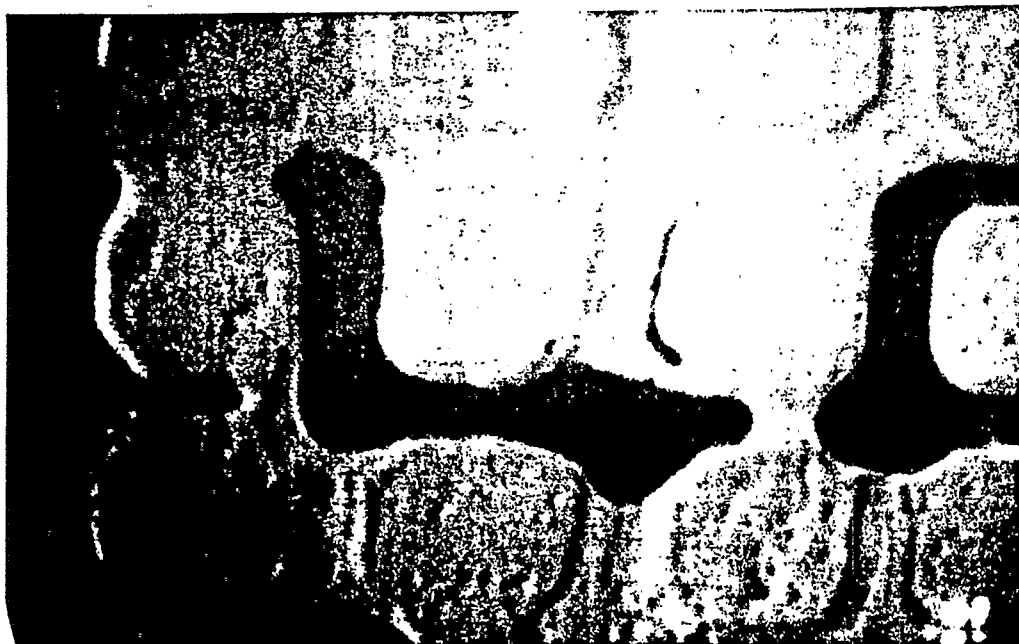


Figure 4.3. Typical NAPL interface configurations in the porespace of the micromodel. Note the cavity-like characteristics (from Jia et al., 1997).

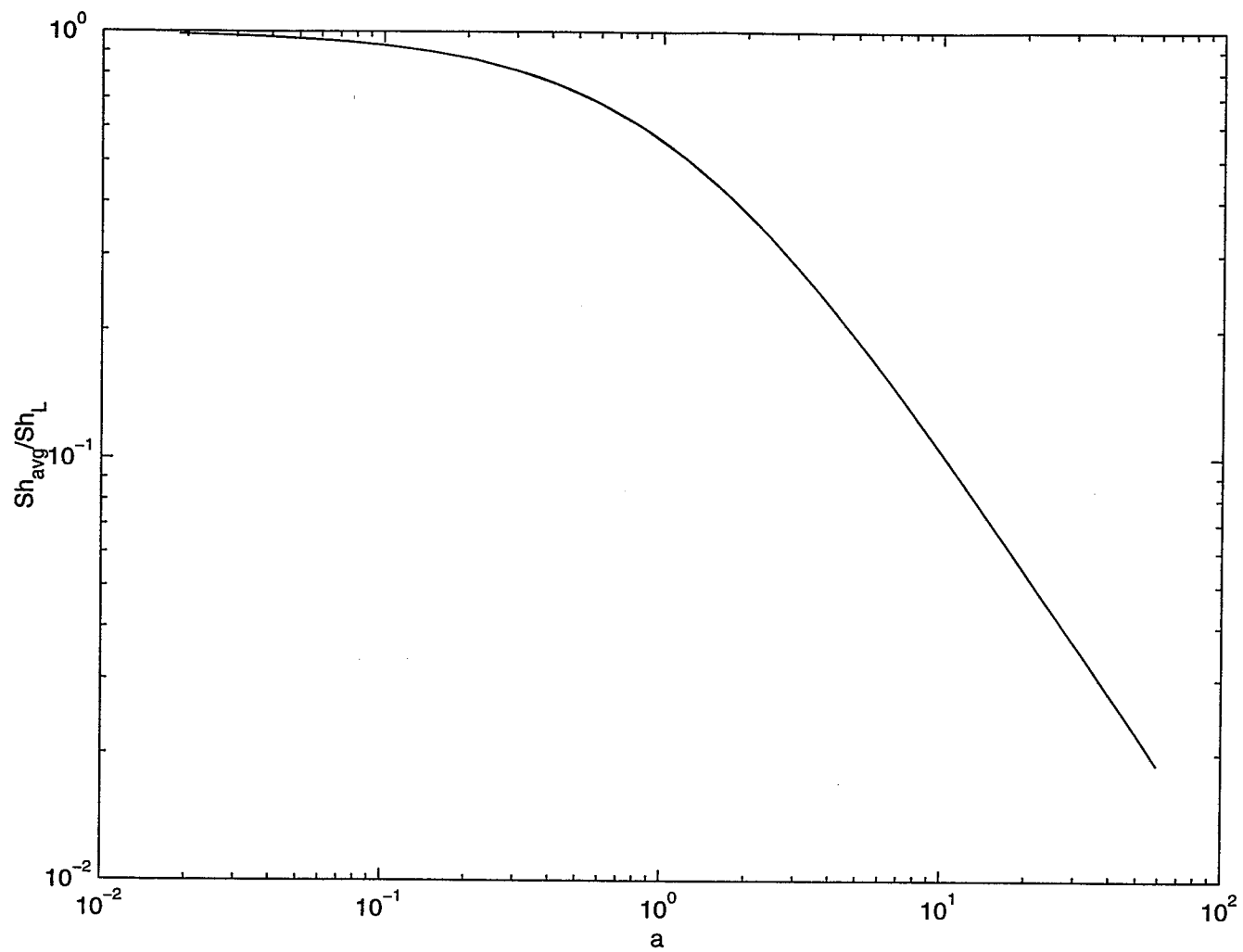


Figure 4.4. The normalized Sherwood number as a function of parameter a .

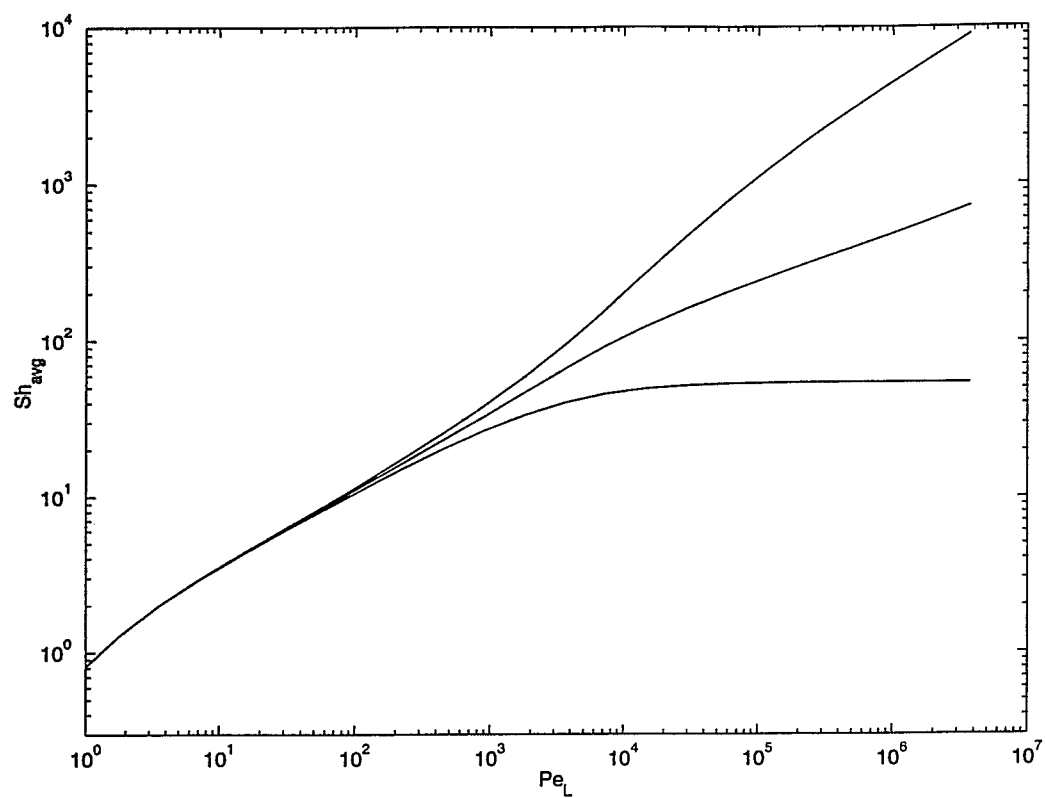


Figure 4.5. Numerical results of Sh_{avg} vs Pe_L for mass transfer over a flat plate and for three local exponents ($c = 0$, $c = 1/3$ and $c = 1/2$, from bottom to top, respectively).

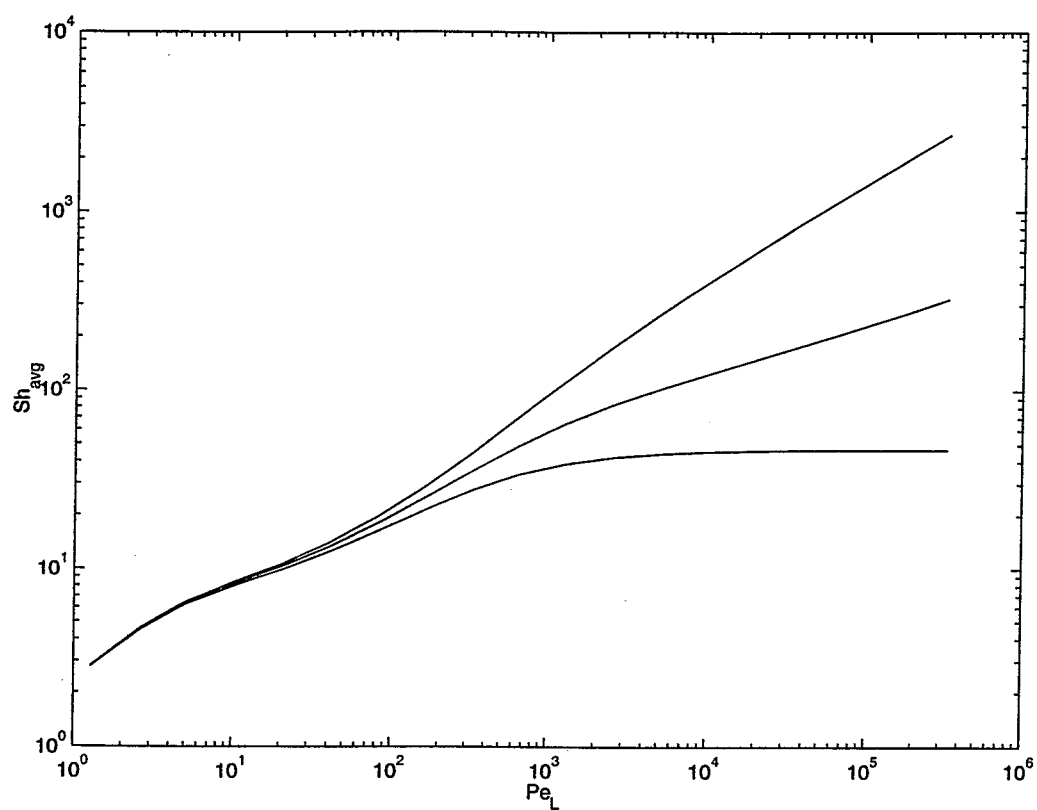


Figure 4.6. Numerical results of Sh_{avg} vs Pe_L for mass transfer over a sphere and for three local exponents ($c = 0$, $c = 1/3$ and $c = 1/2$, from bottom to top, respectively).

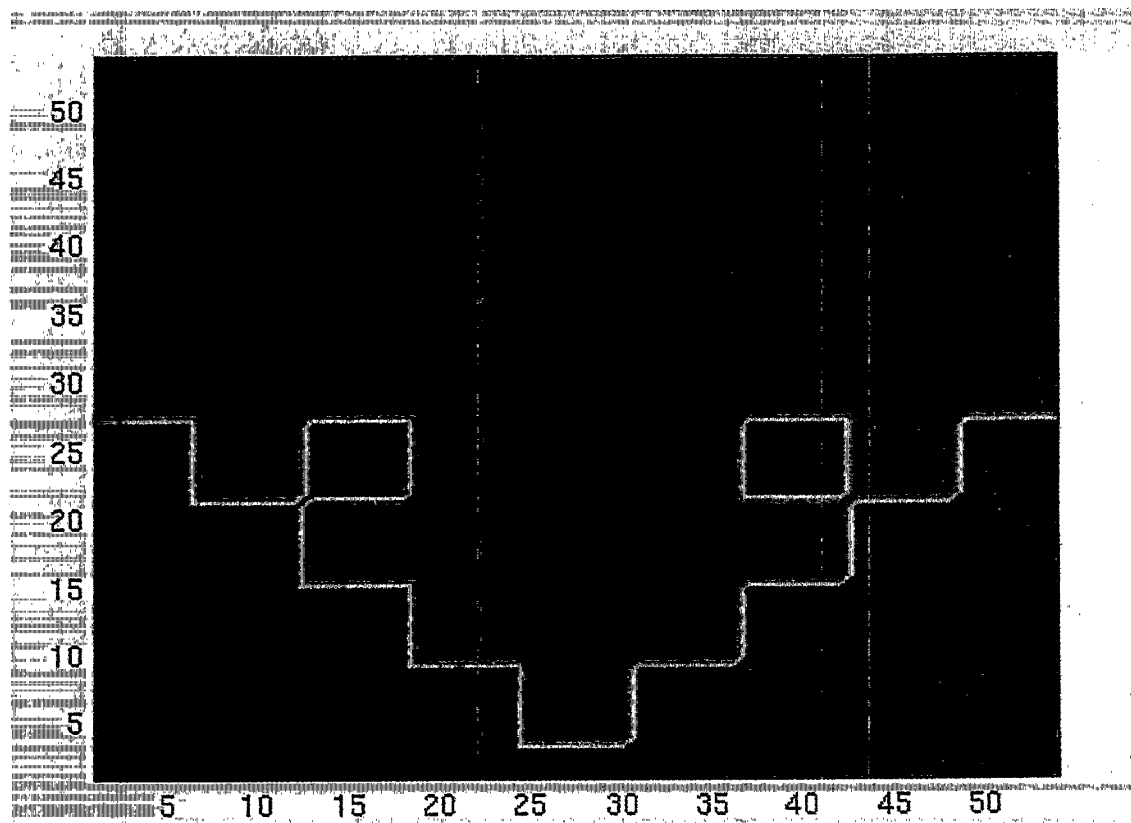


Figure 4.7. A Koch curve of 3 generations used for the simulation of mass transfer over a self-similar surface.

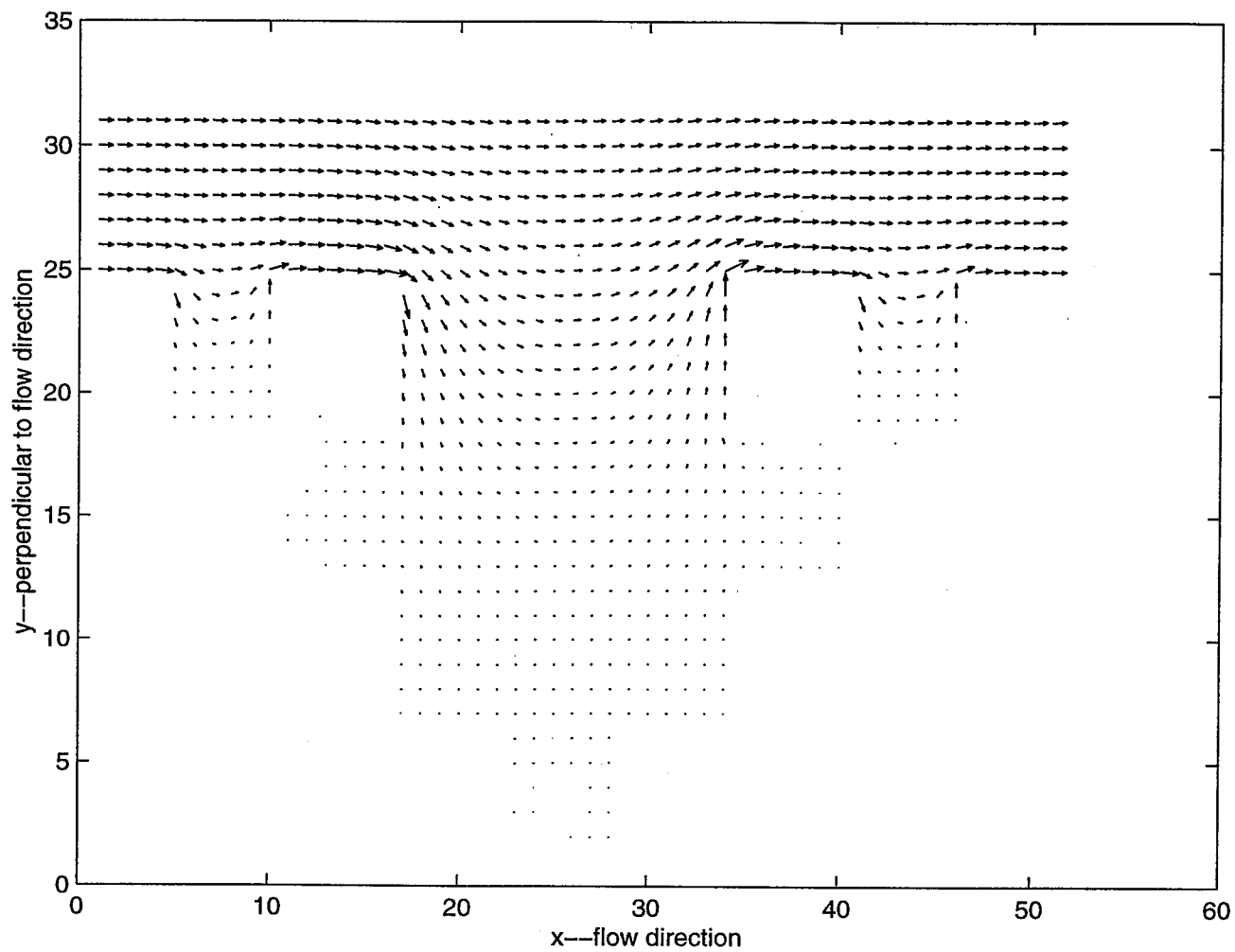


Figure 4.8. Velocity profile for flow over the Koch curve of Figure 4.7.

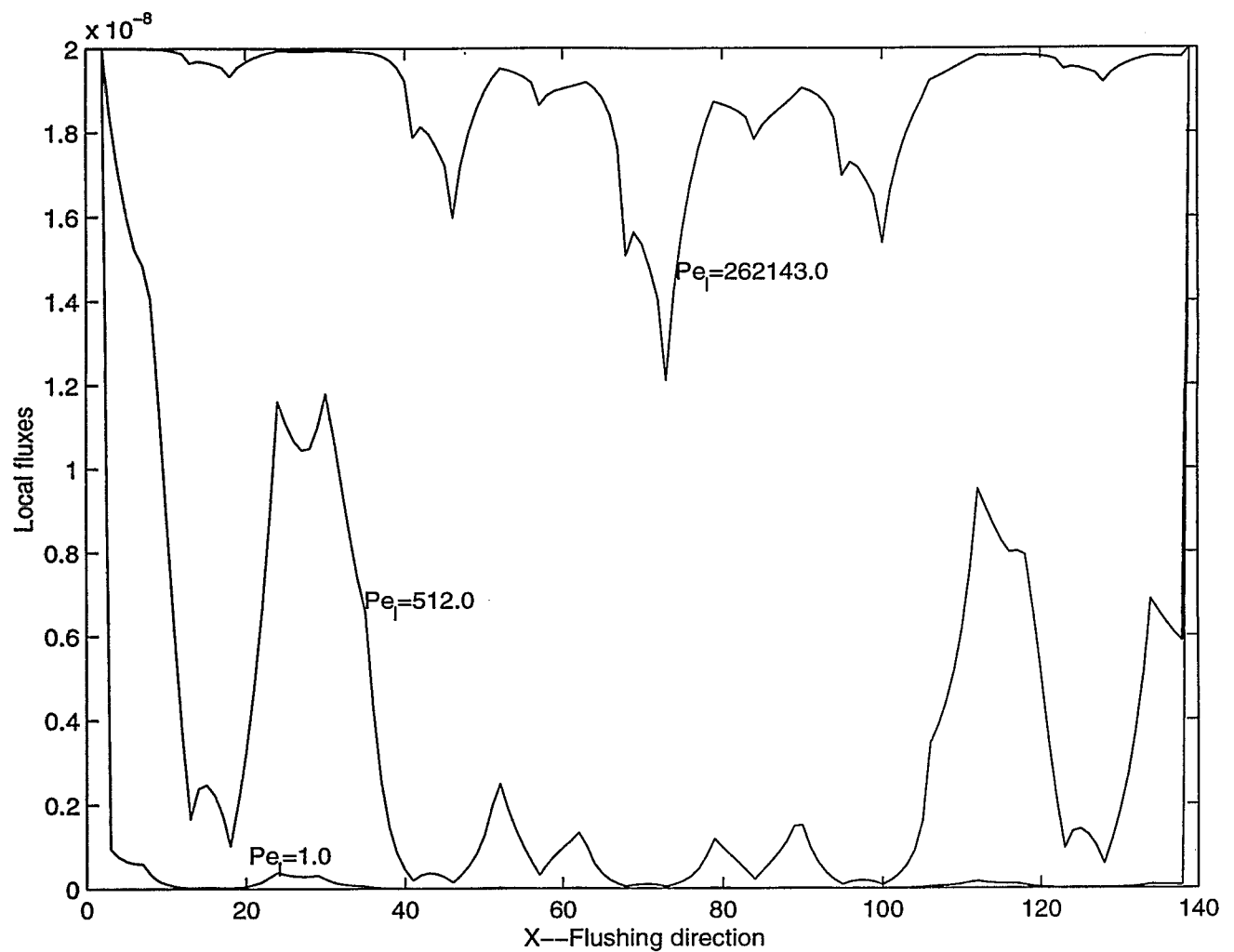


Figure 4.9. The local mass flux profile over the perimeter of the Koch curve of Figure 4.7 for various values of the Peclet number.

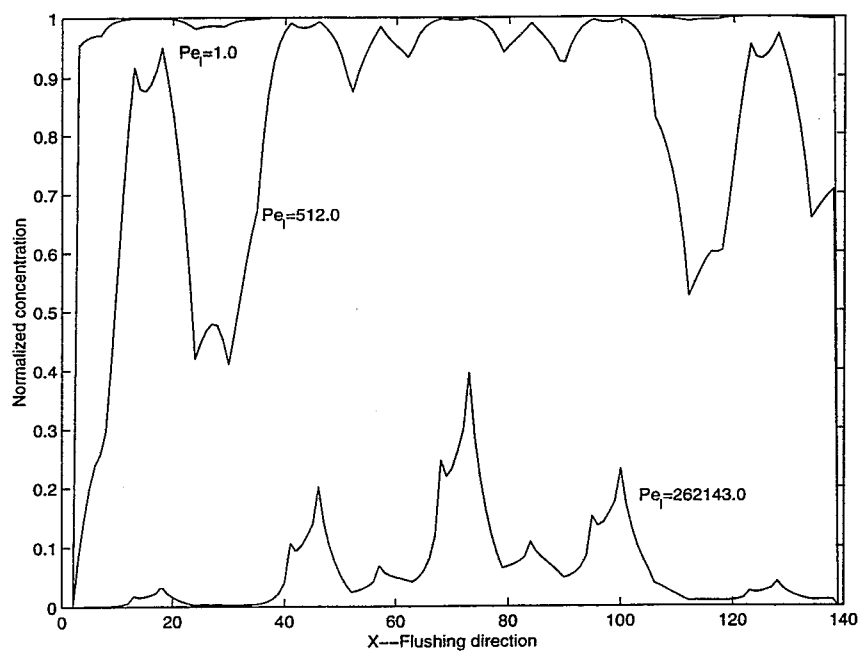
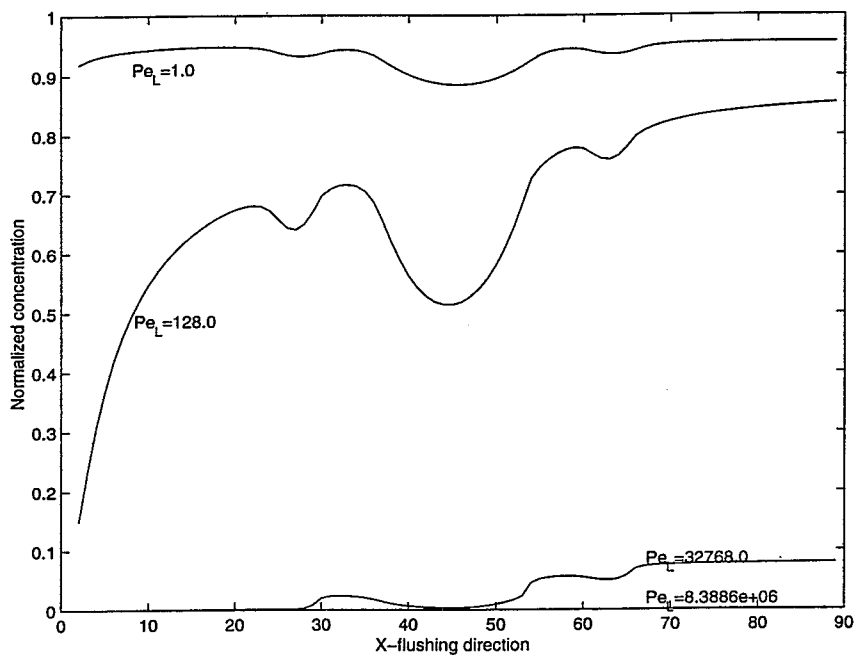


Figure 4.10. The local concentration profile over (a) the streamwise coordinate, (b) the perimeter of the Koch curve of Figure 4.7, for various values of the Peclet number.

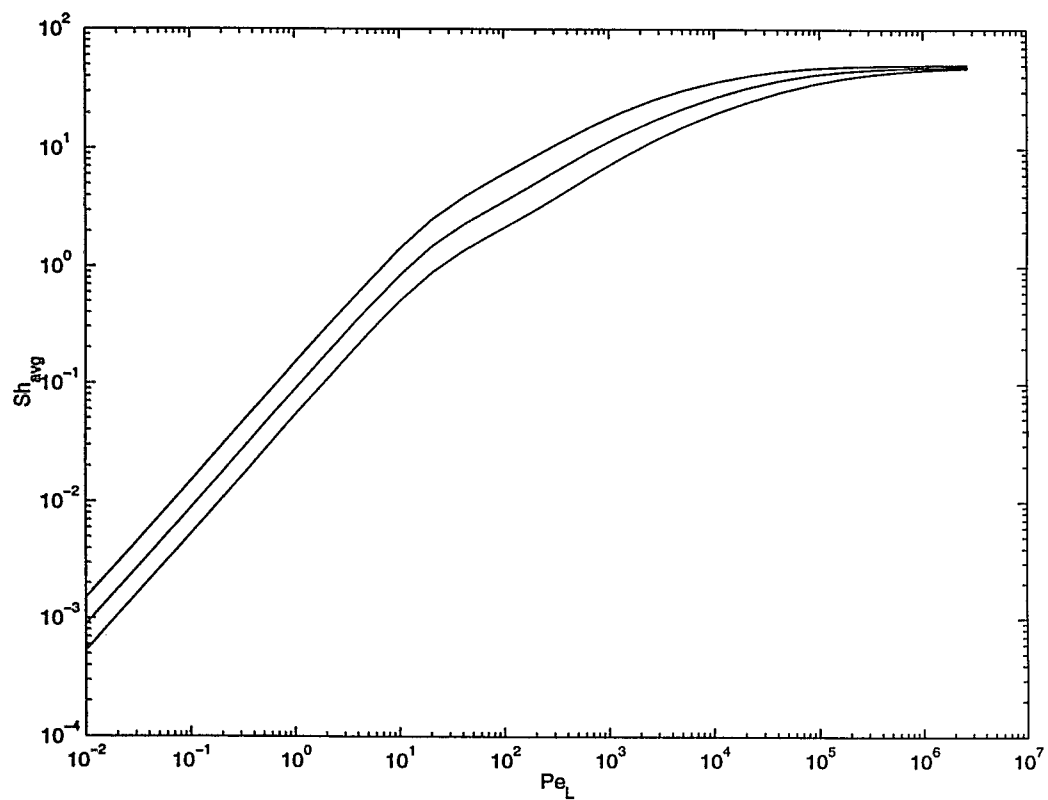


Figure 4.11. Numerical results of Sh_{avg} vs Pe_L for mass transfer over the Koch curve of Figure 4.7 for three different generations and for $c = 0$.

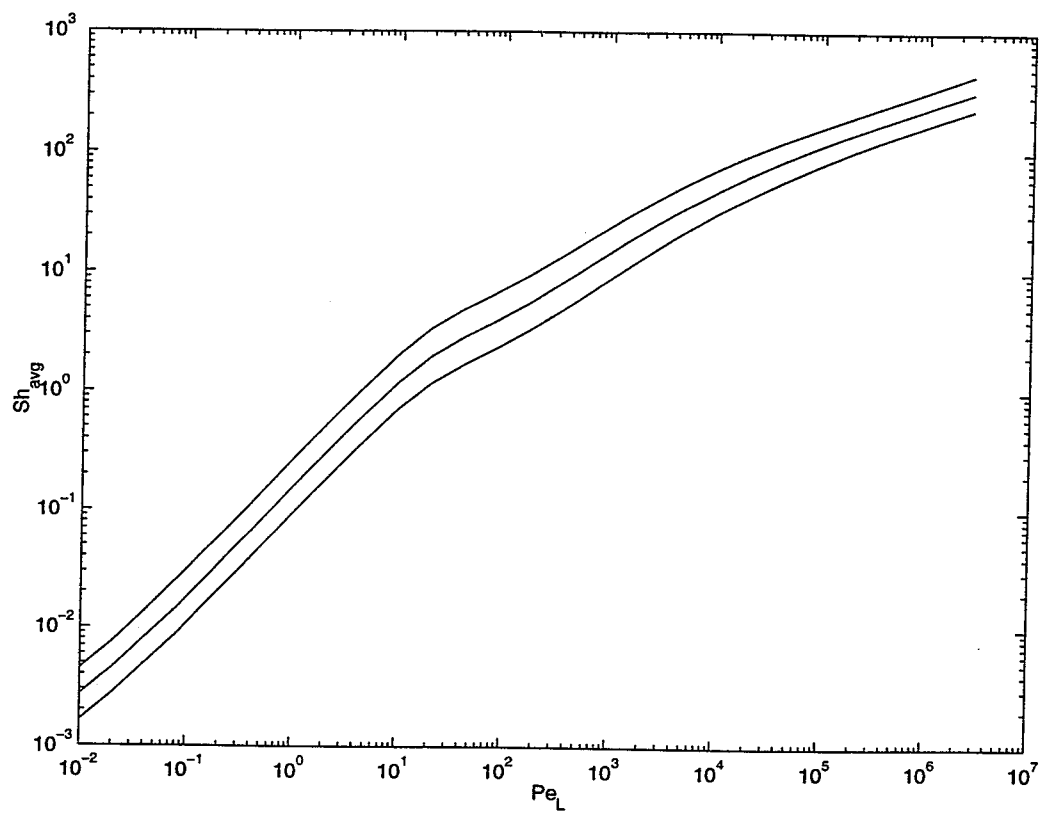


Figure 4.12. Numerical results of Sh_{avg} vs Pe_L for mass transfer over the Koch curve of Figure 4.7 for three different generations and for $c = 1/3$.

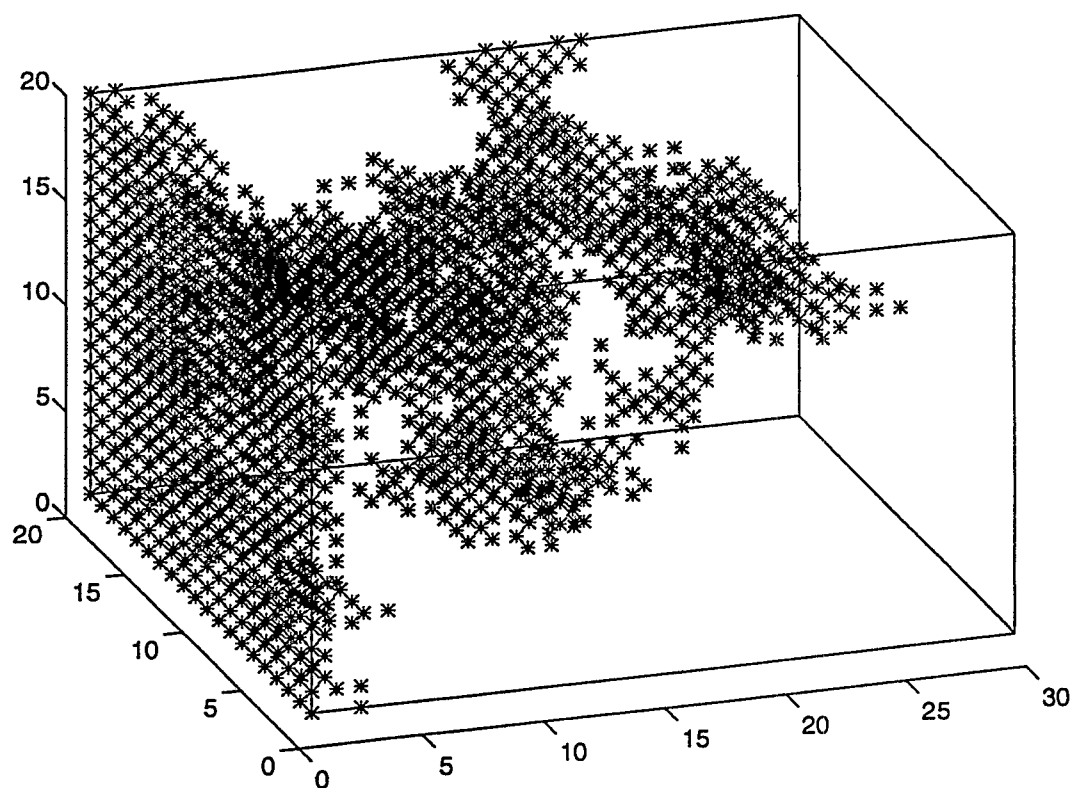


Figure 4.13. Invasion percolation cluster used for the simulation of flow over a source with percolation characteristics.

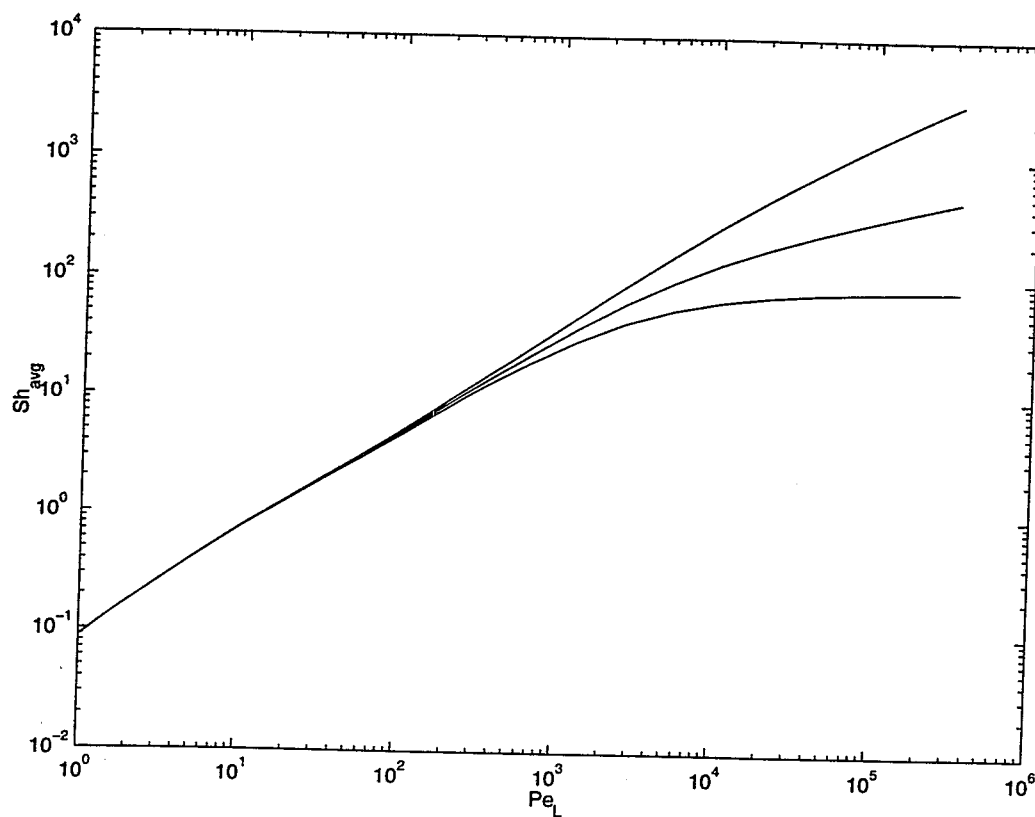


Figure 4.14. Numerical results of Sh_{avg} vs Pe_L for mass transfer over the percolation cluster of Figure 4.13 and for three local exponents ($c = 0$, $c = 1/3$ and $c = 1/2$, from bottom to top, respectively).

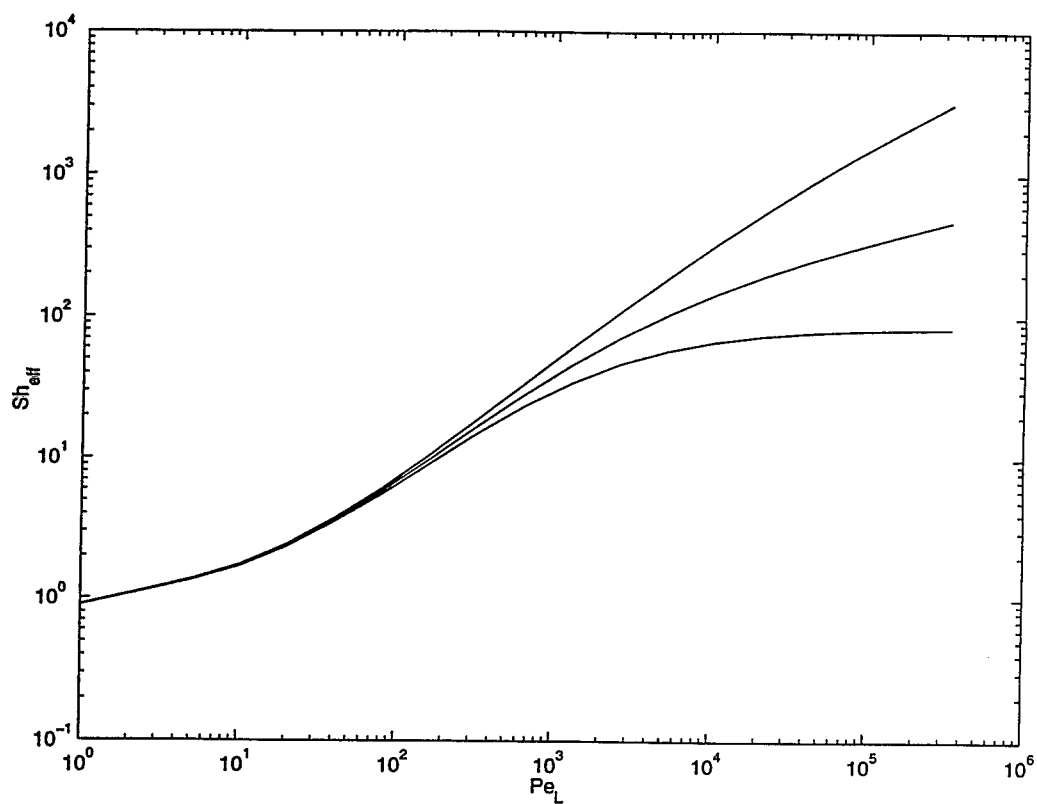


Figure 4.15. Numerical results of Sh_{eff} vs Pe_L for mass transfer over the percolation cluster of Figure 4.13 and for three local exponents ($c = 0$, $c = 1/3$ and $c = 1/2$, from bottom to top, respectively).

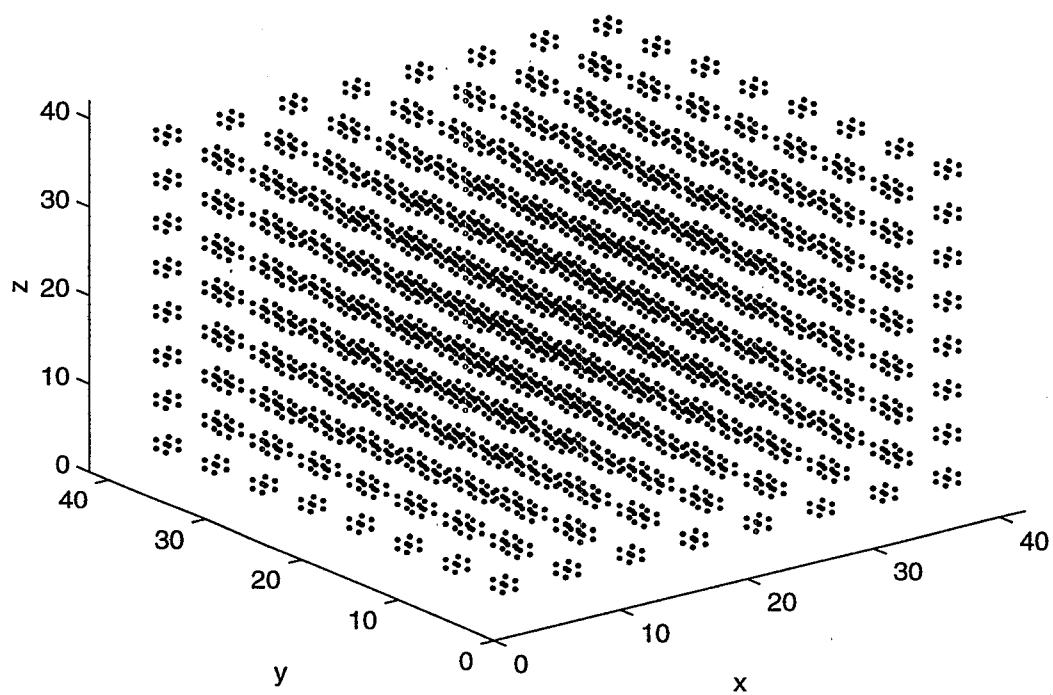


Figure 4.16. Uniformly-distributed sources to simulate flow over a distributed source.

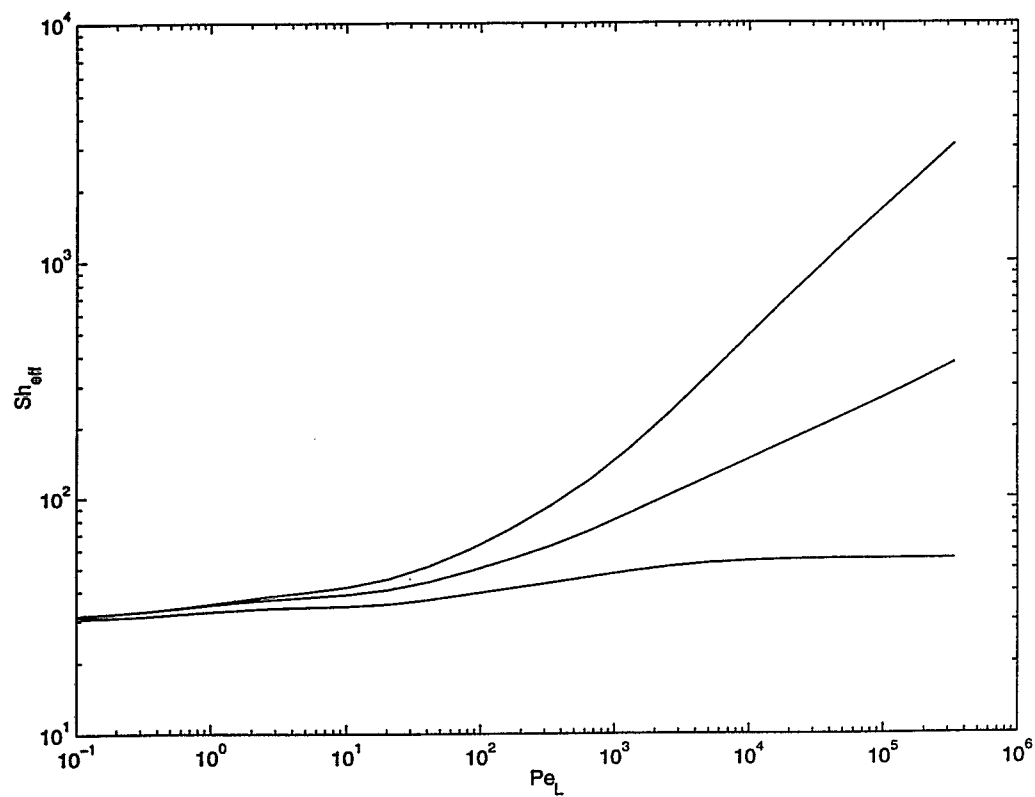


Figure 4.17. Numerical results of Sh_{eff} vs Pe_L for mass transfer over a uniformly-distributed source and for three local exponents ($c = 0$, $c = 1/3$ and $c = 1/2$, from bottom to top, respectively).

Chapter 5

PORE-SCALE INSTABILITIES DURING SOLVENT INJECTION

Maryam Shariati, Kathy Shing and Yanis C. Yortsos

INTRODUCTION

Solvent injection is a currently studied remediation method. It involves the injection of a mixed solvent (frequently a mixture of alcohols) at a site contaminated with organic chemicals (Wood et al., 1990). Typically, in situ solvent injection consists of the following steps: (1) The solvent mixture is injected upstream of the contaminated zone; (2) the solvent with the dissolved contaminants is extracted downstream and treated above ground to recover the solvent and (3) the recovered solvent may be re-injected (Wood et al., 1990). Compared to pump and treat method, the extraction rate of contaminants is enhanced because the addition of remediation fluids leads to an increase in solubility of the nonpolar organic contaminants (Pinal et al., 1990, Wood et al., 1990).

Addition of alcohols alters the physical properties such as viscosity and density of the fluid phase. Other physicochemical effects can occur when the remediation fluid comes into contact with NAPL. For example, as NAPL dissolves in the injected fluid, some alcohol(s) from the remediation fluid may also preferentially dissolve into the NAPL causing swelling. Such changes in the properties of the contacting phases can have profound effects on the effectiveness of remediation treatment. Development of solvent injection processes and the proper selection of remedial fluids to clean up particular organic pollutants are complex tasks. Their success depends to a large extent on our ability to understand (1) the development of miscibility at various scales, (2) the prediction of migration of liquid, vapor, and dissolved organics and (3) the mass transfer and thermodynamic partitioning of these compounds.

It is a well-accepted fact that addition of co-solvents such as alcohols has a significant effect on the aqueous solubility of organic contaminants (Pinal et al., 1990). The solvent phase, in this case, might be quite complex. It may consist of various completely miscible organic solvents, as well as partially miscible organic solvents. The modification of solubility of organic contaminants in the presence of these complex mixtures is frequently referred to as cosolvency. Recent studies by Wood et al. (1990) indicate that with increasing cosolvent content the contaminant elutes at higher concentrations, leading to an improvement in the contaminant removal efficiency. Khodadoust et al. (1994) evaluated the removal of pentachlorophenol (PCP) from contaminated soils using continuous solvent flushing and batch solvent washing. They used two different solvents: acetone and ethanol. It was found that acetone was less effective than ethanol in the removal of PCP. Furthermore, the lowest solvent flow rate removed more PCP, which is believed to be due to longer

hydraulic residence time. Pinal et al. (1990) found that a partially miscible organic solvent (or PMOS) present in a mixed solvent can alter the solubility of a hydrophobic organic chemical (or HOC). In an aqueous environment, PMOSs with strong polar functional groups are most likely to exhibit significant cosolvency effect. Nonpolar PMOSs such as TCE, octanol, toluene and other hydrocarbons on the other hand, are not expected to have appreciable cosolvency. The cosolvency of CMOSs (completely miscible organic solvents) increases with decreasing solvent polarity, whereas the opposite is true for PMOSs.

While the thermodynamic partitioning of contaminants between the solid and fluid phases and the desorption kinetics play key roles in determining the efficiency of extraction (or solubility) based remediation processes, for in situ solvent injection processes, issues such as the mechanisms involved in miscibility, the development of miscibility and microscale flow instabilities are equally important because these impact both the efficiency of delivery of injected solvents to the contaminated sites as well as the surface recovery of the solvents. These issues, however have not received the same level of research interest. Because of the relative lack of understanding of these issues, in this chapter we will examine microscale flow instabilities in mixtures with non-monotonic viscosity-concentration profiles as they are typical of water/alcohol mixtures.

When a solvent system is injected for in situ remediation of NAPL trapped in a porous medium, we must consider the issue of how the injected fluid penetrates the saturated porous medium, either prior to or after contacting the NAPL contaminated regions. The issues of miscible displacement, how miscibility develops and the possibility of microscale instabilities (fingering at the pore scale) naturally arise. These issues are important because the extent of mixing of the injected solvents with water in the saturated medium affects the concentration of the remediation fluid when it comes in contact with the contaminant (often adsorbed on porous medium surfaces or collected in the pores), thus influencing both the thermodynamic partitioning as well as the rate of contaminant transfer into the remediation fluid. The further dilution of the remediation fluid as it flows towards extraction points for collection and treatment prior to recycle also involves miscible displacement and affects the total remediation cost. The development of miscibility and microscale instability depend on a number of factors, including the fluid species present, the geometry of the medium as well as the flow conditions. The system could be either locally fully miscible or it could consist of immiscible and miscible regions depending on the aqueous and NAPL composition and properties of different phases. In case of complete miscibility, a single phase exists, however in case of partial miscibility, two distinct phases may exist. A brief review of previous work on miscible displacement and flow instability is given in the following.

LITERATURE REVIEW

The literature in the study of miscible displacements in porous media can be classified into two categories: Studies dealing with porous media, or Hele-Shaw cells, and studies in single-pore geometries, such as the gap of a Hele-Shaw cell or a capillary. These are reviewed separately below. Comprehensive reviews of viscous fingering can be found in Saffman (1986) and Homsy (1987).

One of the pioneers in the field of miscible displacement was Hill (1952). He studied viscous fingering in miscible displacement. Saffman and Taylor (1958) determined experimentally that when a fluid displaces a more viscous fluid in a Hele-Shaw cell, the interface between them is unstable leading to viscous fingering. The properties of a single penetrating finger were determined. Slobod and Thomas (1963) applied an X-ray technique to visualize displacements in a two-dimensional porous slab. They found that the viscous fingering pattern is determined by the mobility ratio and the velocity of the displacing fluid. Wooding (1969) studied gravity-driven fingering in a

Hele-Shaw cell, a phenomenon analogous to viscous fingering. His experiments at low velocities showed fingering patterns similar to Slobod and Thomas (1963). At a high inclination angle, tip-splitting phenomena were observed, suggestive of the nonlinear interaction between fingers. Pitts (1980) gave another account of the Saffman-Taylor problem. Kopf-Sill and Homsy (1988) conducted experiments in Hele-Shaw cells to study nonlinear viscous fingering. They observed tip splitting, shielding, and spreading. Bacri et al. (1992) studied viscous fingering flow in a rectilinear, homogeneous, and isotropic porous medium in the presence of gravitational forces. Their experimental work indicated the existence of a crossover between a diffusive and a convective regime.

To interpret the behavior of miscible displacement and viscous fingering, a number of stability analyses have been carried out. Saffman and Taylor (1958) analyzed the shape of a single steady translating finger in immiscible displacement in the limit of zero surface tension. Chouke et al. (1959) developed a basic stability theory and showed that if the displacing fluid is less viscous than the displaced fluid, the unfavorable mobility profile will lead to the well-known fingering instability. This causes the displacing fluid to channel through the displaced zone, thereby reducing the efficiency of the displacement process. Hickernell and Yortsos (1986) studied displacement processes in the absence of dispersion and showed that mobility profiles with any segment of decreasing mobility are unstable in the linear regime. Tan and Homsy (1986) analyzed the linear stability of miscible displacements in the presence of dispersion. They computed initial growth rates and wavelengths of the fingers and reported good agreement between their analysis and previous experimental work (Slobod and Thomas, 1963). Tanveer (1987) performed an analytic theory of the Saffman-Taylor finger in the limit of zero surface tension and showed why a finger with half-spacing is the finger selected. Chikhliwala and Yortsos (1988) presented linear and nonlinear stability analysis results for immiscible displacement. Yortsos and Zeybek (1988) analyzed the effect of velocity-dependent anisotropic dispersion on the stability of miscible displacements. They identified a short wave instability for short times and steep concentration profiles, the properties of which depended on the displacement velocity, the mobility ratio, and the velocity-dependent dispersion.

A number of simulation studies have been conducted to predict the behavior of miscible displacement in porous media. Tryggvason and Aref (1983) simulated the interactions between fingers in immiscible displacement in a Hele-Shaw cell. Tan and Homsy (1988) studied the nonlinear behavior of viscous fingering in miscible displacements. They concluded that the spreading and shielding effects are caused by a spanwise secondary instability, and are aided by the transverse dispersion. Zimmerman and Homsy (1991) examined the effect of anisotropic dispersion on nonlinear viscous fingering in miscible displacements. Their simulations for a Hele-Shaw cell produced shielding, spreading, tip splitting, and pairing of viscous fingers. Tchelepi et al. (1993) analyzed stable and unstable displacements experimentally and performed simulations of these displacements. Rogerson and Meiburg (1993) simulated the nonlinear evolution of the interface between two miscible fluids of different densities and viscosities. Finally, Manickam and Homsy (1995) studied fingering instabilities in vertical miscible displacement flows in porous media driven both by viscosity and density contrasts.

The study of displacements at the pore-scale is restricted to flows in the gap of a Hele-Shaw cell or in a cylindrical tube. Reinelt and Saffman (1985) studied theoretically immiscible displacements in the gap of a Hele-Shaw cell in the presence of capillary forces. Paterson (1985) carried out miscible experiments in Hele-Shaw cells. Joseph (1990) performed experiments in which a drop of one fluid moved through another fluid that was miscible in all proportions. Petitjeans and Maxworthy (1996) carried out experiments in a capillary tube using miscible fluids of different viscosities, while Chen and Meiburg (1996) simulated these experiments. Rakotomalala et al. (1996) simulated miscible displacement in the gap of a Hele-Shaw cell using a two-dimensional

BGK lattice gas method. They solved the full Navier-Stokes equation coupled with the convective-diffusive equation. Their findings are similar to those of Yang and Yortsos (1997). The latter authors performed an asymptotic analysis of miscible displacement in the limits of large aspect ratio under conditions of Stokes flow and identified the characteristics of displacement in the gap of a Hele-Shaw cell or a single capillary. Finally, Lajeunesse et al. (1997) conducted experimental work on the downward miscible displacement of a fluid by a lighter and less viscous one in the gap of a Hele-Shaw cell. Their findings were interpreted successfully using the theory of Yang and Yortsos (1997).

In the analysis of miscible displacements, a key difficulty is that the fluid viscosity is a function of concentration, which varies as miscibility develops. As a result, the flow field cannot be decoupled from concentration. In the context of soil remediation, a further complication may arise because several mixtures involved in in-situ solvent injection (1-propanol-water, 2-propanol-water, and methanol-water, for example), have non-monotonic viscosity concentration profiles. Therefore, as miscibility develops, locally varying viscosity results in locally varying mobility ratios which may change from favorable to unfavorable, thus greatly complicating the issue of flow instability. This brings to the forefront, the issue of *non-monotonic* viscosity profiles. So far, the effect of nonmonotonicity of viscosity profiles on the dynamics of transport has been largely unexplored. It is postulated that non-monotonic profiles create the potential for propagation of nonlinear fingers (Manickam and Homsy, 1993). These authors provided the only published work so far on non-monotonic viscosity profile in miscible displacements using Darcy's law. However, for miscible displacements at the pore scale, Darcy's law does not apply. At this scale, no experimental or theoretical work on fluids with non-monotonic viscosity profiles has been conducted at the pore-scale. In addition, viscous fingering experiments involving non-monotonic profiles have also not been reported.

In view of their importance on microscale instabilities, and the relative scarcity in fundamental studies of miscible displacements, we consider in this chapter miscible displacements in systems with non-monotonic viscosity-concentration profiles, which are of interest in alcohol-based solvent injection remediation processes.

First, we consider the application of the methodology of Yang and Yortsos (1997) to develop solutions of Stokes' flow in the gap of Hele-Shaw cell for non-monotonic viscosity profiles. This configuration is a limiting case of the more general problem of miscible displacement in a pore network, which will be explored in a subsequent study. As Yang and Yortsos (1997) have shown, this problem is also qualitatively similar to displacement in a capillary. By taking advantage of the large aspect ratio, we develop a simple asymptotic analysis of miscible displacement. We show that the leading-order term in an expansion with respect to the inverse aspect ratio satisfies a single integro-differential equation for the concentration profile in the gap or in a capillary, the passive case limit of which yields the Taylor-Aris problem. The equation obtained is numerically solved to give concentration profiles at various mobility ratios, α , non-monotonicity features and for different values of the Peclet number and the viscosity ratio. The results are used to delineate the conditions for which transverse averaging and the conventional *CDE* formalism for the associated Hele-Shaw miscible displacement is valid.

Subsequently, we report on some visualization experiments in Hele-Shaw cells involving non-monotonic viscosity profiles, for example using fluid pairs of water, 2-propanol and glycerol. The preliminary experiments show aspects consistent with the stability analysis of Manickam and Homsy (1993) as well as its simplification reported in the next chapter. Microscale (single-pore) instabilities are also indicated. These can be addressed using the approach of Yang and Yortsos (1997) as outlined below.

MISCIBLE DISPLACEMENT IN THE GAP OF A HELE-SHAW CELL FOR NON-MONOTONIC VISCOSITY

Consider the miscible displacement of fluid 1 by fluid 2 between two parallel plates or in a cylindrical capillary of the geometries shown in Figure 5.1. The two fluids are Newtonian and the injection rate q is sufficiently low for the displacement to be in the Stokes regime. We follow the conventional approach for the description of miscible flow, in which, in the absence of volume of mixing, the velocity is divergence-free and the diffusivity is constant (Manickam and Homsy, 1993). The alternative formalism of Joseph (1992), in which an extended divergence-free velocity is defined, is also applicable. However, we ignore *Korteweg* stresses (Joseph, 1992). For simplicity, we restrict this study to displacements in the absence of gravity. The assumption of constant diffusivity does not change qualitatively the results to be obtained (particularly if it is recalled that we are interested in the high velocity limit, where convection predominates).

Mathematical Formulation

In displacement between parallel plates, we are interested in the concentration profile in the gap ($X - Y$) between the two plates (Figure 5.1a), thus we take the displacement independent of the third coordinate Z . At large aspect ratio, this is the geometry of a Hele-Shaw cell, in which the 2-D planar features of miscible displacements in the $X - Z$ plane have been extensively studied (e.g. see Homsy, 1987, for a review). Of interest to this paper are profiles in the gap, for which little is currently known. Under the previous assumptions, we have

$$\frac{\partial C}{\partial T} + \nabla \cdot (\mathbf{U}C) = D \nabla^2 C \quad (5.1)$$

$$\nabla \cdot \mathbf{U} = 0 \quad (5.2)$$

$$0 = -\nabla P + \nabla \cdot \mathbf{T} \quad (5.3)$$

where C denotes the concentration of the injected fluid, T is time, \mathbf{U} is the two-dimensional velocity vector with components U and V , P is pressure, and the deviatoric stress tensor, \mathbf{T} , is

$$T_{XX} = 2\mu \frac{\partial U}{\partial X} \quad (5.4)$$

$$T_{YY} = 2\mu \frac{\partial V}{\partial Y} \quad (5.5)$$

$$T_{XY} = \mu \left(\frac{\partial V}{\partial X} + \frac{\partial U}{\partial Y} \right) \quad (5.6)$$

The viscosity is assumed to be a function of concentration, $\mu(C)$. Using the following dimensionless notation

$$\begin{aligned} x &= \frac{X}{L}; & y &= \frac{Y}{H}; & u &= \frac{U}{q}; & v &= \frac{V}{q}; & p &= \frac{P}{P^*} \\ c &= \frac{C}{C_2}; & \lambda &= \frac{\mu_2}{\mu}; & \epsilon &= \frac{H}{L}; & P^* &= \frac{q\mu_2 L}{H^2}; & t &= \frac{qT}{L} \end{aligned}$$

where subscripts 1 and 2 denote initial and injected fluid respectively, and λ is a normalized mobility, the system of equations can be rearranged as follows

$$\frac{\partial c}{\partial t} + \frac{\partial(uc)}{\partial x} + \frac{\partial(wc)}{\partial y} = N_{TD} \left(\epsilon^2 \frac{\partial^2 c}{\partial x^2} + \frac{\partial^2 c}{\partial y^2} \right) \quad (5.7)$$

$$\frac{\partial u}{\partial x} + \frac{\partial w}{\partial y} = 0 \quad (5.8)$$

$$-\frac{\partial p}{\partial x} + 2\epsilon^2 \frac{\partial}{\partial x} \left(\lambda^{-1} \frac{\partial u}{\partial x} \right) + \epsilon^2 \frac{\partial}{\partial y} \left(\lambda^{-1} \frac{\partial w}{\partial x} \right) + \frac{\partial}{\partial y} \left(\lambda^{-1} \frac{\partial u}{\partial y} \right) = 0 \quad (5.9)$$

$$-\frac{\partial p}{\partial y} + 2\epsilon^2 \frac{\partial}{\partial y} \left(\lambda^{-1} \frac{\partial w}{\partial y} \right) + \epsilon^4 \frac{\partial}{\partial x} \left(\lambda^{-1} \frac{\partial w}{\partial x} \right) + \epsilon^2 \frac{\partial}{\partial x} \left(\lambda^{-1} \frac{\partial u}{\partial y} \right) = 0 \quad (5.10)$$

In the above, we introduced the rescaled transverse velocity $w = \epsilon^{-1}v$ and defined the modified inverse Peclet number, $N_{TD} = \frac{DL}{qH^2} = (\epsilon Pe)^{-1}$, where $Pe = \frac{qH}{D}$.

Consider next the asymptotic limit $\epsilon \rightarrow 0$, N_{TD} finite, arising at large values of the aspect ratio and large Pe . In the context of flow in porous media, this is known as the *Vertical Flow Equilibrium* approximation, (e.g. see Lake 1989, Yortsos, 1995). We proceed with a formal regular asymptotic expansion in powers of ϵ . At zeroth order, we obtain

$$\frac{\partial c}{\partial t} + \frac{\partial(uc)}{\partial x} + \frac{\partial(wc)}{\partial y} = N_{TD} \left[\epsilon^2 \frac{\partial^2 c}{\partial x^2} + \frac{\partial^2 c}{\partial y^2} \right] \quad (5.11)$$

$$\frac{\partial u}{\partial x} + \frac{\partial w}{\partial y} = 0 \quad (5.12)$$

$$-\frac{\partial p}{\partial x} + \frac{\partial}{\partial y} \left(\lambda^{-1} \frac{\partial u}{\partial y} \right) = 0 \quad (5.13)$$

$$-\frac{\partial p}{\partial y} = 0 \quad (5.14)$$

where all variables denote zeroth-order in the corresponding expansion. Equation (5.14) shows that to first-order, pressure changes only in the direction of the displacement, as in the *lubrication* approximation (Ockendon, 1995). This does not imply absence of *transverse* convective mixing, which, as is apparent in (5.11)-(5.12), is retained to leading order. Direct integration of (5.13) and (5.14), and use of the *no-slip* condition at the walls and the incompressibility constraint $\int_0^1 u dy = 1$, leads to a compact result for the streamwise velocity component

$$u = \frac{G(y; \lambda)}{\int_0^1 G dy} \quad (5.15)$$

where we introduced the function

$$G(y; \lambda) \equiv \int_0^y \lambda dy \int_y^1 \lambda y dy - \int_0^y \lambda y dy \int_y^1 \lambda dy \quad (5.16)$$

the notation $G(y; \lambda)$ implying the functional dependence on the viscosity mixing rule. Equations (5.15)-(5.16) show that in this approximation, the longitudinal velocity is explicitly related to the concentration field. Then, the problem reduces to the solution of a single integro-differential equation (5.11), where u is given by (5.15)-(5.16) and w follows from the continuity equation

$$w = - \int_0^y \frac{\partial u}{\partial x} dy \quad (5.17)$$

Equation (5.17) shows that transverse convective mixing exists in all places where u is x -dependent, namely where fronts are not parallel to the streamwise direction. In the passive tracer limit, $\lambda = 1$, we recover the *Poiseuille* problem, with the velocity profile

$$u = 6y(1 - y) \quad (5.18)$$

Numerical Results

The integro-differential equation was numerically solved using a *Total Variation Diminishing* method with flux limiter, which is a dynamic weighting between lower- and higher- order difference schemes (see Blunt and Rubin, 1992). In this approach, time derivatives are approximated by a first-order implicit scheme and the convective term by

$$\frac{\partial(uC)}{\partial x} = \frac{u_{i+1/2}^n C_{i+1/2}^n - u_{i-1/2}^n C_{i-1/2}^n}{\Delta x} \quad (5.19)$$

where

$$C_{i+1/2}^n = C_i^n + \frac{1}{2}\varphi(r_i)(C_{i+1}^n - C_i^n) \quad (5.20)$$

Van Leer's flux limiter (Yee and Warming, 1985) is used, such that

$$\varphi(r_i) = \max \left\{ 0, \min \left(2, \frac{r_i + |r_i|}{1 + r_i} \right) \right\} \quad (5.21)$$

where the gradient ratio is

$$r_i = \frac{C_i^n - C_{i-1}^n}{C_{i+1}^n - C_i^n} \quad (5.22)$$

This method allows for high accuracy without causing numerical oscillations in regions of high concentration gradients. The diffusion terms were discretized by a standard central difference scheme. The resulting difference equations were solved simultaneously by a standard *LSOR* method.

Simulations for both monotonic and non-monotonic viscosity-concentration profiles were carried out. For mixtures with monotonic viscosity-concentration behavior, the "quarter-power" mixing rule was used (Yang and Yortsos, 1997)

$$\mu = \left(c\mu_2^{-1/4} + (1 - c)\mu_1^{-1/4} \right)^{-4} \quad (5.23)$$

where μ_1 and μ_2 are the viscosity of the resident and injected fluids, respectively. For mixtures with non-monotonic viscosity-concentration profiles, the parametric equation of Manickam and Homsy (1993) was used, namely

$$\mu(c) = \mu_m \sin(\xi) \quad (5.24)$$

$$\xi = \xi_0(1 - \eta) + \xi_1\eta \quad (5.25)$$

$$\eta = \frac{(1 + \alpha)c}{1 + \alpha c} \quad (5.26)$$

$$\xi_0 = \sin^{-1} \left(\frac{\alpha}{\mu_m} \right) \quad (5.27)$$

$$\xi_1 = \pi - \sin^{-1}\left(\frac{1}{\mu_m}\right) \quad (5.28)$$

$$a = \frac{c_m - \eta_m}{\eta_m - 1} \quad (5.29)$$

$$\eta_m = \frac{\pi/2 - \xi_0}{\xi_1 - \xi_0} \quad (5.30)$$

The three parameters α , μ_m , c_m characterize the shape of the viscosity-concentration profile. Parameter α is the ratio of the endpoint viscosities, while μ_m is the maximum value of the viscosity, which occurs at the given concentration c_m . Several sets of simulations were performed to examine the effects of these parameters, as well as the effect of dispersion.

Results

Miscible displacements with monotonic and non-monotonic viscosity profiles, to be referred to subsequently as MN, and NMN, respectively, at various endpoint mobility ratios were simulated. It is known from previous work on MN miscible displacements in porous media, that end-point viscosity ratios corresponding to $\alpha > 1$ are unfavorable, while cases with $\alpha < 1$ are favorable. Unfavorable viscosity contrast leads to instabilities in porous media, as reviewed previously.

In their analysis of miscible displacements in the gap of a Hele-Shaw cell using MN profiles, Yang and Yortsos (1997) reported that depending on the endpoint viscosity ratio, two different types of displacements exist. The displacement pattern in the gap of the Hele-Shaw cell viewed from the side of the cell has the characteristics of a finger developing at the center of symmetry when $\alpha > 3/2$ (Figure 5.2a) whereas the displacement has a parabolic shape with a protruding tip (a bullet-like shape) when $\alpha < 3/2$ (Figure 5.2b) (note that in Figure 5.2, M is used in place of α).

For the case of non-monotonic viscosity concentration behavior considered here, the picture is complicated by the fact that the viscosity increases first to a maximum value and then monotonically decreases. As a result, both (locally) favorable (bullet shape) and unfavorable (finger like) displacement patterns may be expected to exist in the same system. Manickam and Homsy (1993) reported that the NMN displacement in the Darcy flow regime has an unstable region adjacent to a stable one. In the unstable region, the viscosity increases with concentration in the flow direction to its maximum, and it is adjacent to a stable region where the viscosity decreases in the flow direction. They also reported that the viscous fingering instabilities become evident in the unstable region. These findings will be compared to experiments below. However, in the case of flow in the gap (or, equivalently, in single-pore level displacements) examined here, there are no available results.

We first simulated the miscible displacement of a fluid by a less viscous one for Stokes flow for both MN and NMN cases. The concentration profile for the monotonic case with $\alpha = 5$ in the absence of diffusion is shown in Figure 5.3. (It must be noted that the spreading apparent in the concentration profile in these and other similar figures is due to numerical dispersion, even though the physical dispersion is set to zero, $N_{TD} = 0$). Corresponding results for the non-monotonic viscosity profile are shown in Figure 5.4. The displacement patterns in both have the general characteristics of a finger developing at the center of symmetry, which is typical of unfavorable displacements. However, in the NMN case there is a slight protrusion at the tip, which is a characteristic of a favorable displacement ($\alpha < 1.5$, compare with Figure 5.2b). This is consistent with the fact that for the NMN case considered here, the viscosity passes through a maximum so that there is a region near the leading edge of the front where the viscosity is decreasing in

the flow direction resulting in locally favorable displacement. For the MN case in Figure 5.3, the viscosity always increases in the flow direction, so the displacement pattern has a finger like shape typical of unfavorable displacement (as in Figure 5.2a). The MN front also propagates slightly a longer distance than in the NMN case. The reverse would be expected if the NMN case involved a viscosity minimum. In the NMN case, the front spreads further in the y -direction, probably a reflection of the partial "bullet-like" shape of favorable displacement patterns associated with regions of decreasing viscosity. The effects of dispersion are shown in Figures 5.5 and 5.6. As expected, dispersion generally has the effect of broadening the mixing zone and to overshadow the differences in local concentration resulting from the differences in viscosity. Consequently, the protrusion in the NMN tip displacement vanishes as dispersion is enhanced.

Figures 5.7 and 5.8 show concentration profiles for a typical "favorable displacement", in which a fluid displaces another of lower viscosity $\alpha = 0.2$. Figure 5.7 is the MN case while Figure 5.8 shows corresponding results for the NMN case. The displacements have an overall similar pattern but there are some differences in the tip area. The NMN case has a more compact nose which is a characteristic of the unfavorable displacement surfacing as a result of non-monotonicity in the viscosity concentration profiles. The effect of dispersion is shown in Figures 5.9 and 5.10. Again, the broadening of the mixing zone as result of dispersion leads to a reduction in the differences in the tip area between the MN and NMN cases. There is an unusual curvature in the tails of the NMN displacement patterns, which is not present in the monotonic displacement, presumably due to the increased complexity of the flow due to a greater viscosity gradient in the NMN case. More pronounced effects of non-monotonicity are shown in the figures to follow.

Figure 5.11 shows the displacement pattern for the case $\alpha = 1$, with a MN viscosity- concentration profile. This profile matches well the classical Poiseuille flow results, as expected in this case of small dispersion. Figure 5.12 shows for comparison purposes the NMN case, also with $\alpha = 1$ but with a maximum (dimensionless) viscosity of 10, resulting from non-monotonicity. Some unusual features are observed here. As a result of the favorable local mobility ratio in regions where the viscosity is decreasing in the flow direction, the NMN displacement pattern has some of the features of the "bullet-like" shape characteristic of favorable displacement, compared to the MN case. Furthermore, the NMN patterns are nonsymmetric indicating the development of a possible instability. Since both systems have end-point viscosity ratio of unity, this unusual behavior in the NMN case could only be explained in terms of the details of the non-monotonic viscosity- concentration profile where the viscosity first increases to a maximum and then decreases to one again. In the region of increasing viscosity, flow instabilities can arise due to the locally unfavorable viscosity ratios. The instabilities are then propagated through the mixing zone (see for example Figure 5.13 where the displacement patterns at 5 successive time intervals are shown). The growth of the unstable region at the tip is very clear. The effect of dispersion is shown in Figures 5.14 and 5.15, for MN and NMN cases, respectively. As before, dispersion broadens the mixing zone, and the extent of asymmetry in the NM case is diminished. However, there is a clear difference between the two profiles, even in the presence of dispersion, in contrast to the previous problems (Figures 5.5 and 5.6, and 5.9 and 5.10, for example). The NMN profile exhibits an expansion of concentration contours at the tip, and a compression at the sides of the tip, compared to the MN case.

Figures 5.16-5.17 show the effect of varying the maximum viscosity on the NMN displacement patterns. The end-point mobility ratio is kept at unity, but parameter m , which is the maximum viscosity relative to the pure component viscosity, was varied (from 8 to 20). Each set of concentration contours corresponds to a time step. The displacement patterns are essentially the same, although the instability is more pronounced at the largest maximum viscosity (Figure 5.17). Further investigations should be carried out to determine if a threshold limit for this behavior exists. Figures 5.18-5.19 depict concentration profiles for various values of c_m , which is the concentration

at which maximum viscosity occurs. The displacement patterns seem to indicate that instabilities are more pronounced as c_m increases. In their study of Darcy flows, Manickam and Homsy (1993) pointed out that the larger the value of c_m , the more efficient it is in stunning the downward propagation of instabilities leading to viscous fingering. They also reported that for non-monotonic viscosity concentration profiles, c_m determines the length of the stable zone. These effects are not present in our analysis, which is a single-pore study and involves Stokes flows, instead. The analysis of these features is still underway.

PRELIMINARY EXPERIMENTS

To assess the effect of non-monotonicity on miscible displacement features, preliminary experiments were also carried out in Hele-Shaw cells. We must note that these experiments were not designed to test the previous theory, although such tests would be desirable and will be conducted in the future. Rather, the experiments probed the predictions of Manickam and Homsy (1993) as well as those presented in the next chapter.

The experiments were carried out in a Hele-Shaw cell. The cell was constructed of two sheets of 0.5-inch thick glass with 11X4" dimensions. The two glass plates were separated with a 0.09-cm thick rubber gasket. The gasket sealed the cell and also maintained a constant thickness between the two glass plates. The plates were clamped together using ten C-clamps. Vacuum grease was applied to the edges of the cell, to prevent air leakage. A schematic diagram of the experimental apparatus is shown in Figure 5.20. The Hele-Shaw cell was first filled with the resident fluid. The lines were de-aired by pumping the fluid at a slow rate. To distinguish the advancing front, water was dyed with Bromocresol dye coloring it dark blue. A Harvard Apparatus 850 model syringe pump was used to inject the invading fluid into the cell. The flow rate of the injected fluid was then set. The experiments were conducted at two different flow rates: (1) 7.48 ml/sec and (2) 1.91 ml/sec. A Javelin digital camera, which was connected directly to a television and VCR set, was used to capture the images. After the breakthrough of the injected fluid was complete, the syringe pump was turned off. The experiments were performed using four different fluids paired with water. Their physical properties are listed in Table 1.

Table 1: List of Miscible Fluids Used

Component	Molecular Weight	Density (g/cm ³)	Viscosity (cp)
1-propanol	60.01	0.802	2.223
2-propanol	60.01	0.912	2.428
Methanol	32	0.785	0.585
Glycerol	92.10	1.158	1759.6

Although a variety of experiments were conducted, only two visualization experiments will be reported, water displacing 2-propanol, and water displacing a water-glycerol mixture. The viscosity-concentration profiles for the two problems are shown in Figures 5.21-5.22. The Figures show that 2-propanol-water mixtures have nonmonotonic viscosity concentration profiles, while the glycerol/water pair has a monotonic viscosity-concentration profile. Non-monotonicity also exists in 1-propanol-water and methanol-water mixtures, as well (not shown here)..

The displacement of 2-propanol by water is shown in Figure 5.23. This miscible displacement has a mobility ratio of 2.223, which is a nominally unfavorable displacement because the invading fluid has a lower viscosity leading to the possibility of flow instability and viscous fingering. The

displacement shows characteristics associated with non-monotonicity. Thus, the leading part of the mixing zone, where the concentration of water is low, appears to be rather stable. By contrast, a fingered zone follows upstream, where the concentration of water is relatively high, and the viscosity-concentration curve of Figure 5.21 indicates a region of increasing viscosity. The existence of these two zones is consistent with the viscosity profiles and the stability analysis of Manickam and Homsy (1993) (see also next chapter).

In order to compare the nonmonotonic viscosity to its monotonic counterpart, a 28-weight percent glycerol/water mixture with a viscosity of 2.274 cP was prepared. Figure 5.24 shows the displacement of this mixture by water at an injection flow rate of 7.48 ml/sec. The mobility ratio for this case is 2.274. Comparison with Figure 5.23 indicates a more unstable displacement in the monotonic case. This is particularly true at the leading edge of the displacement. This is presumably due to the fact that in the non-monotonic case, there is a region in the mixing zone where the displacement is favorable because viscosity is decreasing in the flow direction resulting in a more compact front. Finally, a close-up of the two displacements is shown in Figures 5.25 and 5.26, respectively. Filaments are clearly identified in the close-ups of both displacements. However, for the case of water-glycerol displacements, which corresponds to a monotonic profile, these filaments also exist at the leading edge of the front, in contrast to the non-monotonic case. In either case, the filaments indicate structures of a size of the order of the gap of the Hele-Shaw cell, thus reflecting single-pore level phenomena. We are in the process of analysing these by using the approach outlined at the beginning of this chapter, namely the use of Stokes equations in constricted geometries. An overall analysis of the large-scale instabilities is also presented in the next chapter.

CONCLUSIONS

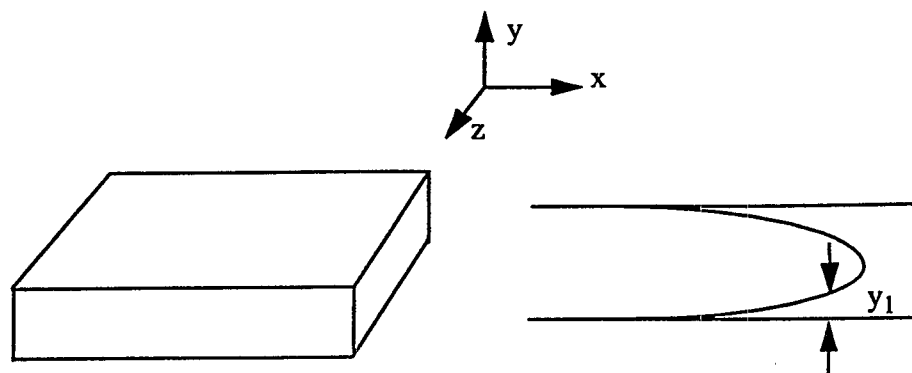
In this chapter, it was shown that non-monotonic viscosity concentration profiles have an important effect on miscible displacements. As a general observation, the displacement profiles have the characteristics of both favorable and unfavorable displacements. This can be explained by the fact that the non-monotonic viscosity concentration profiles possess two regions, one in which the viscosity increases with concentration (unfavorable local mobility ratios), and the other in which the reverse is true. Instabilities were shown to exist both at the large-scale (Darcy scale) and at the small (single-pore) scale, provided that a sufficiently strong non-monotonicity was imposed. The instabilities exist even when the two pure fluids have equal viscosities. This rather interesting behavior needs to be analyzed further at the pore-scale. A further discussion of the large-scale instabilities is presented in the chapter to follow. In either case, the instability that ensues may lead to a reduction of the contact efficiency, hence of the removal efficiency of the process. The degree, however, depends on the maximum mobility contrast that develops.

REFERENCES

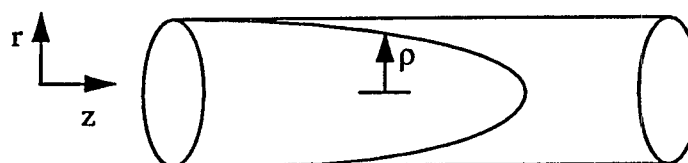
1. Bacri, J. C., Rakotomalala, N., Salin, D. and Woumeni, R., Miscible viscous fingering: experiments versus continuum approach, *Phys. Fluids A*, Vol. 4, 1611-1619 (1992).
2. Blunt, M., and Rubin, B., Implicit flux limiting schemes for petroleum reservoir simulation, *J. Comp. Phys.*, Vol. 102, 194-206 (1992).

3. Chen, C.Y., and Meiburg, E., Miscible displacements in capillary tubes. Part 2: numerical simulations, *J. Fluid Mech.*, Vol. 326, 57-90 (1996).
4. Chikhliwala, E.D., and Yortsos, Y.C., Theoretical investigation on finger growth by linear and weakly nonlinear stability analysis, *SPERE*, 1268-1278 (1988).
5. Chouke, R.L., van Meurs, P., and van der Poel, C., The instability of slow, immiscible, viscous liquid-liquid displacements in permeable media, *Trans. AIME*, Vol. 216, 188-194 (1959).
6. Hickernell, F.J., and Yortsos, Y.C., Linear stability of miscible displacement processes in porous media in the absence of dispersion, *Stud. Appl. Math.*, Vol. 74, 93-115 (1986).
7. Homsy, G.M., Viscous fingering in porous media, *Ann. Rev. Fluid Mech.*, Vol. 19, 271-311 (1987).
8. Joseph, D.D., Fluid dynamics of two miscible liquids with diffusion and gradient stresses, *Eur. J. Mech. B/Fluids*, Vol. 9, 82-88 (1990).
9. Joseph, D.D., and Renardy, Y.Y., "Fundamentals of Two Fluid Dynamics, Part II: Lubricated Transport Drops and Miscible Liquids", Springer-Verlag (1992).
10. Khodadoust, A.P., Wagner, J.A., Mackram, T.S., and Steven, I.S., Solvent washing of PCP contaminated soils with anaerobic treatment of wash fluids, *Water Environ. Research*, Vol. 66, 692-697 (1994).
11. Koch, D.L., and Brady, J.F., A non-local description of advection-diffusion with application to dispersion in porous media, *Phys. Fluids*, Vol. 31, 242-249 (1988).
12. Lajeunesse, E., Martin, J., Rakotomalala, N., and Salin, D., 3D instability of miscible displacements in a Hele-Shaw cell, *Phys. Rev. Lett.*, Vol. 79, 5254-5257 (1997).
13. Lake, L.W., "Enhanced Oil Recovery", Prentice Hall, New York (1989).
14. Manickam, O., and Homsy, G.M., Stability of miscible displacements in porous media with nonmonotonic viscosity profiles, *Phys. Fluids A*, Vol. 5, 1356-1367 (1993).
15. Manickam, O., and Homsy, G.M., Fingering instabilities in vertical miscible displacement flows in porous media, *J. Fluid Mech.*, Vol. 288, 75-102 (1995).
16. Ockendon, H., and Ockendon, J.R., "Viscous Flow", Cambridge University Press (1995).
17. Patterson, L., Fingering with miscible fluids in a Hele-Shaw cell, *Phys. Fluids*, Vol. 28, 26-30 (1985).
18. Petitjeans, P., and Maxworthy, T., Miscible displacements in capillary tubes. Part 1: experiments, *J. Fluid Mech.*, Vol. 326, 37-56 (1996).
19. Pinal, R., Rao, P.S.C., Lee, L.S., Cline, P.V., and Yalkowsky, S.H., Cosolvency and solubility of hydrophobic organic chemicals in mixed solvents: evaluation using partially-and completely-miscible organic solvents, *Environ. Sci. Tech.* Vol. 24, 639-647 (1990).
20. Rakotomalala, N., Salin, D., and Watzky, P., Saffman-Taylor finger in parallel Stokes flow, *J. Fluid Mech.*, Vol. 338, 277-297 (1997).

21. Reinelt, D.A., and Saffman, P.G., The penetration of a finger into a viscous fluid in a channel and tube, *SIAM J. Sci. Stat. Comput.*, Vol. 6, 542-561 (1985).
22. Rogerson, A., and Meiburg, E., Numerical simulation of miscible displacement processes in porous media flows under gravity, *Phys. Fluids A*, Vol. 5, 2644-2660 (1993).
23. Saffman, P.G., Viscous fingering in Hele-Shaw cells, *J. Fluid Mech.*, Vol. 173, 73-94 (1986).
24. Saffman, P.G., and Taylor, G.I., The penetration of a fluid into a porous medium or Hele-Shaw Cell containing a more viscous fluid, *Proc. Roy. Soc. A.*, Vol. 245, 312-329 (1958).
25. Slobod, R.L., and Thomas, R.A., Effect of transverse diffusion on fingering in miscible-phase displacement, *Soc. Pet. Eng. J.*, Vol. 3, 9-13 (1963).
26. Tan, C.T., and Homsy, G.M., Stability of miscible displacements in porous media: rectilinear flows, *Phys. Fluids*, Vol. 29, 3549-3556 (1986).
27. Tan, C.T., and Homsy, G.M., Simulation of nonlinear viscous fingering in miscible displacement, *Phys. Fluids*, Vol. 31, 1330-1338 (1988).
28. Tanveer, S., Analytic theory for the linear stability of the Saffman-Taylor finger, *Phys. Fluids*, Vol. 30, 2318-2342 (1987).
29. Tchelepi, H.A., and Orr Jr., F.M., Dispersion, permeability heterogeneity, and viscous fingering: acoustic experimental observation and particle-tracking simulations, *Phys. Fluids A*, Vol. 5, 1558-1574 (1993).
30. Tryggvason, G., and Aref, H., Numerical experiments on Hele-Shaw flow with a sharp interface, *J. Fluid Mech.*, Vol. 136, 1-30 (1983).
31. Wood, A.L., Bouchard, D.C., Brusseau, M.L., and Rao, P.S.C., Cosolvent effect on sorption and mobility of organic contaminants in soils, *Chemosphere*, Vol. 21, 575-587 (1990).
32. Wooding, R.A., Growth of fingers at an unstable diffusing interface in a porous medium or Hele-Shaw cell, *J. Fluid Mech.*, Vol. 39, 477-495 (1969).
33. Yang, Z., and Yortsos, Y.C., Asymptotic solutions of miscible displacements in geometries of large aspect ratio, Vol. 9, 286-298 (1997).
34. Yee, H.-C., and R. F. Warming, Implicit total variation diminishing (TVD) schemes for steady-state calculations, *J. Comp. Phys.*, Vol. 57, 327-338 (1985).
35. Yortsos, Y.C., A theoretical analysis of vertical flow equilibrium, *Transp. Porous Media*, Vol. 18, 107-129 (1995).
36. Yortsos, Y.C., and Zeybek, M., Dispersion driven instability in miscible displacement in porous media, *Phys Fluids*, Vol. 31, 3511-3518 (1988).
37. Zimmerman, W.B., and Homsy, G.M., Nonlinear viscous fingering in porous media with anisotropic dispersion, *Phys. Fluids A*, Vol. 3, 1859-1872 (1991).



(a) Geometry for Flow Between Parallel Plates



(b) Geometry for Flow in Cylindrical Capillary

Figure 5.1: Typical displacement geometries (from Yang and Yortsos, 1997).

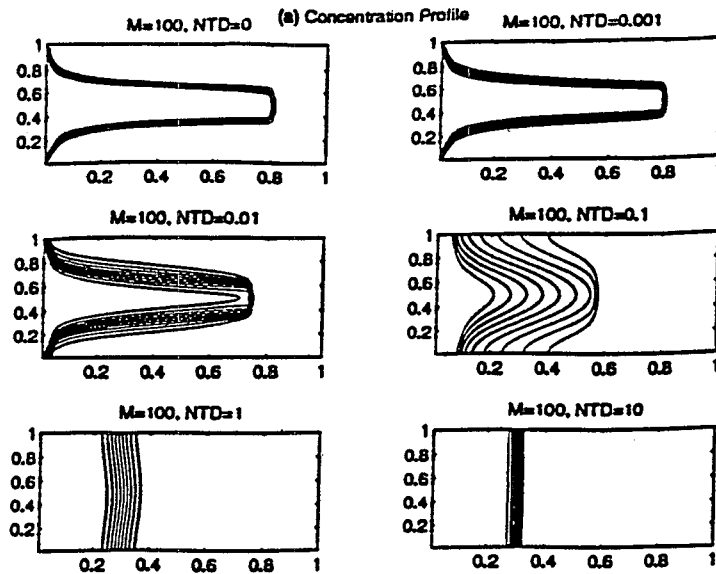


Figure 5.2-a: Concentration profiles for Miscible Displacements with a Monotonic Viscosity-Concentration Profile Between Parallel Plates at Time Step=0.3 and $M=100$ for Various Values of the Dispersion Coefficient N_{TD} . M is the endpoint viscosity mobility ratio, which is defined as the ratio of the viscosities of the initial to the injected fluid. $N_{TD}=(\epsilon Pe)^{-1}$, where $Pe=qH/D$, q is the injection rate, H is the gap width, D is the diffusion coefficient [Yang and Yortsos, 1997].

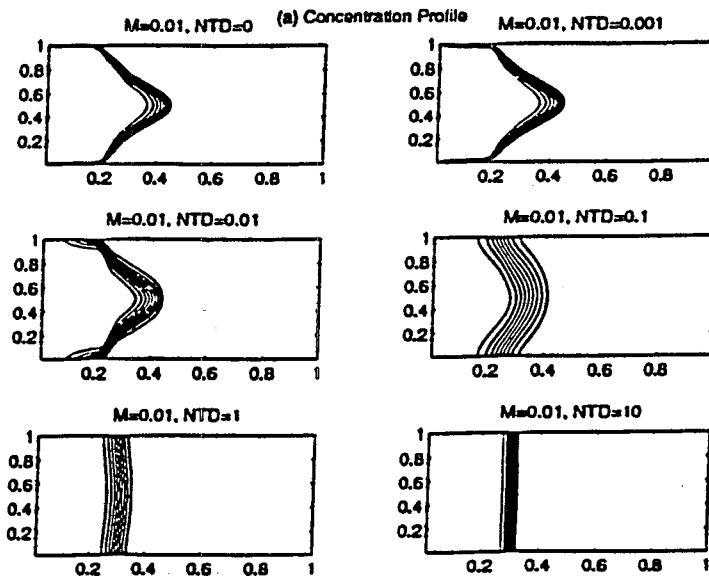


Figure 5.2-b: Concentration profiles for Miscible Displacements with a Monotonic Viscosity-Concentration Profile Between Parallel Plates at Time Step=0.3 and $M=0.01$ for Various Values of the Dispersion Coefficient N_{TD} . M is the endpoint viscosity mobility ratio, which is defined as the ratio of the viscosities of the initial to the injected fluid. $N_{TD}=(\epsilon Pe)^{-1}$, where $Pe=qH/D$, q is the injection rate, H is the gap width, D is the diffusion coefficient [Yang and Yortsos, 1997].

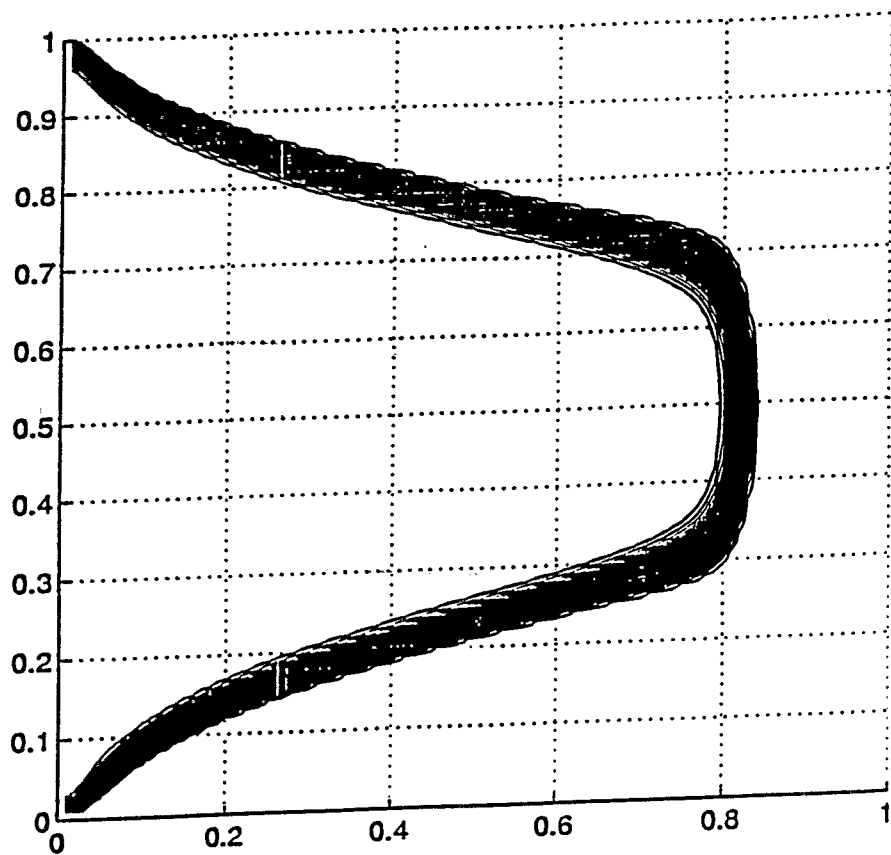


Figure 5.3: Monotonic viscosit- unfavorable mobility ratio ($\alpha = 5$, $\text{NTD}=0$, $\text{Time}=0.5$).

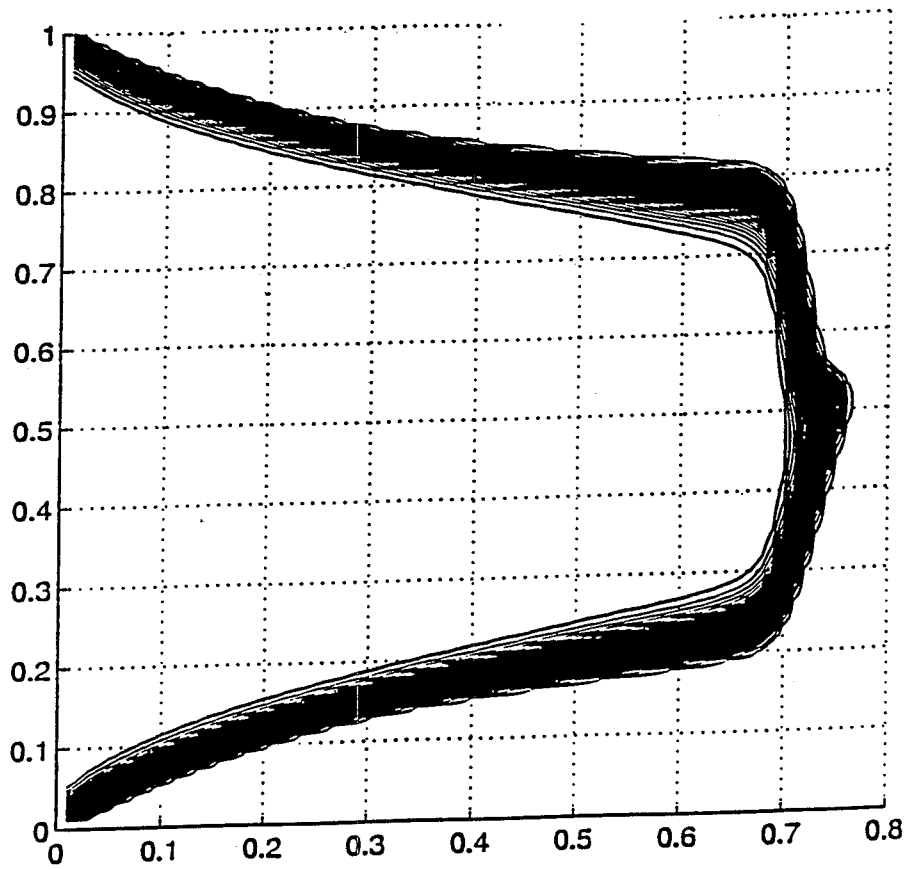


Figure 5.4: Non-monotonic viscosity- unfavorable mobility ratio ($\alpha = 5$, $\mu_m = 10$, $c_m = 0.5$, NTD=0, Time=0.5).

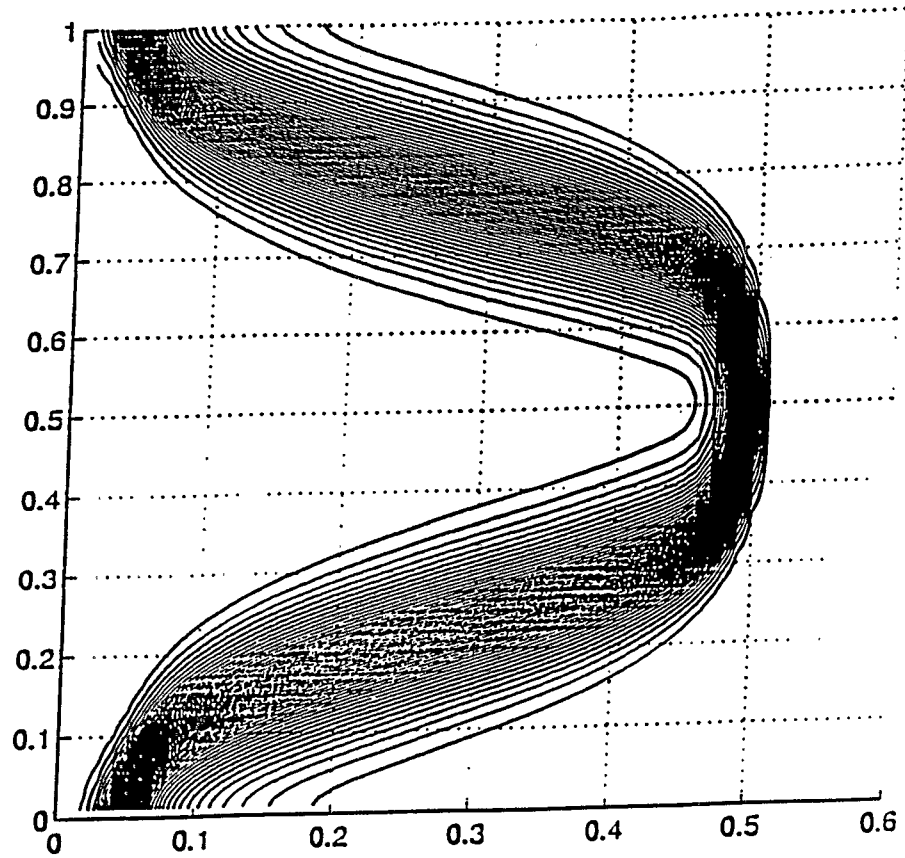


Figure 5.5: Monotonic viscosity. Effect of dispersion ($\alpha = 5$, $\text{NTD}=0.01$, $\text{Time}=0.3$).

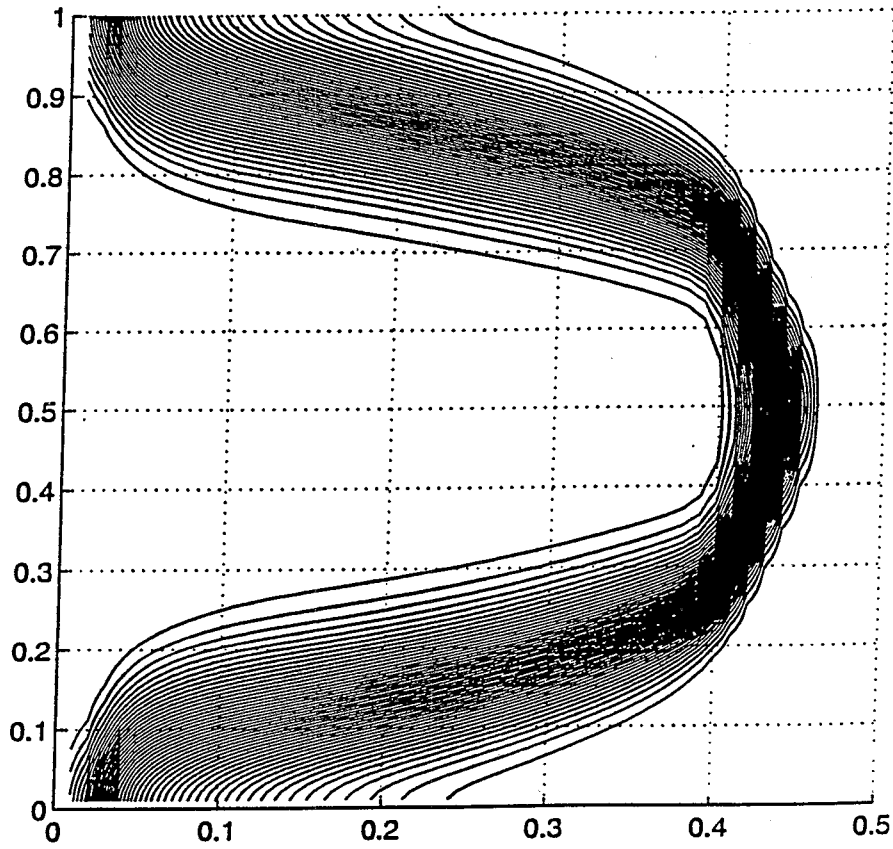


Figure 5.6: Non-monotonic viscosity. Effect of dispersion ($\alpha = 5$, $\mu_m = 10$, $c_m = 0.5$, NTD=0.01, Time=0.3).

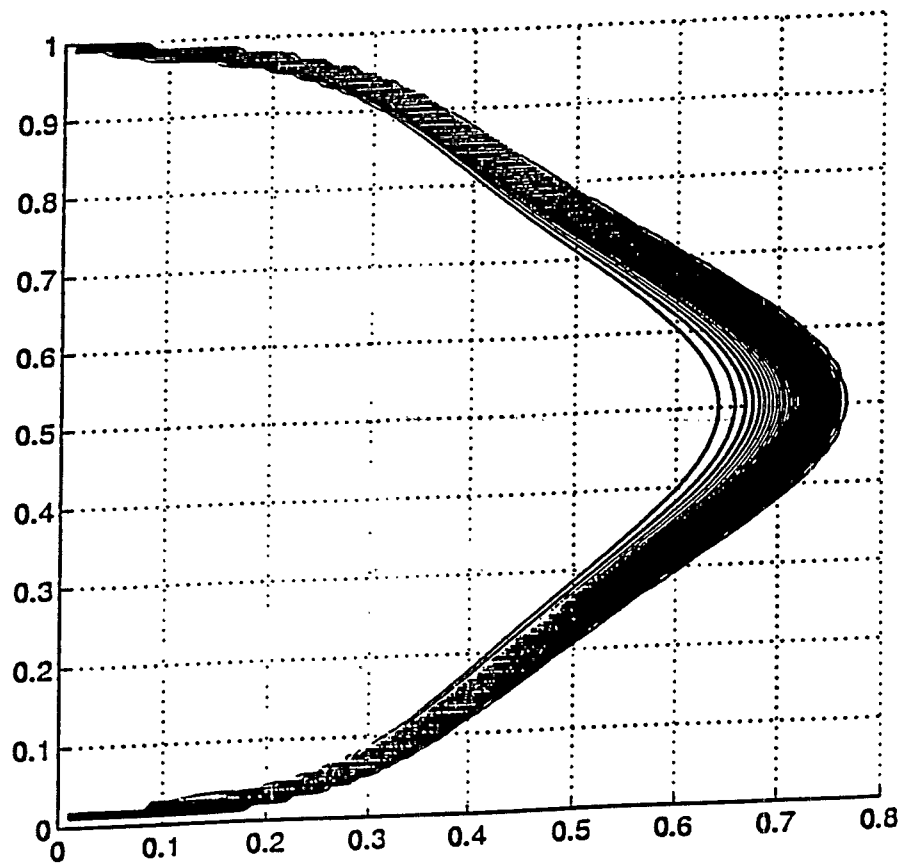


Figure 5.7: Monotonic viscosity- favorable mobility ratio ($\alpha = 0.2$, $NTD=0$, $Time=0.5$).

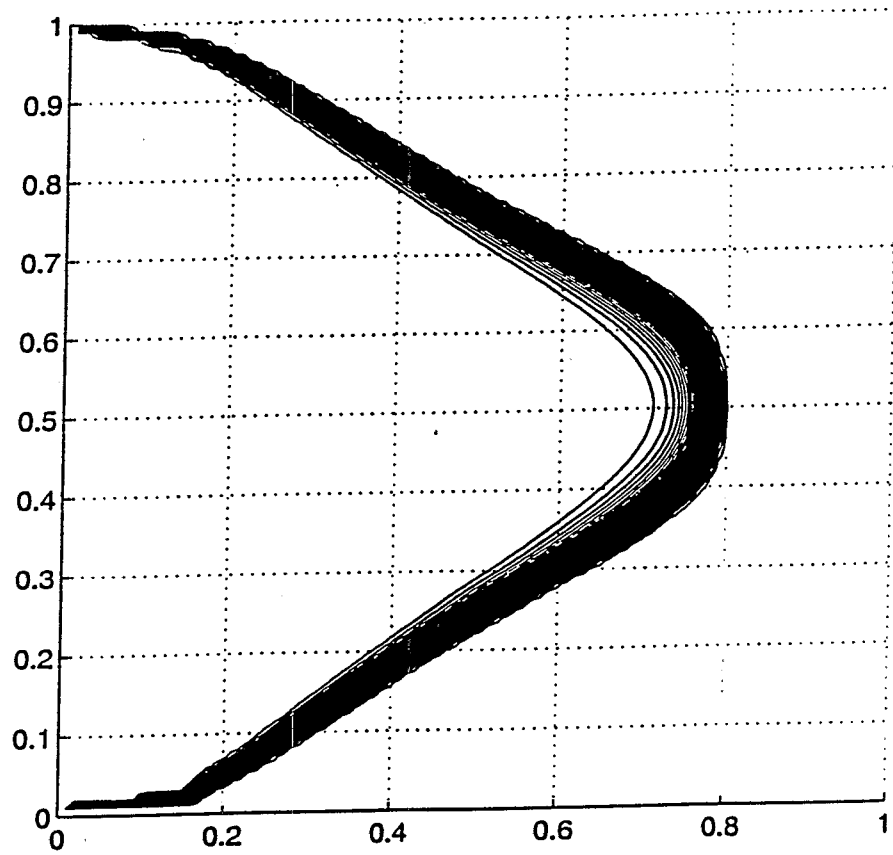


Figure 5.8: Non-monotonic viscosity- favorable mobility ratio ($\alpha = 0.2$, $\mu_m = 10$, $c_m = 0.5$, NTD=0.01, Time=0.5).

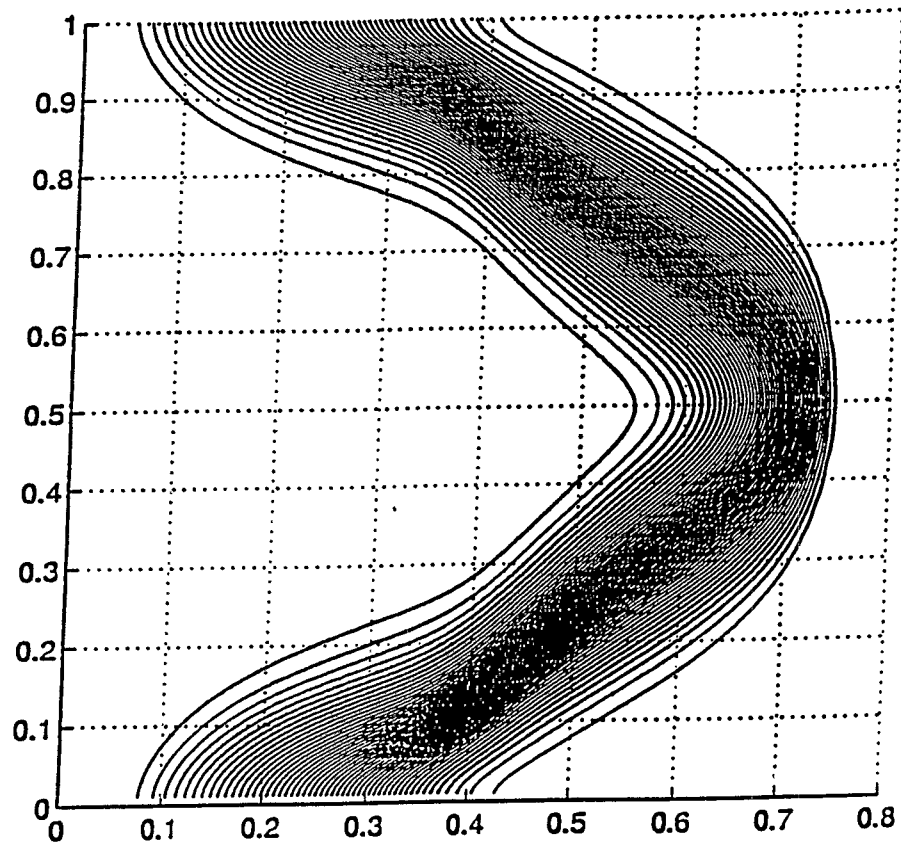


Figure 5.9: Monotonic viscosity- favorable mobility ratio. Effect of dispersion ($\alpha = 0.2$, $\text{NTD}=0.01$, $\text{Time}=0.5$).

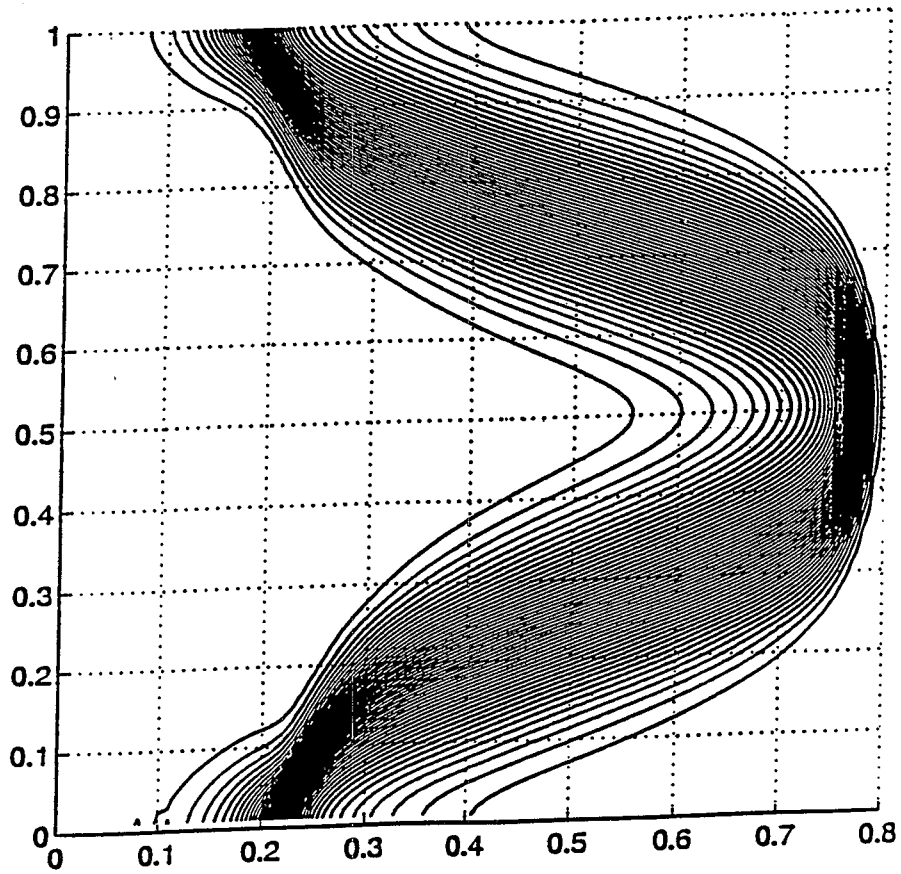


Figure 5.10: Non-monotonic viscosity- favorable mobility ratio. Effect of dispersion ($\alpha = 0.2$, $\mu_m = 10$, $c_m = 0.5$, NTD=0.01, Time=0.5).

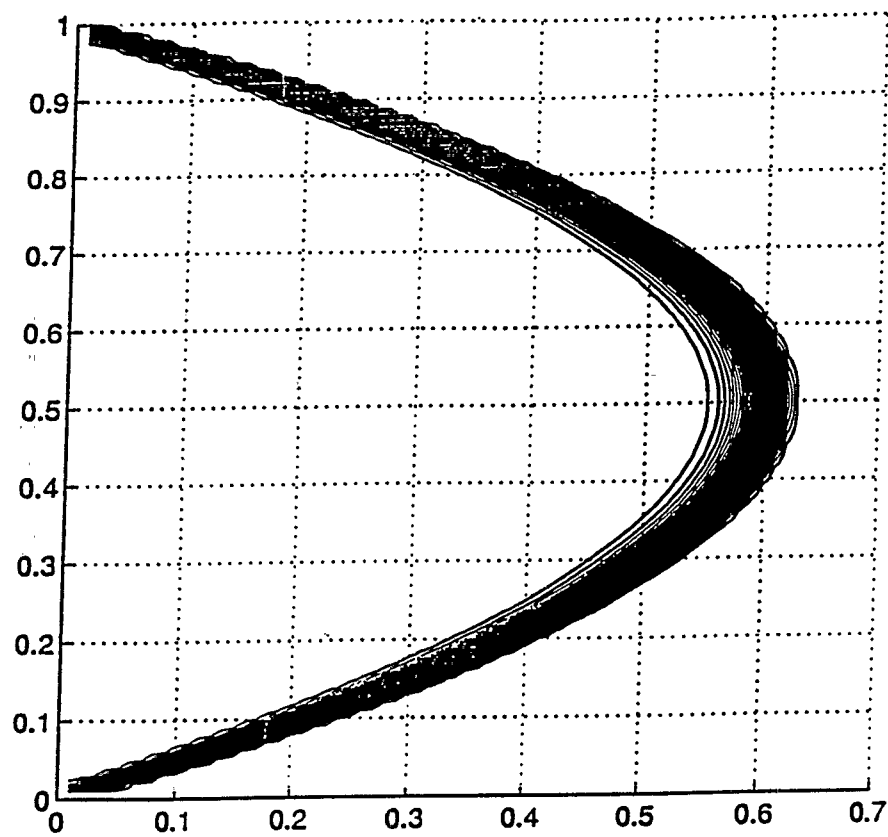


Figure 5.11: Monotonic viscosity- Poiseuille flow ($\alpha = 1$, $\text{NTD}=0$, $\text{Time}=0.4$).

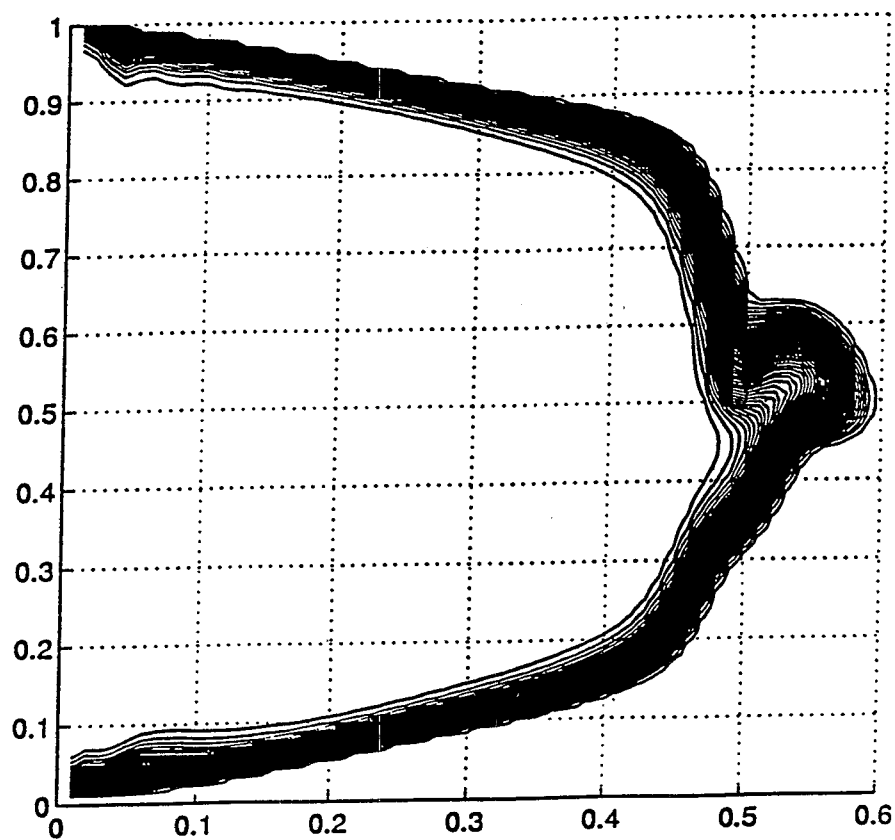


Figure 5.12: Non-monotonic viscosity at Poiseuille flow conditions ($\alpha = 1$, $\mu_m = 10$, $c_m = 0.5$, NTD=0, Time=0.4).

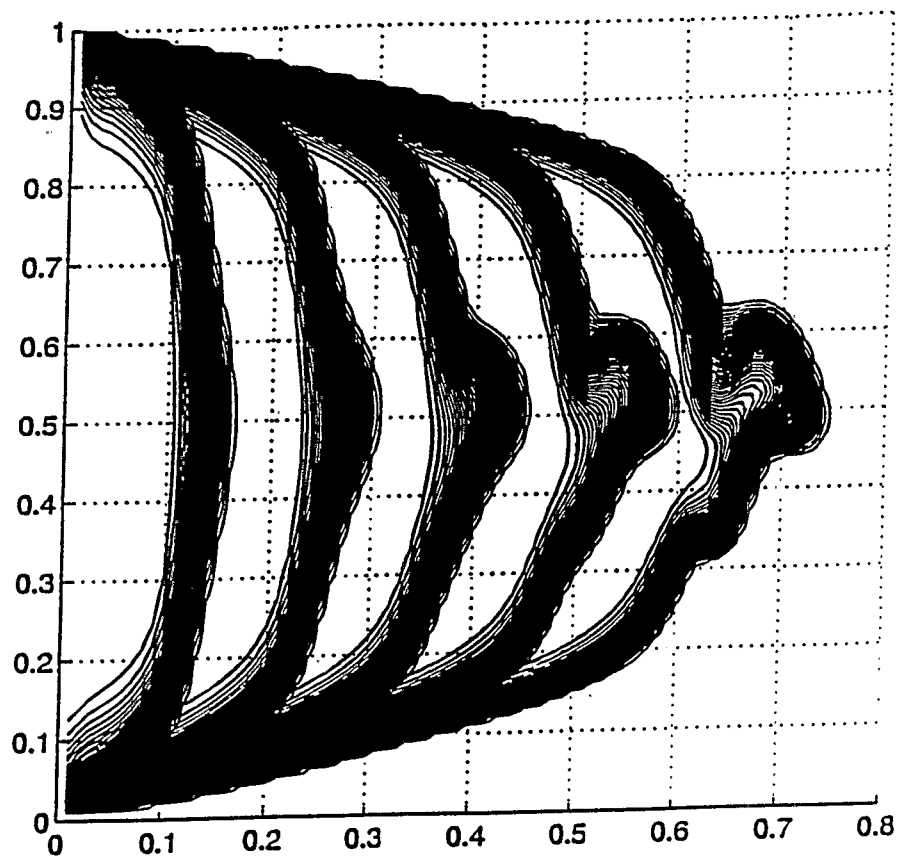


Figure 5.13: Effect of t on non-monotonic viscosity for $\alpha = 1$ ($\mu_m = 7$, $c_m = 0.5$, $\text{NTD}=0$).

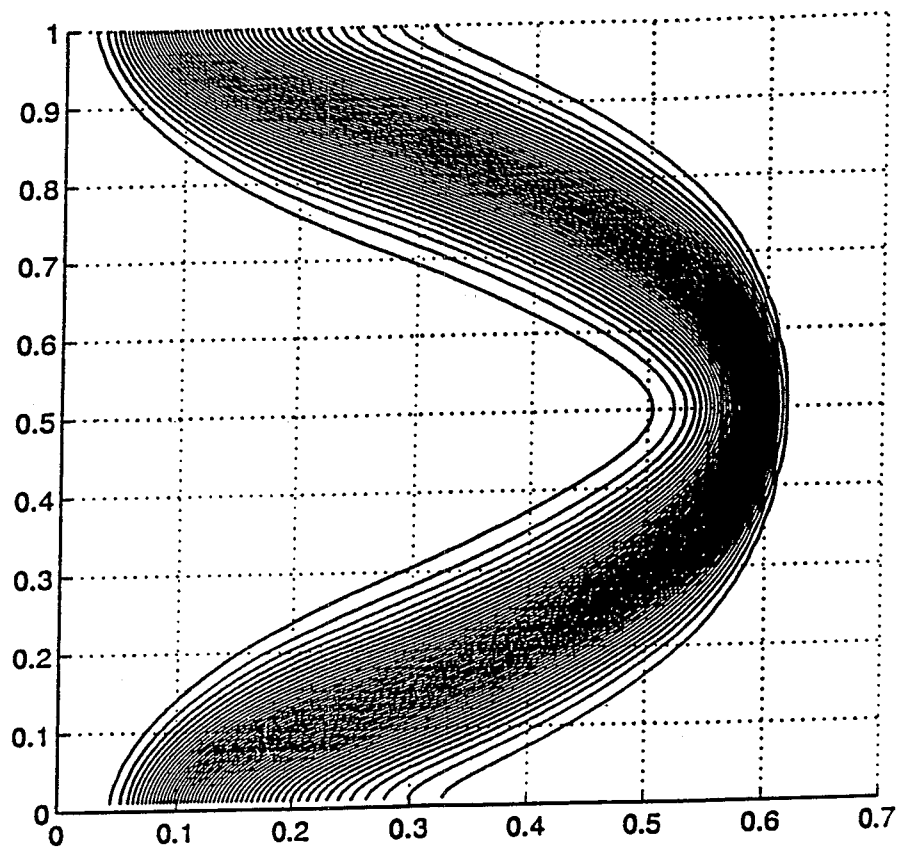


Figure 5.14: Monotonic viscosity- Poiseuille flow. Effect of dispersion ($\alpha = 1$, $\text{NTD}=0.01$, $\text{Time}=0.4$).

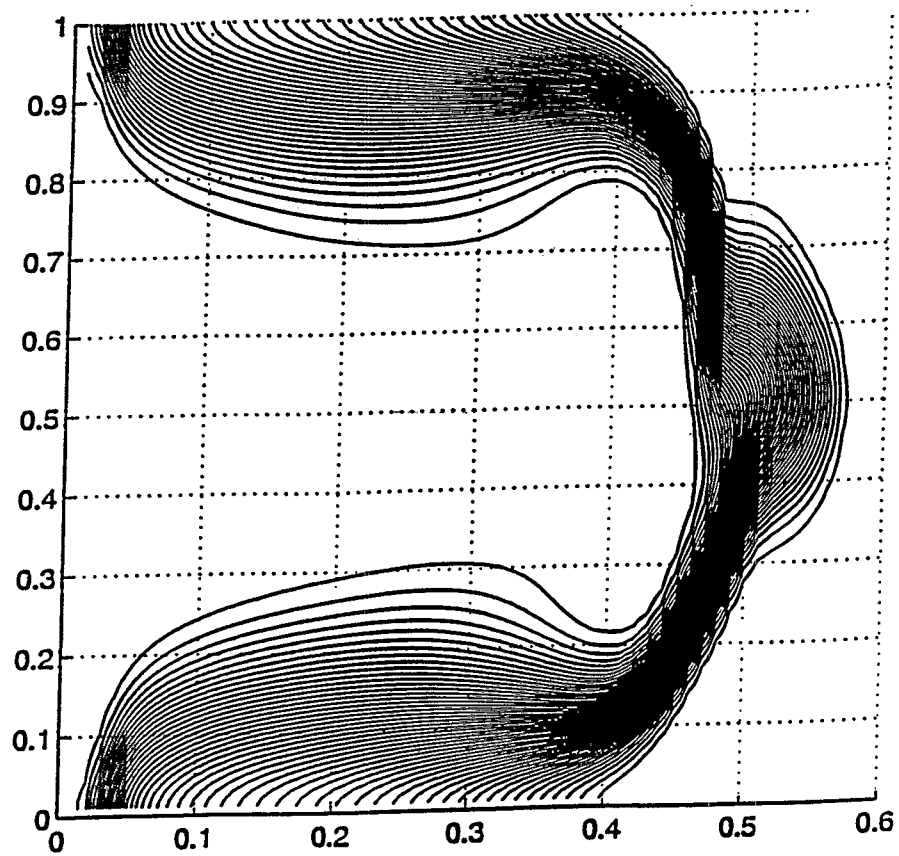


Figure 5.15: Non-monotonic viscosity at Poiseuille flow conditions. Effect of dispersion ($\alpha = 1$, $\mu_m = 10$, $c_m = 0.5$, $\text{NTD}=0.01$, $\text{Time}=0.4$).

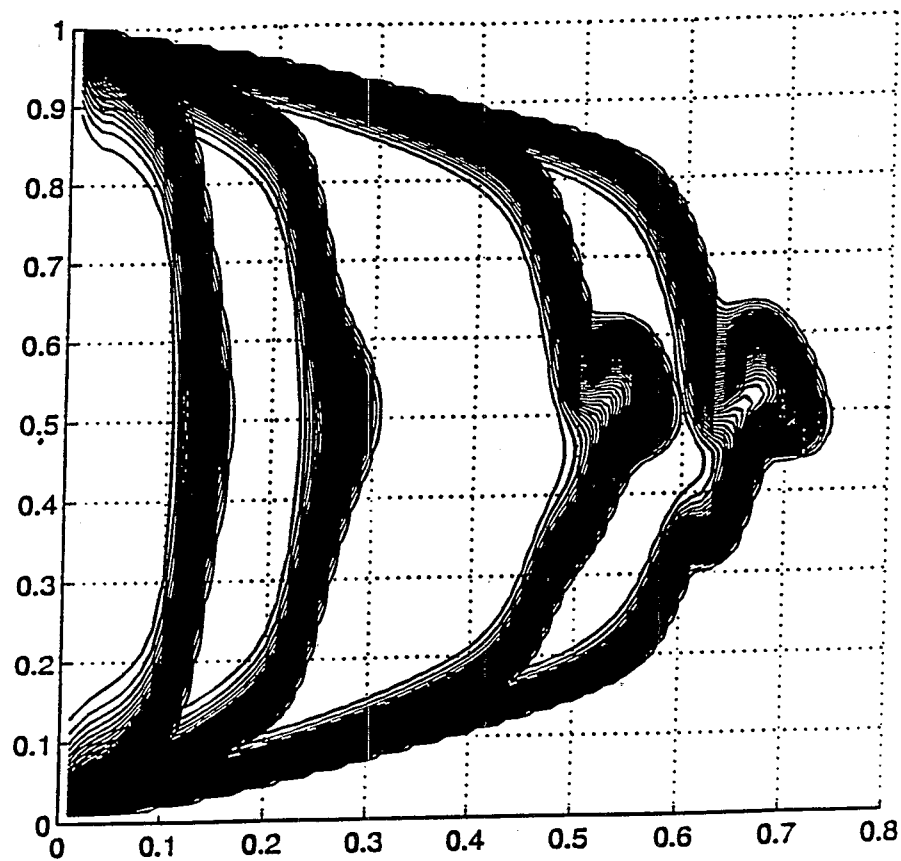


Figure 5.16: Non-monotonic viscosity- effect of μ_m ($\alpha = 1$, $\mu_m = 8$, $c_m = 0.5$, $\text{NTD}=0$).

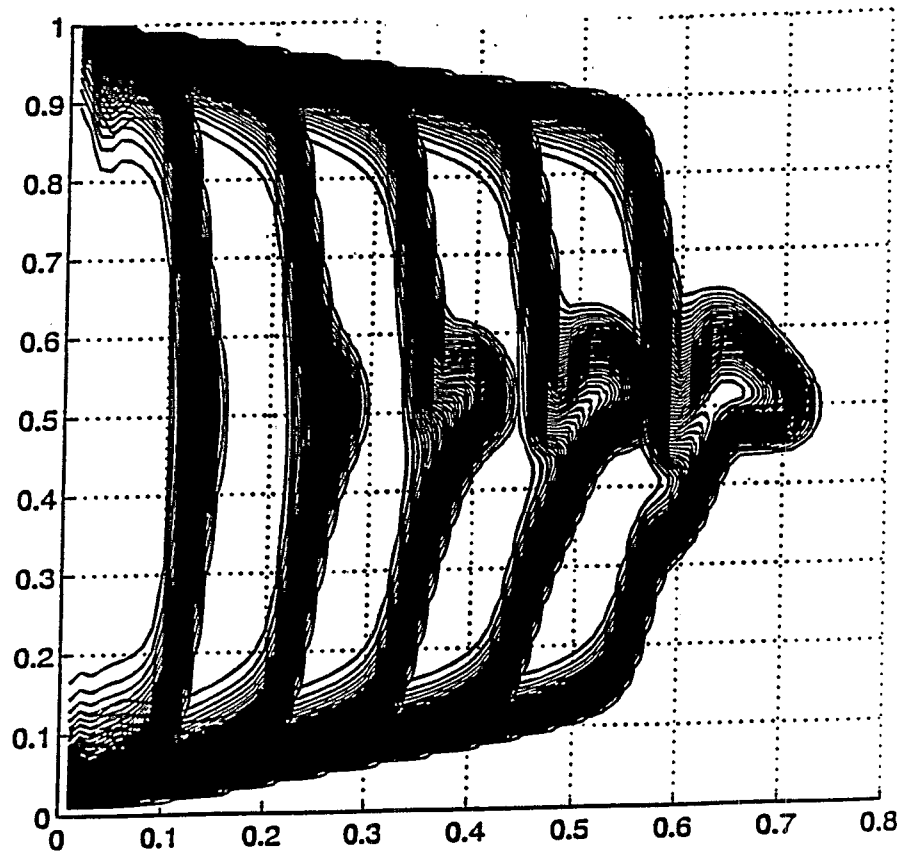


Figure 5.17: Non-monotonic viscosity- effect of μ_m ($\alpha = 1$, $\mu_m = 20$, $c_m = 0.5$, $\text{NTD}=0$).

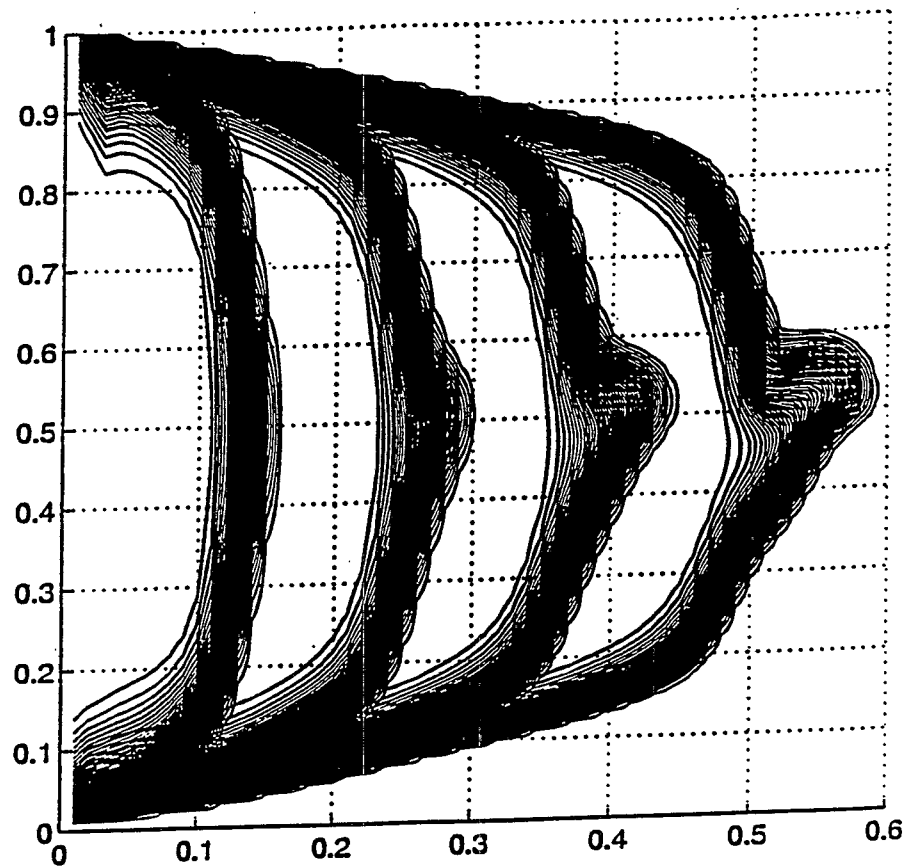


Figure 5.18: Non-monotonic viscosity- effect of c_m ($\alpha = 1$, $\mu_m = 10$, $c_m = 0.05$, $\text{NTD}=0$).

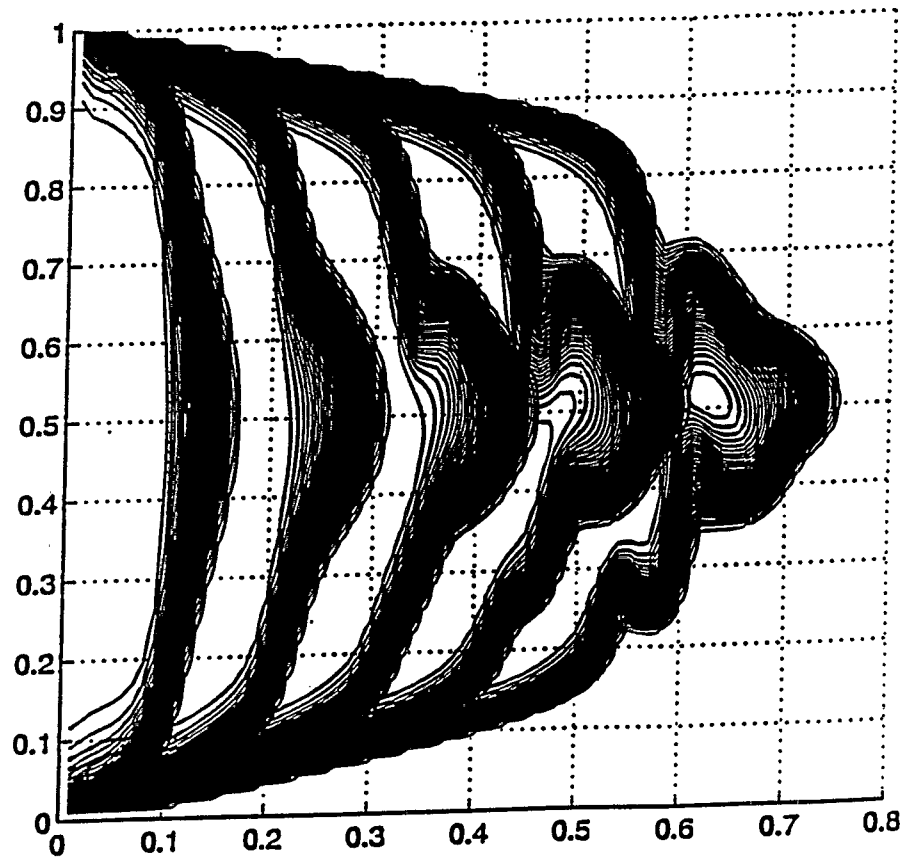


Figure 5.19: Non-monotonic viscosity- effect of c_m ($\alpha = 1$, $\mu_m = 10$, $c_m = 0.9$, $\text{NTD}=0$).

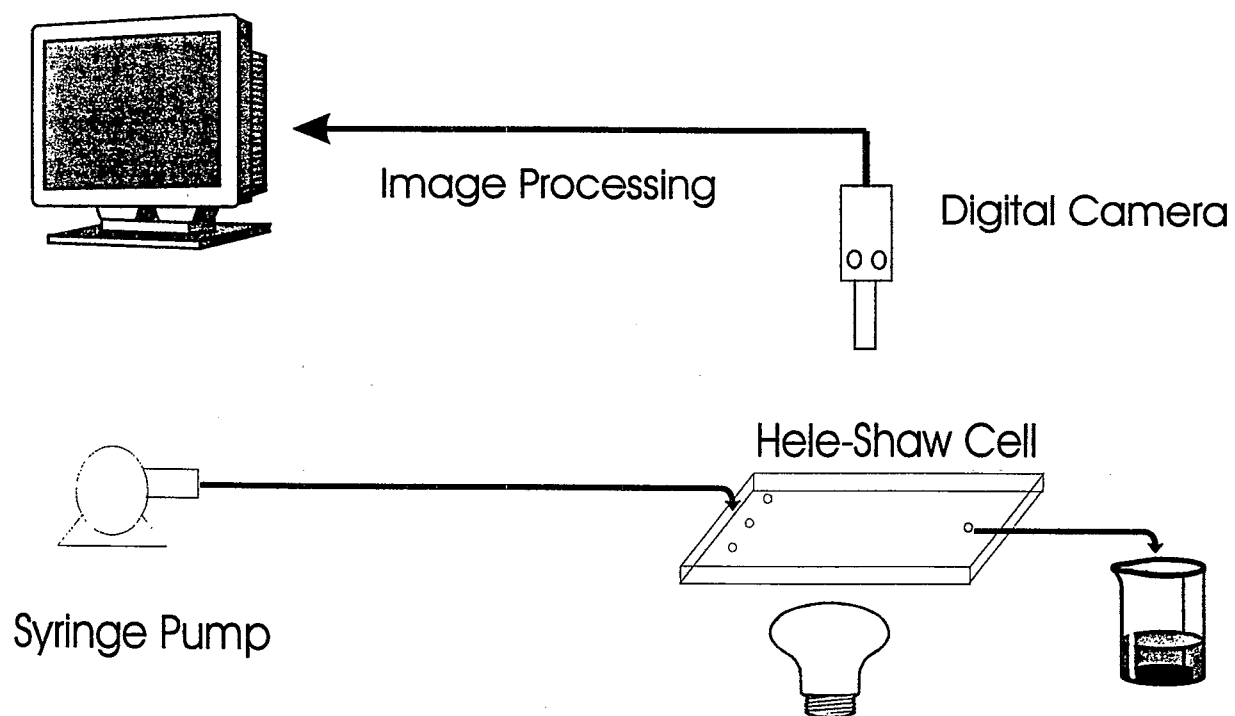


Figure 5.20: Schematic of the Experimental Apparatus Setup.

Figure 21: 2-Propanol/Water Mixture

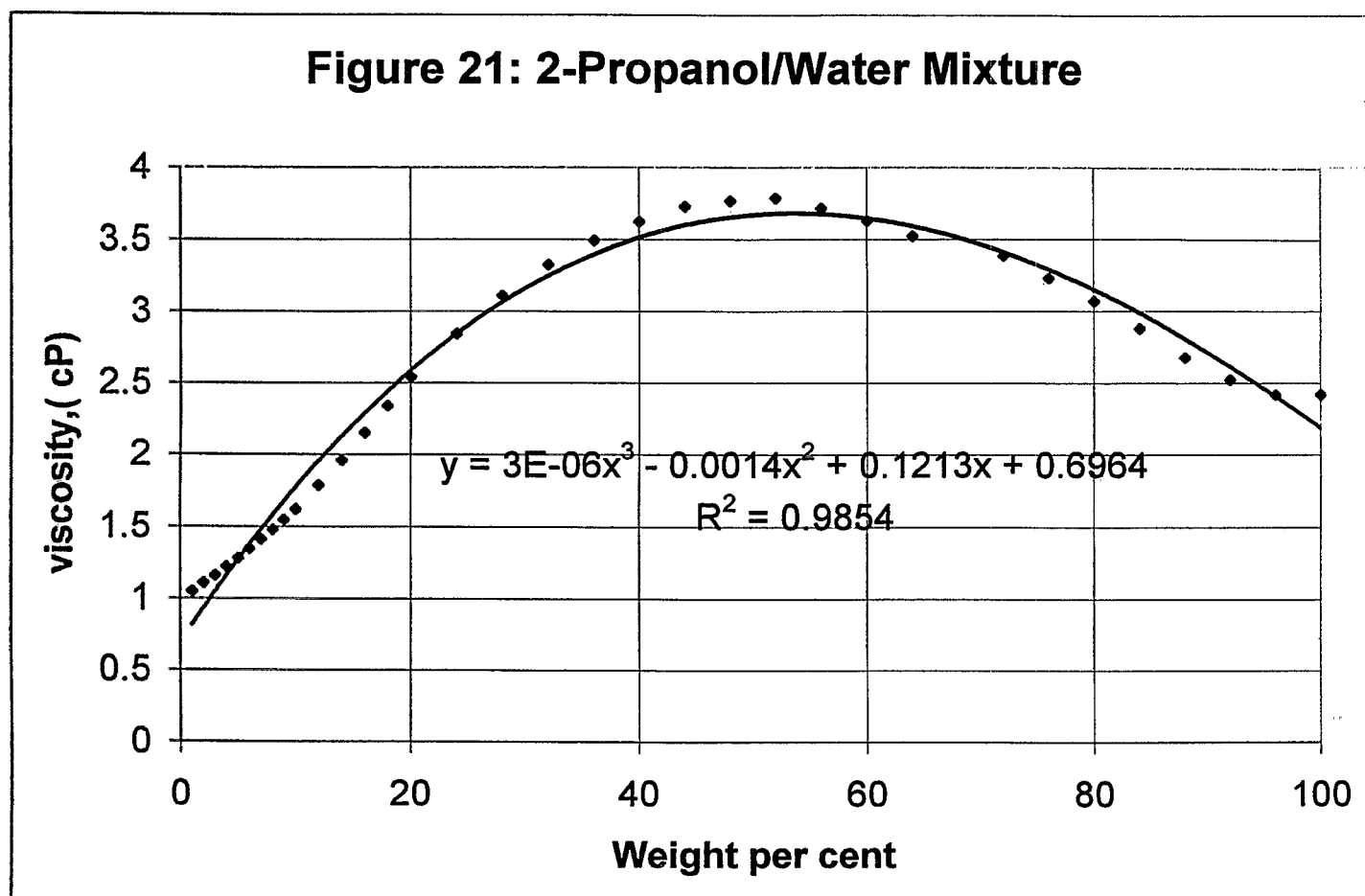


Figure 5.21: Viscosity-concentration profile for a 2-propanol/water mixture.

Figure 22: Glycerol/Water Mixture

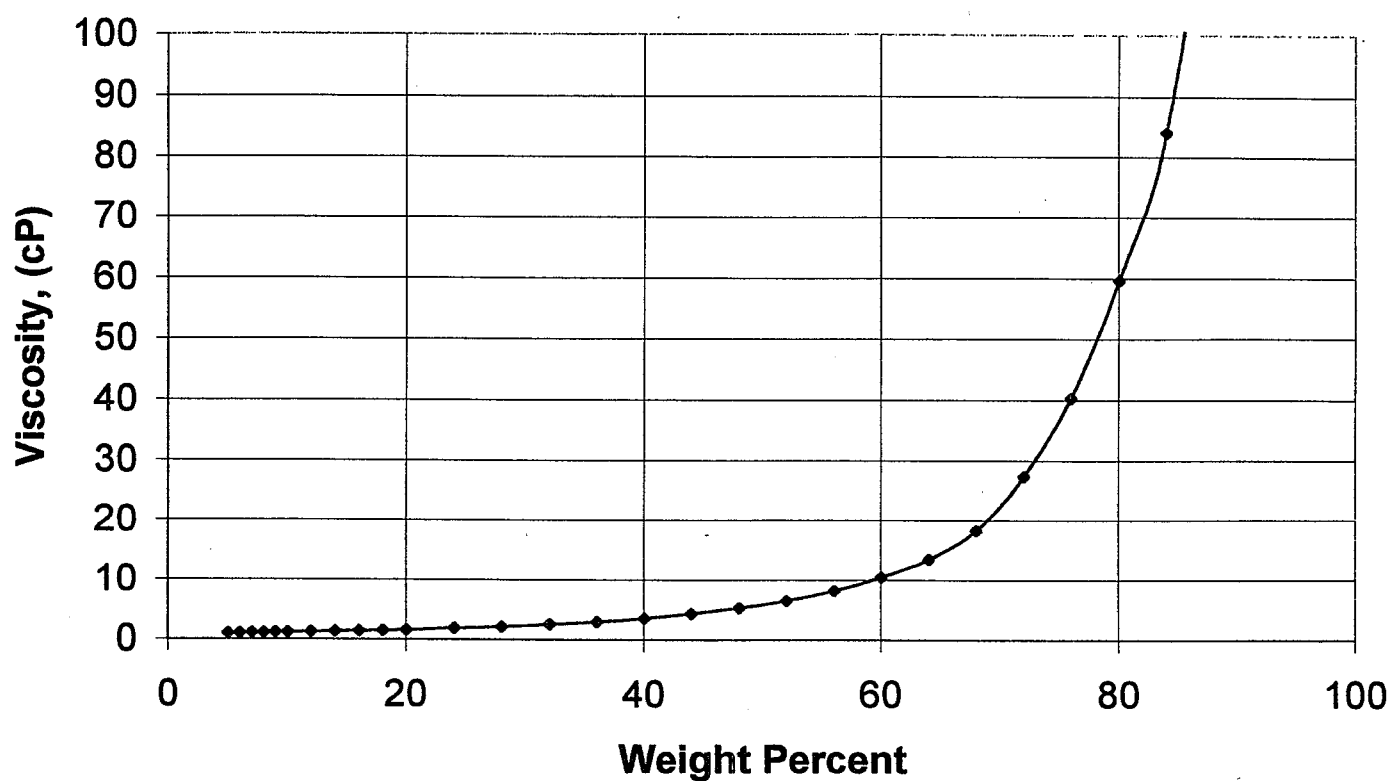


Figure 5.22: Viscosity-concentration profile for a glycerol/water mixture.

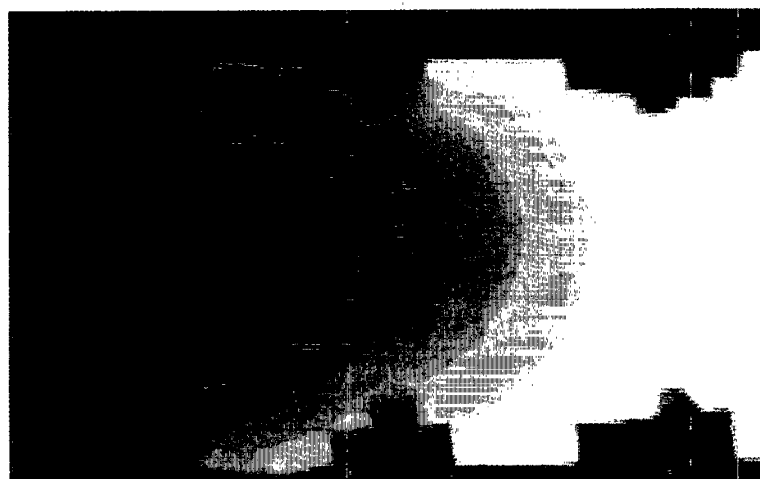


Figure 5.23: Typical image of water displacing 1-propanol.

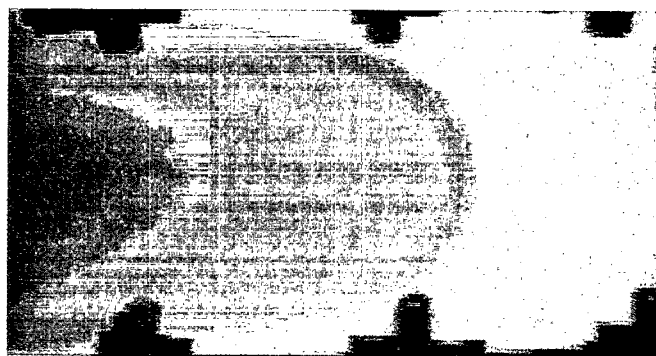


Figure 5.24: Typical image of water displacing glycerol.

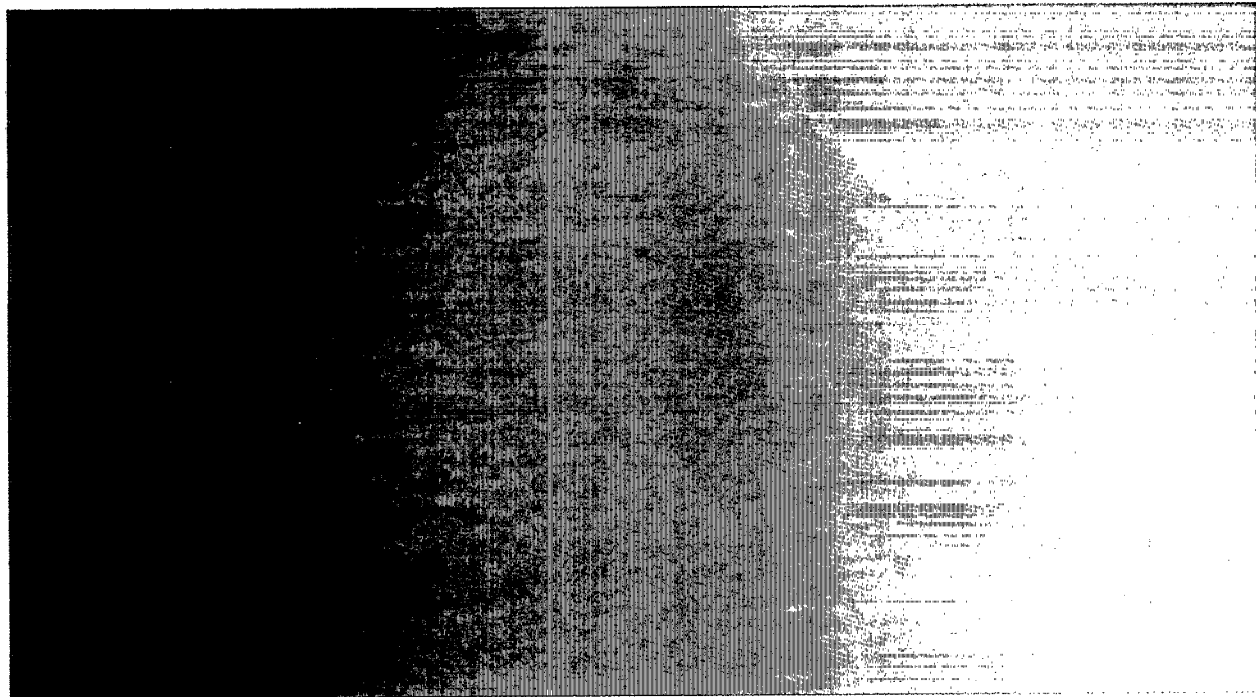


Figure 5.25: Close-up of water displacing 2-propanol.

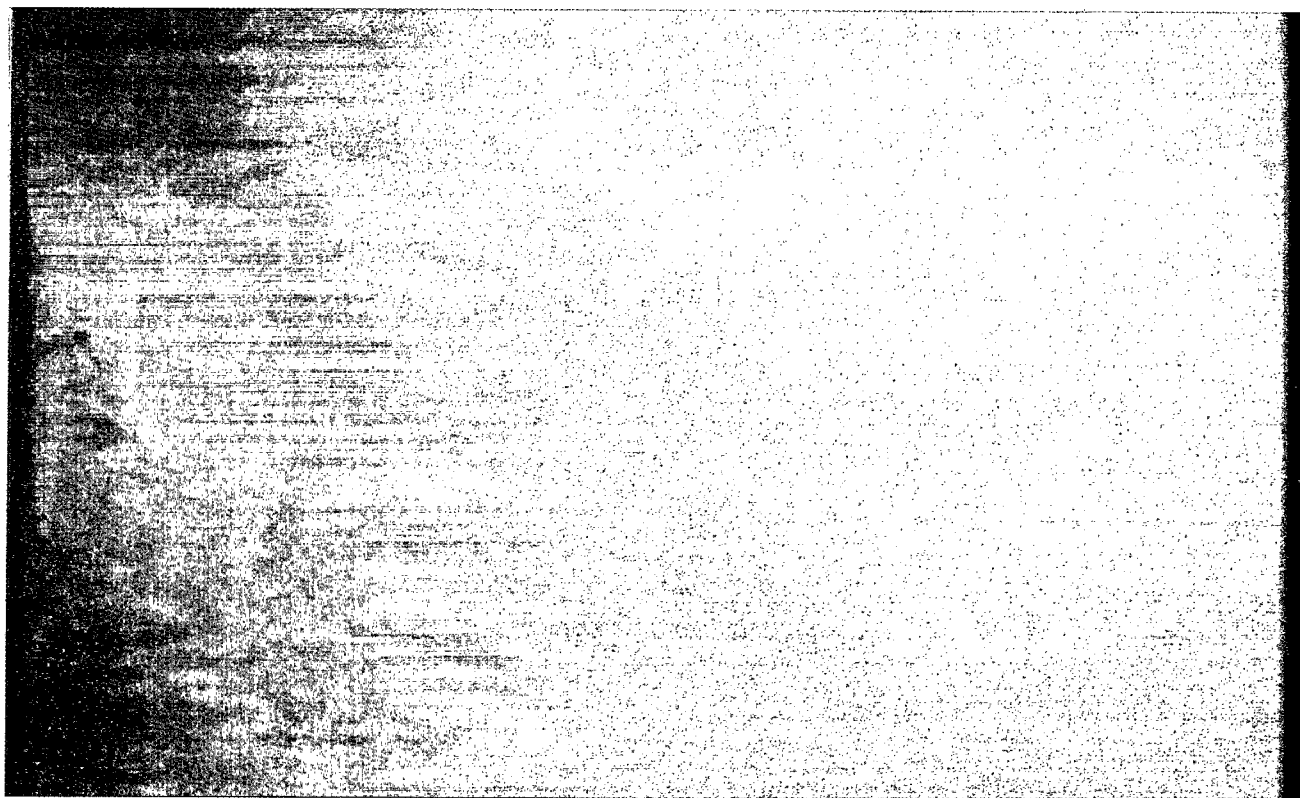


Figure 5.26: Close-up of water displacing glycerol mixture.

Chapter 6

A NOTE ON THE EFFECT OF DISPERSION ON THE STABILITY OF NON-MONOTONIC MOBILITY PROFILES IN POROUS MEDIA

Yanis C. Yortsos (with the collaboration of Didier Loggia and Dominique Salin)

INTRODUCTION

In the previous chapter we discussed the relevance of non-monotonic behavior at the single-pore scale. The final chapter of this report is a short discussion of the effect of non-monotonicity in promoting viscous instabilities at the larger scale.

In a recent paper by Manickam and Homsy (1993), to be referred to subsequently as MH, the stability of non-monotonic mobility profiles in miscible displacements in porous media was analysed. This problem involves the miscible displacement of one fluid (at dimensionless concentration $C = 0$) by another fluid (at $C = 1$) at constant rate q . Non-monotonicity in mobility may result either from a non-monotonic viscosity function $\mu(C)$, when gravity effects are not considered, or from a monotonic, but non-linearly dependent on density, viscosity function, when gravity is included (Manickam and Homsy, 1995). In this chapter we focus on the first case, the extension to the gravity problem being discussed elsewhere (Loggia et al., 1995). The base state profile, \bar{C} , propagating in the direction of displacement x , satisfies the equation

$$\bar{C} = \frac{1}{2} \operatorname{erfc} \left(\frac{\xi}{b} \right) \quad (6.1)$$

where $\xi = x - qt$ is the moving coordinate, $b = 2\sqrt{(D_{\parallel}t)}$ is the length of the transition region, and D_{\parallel} denotes the longitudinal dispersion coefficient. In stability problems of this kind, it is important to differentiate between the two cases $M > 1$ and $M < 1$, respectively, where $M = \frac{\mu(0)}{\mu(1)}$ is the ratio in the mobilities at the two end points.

In the absence of dispersion, the linear stability of general mobility profiles (which include non-monotonic and gravity cases) was analysed by Hickernell and Yortsos (1986), to be referred to subsequently as HY. Using normal modes, they derived the following eigenvalue problem

$$\frac{d}{d\xi} \left[\mu \frac{d\Psi}{d\xi} \right] = \alpha^2 \left(\mu - \frac{q}{\omega} \frac{d\mu}{d\xi} \right) \Psi \quad (6.2)$$

where $\alpha = 2\pi/\lambda$ and ω are the wavenumber and the rate of growth of the disturbance, respectively. They showed that (6.2) admits a discrete spectrum of infinitely many eigenvalues ω with the following properties:

(i) When $M > 1$, the dominant (more unstable) eigenvalue has the long wavelength (LW) expansion

$$\omega = q \left(\frac{M-1}{M+1} \right) \alpha + O(\alpha^2) \quad (6.3)$$

the leading term of which can be recognized as the Saffman-Taylor (1958) term, and the short wavelength (SW) limit

$$\omega \rightarrow \omega_{max} = q \max_{\xi} \frac{d \ln \mu}{d \xi} \text{ as } \alpha \rightarrow \infty \quad (6.4)$$

All other eigenvalues are subdominant.

(ii) When $M < 1$, the dominant eigenvalue has the different LW expansion

$$\omega = q \omega_2 \alpha^2 + O(\alpha^3) \quad (6.5)$$

the SW limit remaining the same as in (6.4). Here, ω_2 is a non-negative constant (positive in the non-monotonic mobility case and zero, otherwise) with dimensions of length. For example,

$$\omega_2 = \frac{4}{\pi^2} \left(\int_{\xi_0}^{\infty} \sqrt{\frac{d \ln \mu}{d \xi}} d \xi \right)^2 \quad (6.6)$$

where we assumed $\frac{d \ln \mu}{d \xi} \geq 0$ for $\xi \geq \xi_0$ and $\frac{d \ln \mu}{d \xi} = 0$ at $\xi = \xi_0$. A mode with the Saffman-Taylor behavior (6.3) also exists, but it is subdominant. For this case, therefore, the ratio $\frac{M-1}{M+1}$ is not the relevant instability index.

In MH the linear stability analysis includes dispersion following a quasi-steady-state approximation, as in previous works (Gardner and Ypma, 1982, Tan and Homsy, 1986, Yortsos and Zeybek, 1988, and Bacri et al., 1992). Analytical results were derived (when $\Lambda > 0$, see below), for the LW expansion of an arbitrary base state. At leading-order, the dominant eigenvalue was found to have the same LW expansion as (6.3), except that the role of the index $\frac{M-1}{M+1}$ is here played by

$$\frac{1}{2} \Lambda = - \frac{\left(\frac{d \mu}{d C} \right)_{C=0} + \left(\frac{d \mu}{d C} \right)_{C=1}}{2(\mu_0 + \mu_1)} \quad (6.7)$$

Thus, in the MH analysis, it is the difference in the derivative of the mobility at the end-points, rather than the mobility itself, that dictates LW instability. MH also analyzed numerically the stability of more general, diffuse profiles, parametrized by time, and reached the following conclusions:

(i) When $M > 1$, the displacement is LW unstable, as long as $\Lambda > 0$. However, if $\Lambda < 0$, a critical time, to be subsequently denoted by $t_{c,1}$, was found, below which the displacement is unconditionally stable. $t_{c,1}$ is of the order of $D_{||}/q^2$, at which time the base state has spread over a distance of the order of a pore (assuming that $D_{||} \sim a q$, where a is a characteristic measure of the microstructure). This result, predicting stability, even though the end-point mobility ratio is unfavorable, is unexpected.

(ii) When $M < 1$, another critical time, to be denoted by $t_{c,2}$, was found such that the displacement is unconditionally stable for $t < t_{c,2}$. For appropriate viscosity functions, this critical time can be several orders of magnitude larger than $t_{c,1}$, thus corresponding to a base-state spread over a sufficiently large number of pores for a continuum description to be acceptable. The existence of such a critical time, above which a displacement with $M < 1$ may become unstable, is a key

contribution of MH. The authors explained the onset of this instability in terms of the spreading of the base-state due to diffusion, hence of the development of unfavorable mobility regions, using an extension to small wavelengths of their LW instability criterion (6.7) based on Λ .

In this note, we follow a different approach to this problem. First, we provide a heuristic method which explains the main findings of MH, particularly those of (ii) above, but in which the main parameter is $M - 1$ rather than Λ . The validity of this method in the large time limit, $\epsilon = \frac{D_{\parallel}}{bq} \ll 1$ is subsequently discussed. Here, we note the relationship $\epsilon = \frac{1}{2\sqrt{t_D}}$, where t_D is the dimensionless time of MH.

THEORY

Consider the linear stability of

$$\frac{\partial C}{\partial t} + \mathbf{q} \cdot \nabla C = D_{\parallel} \frac{\partial^2 C}{\partial x^2} + D_{\perp} \frac{\partial^2 C}{\partial y^2} \quad (6.8)$$

where y is the transverse direction, and

$$\mathbf{q} = -\frac{k}{\mu(C)} \nabla P \quad (6.9)$$

with

$$\nabla \cdot \mathbf{q} = 0 \quad (6.10)$$

Assume, next, that the effect of longitudinal dispersion is only in the development of the base state (for example, as in (6.1), and which will be used to scale the profile's dependence on ξ) and not in the stability analysis, in which we will keep only the effect of transverse dispersion. This separation of the effect of dispersion is consistent with the qualitative interpretation of the main effect of dispersion given in MH. By taking normal modes $c' = \Sigma \exp(\omega t + i\alpha y)$, $p' = \Pi \exp(\omega t + i\alpha y)$, and proceeding as in HY, we obtain the following eigenvalue problem

$$\mu(\bar{C}) \frac{d}{d\xi} \left[\frac{1}{\mu(\bar{C})(\omega + D_{\perp} \alpha^2 - \frac{q}{\mu(\bar{C})} \frac{d\mu}{d\xi})} \frac{d\Pi}{d\xi} \right] = \frac{\alpha^2 \Pi}{\omega + D_{\perp} \alpha^2} \quad (6.11)$$

Define, now

$$\sigma' \equiv \omega + D_{\perp} \alpha^2 \quad (6.12)$$

and make the further substitution $\Psi = \frac{\Pi}{\mu}$. Upon integration, the resulting problem becomes identical to (6.2), but with σ' substituted in place of ω . Consider now the rescaled variables $n = b\alpha$ and $s = \frac{b\sigma'}{q}$, and $\bar{C} = \bar{C}(z) \equiv \frac{1}{2} \operatorname{erfc} z$, where $z = \xi/b$, in terms of which the eigenvalue problem reads

$$\frac{d}{dz} \left[\mu \frac{d\Psi}{dz} \right] = n^2 \left(\mu - \frac{1}{s} \frac{d\mu}{dz} \right) \Psi \quad (6.13)$$

Given, therefore, the $\bar{C}(z)$ dependence (e.g. the erfc solution) and a $\mu(C)$ functional relation (here, non-monotonic), the solution of (6.13) provides the dimensionless growth rate, $s \equiv s_{HY}(n)$, in terms of $s_{HY}(n)$, the properties of which were studied in detail in HY.

We recall that the dominant eigenvalue has the asymptotic behavior (6.3)-(6.5)), namely

(i) $s \sim \left(\frac{M-1}{M+1}\right)n$ when $M > 1$, and $s \sim s_2 n^2$ when $M < 1$, at small n , where in parallel with (6.6) we have

$$s_2 = \frac{4}{\pi^{\frac{5}{2}}} \left(\int_{z_0}^{\infty} \sqrt{-\frac{d\ln\mu}{d\bar{C}}} \exp(-z^2/2) dz \right)^2 \quad (6.14)$$

(ii) $s \rightarrow s_{max} = \max_z \frac{d\ln\mu}{dz}$ at large n .

For a non-monotonic viscosity profile, $s_{HY}(n)$ is positive (and so are s_2 and s_{max}) and monotonically increasing (see Figure 6.1). Back substitution in (6.12) gives the following result for the rate of growth

$$\omega(\alpha; b) \approx -D_{\perp} \alpha^2 + \frac{q}{b} s_{HY}(b\alpha) \quad (6.15)$$

This relation is the main result of this note. It shows that in this approximation the growth rate consists of the additive contributions of a viscous instability (second term in the RHS of (6.15)) and of a transverse dispersion stability (first term in the RHS of (6.15)). Longitudinal dispersion enters indirectly through b , which scales with the square root of time and affects the magnitude of the destabilizing contribution. From the properties of s_{HY} , it is apparent that for a fixed wavenumber α , the destabilizing contribution increases with time (increasing b), until a maximum is reached, following which the instability decays asymptotically. The following results follow from (6.13)-(6.15):

- (i) When $M > 1$, the problem is LW unstable (but SW stable), regardless of the particular mobility details. This prediction differs from the findings of MH, which rely on the sign of Λ (see also below).
- (ii) When $M < 1$, the displacement is stable at sufficiently small b (or t). As t increases, however, b also increases, as a result of longitudinal dispersion, and a critical time t_c may be reached when the displacement becomes unstable. To show this more concretely, consider the LW expansion of (6.15), which reads (e.g. compare with (6.5))

$$\omega \sim -D_{\perp} \alpha^2 + q b s_2 \alpha^2 = \alpha^2 (-D_{\perp} + s_2 q b) \quad (6.16)$$

For the non-monotonic case, we have $s_2 > 0$, thus, at a sufficiently large time, $t = t_c$, (sufficiently large b), the quantity in parenthesis becomes positive and instability will set in. This result is in qualitative agreement with the effect of the longitudinal dispersion in promoting instability, discovered by MH. Comparison with (6.14) shows that t_c increases as the degree of non-monotonicity decreases. However, in our approach, it is the aggregate behavior of the mobility profile, for example as reflected in the integral of (6.14), rather than the end-point mobility derivatives, which controls the onset of this instability. One should also note that because of the infinite family of eigenvalues of (6.13), the rate of growth contains a similar multiplicity (evidence of multiplicity was also found numerically in MH). Because in the non-monotonic case $s_{HY} > 0$, this multiplicity is restricted to eigenvalues $s > 0$, namely to $\omega + D_{\perp} \alpha^2 > 0$. This is also consistent with the numerical findings of MH.

Typical dispersion curves obtained from (6.15) are shown in Figures 6.2 and 6.3 for two characteristic viscosity profiles taken from the representation used in MH and for the case of isotropic dispersion. In the Figures we plot the dimensionless rate of growth, $\sigma = \frac{\omega D_{\parallel}}{q^2}$, vs. the dimensionless wavenumber, $k = \epsilon a b$, as defined in MH. The case $M > 1$ (Figure 6.2) shows instability for all profiles (all times t). This is in contrast to Figure 6.7a of MH. On the other hand, the case $M < 1$ (Figure 6.3) clearly shows the effect of longitudinal dispersion (time) in making conditionally unstable an initially stable profile (although the rather small values of the rate of growth should be noted). This is consistent with the main findings of MH.

Although correctly predicting the main qualitative features, equation (6.15) cannot be expected to be in strict quantitative agreement with MH, certainly not in the case $bq/D_{||} = O(1)$. For example, the mismatch with the step profile predictions of MH is due to the fact that the latter actually correspond to the long-wave limit, but with the product $D_{||}a/q$ fixed (large diffusion). The same problem arises in the analysis of the Orr-Sommerfeld equation using step profiles (e.g. see Drazin, 1981) and has also been noted in the stability of immiscible displacements in porous media (see Huang and Yortsos, 1984). A closer agreement should exist when time is large compared to $D_{||}/q^2$, namely in the limit $\epsilon \ll 1$. It should be pointed out that in the present context, this limit is actually the most physically relevant, as the base state has time to spread to a sufficient extent over the microstructure for the continuum equations used in the present description to be used with confidence. (The same cannot be said when time is of the order of $D_{||}/q^2$, as is the case with t_{c1} , where the profile varies sharply over distances of the order of the microscale. This may be the origin of the intuitively unexpected prediction of MH when $M > 1$ and $\Lambda < 0$, see above).

Consider, now, the full eigenvalue problem including dispersion. In our nomenclature, we obtain the fourth-order system

$$\epsilon \Sigma_{zz} - \Sigma \left(s + \frac{\lambda_z}{\lambda} \right) + \lambda \left(\frac{\Psi_z}{\lambda} \right)_z \bar{C}_z = 0 \quad (6.17)$$

and

$$\Psi_{zz} - \frac{\lambda_z}{\lambda} \Psi_z - n^2 \Psi = \Sigma \frac{\lambda_z}{\lambda \bar{C}_z} \quad (6.18)$$

where we defined the mobility $\lambda = 1/\mu$. In the relevant limit $\epsilon \rightarrow 0$, a numerical analysis of (6.17) and (6.18) showed that $s \rightarrow s_{HY}(n)$, although non-uniformly in n . At small n , of main interest to the present study, this limit is singular and a boundary layer, $\delta(\epsilon)$ (where $\delta(\epsilon) \rightarrow 0$, as $\epsilon \rightarrow 0$) must be inserted, namely

$$s = s_{HY}(n)g \left(\frac{n}{\delta(\epsilon)} \right) \quad (6.19)$$

From our numerical results, the cross-over function $g(u)$ approaches 1 as $u \rightarrow \infty$, although its particular behavior at $u \rightarrow 0$ depends on the mobility profile details at the end points. In this limit, therefore, the quantitatively correct expression for ω should read

$$\omega(\alpha; b) = -D_{\perp} \alpha^2 + \frac{q}{b} s_{HY}(b\alpha) g \left(\frac{b\alpha}{\delta(\epsilon)} \right) \quad (6.20)$$

which should replace (6.15) for accurate quantitative predictions. The main effect of this correction is to shift the critical wavenumber at which instability first sets in to a larger value, in agreement with the numerical results of MH. The specific features of $\delta(\epsilon)$ and of the small u behavior of $g(u)$ require further study.

REFERENCES

1. Bacri, J.-C., Salin, D., and Yortsos, Y.C., Analyse linéaire de la stabilité de l'écoulement de fluides miscibles en milieux poreux, C.R. Acad. Sci. Paris, Vol. 314, 139-144 (1992).
2. Drazin, P.G., Discontinuous velocity profiles for the Orr-Sommerfeld equation, J. Fluid Mech., Vol. 10, 571-586 (1961).

3. Gardner, J.W., and Ypma, J.G.J., SPE paper 10686, presented at the 1982 SPE Enhanced Oil Recovery Symposium, Tulsa, OK (1982).
4. Hickernell, F.J., and Yortsos, Y.C., Linear stability of miscible displacement processes in porous media in the absence of dispersion, *Stud. Appl. Math.*, Vol. 74, 93-115 (1986).
5. Loggia, D., Rakotomalala, N., Salin, D., and Yortsos, Y.C., Evidence of new instability thresholds in miscible displacements in porous media, *Europhys. Lett.*, Vol. 32, 633-638 (1995).
6. Manickam, O., and Homsy, G.M., Stability of miscible displacements in porous media with nonmonotonic viscosity profiles, *Phys. Fluids A*, Vol. 5, 1356-1367 (1993).
7. Manickam, O., and Homsy, G.M., Fingering instabilities in vertical miscible displacement flows in porous media, *J. Fluid. Mech.*, Vol. 288, 75-102 (1995).
8. Saffman, P.G., and Taylor, G.I., The penetration of a fluid into a porous medium or Hele-Shaw cell containing a more viscous liquid, *Proc. Roy. Soc. London.*, Vol. A 24, 312-329 (1958).
9. Tan, C.T., and Homsy, G.M., Stability of miscible displacements in porous media: Rectilinear flow, *Phys. Fluids*, Vol. 29, 3549-3556 (1986).
10. Yortsos, Y.C., and Huang, A.B., Linear stability analysis of immiscible displacement: Part 1- Simple basic flow profiles, *SPE Reservoir Engineering*, 378-390 (1986).
11. Yortsos, Y.C., and Zeybek, M., Dispersion-driven instability in miscible displacement in porous media, *Phys. Fluids*, Vol. 31, 3511-3518 (1988).

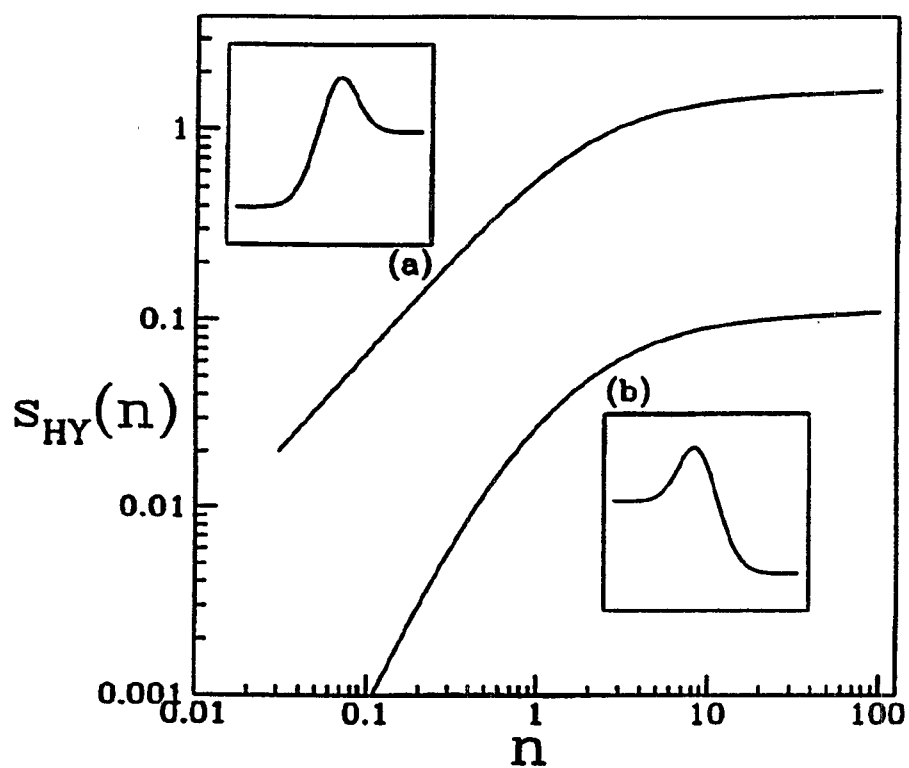


Figure 6.1. The dominant eigenvalue $s_{HY}(n)$ for a non-monotonic viscosity profile with $M > 1$ (curve a) and $M < 1$ (curve b) .

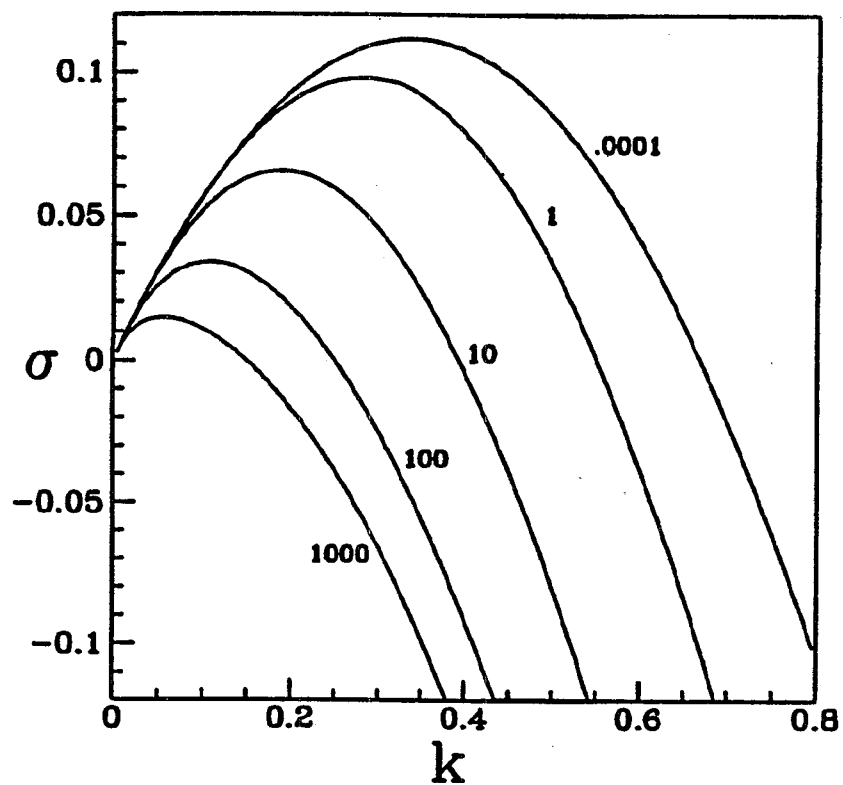


Figure 6.2. The dispersion relation $\sigma(k; \epsilon)$ for different values of the dimensionless time $\frac{1}{4\epsilon^2}$ as predicted from equation (6.15) for the conditions of case (a) of Figure 1.

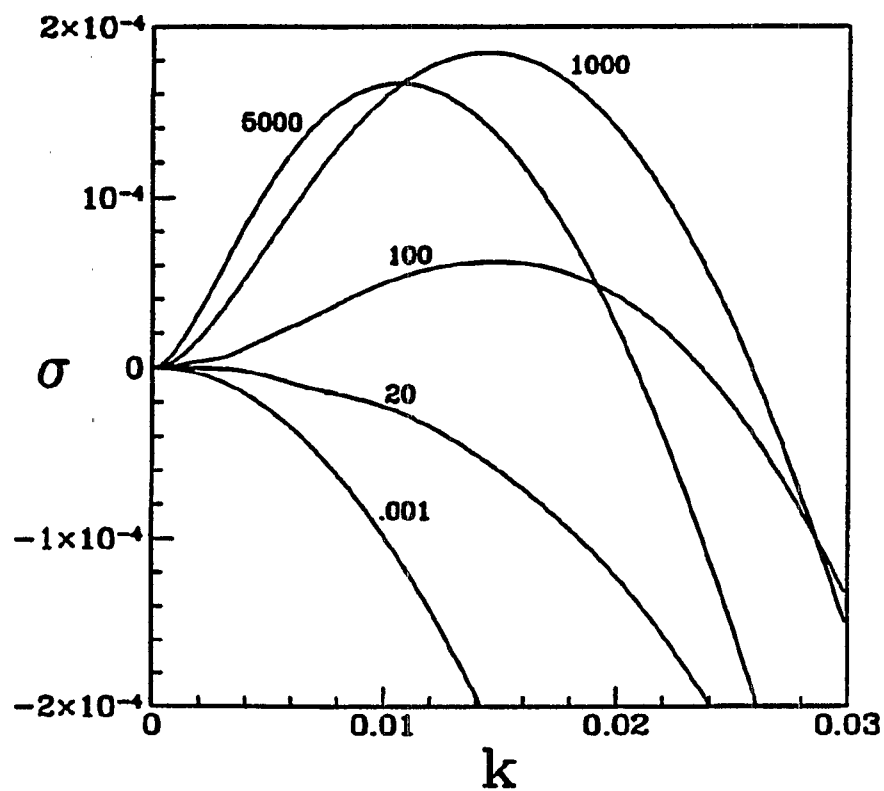


Figure 6.3. The dispersion relation $\sigma(k; \epsilon)$ for different values of the dimensionless time $\frac{1}{4\epsilon^2}$ as predicted from equation (6.15) for the conditions of case (b) of Figure 1.

Chapter 7

CONCLUSIONS

In this report we presented studies on *NAPL* immiscible displacement patterns using pore-network simulation, *NAPL* dissolution experiments using micromodels, the theory of mass transfer in porous media using distributed sources, the development of single-pore flow instabilities in non-monotonic viscosity fluids, expected in solvent flushing, and the stability of displacements in porous media using the same fluids.

The effect of viscous forces on drainage displacements in porous media was studied. We recognized that the process, at least near the front, shares common aspects with *IPG*. When M is sufficiently small, the displacement can be modeled by a form of Gradient Percolation in a *stabilizing* gradient. We developed the scaling of the front width and the saturation profile, in terms of the capillary number. As the stabilized regime is described by the Buckley-Leverett equation, the two share the same constraints for their validity. In the opposite case, the displacement is described by Gradient Percolation in a *destabilizing* gradient and leads to fingering. The particular regime involves a competition between capillary and viscous forces and was identified for the first time in the context of viscous displacements. The theory shows that the conventional continuum approach should be used with caution near the front.

We used pore network models, both full-scale simulation and simpler statistical physics models, for describing immiscible displacement patterns. In particular we used a simple version of *IPG* with both transverse and parallel gradients, to simulate the spreading of *DNAPLs*. It was shown that the spreading of *DNAPL* on the top of an impermeable medium may well have strong percolation (namely fractal-like) characteristics, when the rate of penetration is slow, so that gravity and capillarity dominate over viscous forces (and also in the case of unfavorable mobility ratio). In such cases, the percolation characteristics must be carefully considered in the design of remediation processes.

Subsequently, we reported on visualization experiments and numerical simulations in pore networks conducted to understand basic aspects of mass transfer during the solubilization of residual *NAPLs*. The experiments were carried out in 2-D etched-glass micromodels with randomly distributed pore sizes. We monitored the concentration of the effluent at steady-state as a function of the Peclet number to study the dependence of the overall mass transfer rate on injection velocity. A pore network numerical model, based on the convection-diffusion equation using appropriate modifications for the local mass transfer coefficients, was developed to simulate mass transfer during the solubilization of a residual phase. The pore network simulator was found to match well the experimental results, provided that the local mass transfer was properly accounted for. Expressions for mass transfer over cavities were used to represent the latter. Sensitivity studies were subsequently conducted to investigate the dependence of the overall solubilization rate on parameters,

such as the Peclet number. A scaling law was developed for the resulting overall mass transfer rate assuming a uniform local mass transfer coefficient.

In the subsequent chapter, we developed a theoretical analysis and a corresponding numerical simulation of convective mass transfer from stationary distributed sources in a porous medium. The key assumption made in the analysis is the use of a traditional, effective porous medium description in the porespace outside of the sources, coupled with a flux condition (rather than a constant concentration condition) at the source interface, to reflect the effect of the local microstructure on the mass transfer rate, as well as the fact that the effective description breaks down in such places. We developed theoretical predictions for the dependence of the overall mass transfer coefficient on the flow velocity and the source geometry. In general, we derived the asymptotics of the problem at both small and large Pe_L . We expect that the asymptotics at low Pe_L should be particularly useful to macroscopic simulations. It was shown that the large Pe_L behavior reflects the local mass transfer exponent c , thus offering an interpretation on the various experimental correlations. Particular emphasis was placed on mass transfer from a self-similar surface, such as a Koch curve or a percolation cluster. A scaling theory was proposed for these surfaces but not proved. Additional work is needed in this direction. Finally, we established a connection between the macroscopic equation typically used for analyzing data, and the microstructure of the problem, and used pore-network simulation to compute the effective parameters. This methodology should be useful for macroscopic simulation.

Finally, it was shown that non-monotonic viscosity concentration profiles have an important effect on miscible displacements. As a general observation, the displacement profiles have the characteristics of both favorable and unfavorable displacements. This can be explained by the fact that the non-monotonic viscosity concentration profiles possess two regions, one in which the viscosity increases with concentration (unfavorable local mobility ratios), and the other in which the reverse is true. Instabilities were shown to exist both at the large-scale (Darcy scale) and at the small (single-pore) scale, provided that a sufficiently strong non-monotonicity was imposed. The instabilities exist even when the two pure fluids have equal viscosities. This rather interesting behavior needs to be analyzed further at the pore-scale. A further discussion of the large-scale instabilities was also presented, emphasizing the importance of diffusion in the onset, growth and decay of the instabilities.